Moment Method in Rarefied Gas Dynamics: Applications to Heat Transfer in Solids and Gas-Surface Interactions

by

Alireza Mohammadzadeh
B.Sc., University of Tehran, 2009
M.Sc., Ferdowsi University of Mashhad, 2012

A Dissertation Submitted in Partial Fulfillment of the
Requirements for the Degree of

DOCTOR OF PHILOSOPHY

in the Department of Mechanical Engineering

Moment Method in Rarefied Gas Dynamics: Applications to Heat Transfer in Solids and Gas-Surface Interactions

by

Alireza Mohammadzadeh
B.Sc., University of Tehran, 2009
M.Sc., Ferdowsi University of Mashhad, 2012

Supervisory Committee

Dr. Henning Struchtrup, Supervisor
(Department of Mechanical Engineering)

Dr. Peter Oshkai, Departmental Member
(Department of Mechanical Engineering)

Dr. Reuven Gordon, Outside Member
(Department of Electrical Engineering)

Supervisory Committee

Dr. Henning Struchtrup, Supervisor
(Department of Mechanical Engineering)

Dr. Peter Oshkai, Departmental Member
(Department of Mechanical Engineering)

Dr. Reuven Gordon, Outside Member
(Department of Electrical Engineering)

ABSTRACT

It is well established that rarefied flows cannot be properly described by traditional hydrodynamics, namely the Navier-Stokes equations for gas flows, and the Fourier's law for heat transfer. Considering the significant advancement in miniaturization of electronic devices, where dimensions become comparable with the mean free path of the flow, the study of rarefied flows is extremely important. This dissertation includes two main parts.

First, we look into the heat transport in solids when the mean free path for phonons are comparable with the length scale of the flow. A set of macroscopic moment equations for heat transport in solids are derived to extend the validity of Fourier's law beyond the hydrodynamics regime. These equations are derived such that they remain valid at room temperature, where the MEMS devices usually work. The system of moment equations for heat transport is then employed to model the thermal grating experiment, recently conducted on a silicon wafer. It turns out that at room temperature, where the experiment was conducted, phonons with high mean free path significantly contribute to the heat transport. These low frequency phonons are not considered in the classical theory, which leads to failure of the Fourier's law in describing the thermal grating experiment. In contrast, the system of moment equations successfully predict the deviation from the classical theory in the experiment, and suggest the importance of considering both low and high frequency phonons at room temperature to capture the experimental results.

In the second part of this study, we look into the gas-surface interactions for conventional gas dynamics when the gas flow is rarefied. An extension to the well-known Maxwell boundary conditions for gas-surface interactions are obtained by considering velocity dependency in the reflection kernel from the surface. This extension improves the Maxwell boundary conditions by providing an extra free parameter that can be fitted to the experimental data for thermal transpiration effect in non-equilibrium flows. The velocity dependent Maxwell boundary conditions are derived for the Direct Simulation Monte Carlo (DSMC) method and the regularized 13-moment (R13) equations for conventional gas dynamics. Then, a thermal cavity is considered to test and study the effect of these boundary conditions on the flow formation in the slip and early transition regime. It turns out that using velocity dependent boundary conditions allows us to change the size and direction of the thermal transpiration force, which leads to marked changes in the balance of transpiration forces and thermal stresses in the flow.

Contents

List of Figures

ACKNOWLEDGEMENTS

First and foremost, I would like to express my deepest gratitude to my teacher and research guide Prof. Henning Struchtrup, whose encouragement, guidance and support during my study and research at University of Victoria enabled me to develop an understanding of the subject. He showed me how to think and question everything, that led to amazing years of research for me. I would have been lost without him.

I deeply acknowledge the support from my friends and colleagues Dr. Anirudh Rana, Michael Fryer, Behnam Rahimi, Samira Soltani, Alex Beck, John Jancowski, Meysam Karimi, Devesh Bharadwaj for providing a stimulating and fun environment in which I learned and grew.

I would like to thank my teachers and friends at Ferdowsi University of Mashhad, Dr. Ehsan Roohi whose passion and insights in the DSMC method enlightened new ideas for this research.

My deepest gratitude goes to my parents and my two beautiful sisters, Leila and Zahra, for their love and blessings. Without their encouragement, understanding and loving, this research would never been finished.

The financial support of Natural Sciences and Engineering Research Council (NSERC) of Canada is gratefully acknowledged.

Alireza Mohammadzadeh
Victoria, BC
Fall 2016

Chapter 1

Introduction

As a result of recent technological advances of micro- and nano-machining and fabrication, the miniaturization of mechanical and electrical devices has become an important focus of interest [41]. This rapid development of micro/nano electro mechanical systems (MEMS/NEMS) requires a deeper understanding of the flow characteristics and heat transfer mechanisms at micro/nano scales.

One important area of research in nano-technology is the study of heat transport. The tiny size of modern electronic systems combined with their relative large heat fluxes can lead to huge changes in temperature. Therefore, we need accurate models for heat transfer that guarantee an effective long-lasting thermal design of modern micro/nano scale systems [70].

The heat transfer in solids can be studied and described using the phonon model. Phonons are the particle representative of the energy waves, that are generated due to vibration of atoms around their mean position on the crystal lattice [42]. Using the phonon gas model, the energy transport inside a solid can be treated analogous to the transport processes in gases [17, 20].

Gas flows at micro scale can exhibit very different behavior than macro scale. Effects that are negligible at macro scales can dominate at micro and nano scales. For example, the characteristic length of a flow can become small enough that surface effects at interfaces dominate over the bulk properties of the flow, and lead to a breakdown at the classical laws of continuum mechanics.

Despite the differences between the heat transfer in solids, and the conventional gas flows at interfaces, they can both be modeled using the transport process of rarefied gas dynamics.

When the mean free path λ, i.e., the average distance that a particle travels between successive collisions becomes comparable with the characteristic length of the flow domain L, the flow exhibits rarefaction effects. This includes development of the Knudsen layer in which the gas undergoes velocity slip and temperature jump at the surface [10], as well as the appearance of the second sound effect that transfers heat in solids [28].

The degrees of rarefaction in a gas is characterized by the Knudsen number, Kn, which is the ratio of the mean free path to the characteristic length of the flow domain, $\mathrm{Kn} = \frac{\lambda}{L}$. Based on the value of the Knudsen number, the gas flow can be classified into four regimes, namely, hydrodynamic flow regime (for $\mathrm{Kn} \lesssim 0.001$), slip flow regime (for $0.001 \lesssim \mathrm{Kn} \lesssim 0.1$), transition regime (for $0.1 \lesssim \mathrm{Kn} \lesssim 10$), and free molecule flow regime (for $\mathrm{Kn} \gtrsim 10$) [41].

The classical Navier-Stokes equations for gas flows and the Fourier's law for heat transfer are only valid in the hydrodynamic regime, where the deviation from equilibrium state is very small, i.e., $\mathrm{Kn} \ll 1$ [41]. In order to properly describe the rarefied flow outside the hydrodynamic regime, we need an extended form of macroscopic equations that are easy to solve, and can indeed capture rarefaction effects.

In this dissertation we look into the rarefied flows, and use the *moment method* as a tool to derive extended macroscopic models for this regime. This dissertation includes two main parts.

First, we look into the heat transfer problem in solids when the size of the flow is small enough, that the classical theory for heat transfer is not valid anymore. In this part, we extend a macroscopic model beyond the continuum regime to model heat transport in the crystal lattice.

In the second part, we look into the gas-surface interactions for conventional gas-dynamics in rarefied flows. In this part, we propose an extension to the classical Maxwell boundary conditions to provide a more general boundary model for thermally driven rarefied flows.

Despite the differences between solids and gases, we look into the unconventional phenomena that appear due to rarefaction effects in both systems, and use the moment method to identify and describe them.

This dissertation follows the paper-based format, where each chapter is already published or ready for submission as a journal article.

1.1 Heat transport in solids

In the first part of this dissertation we derive a macroscopic model for heat transport beyond the hydrodynamic regime. This part includes chapters 2 and 3.

1.1.1 Phonons and energy transport

Atoms are fixed in a crystal lattice, and hold their average positions by the attractive/repulsive intermolecular forces. These forces can be Lennard-Jones potential, ionic bonds, covalent bonds or metallic bonds [42, 75]. The energy is transported in solids when atoms vibrate around their mean positions on the crystal lattice. The particle representative of the resulting energy wave due to these vibrations is called phonon. Phonons have energy and momentum; they can interact among themselves and with other particles, including photons, electrons, and crystal boundaries. They can also interact with crystal impurities and dislocations and lose momentum [42]. The thermal properties of the crystal, such as temperature and heat flux can be obtained by taking appropriate averages of microscopic properties of the phonon gas. In order to describe phonons, one can use the classical approach or employ the quantum mechanics to study the phonon transport.

In the classical approach, the crystal is modeled by a chain of particles that are connected to each other by ideal springs. Using Hooke's law to derive the equation of motion for atoms in the crystal, gives the general solution as the superposition of plane harmonic waves. In order to describe the energy transfer [42], these waves should be localized as packets of waves, which are called phonons in the classical theory. The classical theory of phonons, however, is limited in capturing some features of phonons, including interaction of lattice waves and the thermal expansion [42].

The important properties from quantum mechanics allow phonons to be localized as particles instead of waves. In the phonon model the crystal is replaced by a box containing the gas of phonons, such that the energy transport can be treated analogous to the transport processes in gases [17, 20]. The eigen-vibration of the lattice with the frequency ω and the wave vector $\mathbf{k}$ in the crystal corresponds to phonons with the energy $\hbar\omega$ and the momentum $\hbar\mathbf{k}$, where $\hbar$ is Planck's constant. The dispersion relation $\omega(\mathbf{k})$ determines the relationship between the frequency and the wave vector, which follows from the quantum mechanics equation of motion for atoms in the crystal [42]. This relation is periodic in nature, with a full period equal to the Brillouin zone. Phonons travel with the group velocity, $\mathbf{c} = \frac{\partial\omega}{\partial\mathbf{k}}$.

In the phonon model, we distinguish between the optical phonons and the acoustic phonons. The optical phonons only appear at high frequencies, when the smallest unit cell in the crystal has more than one atom. Optical phonons can be neglected in single element crystal, and at moderate temperatures [42]. The acoustic phonons, however, have all range of frequencies, and polarize into 2 transversals and 1 longitudinal modes.

We distinguish two types of phonon interactions, *Normal* and *Resistive* processes. In the Normal process, phonons conserve both energy and momentum, while in the Resistive process only the energy remains conserved.

These two types of interactions lead to three different modes of heat transfer is solids. The *diffusive* heat transfer happens when Resistive phonon-phonon interactions are the dominant process in the flow. In this regime, energy waves are damped in a very short length, and the Fourier's law governs the heat transfer process [42]. The second mode takes place when the Normal processes are the dominant phonon-phonon interactions, which leads to a wave like energy transport known as the *second sound* [19, 28]. The third mode happens when the energy is transported via *ballistic* phonons [31],i.e., phonons that travel inside the crystal without any interactions.

Fourier's law only considers the diffusive heat transfer, and cannot provide agreement with the experimental data when the other two mechanisms are also playing a role in the energy transfer.

1.1.2 Phonon transport

Microscopic approach

The phonon-Boltzmann equation describes the transport of phonons in the crystal lattice [64]. This equation relates the time evolution of the phonon distribution function to phonon convection and collisions with other phonons, as well as other particles. While the phonon-Boltzmann equation is valid for all degrees of rarefaction, its direct solution, due to the complexity in the phase-space dimension as well as the non-linearity in the collision term, is a formidable task [13].

Due to the complexity of the collision term in this equation, the well-known Callaway model [9] was proposed to provide an approximation for the collision term. In this model, the collision is described as a process that relaxes the distribution function of phonons to the appropriate equilibrium state for the collision type, with the relaxation time τ that needs to be provided.

Many different relaxation time models have been proposed to express the collision process. The well-known Klemens's model [43] considers a quadratic dependency of the

Resistive relaxation time on the frequency of phonons, $\tau_R(\omega) \sim \frac{1}{\omega^2}$ in the bulk of a pure crystal. This model provides good agreement with the experimental results for the thermal conductivity of the crystal at low and relatively high temperatures [43]. However, the model was originally obtained for low-frequency phonons, i.e., at low temperatures. More recently, by using the ab initio approach [100], it was seen that at higher frequencies (room temperature) the dependency of the Resistive relaxation time on the frequency becomes stronger, and is better modeled by $\tau_R(\omega) \sim \frac{1}{\omega^4}$.

Macroscopic approach

Macroscopic approaches provide an alternative to describe the energy transport, using macroscopic properties of the crystal. In the classical theory, the Fourier's law relates the heat flux to the gradient of the energy in the crystal. When the mean free path for the Resistive process is very smaller than the length scale of the flow, i.e., $\mathrm{Kn}_R \ll 1$, by performing Chapman-Enskog expansion [12] on the phonon-Boltzmann equation equipped with Callaway model, one can obtain Fourier law as the heat flux equation. Fourier law provides an explicit expression for the thermal conductivity, that can be determined by experimental measurements. However, since the second sound and ballistic phonons are not included in Fourier law, it cannot provide satisfactory results when diffusion does not dominate the heat transport process [22, 49, 15].

Another approach to derive a macroscopic model from the phonon-Boltzmann equation is using the well-known Grad's moment method [26]. In this method, macroscopic moments are defined using moments of the distribution function for phonons. Then, the transport equations for these macroscopic moments are derived by taking integral moments of the phonon-Boltzmann equation. The degrees of rarefaction, characterized by the Knudsen number, determines the required number of macroscopic transport equations in this approach. The system of Grad's moment equations are then closed using the distribution function, by relating higher order fluxes to the macroscopic moments [26].

Considering that we neglect the effect of electrons and their contributions to heat transfer in this study, the resulting system of equations will only predict the process of heat transfer in materials with no or very small population of free electrons. This means that the resulting equations are capable of predicting heat transfer in non-conductors as well as semi-conductors [103]. In metals, the contribution of electrons to heat transfer dominates, and must be addressed and considered in the governing equations.

1.1.3 Earlier Studies

For relatively low temperatures, the dispersion relation can be approximated as a linear relation, where the frequency of phonons is related to the wavevector by the constant Debye speed [42]. Debye speed is an appropriate average in the 3 polarizations for phonons [42]. Using Debye speed assumption, and considering relatively low temperatures, the equilibrium distribution function becomes zero towards the boundaries of the Brillouin zone. This provides an opportunity to expand the boundaries of integrations to infinity, when deriving macroscopic models from microscopic properties of phonons [61]. However, the validity of these assumptions are dependent on the working temperature of the system. One can show that for Silicon, Debye assumptions are only valid for temperatures less than $T < 65\ K$ [61].

In earlier studies, Struchtrup and co-workers [19, 24] proposed a simple macroscopic model for phonon transport in solids. They employed Debye assumption and considered *constant* relaxation time in Callaway model to derive a system of macroscopic equations. These two assumptions led to fast access to a system of moment equations that, in principle, could describe the phonon transport process, but in practice, could not provide good agreement with the experimental data. More specifically, this system of moments could not predict the rarefaction effects at the corresponding Knudsen number that was experimentally observed at the room temperature. The discrepancy was attributed to the simplifying assumptions employed in deriving the macroscopic equations.

1.1.4 Thermal grating experiment

Recently Johnson and his co-workers [38] used the laser-induced transient thermal grating technique to study the effect of length scale on the heat transfer regime. In this experiment, two recurring short laser pulses were crossed on a specimen to generate an interference pattern with period L, which was altered by changing the angle between the beams. As the laser beam was absorbed by the specimen, a periodic thermal profile was generated on the silicon wafer, and the decay of this temperature grating by thermal transport was monitored via diffraction of a probe laser beam.

In the experiment they used a $400nm$ thick silicon wafer with $400\times400\mu m^2$ freestanding area to ensure that the heat transport is one-dimensional. The above-band-gap photons were absorbed in the silicon membrane, which led to excitation of hot carriers. As the hot carriers relaxed to the bottom of the conduction band, the energy was transferred to the lattice and absorbed by the specimen [25]. Although the measurements were performed in the ambient air, the effect of thermal conductivity of air on the thermal grating decay in the membrane was negligible [38].

The pump laser pulses were detected with a continuous prob beam. The increased temperature in the silicon wafer induced changes in the transmittance, which led to a time-dependent diffraction of the continuous prob beam. In the experiment, they used optical heterodyne detection, where the diffracted signal was superposed with a reference beam to increase the signal level [53]. The signal and the reference beam were then directed to a detector, and the output was recorded on a oscilloscope.

The optical fields of the probe and the reference beams incident on the sample, were approximated as plane waves [89]. By assuming that the temperature grating is very small, Johnson et al. [89] showed that the intensity of the interference is determined by the amplitude of the temperature grating. The details of their calculations and employed optics assumptions are not shown in here and can be found in Ref. [89]. Johnson et al. reported the decay curve for the intensity of the signal, which is directly proportional to the decay of grating temperature.

In the thermal grating experiment the influence of electrons were also considered. The excitation of electrons, due to absorbing the laser beam, and their transport in the wafer which led to a diffraction pattern in the continuous wave probe beam was addressed when interpreting the results. Fortunately, the diffusion coefficient for ambipolar carriers in silicon is an order of magnitude larger than the thermal diffusivity [50]. Therefore, Johnson and his co-workers observed that the electronic and thermal relaxation were well separated in the time domain [38]. They observed that, first, the carrier grating completely relaxed due to the carrier diffusion, and then the thermal grating started to diffuse. For a typical experiment, the decay time for carriers was in the order of $1.7ns$ while for the thermal grating this value was around $26ns$.

The text-book mean free path for silicon is $\lambda = 43nm$. Considering that in semiconductors heat is mostly transported by phonons, the ratio of phonons mean free path λ and the length scale of the flow L determines the regime of this energy transfer, i.e, diffusive or ballistic. At low temperatures most phonons have rather large mean free path, which leads to ballistic phonon transport in that temperature range. At room temperature, the mean free path for most phonons are in the range of nanometers, therefore, one does not expect deviation from the diffusion equations when the length scale is significantly larger than nanometers.

However, theoretical and experimental studies [40] have suggested the role of phonons, with rather large mean free path, at room temperature. Researchers proposed to revise the effective mean free path for silicon at room temperature to $260-300nm$ to account for phonons with large mean free path [14]. One study shows that phonons with mean free path exceeding than $1\mu m$ have an almost 40% contribution to the thermal conductivity in silicon at the room temperature [35].

The thermal grating experiment motivated us to start again from the basis, and reconsider the assumptions to derive a macroscopic model that is also accurate at room temperature.

1.1.5 Methodology

In this contribution, we follow Grad's moment method and define macroscopic moments using a polynomial of frequency and wavevector of phonons. We consider a quadratic dispersion relation to accurately describe the dependency of frequency on wavevector at room temperature [67]. Moreover, the Brillouin zone is considered to be a sphere with finite radius, which depends on the working temperature of the system [42]. Most importantly, the dependency of relaxation time on frequency is considered in Callaway model, to account for phonon interactions at low and high frequencies [100]. The resulting system of equations extend the validity of diffusion equation further in to the rarefaction regime. By following Grad's method [26], we obtain boundary conditions for macroscopic moments. The free parameters in our macroscopic model are fixed using experimental data for specific heat and thermal conductivity. The resulting system of equations are used to study the heat transfer problem in a few simple geometries including the thermal grating experiment [38]. Good agreement with the experimental data is observed, that suggests the importance of considering frequency dependency in both relaxation times and the group velocity for phonons at room temperature.

Compared to other macroscopic models that were proposed to replace Fourier's law [19, 24, 31], the current system of equations is derived under less limiting assumptions. The employed simplifications used in earlier models where only valid at low temperatures, or when the frequency of R and N-processes have certain ratios. In deriving current moment equations , however, we do not put any limitation on this frequency, and these collisions are being treated independently.

The moment method provides a clear relation between the microscopic properties of phonons and macroscopic moments. Properties in the microscopic model can be altered, and the resulting effects will be observed in the macroscopic equations.

Moreover, the current system of equations provide a lot of freedom in the choice of relaxation time model. Different models for R and N-processes can be selected, and resulting matrices of production term can be compared.

In order to capture rarefaction effects by moment equations, we need to consider many macroscopic moments. Therefore, the resulting system of equations at the current form is large; it is hard to use this system for solving two and three dimensional heat transfer problems.

The resulting system of equations is a set of linear partial differential equations that can be solved in different geometries. This system of moments has the corresponding terms to describe the Knudsen layer is capable of capturing higher order rarefaction (higher than Fourier's order) effects, and gives a better approximation to the non-equilibrium phenomena than the classical theory.

Considering that the theories and measurements to obtain the mean free path of materials were classically done at low temperature ranges, and the phonons characteristics are different at higher temperatures, the system of moment equations can be used at room temperature to model the energy transport, and revise the mean free path.

1.2 Gas-Surface interactions in conventional gas dynamics

In the second part of this thesis we focus on conventional gas dynamics, and propose and evaluate a general boundary model for gas-surface interaction in rarefied flows. This part includes chapters 4, 5 and 6.

1.2.1 Rarefaction in gas flows

At sufficiently small Knudsen number classical hydrodynamics prevails. In this regime the slip velocity and temperature jump at the surface is small enough, that the gas at the boundary assumes velocity and temperature of the wall, and the classical constitutive relations for shear stress and heat flux are valid [77, 81]. In this limit of Knudsen number, the shear stress is only related to the gradient of velocity, i.e., Stokes' law, and the heat flux is only related to the gradient of temperature, i.e., Fourier's law. In this regime, the conservation equations for mass density, velocity and energy are closed using the Stokes and Fourier's law to provide a macroscopic model when the deviation from equilibrium is very small.

Rarefaction leads to deviation from this behavior, so that the Knudsen layer appears and the gas experiences velocity slip and temperature jump at the wall [10, 77, 81]. In the bulk of the flow, the shear stress is caused not only by the gradient of the velocity, but also by the gradient of the heat flux, known as thermal stress [77, 81]. A particularly interesting rarefaction boundary effect is transpiration flow (also known as thermal creep flow), [77, 72, 46, 68] where velocity slip is induced by a temperature gradient in the wall, i.e., the gas is forced into motion at the boundary. Based on this effect, small amounts of gas can be moved in Knudsen pumps [2].

The employed macroscopic model for the rarefaction regime should be complex enough to properly describe and capture these effects.

1.2.2 Gas-Surface interactions

While the microscopic interaction between gas particles and a solid boundary is a complicated affair, it is common in kinetic theory of gases to use simplified microscopic gas-wall interaction models. In the well-known Maxwell model [51] the particles hitting the surface are assumed to either thermalized with the wall, or perform specular reflection. In thermalization, the gas exchanges momentum and energy with the wall, while in the specular reflection only the normal momentum of the particle is inverted. The Maxwell model provides one single accommodation coefficient that is used to change the strength of the temperature jump and velocity slip [10].

Macroscopically, the interaction between gas molecules and solid walls manifests itself in temperature jump and velocity slip at the gas-surface boundary [81, 48, 11]. According to the measurements, the accommodation coefficients that describe the velocity slip and temperature jump are different, which shows the shortcoming of the Maxwell model to fully describe experiments [72].

Experiments with thermal beams show that the beam is scattered into a plume-like structure around the line of specular reflection [10, 36]. The structure of the reflected beam becomes particularly important when scattered particles are free to move for a long distance inside the bulk gas, i.e., rarefied flows. This plume-like structure is described and captured by Cercignani-Lampis (CL) model [11, 48], where the shape of the reflection plume strongly depends on the values of the normal and tangential accommodation coefficients, α_n and α_t. Although the CL model can be fitted to slip velocity and temperature jump, it does not provide sufficient flexibility to be fitted to the data for thermal transpiration coefficient [72].

For moderate Knudsen numbers, i.e., in the transition flow regime, the particles reflected from the surface travel a rather short distance before their first inter-molecular collision. In this regime the exact shape of the reflection plume is not required to express boundary conditions, but an appropriate approximation can model the gas-surface interaction. This motivated us to study the gas-surface interactions in early transition regime, and propose a model that is simpler than CL and can be fitted to the thermal transpiration coefficient.

1.2.3 Velocity dependent Maxwell model

The velocity dependent Maxwell (VDM) model presents a modification to the Maxwell's boundary conditions by including the corresponding term for isotropic scattering, as well as the dependency of microscopic accommodation coefficients on the microscopic impact velocity [83]. The isotropic scattering part of the reflection kernel accounts for those interactions that gas particles adiabatically exchange tangential momentum with the surface. This happens when the gas particle hitting the wall is considerably lighter than the surface particle [57]. In the VDM boundary conditions, a particle colliding with the surface is either thermalized, specularly reflected, or scattered in an arbitrary direction, where the probabilities for the different processes depend on the impact velocity. The model provides wide flexibility for the choice of the velocity dependent accommodation coefficients. We assume that the gas-wall interaction can be described as a thermally activated process, where particles with higher velocities are more likely to be specularly reflected or isotropically scattered from the surface, while particles with smaller velocity are more likely to be thermalized.

The VDM model is used to derive microscopic and macroscopic boundary conditions, and solve a thermally driven flow in the rarefaction regime.

1.2.4 Modeling rarefied gas flows

In this part, we use both microscopic and macroscopic approaches to model rarefied flows. Traditionally microscopic approaches provides high accuracy results at the expanse of large computational overheads. Macroscopic approaches, on the other hand, are more efficient in computational costs, but have limited validity in the rarefaction regime.

Microscopic approach

Considering the associated problems with the direct solution of the Boltzmann equation, particle methods provide an alternative to the direct solution of this equation. This includes deterministic approaches (like molecular dynamics) [54] to track each individual particle in the gas, or using statistical approaches (like DSMC) [5] to cloud a group of particles and study their behavior.

Employing the stochastic assumptions in the DSMC method compared to the deterministic nature of molecular dynamics significantly reduces the computational costs [5, 6]. The DSMC method used in this study follows the scheme proposed by Bird [5]. In this method the gas is modeled by using many independent simulating particles, where each particle is representative of a large number of gas molecules. The simulating particles move with different microscopic speed and collide; however, the motion and collision of the particles are assumed to be decoupled. The time step Δt is chosen as a fraction of mean collision time to ensure pure motion in the elapsed movement time [5]. In order to use the DSMC for flow simulation, the flow field must be divided into computational cells. The size of each cell should be small enough to result in small changes in thermodynamic properties across each cell. The cells provide geometric boundaries and volumes required for sampling the macroscopic properties. They are also used as a unit where only molecules located within the same cell at a given time are allowed for collision. The cells are then divided into sub-cells in each direction to facilitate the selection of collision pairs. In each time step particles perform a deterministic movement followed by stochastic collision. In the end, the macroscopic thermodynamic properties are sampled from molecular properties within each cell. The DSMC solutions are proved to converge to the solution of the Boltzmann equation in the limit of infinite simulating particles in each computation cell [97].

The DSMC method is a very powerful numerical tool, which can simulate very complicated process including polyatomic gases, dense gases, and chemical reactions [5, 6]. Although the DSMC method has been improved significantly over the past decade, it still suffers from expensive computational overheads. At small flow velocities the ratio of statistical noises, inherited by the nature of the DSMC, to the average speed of the flow becomes large, which increases the required computational overheads to get a converged solution [34]. More recently a variance-reduction formulation has been proposed to improve the traditional DSMC scheme, when the average velocity is small [33]. In this method, the stochastic particle description is only solved for the deviation from a nearby equilibrium, that leads to significant speed up compared to standard DSMC. In addition to the rather large computational costs in this particle method, due to its microscopic nature, the DSMC cannot provide further information regarding the causes of predicted rarefaction effects.

Macroscopic approach

In contrast to the microscopic methods, macroscopic equations can pinpoint the corresponding terms responsible for rarefaction effects. In the theory of macroscopic methods the behavior of a gas is described through physical quantities such as mass density, temperature, velocity, heat flux, stress tensor, and so on. In Grad's moment method for conventional gas dynamics [26], the Boltzmann equation is multiplied by the polynomial of velocities and is integrated over the velocity space. Grad's moment system, however, due to hyperbolicity predicts un-physical sub-shocks for Mach number $\mathrm{Ma} \gtrsim 1.65$. Struchtrup and Torrilhon [85, 81] combined elements of Chapman-Enskog expansion [12] method and Grad's moment method to obtain a system of equations that is valid up to the third order of Knudsen number, and presented regularized 13-moment (R13) equations. The R13 equations are always stable [80] and give smooth shock structures for all Mach numbers. Furthermore, the linear R13 equations are accompanied by an H-theorem [86], and are equipped with a complete set of boundary conditions [93].

1.2.5 Methodology

In the second part of this thesis, we employ the VDM reflection model [83] to account for the effect of impacting velocities of particles hitting the surface in the reflection kernel. The corresponding boundary conditions for the DSMC are obtained by sampling the velocities of particles reflecting from the surface using this distribution function. The corresponding boundary equations for the R13 are derived by using the reflection kernel in the boundary condition theory for moments. We employ microscopic and macroscopic models to study the flow formation in a square cavity when the top and bottom walls are at different temperatures. The VDM model provides three parameters that can fit to the slip velocity, temperature jump and thermal transpiration data. This model provides an opportunity to change the size and direction of the thermal transpiration force at the wall, which changes the balance of the thermal forces in the rarefied flow. We use the DSMC results to validate our macroscopic solutions, and use the R13 results to interpret the rarefaction effects exhibited by the flow. The R13 equations by benefiting from the Knudsen layer terms [81], can successfully resolve the interplays between the boundary and the bulk, and provide good agreement with the DSMC solution at much lower computational costs up to early transition regime.

In order to fix the free parameters in the VDM model, we require experimental results for slip velocity, temperature jump and thermal transpiration. In our study, we look at the most extreme cases for these coefficients to test the flexibility of our reflection model, and magnify the interplays between bulk effects and Knudsen layer effects.

1.3 Original Contributions

This dissertation follows the paper-based format, and is based on five papers, that four of them are already published and one is ready for submission as a journal article.[1]

In chapter 2 we use the moment method to derive a system of macroscopic equations for phonon transport from the phonon-Boltzmann equation. Then, using a simple model for phonon-surface interaction, the macroscopic boundary equations for this system are derived and presented. The free parameters in the system of equations are fixed using experimental values for specific heat and thermal conductivity. The system of moment equations are then solved in two simple one-dimensional geometries to study the heat transfer problem. This chapter is published in the journal of *Continuum Mechanics and Thermodynamics* [61].

In chapter 3 the presented system of equations are used to model the thermal grating experiment. Considering the two-dimensional nature of this experiment, we propose an intuitive approach to explicitly express the effect of boundaries in the governing equations, and analytically solve a modified form of one-dimensional equations to model the experiment. This chapter is ready for submission as a journal article.

In chapter 4 we use an isotropic scattering kernel to model the adiabatic surfaces using the DSMC method and R13 equations. We observe and report the *viscous slip heating* phenomenon, a second order rarefaction boundary effect in the vicinity of the adiabatic surfaces. This higher order effect is due to intermolecular collisions in the adjacent DSMC cell to the surface, which is captured by the R13 equations and interpreted as the product of slip velocity and shear stress at the boundaries. This Chapter is published in *International Journal of Thermal Science* [57].

In chapter 5 we use the velocity dependent Maxwell model to derive microscopic

---

[1] The author of this dissertation also contributed in publishing Ref. [68].

boundary conditions for the DSMC method. Then, we model a thermal cavity, where the temperature gradient at walls are the driving forces of the rarefied flow, and study the capability of the model to change the size of the transpiration force. We observe and report the possibility of the inverted thermal transpiration force that could potentially drive the flow from hot-to-cold. This chapter is published in *International Journal of Heat and Mass Transfer* [60].

In chapter 6 we use the velocity dependent Maxwell boundary conditions to study the complicated interplay between the thermal stress in the bulk and the thermal transpiration at the boundaries. We use the DSMC as well as three macroscopic models with different complexity to systematically identify and relate the flow patterns to the macroscopic rarefaction terms. This chapter is published in *Physics of Fluids* [56].

1.4 Outline

The contents of this dissertation are divided into two parts with five chapters. In Part I, which includes two chapters, we focus on the derivation and solution of macroscopic transport equations for phonon gasses. In Part II, which includes three chapters, we study an extended model of gas-surface interactions for conventional gas dynamics.

Part I: MACROSCOPIC TRANSPORT EQUATIONS FOR PHONON GASSES

In chapter 2 we start from the kinetic theory of phonons, and propose a dispersion relation that fits to the experimental data for the specific heat. Then, we look into the Callaway model for the collision term in the Phonon-Boltzmann equation, and propose relaxation times that are valid at room temperature. In Sec. 2.3 we define a general form of macroscopic moments, and obtain their corresponding macroscopic transport equations. The resulting system of moment equations is then closed by obtaining the Grad-type distribution function for phonons. In Sec. 2.4 we use a phonon-surface interaction model, and derive boundary conditions for the system of moment equations. The final form of moment equations accompanied with their boundary conditions are presented in Sec. 2.5. Then, we use the order of magnitude method to obtain the thermal diffusivity for the system of moments, and fix the free parameter in Callaway model to fit the thermal diffusivity to the experimental data. In Sec. 2.6 the system of moment equations are analytically solved in two simple geometries, and the results are compared with the classical solutions. This chapter ends with our conclusion in Sec. 2.7.

In chapter 3 we use the system of moments presented in chapter 2 to model the thermal grating experiment as a two-dimensional Poiseuille flow of phonons. First, we solve the system of equations for the case of steady state one-dimensional Poiseuille flow, where there is an energy gradient along the flow direction. Then, using this solution in each cross section of the two-dimensional flow, we analytically solve the modified equations to model the thermal grating experiment. The solution is then compared with the experimental data, and the importance of considering a frequency dependent relaxation time in Callaway model is pointed out.

Part II: VELOCITY DEPENDENT MAXWELL MODEL FOR CONVENTIONAL GAS DYNAMICS

In chapter 4 we use the isotropic scattering kernel to model adiabatic surfaces by the DSMC as well as the R13 equations. In Sec. 4.3 we study the dynamics of gas-surface interactions, when a light gas particle collides with a heavy surface particle. Then, using the isotropic scattering kernel we obtain the velocities of particles reflecting from an adiabatic wall in the DSMC method. The corresponding boundary equations for the adiabatic surface in the R13 equations are then derived in Sec. 4.3.4. The DSMC method and the R13 equations are used to model a lid-driven cavity with three adiabatic walls in Sec. 4.4. The viscous slip heating, a rarefaction effect which is the product of slip velocity and shear stress at the boundaries, is predicted by the DSMC method, and captured by the R13 equations and discussed in Sec. 4.4.5. This chapter ends with our conclusion in Sec. 4.5.

In chapter 5 the velocity dependent Maxwell boundary conditions are presented and used to obtain appropriate boundary conditions for the DSMC method. The three possible considered scenarios when a particle collides with the surface are studied, and the criteria for each reflection type is discussed in Sec. 5.3.1. Then, these boundary conditions are implemented in the DSMC, and used to model a thermal cavity in Sec. 5.4.2. The capability of the velocity dependent Maxwell boundary conditions to change the size of the thermal transpiration force is shown, and the potential for the inverted transpiration flow is discussed in Sec. 5.4.3. This Chapter ends with our conclusion in Sec. 5.5.

In chapter 6 we use the microscopic and macroscopic approaches to study a thermal driven flow in a square cavity. The transport equations for the R13, slow non-isothermal flow (SNIF) and Navier Stokes Fourier (NSF) are presented, and their corresponding boundary equations for the velocity dependent Maxwell model are derived in Sec. 6.3.4. Then, microscopic and macroscopic equations are solved and compared in a thermal cavity geometry. Using macroscopic methods, the interplay between the thermal transpiration at the boundaries and the thermal stress in the bulk is discussed, and the corresponding terms for this rarefaction effect is identified in Sec. 6.4.3. This chapter ends with our conclusion in Sec. 6.5.

The dissertation ends with our final conclusion and recommendations given in chapter 7.

Chapter 2

A Moment Model for Phonon Transport at Room Temperature

Abstract: *Heat transfer in solids is modeled by deriving the macroscopic equations for phonon transport from the phonon-Boltzmann equation. In these equations, the Callaway model with frequency dependent relaxation time is considered to describe the Resistive and Normal processes in the phonon interactions. Also, the Brillouin zone is considered to be a sphere, its diameter depends on the temperature of the system. A simple model to describe phonon interaction with crystal boundary is employed to obtain macroscopic boundary conditions, where the reflection kernel is the superposition of diffusive reflection, specular reflection and isotropic scattering. Macroscopic moments are defined using a polynomial of the frequency and wave vector of phonons. As an example, a system of moment equations, consisting of* 3 *directional and* 7 *frequency moments, i.e.,* 63 *moments in total, is used to study one-dimensional heat transfer, as well as Poiseuille flow of phonons. Our results show the importance of frequency dependency in relaxation times and macroscopic moments to predict rarefaction effects. Good agreement with data reported in the literature is obtained.*

A. Mohammadzadeh and H. Struchtrup. A moment model for phonon transport at room temperature. Continuum Mech. Therm. (2016) 28 pages (First Online DOI: 10.1007/s00161-016-0525-y)

2.1 Introduction

Miniaturization of devices in the last 50 years has attracted the attention of many researchers [41]. The rapid development of micro/nano electro mechanical systems (MEMS/NEMS) requires a deeper understanding of the flow characteristics and heat transfer mechanisms at micro/nano scales. Effects that are negligible at macro scales can dominate at micro and nano scales. For example, the characteristic length of a flow can become small enough that surface effects at interfaces dominate over the bulk properties of the flow, and subsequently lead to a breakdown at the classical laws of continuum mechanics.

The Knudsen number [5] is defined as the ratio of the mean free path (λ) to the characteristic length of flow (L), $\mathrm{Kn} = \frac{\lambda}{L}$, and indicates the degrees of rarefaction. The classical assumptions in continuum mechanics [5] start to break down as Kn becomes larger than 0.001.

One important area of research in nano-technology is the study of heat transport. The tiny size of modern electronic systems combined with the relative large power of lasers can lead to huge changes in temperature. Therefore, we need accurate models for heat transfer that guarantee an effective long-lasting thermal design of modern micro/nano scale systems [70].

Heat transport in solids is due to the exchange of energy between the particles that vibrate on the crystal lattice, with respect to their mean position [42, 75]. These vibrations lead to an energy wave inside the solid, that can be quantized into particles, known as phonons. The macroscopic properties of a crystal, such as temperature, internal energy and heat flux can be obtained by taking suitable averages of phonons properties, such as energy and momentum [42].

Phonons can interact among themselves, and with other particles, including photons, electrons and crystal boundaries. In phonon-phonon collisions, phonons always conserve energy, but can lose momentum [42]. The interactions in which phonons conserve both energy and momentum are called *Normal* processes. The phonon processes in which the momentum does not remain conserved are called *Resistive* processes [42, 75].

Based on the magnitude of the Knudsen numbers for Resistive and Normal processes, we distinguish three modes of heat transfer in solids:

> The *diffusive* heat transfer, that dominates the heat transfer mechanisms when the mean free path for Resistive processes is much smaller than the characteristic length of the flow, $\lambda_R \ll L$. In this mode, phonons mainly undergo interactions that do

not conserve momentum, as a results, the energy waves are damped in a very short length. In this regime the Fourier law governs the heat transfer process [42].

The second mechanism happens when the mean free path for the Resistive process is much larger than the characteristic length of the flow $\lambda_R \gg L$, while the mean free path for the Normal process is smaller or comparable with the characteristic length of the flow, $\lambda_N \lesssim L$. In this regime, Normal processes by conserving the phonon momentum dominates the heat transfer mechanism, and leads to a wave like energy transport known as second sound [19, 28].

The energy can also be transported in solids via *ballistic* phonons [31]. In this regime the mean free path for Resistive and Normal process are both larger than the characteristic length of the flow, i.e., $\lambda_R, \lambda_N > L$. In this Knudsen flow, phonons travel inside the crystal without any interactions.

In general, the energy transport in solids is a combination of the above mechanisms. Depending on the temperature range and the crystal properties, each of the above transport regimes can dominate.

The phonon-Boltzmann equation, first formulated by Peierls [64], describes the transport of phonons in the crystal lattice. This equation relates the time evolution of the phonon distribution function to phonon convection and collisions with other phonons, as well as other particles. While the phonon-Boltzmann equation is valid for all degrees of rarefaction, its direct solution, due to the complexity in the phase-space dimension as well as the non-linearity in the collision term, is a formidable task [13].

As an alternative to the direct solution, one can use discrete particle methods to track each individual phonon in the crystal, and use the deterministic approach (a branch of molecular dynamics) to study the phonon transport [54]. Another approach, known as direct simulation Monte Carlo (DSMC), is using statistical assumptions to group a cloud of phonons, and study their behavior [5]. Employing the stochastic assumptions in the DSMC method compared to the deterministic nature of molecular dynamics significantly reduces the computational costs. However, DSMC still suffers from expensive computational overheads [58]. More recently, a variance-reduction formulation has been proposed to improve the traditional Monte Carlo method, when the temperature difference is small [65]. In this method, the stochastic particle description is only solved for the deviation from a nearby equilibrium, that leads to significant speed up compared to standard DSMC. Peraud and Hadjiconstantinou [66] also showed that in the case where the governing deviational formulation for solving phonon-Boltzmann equation can be linearized, additional speed up will be obtained,which provides a suitable algorithm for using DSMC in three-dimensional geometries.

Due to the complexity of the collision term in the phonon-Boltzmann equation, the well-known Callaway model [9] was proposed to provide an approximation for this term. In this model, the collision is described as a process that relaxes the distribution function of phonons to the appropriate equilibrium state for collision type, with the relaxation time τ that needs to be provided.

When the mean free path for the Resistive process is very smaller than the length scale of the flow, i.e., $\mathrm{Kn}_R \ll 1$, by performing the Chapman-Enskog expansion [12] on the phonon-Boltzmann equation equipped with the Callaway model, one can obtain the Fourier law as the heat flux equation. The Fourier law provides an explicit expression for the heat conductivity, which can be determined by experimental measurements. However, since the second sound and ballistic phonons are not included in the Fourier law, it cannot provide satisfactory results when diffusion does not dominate the heat transport process [22, 49, 15, 39].

By considering certain ratios between Resistive and Normal relaxation times, researchers derived macroscopic equations to extend the validity of classical hydrodynamics beyond the Fourier regime. Guyer and Krumhansl [31, 29, 30] solved the linearized form of the phonon-Boltzmann equation in terms of eigenvectors of the Normal process when the ratio of Resistive and Normal processes are very small or very large. They showed that this condition leads to the Fourier law in the former, while a set of equations that can capture the second sound was obtained in the latter. Although these equations predicted the second sound effect, they were only valid at low temperature where the employed assumptions held.

Another approach to obtain a system of macroscopic equations with extended validity beyond the Fourier's regime is using higher order moments of the distribution function. This method, known as moment method, has been successful in rarefied gas dynamics, and shown to be capable of predicting and explaining the flow behavior up to mid-transition regime ($Kn \lesssim 0.5$). In the seminal work of Grad, a generic form of macroscopic moments was considered, and a set of transport equations were derived by taking integral moments of the Boltzmann equation [26, 18]. This approach provides an infinite number of transport equations for macroscopic moments, where in theory, its solution is equivalent to the solution of Boltzmann equation. However, in order to make this system of infinite number of equations practical, we need to truncate it at some point. Using Grad-type distribution function to provide closure for the system of moments is a common approach; however, this closure brings approximation to the system [26, 81]. In this method, the Knudsen number determines degrees of rarefaction in the flow, and subsequently, the required extra terms and equations to capture non-equilibrium. A big advantage of accessing to macroscopic equations compared to particle methods is the opportunity to relate non-equilibrium phenomena to macroscopic terms. These macroscopic terms in the system of moments can be simply switched on and off so that we study their effect to help us explain the non-equilibrium phenomena. So far, we had a great success in capturing and explaining thermal driven flows by system of moments in rarefied gas dynamics [68, 56, 69].

Struchtrup and co-workers [19, 24] followed Grad's moments method, and presented a simple model for the phonon transport in solids. Although this model described the interplay between Normal and Resistive processes, and included the second sound and ballistic phonon effects, due to its simplifying assumptions it could not provide good agreement with experimental data. The main simplifications considered in their model were (a) linear dispersion relation between phonon energy and momentum, (b) extension of the Brillouin zone to infinity, and (c) considering a constant relaxation time for the Callaway model. These simplifications provided fast access to a system of moments that could describe the rarefied phonon gas in principle, but fail to give accurate results at room temperature.

By aiming to access to a system of moments that can indeed capture the phonon transport at room temperature, we replace the simplifying assumptions employed in Ref. [24] with a more realistic model. We consider a quadratic dispersion relation to accurately describe the dependency of frequency on wavevector at room temperature. Moreover, the Brillouin zone is considered to be a sphere with finite radius, which depends on the working temperature of the system. Most importantly, the dependency of relaxation time on frequency is considered in the Callaway model, to account for phonon interactions at low and high frequencies.

Macroscopic moments are defined using a polynomial of frequency and wavevector of phonons. Using the aforementioned assumptions, the resulting transport equations for macroscopic moments are derived, and presented. The finite size of Brillouin zone as well as the frequency dependency in relaxation time makes the derivation of the transport equations more complicated compared to Ref. [24]. In particular, providing a closed form of integration at room temperature becomes a formidable task, and most integrations have to be numerically calculated.

In order to describe the phonon-surface interactions, we used an extension to the boundary condition model presented in Ref. [24]. In this model, three types of interactions are considered: thermalization, specular reflection and isotropic scattering. Based on the proportions of these three types, the free parameters in the reflection model can be altered to fit to the experimental data.

In order to fix the free parameters in our model, we use the experimental data for specific heat and thermal conductivity. We use the specific heat to fix the dispersion relation, and then by employing this relation, we use the thermal conductivity to fix the relaxation time in the production term. Then, the resulting equations are used to analytically solve the heat transfer problem in two simple geometries.

As the first application we model the thermal grating experiment [38], considering infinite width for the silicon specimen to neglect the effects of boundary conditions. This assumption leads to a one-dimensional flow problem, that can be solved using eigenvalue-eigenvector analysis. We compare the predicted results of our system with the reported data in Ref. [38]. The results show the importance of considering low frequency phonons as well as high frequency phonons in the relaxation time model, to get a good agreement with the reported data in Ref. [38]. Then, we use the system of moments to solve Poiseuille flow of phonons in a heat conductor with adiabatic boundaries. In this problem, the effect of boundary conditions on the heat transfer is studied. Moreover, we show the deviation of our results from the Fourier's solution, and discuss the role of relaxation time model on this deviation.

The remainder of the paper is organized as follows: In Sec. 2.2 we recall the kinetic theory of phonons, and introduce the dispersion relation as well as the specific heat. Then we do a quick review on the Callaway model, and introduce the relaxation times considered in this study. Macroscopic moments are presented in Sec. 2.3, and the system of moment equations are derived from the phonon-Boltzmann equation. This system is then closed using the Grad distribution function in Sec. 2.3.2. The details of phonon-boundary interactions are presented in Sec. 2.4. Then, the closed system of moment equations as well as their boundary conditions, and the thermal conductivity predicted by this system is presented in Sec. 2.5. In Sec. 2.6 the system of moments are used in two simple geometries to solve heat transfer problems. The paper closes with conclusion is Sec. 2.7.

2.2 Phonons

2.2.1 Phonon model

The energy is transported in solids when atoms vibrate around their mean positions on the crystal lattice. The particle representative of the resulting energy wave due to these vibrations is called phonon. Phonons have energy and momentum; they can interact among themselves and with other particles, including photons, electrons, and crystal boundaries. They can also interact with crystal impurities and dislocations and lose momentum [42]. The thermal properties of the crystal, such as temperature and heat flux can be obtained by taking appropriate averages of microscopic properties of the phonon gas.

In the phonon model the crystal is replaced by a box containing the gas of phonons, such that the energy transport can be treated analogous to the transport processes in gases [17, 20]. The eigen-vibration of the lattice with the frequency ω and the wave vector $\mathbf{k}$ in the crystal corresponds to phonons with the energy $\hbar\omega$ and the momentum $\hbar\mathbf{k}$, where $\hbar$ is Planck's constant. The dispersion relation $\omega(\mathbf{k})$ determines the relationship between the frequency and the wave vector, which follows from the quantum mechanics equation of motion for atoms in the crystal [42]. This relation is periodic in nature, with a full period equal to the Brillouin zone. Phonons travel with the group velocity, $\mathbf{c} = \frac{\partial\omega}{\partial\mathbf{k}}$.

In contrast to the transport process for gas molecules, phonons do not follow the law of number conservation; they can be created or destroyed during interactions. The energy, on the other hand, is always conserved in the phonon-phonon interaction [64],

$$\hbar\omega^{'} + \hbar\omega^{''} = \hbar\omega^{'''} \quad \text{or} \quad \hbar\omega^{'} = \hbar\omega^{''} + \hbar\omega^{'''} .$$

In this process two phonons with frequencies $\omega^{'}$ and $\omega^{''}$ interact, and create a phonon with the frequency $\omega^{'''}$, or a phonon with frequency $\omega^{'}$ splits into two phonons with frequencies $\omega^{''}$ and $\omega^{'''}$. Phonon momentum is generally not conserved, but obeys

$$\hbar\mathbf{k}^{'} + \hbar\mathbf{k}^{''} = \hbar\mathbf{k}^{'''} + \hbar\mathbf{G} \quad \text{or} \quad \hbar\mathbf{k}^{'} = \hbar\mathbf{k}^{''} + \hbar\mathbf{k}^{'''} + \hbar\mathbf{G} ,$$

where $\mathbf{G}$ is the reciprocal lattice vector. The phonon momentum is conserved when the reciprocal lattice vector is zero. This interaction is called Normal process. If the interaction between phonons leads to a momentum vector outside the Brillouin zone, the non-zero reciprocal vector $\mathbf{G}$ brings back the momentum vector to the Brillouin zone.

This type of process is called Umklapp (flip over). The phonons can also interact with the lattice imperfections and boundaries, and lose momentum while conserving energy. All processes that do not conserve momentum are called Resistive processes [42, 75].

We distinguish two different types of phonons: optical phonons and acoustic phonons. Optical phonons appear in crystals with more than one atom in the smallest unit cell, and only have high frequencies. Therefore, they can be neglected in single element crystals, and at moderate temperatures range [42]. Acoustic phonons, on the other hand, can have very low to high frequencies. Acoustic phonons have 3 polarizations, 2 transversals and 1 longitudinal. In the current study we only consider acoustic phonons, and group their three polarizations into a single mode with a single velocity and single deformation potential [17].

2.2.2 Kinetic theory of phonons

In kinetic theory, the state of the phonon gas is described by the distribution function, $f(\mathbf{x}, \mathbf{k}, t)$, defined such that the number of phonons in a phase space element, $d\mathbf{k}d\mathbf{x}$ at time t is given by

$$dN = f(\mathbf{x}, \mathbf{k}, t)\, d\mathbf{k} d\mathbf{x} \ .$$

Here, $\mathbf{x}$ is the three-dimensional space vector. The phonon-Boltzmann equation reads [19, 64]

$$\frac{\partial f}{\partial t} + c_i \frac{\partial f}{\partial x_i} = S_R(f) + S_N(f) \ , \tag{2.1}$$

where $c_i = \frac{\partial \omega}{\partial k_i}$ is the group velocity of phonons, and $S(f)$ is the collision operator including the Resistive $S_R(f)$ and the Normal process $S_N(f)$.

Moments of the distribution function provide the macroscopic properties of phonon system. The energy density, energy flux and momentum density in the phonon gas are obtained as

$$e(t, \mathbf{x}) = \int_{BZ} \hbar \omega f(\mathbf{x}, \mathbf{k}, t)\, d\mathbf{k} \tag{2.2a}$$

$$q_i(t, \mathbf{x}) = \int_{BZ} \hbar \omega c_i f(\mathbf{x}, \mathbf{k}, t)\, d\mathbf{k} \tag{2.2b}$$

$$p_i(t, \mathbf{x}) = \int_{BZ} \hbar k_i f(\mathbf{x}, \mathbf{k}, t)\, d\mathbf{k} \tag{2.2c}$$

where BZ denotes the Brillouin zone of the lattice. We assume that the dispersion relation only depends on the absolute value of the wave vector. This assumption leads to a spherical Brillouin zone [42] with the boundaries of

$$-\frac{\pi}{a} \leq k_i \leq \frac{\pi}{a} \ , \tag{2.3}$$

where a is the lattice spacing.

Phonons are Bose particles [42], and their entropy density reads

$$s = -k_B \int_{BZ} \left(f \ln\left(\frac{f}{y}\right) - y \left(1 + \frac{f}{y}\right) \ln\left(1 + \frac{f}{y}\right)\right) d\mathbf{k} \ , \tag{2.4}$$

where k_B is the Boltzmann's constant, and $y = \frac{3}{8\pi^3}$ is the density of states [42]. Note that the factor 3 in this constant is related to the 3 phonon polarizations, with 2 branches for transversal and 1 branch for longitudinal modes. In the equilibrium state, phonons follow the Bose distribution function [42],

$$f_E = \frac{y}{\exp\left(\frac{\hbar\omega}{k_B T}\right) - 1} \ . \tag{2.5}$$

2.2.3 Dispersion relation and specific heat

In order to relate the microscopic properties of phonons to the macroscopic properties of lattice, we need to express the dependency of frequency on the wave vector. We use an isotropic quadratic function, as suggested in Ref. [67], to approximate the dispersion relation as

$$\omega\left(k\right) = v_1 k + v_2 k^2 \ , \tag{2.6}$$

where v_1 and v_2 are constants. The group velocity is obtained by

$$c_i = \frac{\partial \omega}{\partial k_i} = \left(v_1 + 2 v_2 k\right) n_i \ , \tag{2.7}$$

where

$$n_i = \frac{k_i}{k} \ ,$$

is the phonon direction vector.

Specific heat is obtained by taking the temperature derivative of the energy moment

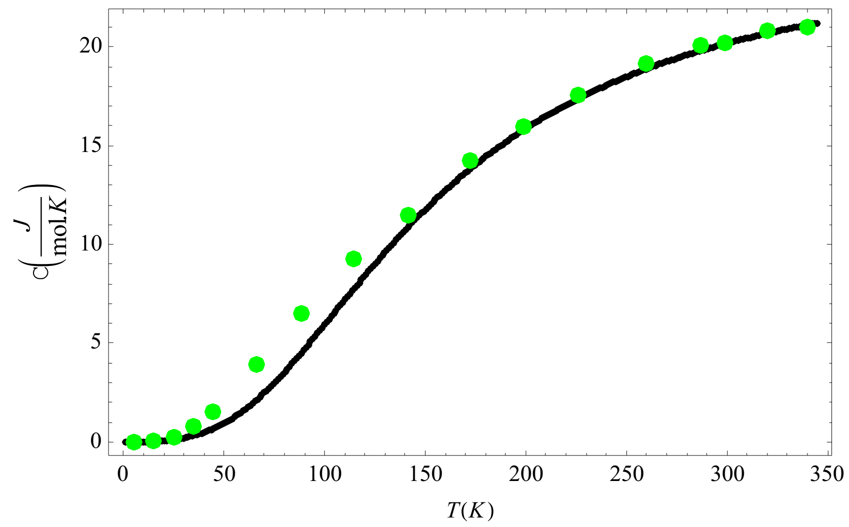

Figure 2.1: Specific heat for Silicon predicted with the quadratic dispersion relation.

in equilibrium, where f is the Bose distribution function

$$C = \frac{\partial e}{\partial T} = \frac{\partial \left(\int_{BZ} \hbar \omega f_E d\mathbf{k} \right)}{\partial T} . \tag{2.8}$$

We set v_1 to the Debye speed c_0, and choose v_2 such that we get the best fit to the experimental values for specific heat at room temperature. The Debye speed c_0 is defined as

$$\frac{1}{c_0^3} = \frac{1}{3} \sum_{i=1}^{3} \frac{1}{c_i^3} ,$$

which is an appropriate average in the 3 polarizations for phonons [42]. Using literature [42] to set $c_0 = 5883 \ \frac{m}{s}$, we choose $v_2 = -1.0103 \times 10^{-10} \ \frac{m^2}{s}$ to fit to the experimental values for specific heat. Figure 2.1 shows the variation of specific heat with temperature obtained from the considered model, compared with the experimental data in Ref. [42]. The deviation that occurs around $T \simeq 100 \ K$ is due to the value of v_2 employed in the dispersion relation, that we chose to, specifically, fit to the values around room temperature. Note that we can extend the comparison to higher temperatures, however, in the current study we are interested in the room temperature comparison.

2.2.4 Callaway model

We use the Callaway model [9] to describe the production term in the phonon-Boltzmann equation. This model is analogous to the BGK model in the kinetic theory of classical gases [4]. In this model, the phonon distribution function, f relaxes to the reference distribution functions, f_R and f_N, with the relaxation times τ_R and τ_N for the Resistive (R) and Normal (N) processes, respectively. The idea behind this model comes from the concept of maximum entropy at the equilibrium state. All phonon interactions are supposed to increase entropy, and drive the distribution function toward the equilibrium state corresponding to their type of interactions. The relaxation time relates to the phonon mean free path, and shows the rate of this increase in the flow. The Callaway model reads

$$S(f) = -\frac{1}{\tau_R(\omega)}(f - f_R) - \frac{1}{\tau_N(\omega)}(f - f_N) \ . \tag{2.9}$$

The equilibrium distributions f_R and f_N, must be chosen to satisfy the conservation conditions for energy and momentum. In all R-processes the energy is conserved, hence

$$\int_{BZ} \frac{\hbar\omega}{\tau_R(\omega)}(f - f_R) d\mathbf{k} = 0 \ , \tag{2.10}$$

and in all N-processes both energy and momentum are conserved,

$$\int_{BZ} \frac{\hbar\omega}{\tau_N(\omega)}(f - f_N) d\mathbf{k} = 0 \quad \text{and} \quad \int_{BZ} \frac{\hbar k_i}{\tau_N(\omega)}(f - f_N) d\mathbf{k} = 0 \ . \tag{2.11}$$

In order to obtain the appropriate expressions for the equilibrium distributions f_R and f_N, we maximize the entropy density Eq. (2.4), under the constraints of Eq. (2.10) and Eq. (2.11), respectively. This leads to

$$f_R = \frac{y}{e^{\frac{\hbar\omega}{k_B}\gamma} - 1} \quad \text{and} \quad f_N = \frac{y}{e^{\left(\frac{\hbar\omega}{k_B}\gamma' + \frac{\xi_j \hbar k_j}{k_B}\right)} - 1} \ , \tag{2.12}$$

where γ, $\gamma^{'}$ and ξ_j are the Lagrange multipliers. We assume that the phonon gas is not very far from the local equilibrium, so that the above distribution functions deviate only slightly from the local equilibrium distribution functions. This allows us to linearize these distribution function in Lagrange multipliers to get

$$\begin{aligned} f_R &= f_E + \frac{\partial f_R}{\partial \gamma}|_E \left(\gamma - \gamma_E\right) \ , \\ f_N &= f_E + \frac{\partial f_N}{\partial \gamma^{'}}|_E \left(\gamma^{'} - \gamma^{'}_E\right) + \frac{\partial f_N}{\partial \xi_j}|_E \left(\xi_j - \xi_{j,E}\right) \ . \end{aligned} \tag{2.13}$$

Note that by comparing Eq. (2.12) with the Bose distribution function, we have

$$\gamma_E = \gamma^{'}_E = \frac{1}{T} \quad \text{and} \quad \xi_{j,E} = 0 \ .$$

The relaxation times in the Callaway model plays a very important role in predicting the phonon transport characteristics. The relaxation time for the R-processes reads [55]

$$\frac{1}{\tau_R\left(\omega\right)} = \frac{1}{\tau_U\left(\omega\right)} + \frac{1}{\tau_B\left(\omega\right)} + \frac{1}{\tau_X\left(\omega\right)} \ ,$$

where τ_U denotes the relaxation time for the Umklapp processes, τ_B denotes the relaxation time for the phonon-boundary interaction, and τ_X takes the effects of impurities into account. The effects of phonon-surface interactions will be considered in the boundary condition model in Sec. 2.4. Moreover, we consider a *pure* crystal without any imperfection, i.e., $\frac{1}{\tau_X(\omega)} = 0$.

For the relaxation time in the Umklapp processes we use the results reported in Ref. [100]. Ward and Broido [100] employed the first principle approach to obtain the relaxation times, and observed that at low frequency $\tau_U \propto \frac{1}{\omega^2}$, while at high frequencies this dependency is stronger, $\tau_U \propto \frac{1}{\omega^4}$.

Considering that at low frequency this relation is in accordance with the well-known Klemens's expression [43, 55]

$$\tau_U\left(\omega\right) = \frac{1}{B_U T \exp\left(-\frac{D}{T}\right)} \frac{1}{\omega^2} \ , \tag{2.14}$$

with $B_U = 1.73 \times 10^{-19} \frac{s}{K}$ and $D = 137.39K$, we used Eq. (2.14) for the relaxation time at low frequency in U-processes.

Considering that the relaxation time has a stronger frequency dependency at higher frequencies [100], we employed a similar expression to the well-known Eq. (2.14), but with larger powers of frequencies to express the relaxation time at higher frequencies. We considered that the relaxation time follows

$$\tau_U(\omega) = \begin{cases} \frac{1}{B_U T \exp\left(-\frac{D}{T}\right)} \frac{1}{\omega^2}, & \omega \leq \omega_C \\ \frac{1}{S_U T \exp\left(-\frac{D}{T}\right)} \frac{1}{\omega^4}, & \omega \geq \omega_C \end{cases} , \tag{2.15}$$

where ω_C is the cross-over frequency. Here, S_U is chosen such that we observe a continuous relaxation time at ω_C,

$$S_U = \frac{B_U}{\omega_C^2} .$$

The cross-over frequency, ω_C, is then chosen to fit to the experimental data for thermal conductivity.

For the N-process we follow Ref. [37], and assume that the relaxation time is approximated as

$$\tau_N(\omega) = \frac{1}{B_N T \omega^2} , \tag{2.16}$$

where B_N can be used to adjust to the experimental data.

2.3 System of moments

2.3.1 Moment equations

Following Grad's moment method [26], we derive a set of macroscopic transport equations that can approximate the phonon-Boltzmann equation. For this means, we define the general macroscopic moment

$$u^{\alpha}_{<i_1,..i_n>} = \int_{BZ} \omega^{\alpha} n_{<i_1 \ldots} n_{i_n>} f(\mathbf{x}, \mathbf{k}, t)\, d\mathbf{k} , \tag{2.17}$$

to relate the phonon properties to the macroscopic properties of the crystal. The indices in the angular brackets denotes the trace-free and symmetric part of the tensor. Our moment definition contains the powers of frequencies ω^{α} with $\alpha = 0, 1, 2, ...$, and the wave vector in the form of direction vectors, $n_{<i_1..i_n>} = \frac{k_{<i_1...i_n>}}{k^n}$.

Following Eq. (2.17), the energy density is obtained by

$$\frac{e(\mathbf{x}, t)}{\hbar} = u^1_0(\mathbf{x}, t) .$$

The energy density flux and the momentum density of phonons will be related to the vectorial moments u_i^α, by using the constitutive relations in the sequel.

In order to get a hierarchy of balance equations for the moments, we multiply the phonon-Boltzmann equation with the generic term

$$\Upsilon^\alpha_{i_1,..i_n} = \omega^\alpha n_{i_1...}n_{i_n} \ , \tag{2.18}$$

and perform an integration over the **k**-space in the Brillouin zone. This leads to a system of moment equations of the generic form

$$\frac{\partial u^\alpha_{i_1,..i_n}}{\partial t} + \frac{\partial F^\alpha_{i_1,..i_n i_{n_p}}}{\partial x_{n_p}} = P^\alpha_{i_1,..i_n} \ , \tag{2.19}$$

with the fluxes

$$F^\alpha_{i_1,..i_n i_{n+1}} = \int_{BZ} c_{i_{n+1}} \omega^\alpha n_{i_1...} n_{i_n} f d\mathbf{k} \ ,$$

and the productions

$$P^\alpha_{i_1,..i_n} = \int_{BZ} \omega^\alpha n_{i_1...} n_{i_n} S(f)\, d\mathbf{k} \ .$$

For the scalar moments u_0^α, we separate the equilibrium part from the non-equilibrium part, and define

$$v_0^\alpha = u_0^\alpha - u^\alpha_{0|E} \ . \tag{2.20}$$

Here, the equilibrium part of the scalar moment is defined as

$$u^\alpha_{0|E} = \int_{BZ} \omega^\alpha \ f_E d\mathbf{k} \ .$$

Note that $F^\alpha_{i_1,..i_n}$ has been defined as a rank n tensor. It is helpful in the further calculation to decouple the trace and trace-free parts of tensors, and indicate the trace-free tensor by angled brackets around the indices. For example, for the second order tensor we can write

$$F^\alpha_{ij} = F^\alpha_{<ij>} + \frac{1}{3} F^\alpha_0 \delta_{ij} \ ,$$

where δ_{ij} is the Kronecker delta function. Using similar tensorial calculation [81], we can decouple the trace and trace-free parts of a rank n tensor. Therefore, the hierarchy of moment equations, using the trace-free symmetrical tensors, can be written as

$$\begin{gathered}
\frac{\partial u_0^1}{\partial t} + \frac{\partial F_i^1}{\partial x_i} = 0 \ , \\
\frac{\partial v_0^\alpha}{\partial t} - \frac{\partial u_{0|E}^\alpha}{\partial u_0^1}\frac{\partial F_i^1}{\partial x_i} + \frac{\partial F_i^\alpha}{\partial x_i} = P_0^\alpha \qquad \alpha \geq 0, \neq 1 \ , \\
\frac{\partial u_i^\alpha}{\partial t} + \frac{\partial F_{<ij>}^\alpha}{\partial x_j} + \frac{1}{3}\frac{\partial F_0^\alpha}{\partial x_i} = P_i^\alpha \ , \\
\frac{\partial u_{<ij>}^\alpha}{\partial t} + \frac{\partial F_{<ijp>}^\alpha}{\partial x_p} + \frac{2}{5}\frac{\partial F_{<i}^\alpha}{\partial x_{j>}} = P_{<ij>}^\alpha \ , \\
\frac{\partial u_{<i_1 i_2 \ldots i_n>}^\alpha}{\partial t} + \frac{\partial F_{<i_1 i_2 \ldots i_n i_{n+1}>}^\alpha}{\partial x_{n+1}} + \frac{n}{2n+1}\frac{\partial F_{<i_1 i_2 \ldots i_{n-1}}^\alpha}{\partial x_{i_n>}} = P_{<i_1 i_2 \ldots i_n>}^\alpha \qquad n > 2 \ .
\end{gathered} \tag{2.21}$$

Note that based on the definition of moments, we have $u_{i_1 i_2 \ldots i_n kk} = u_{i_1 i_2 \ldots i_n}$. Moreover, α is the number of frequency powers in the non-equilibrium moments. The first equation in this hierarchy is the conservation of energy, where production term is zero in the right hand side.

2.3.2 Closure for system of moments

Taking moments of the phonon-Boltzmann equation generates a large system, consisting of an infinite number of balance equations (2.21). This system includes flux terms $F^\alpha_{<i_1 i_2 \ldots i_n i_{n+1}>}$, as well as production terms $P^\alpha_{<i_1 i_2 \ldots i_n>}$, that need to be determined to get a closed system of equations. The solution to this closure problem in kinetic theory, was first proposed by Grad [26], and then extended to the phonon kinetic theory in Ref. [19, 24]. Since flux and production terms are expressed through the distribution function, the closure problem is solved when we find the distribution function, that indeed depends on the moments. For this means, we follow the Grad's [26] idea to express the distribution function as a function of moments in Appendix A. Here, we present the final result as

$$f_G = f_E + \frac{a^3}{32\pi}\sum_{\substack{\eta,m \\ \neq E}} \frac{(2m+1)!!}{m!}\Phi^\eta X_M^{\eta+1}\left[\frac{u^\eta_{<j_1,..j_m>} - u^\eta_{<j_1,..j_m>E}}{\omega_M^\eta}\right] n_{<j_1}\ldots n_{j_m>} \ , \tag{2.22}$$

where $\omega_M = \frac{2c_0}{a}$ is the reference frequency, and $X_M = \frac{\hbar\omega_M}{k_B T}$ is the non-dimensional inverse of temperature. For the detailed derivation of the distribution function, as well as the expressions for Φ^η see Appendix A.

Flux terms

Using the Grad distribution function, we can determine the fluxes as functions of moments. The fluxes have the general form

$$F^{\alpha}_{<i_1 i_2 \ldots i_n i_{n+1}>} = \int_{BZ} c_{i_{n+1}} \omega^{\alpha} n_{<i_1 \ldots} n_{i_n>} f_G d\mathbf{k} \ . \tag{2.23}$$

Substituting Eq. (2.22), and rearranging the equations gives

$$F^{\alpha}_{<i_1 i_2 .. i_n>} = \begin{cases} c_0 \omega^{\alpha}_M \left(A^{\alpha}_E \frac{u^{\alpha}_{0|E}}{\omega^{\alpha}_M} + \sum\limits_{\substack{\eta=0 \\ \neq 1}}^{n_F} A^{\alpha,\eta}_0 \frac{v^{\eta}_0}{\omega^{\eta}_M} \right), & n = 0 \\ c_0 \omega^{\alpha}_M \left(\sum\limits_{\eta=0}^{n_F} A^{\alpha,\eta}_n \frac{u^{\eta}_{<i_1,..i_n>}}{\omega^{\eta}_M} \right), & n \neq 0 \end{cases} , \tag{2.24}$$

The detailed derivation of this relation, as well as the expressions for $A^{\alpha,\eta}_n$ and A^{α}_E can be found in Appendix B.

Production terms

Similar to the flux terms, we use the Grad distribution function to express the production terms as functions of moments. The production terms have the general form

$$P^{\alpha}_{<i_1 i_2 .. i_n>} = \int_{BZ} \omega^{\alpha} n_{<i_1 \ldots} n_{i_n>} S(f_G) d\mathbf{k} \ , \tag{2.25}$$

where $S(f_G)$ is obtained by using the Callaway model in Eq. (2.9). It is worth noting that by using the moment method R and N-processes can be treated completely independently

$$P^{\alpha}_{<i_1 i_2 \ldots i_n>} = P^{\alpha}_{<i_1 i_2 \ldots i_n>,R} + P^{\alpha}_{<i_1 i_2 \ldots i_n>,N} \ . \tag{2.26}$$

Resistive process Considering the conservation of energy in the R-process Eq. (2.10), and expressing f_R as a function of the non-equilibrium moments, we obtain the production moments for R-processes as

$$P^{\alpha}_{<i_1 i_2 \ldots i_n>,R} = \begin{cases} -\frac{\omega^{\alpha}_M}{\tau^0_R} \sum\limits_{\substack{\eta=0 \\ \neq 1}}^{n_F} J^{\alpha,\eta}_{0,R} \frac{v^{\eta}_0}{\omega^{\eta}_M} & n = 0 \\ -\frac{\omega^{\alpha}_M}{\tau^0_R} \sum\limits_{\eta=0}^{n_F} J^{\alpha,\eta}_{n,R} \frac{u^{\eta}_{<i_1,..i_n>}}{\omega^{\eta}_M} & n \neq 0 \end{cases} , \tag{2.27}$$

Here, τ_R^0 is the reference relaxation time for R-process that depends on the crystal, and will be discussed in the sequel. Note that we have $J_{0,R}^{1,\eta} = 0$, which implies zero production in the case of energy moment, i.e., $n = 0$ and $\alpha = 1$. The detailed derivation of the above production matrix, as well as the expression for $J_{n,R}^{\alpha,\eta}$ can be found in Appendix C.

Normal process Using Eq. (2.11), we express f_N as a function of non-equilibrium moments, and obtain the N-production moment as

$$P^{\alpha}_{<i_1 i_2 \ldots i_n>,N} = \begin{cases} -\frac{\omega_M^\alpha}{\tau_N^0} \sum\limits_{\substack{\eta=0 \\ \neq 1}}^{n_F} J_{0,N}^{\alpha,\eta} \frac{v_0^\eta}{\omega_M^\eta} & n = 0 \\ -\frac{\omega_M^\alpha}{\tau_N^0} \sum\limits_{\eta=0}^{n_F} J_{1,N}^{\alpha,\eta} \frac{u_i^\eta}{\omega_M^\eta} & n = 1 \\ -\frac{\omega_M^\alpha}{\tau_N^0} \sum\limits_{\eta=0}^{n_F} J_{n,N}^{\alpha,\eta} \frac{u_{<i_1 i_2 \ldots i_n>}^\eta}{\omega_M^\eta} & n > 1 \end{cases} . \tag{2.28}$$

Here, τ_N^0 is the reference relaxation time for N-process that also depends on the crystal, and will be discussed in the sequel. The detailed derivation of the above production matrix and an expression for $J_{n,N}^{\alpha,\eta}$ can be found in Appendix D.

2.4 Boundary conditions

So far, we have derived the system of moments equations, and provided expressions for the flux and production terms to it. In this section we will derive the appropriate boundary conditions for this system of equations.

2.4.1 Microscopic model for the phonon-Boltzmann equation

In order to describe the phonon-surface interactions we need a microscopic boundary condition that can be used to solve the phonon-Boltzmann equations. Later, this microscopic model will be utilized to obtain the macroscopic boundary conditions for the moment equations.

We use a phonon-surface model similar to the Maxwell boundary condition in classical theory [51], where the reflection kernel is a superposition of the kernels for diffusive reflection and specular reflection.

For phonons, we consider three possible scenarios when colliding with the surface [24, 83] :

> Thermalization: This process occurs when the impacting phonon with the surface is absorbed at the wall, and new phonons are emitted from the surface to the gas. The generated phonons will leave the surface at the equilibrium Bose distribution (2.5), with the temperature of the surface. In this process, impacting phonons exchange energy and momentum with the surface, which subsequently leads to an energy transfer across the crystal boundary.
>
> Specular reflection: In this process the energy and tangential momentum of the impacting phonons with the surface remain conserved, and only their normal momentums become inverted. This interaction does not lead to any energy transfer, or drag (like) forces across the crystal boundary.
>
> Isotropic scattering: This process accounts for the adiabatic interactions, while phonons transfer tangential momentum to the surface. The incoming phonons are reflected in a random direction, while keeping their impacting energy. This process is in analogy to the collision of a light gas particle to the heavy surface particle for classical gasses [57].

In order to describe the phonon-surface behavior we need the distribution function in an infinitesimal neighborhood of the wall, that we write as

$$\overline{f} = \begin{cases} f^* \left(\mathbf{x}, \mathbf{k}, t\right), & n_i \nu_i \geq 0 \\ f\left(\mathbf{x}, \mathbf{k}, t\right), & n_i \nu_i \leq 0 \end{cases} . \tag{2.29}$$

Here, ν_i is the surface normal unit vector, and $n_i = \frac{k_i}{k}$ is the unit phonon direction vector. The distribution function for phonons leaving the surface $\left(n_i \nu_i \geq 0\right)$ is expressed by f^*, and is described by the reflection model.

We define β as the portion of phonons that are scattered or specularly reflected from the wall. Noting that the number of phonons are conserved in these two process, we assume that γ of them are specularly reflected, and $\left(1 - \gamma\right)$ are isotropically scattered. Moreover, α is the relative amount of thermalized phonons. Thus, the distribution function for the particles leaving the surface reads

$$f^* = \alpha f_E \left(T_s, k\right) + \beta \gamma f \left(k_i - 2 k_j \nu_j \nu_i\right) + \beta \frac{\left(1 - \gamma\right)}{\pi} \frac{1}{c} \int_{n_k \nu_k < 0} c \left(-n_k \nu_k\right) f \left(k_j\right) d\Omega \ . \tag{2.30}$$

Here, the first term in the right hand side denotes the thermalized phonons, which will be emitted with the equilibrium distribution function at the wall temperature, T_s. The second term describes the specular reflection of phonons, in which only the normal momentum will be inverted. The isotropic scattering of phonons, where phonons are reflected with a random angle, is described in the third term of Eq. (2.30).

This relation must also hold in the equilibrium state, when both incoming and outgoing particles follow the equilibrium distribution f_E at $T = T_s$. Substituting this condition in Eq. (2.30) gives

$$\alpha = (1 - \beta)\ .$$

Therefore, based on the crystal properties, this model for boundary condition introduces β and γ as the free parameters to fit to experimental data.

2.4.2 Boundary conditions for moments

To obtain the macroscopic boundary conditions for moments, we follow the ideas of Grad as outlined in [26, 93]. In this method, first we assume that the phonon distribution function can be approximated with the Grad distribution Eq. (2.22), and set $f = f_G$. Then, we require the continuity of certain normal fluxes over an infinitessimal surface element, that by using Eq. (2.29) gives

$$\int \Upsilon_A n_k \nu_k \overline{f} d\mathbf{k} = \int \Upsilon_A n_k \nu_k f_G d\mathbf{k} \tag{2.31}$$

where Υ_A is the polynomial of the frequency and the direction vector, that we already defined in Eq. (2.18). Following this method we obtain relations between the macroscopic moments and the wall properties, which shall be used as the boundary conditions for the macroscopic moments. Since $\overline{f}$ and f_G agree for the incident particles, the above relation simplifies to

$$\int_{n_i\nu_i>0} \omega^\alpha n_{i_1\ldots} n_{i_n} n_k \nu_k f^* d\mathbf{k} = \int_{n_i\nu_i>0} \omega^\alpha n_{i_1\ldots} n_{i_n} n_k \nu_k f_G d\mathbf{k}\ . \tag{2.32}$$

In order to perform the directional integration on the half space, it is best to use the normal-tangential frame with respect to the surface, where the phonon direction vector can be expressed as $n_k = \{\tau_A, \nu\}_k$. In this frame, the normal and tangential components to the surface can be written as

$$\nu = n_k \nu_k = \cos\theta \quad \text{and} \quad \tau_A = \{\sin\theta\cos\phi, \sin\theta\sin\phi\}_A$$

Using this notation, Eq. (2.32) simplifies to

$$\int_{\nu>0} \omega^{\alpha} \tau_{A_1} ... \tau_{A_r} \nu^{n-r+1} f^{*} d\mathbf{k} = \int_{\nu>0} \omega^{\alpha} \tau_{A_1} ... \tau_{A_r} \nu^{n-r+1} f_G d\mathbf{k} \ , \tag{2.33}$$

where $r \leq n$. Grad [26] observed that in order to get a meaningful set of boundary conditions Υ_A must be even in the normal component of the directional vectors, hence $n-r$ must be even. Performing the integration in Eq. (2.32) leads to the general relation for the boundary conditions

$$\begin{aligned} &\frac{32\pi}{a^3 X_M^{\alpha+1}} (1-\beta) \left(\int_{BZ} X^{\alpha} \left(f_E - \overline{f_E} (T_s) \right) G(X)\, dX \right) \xi_s^m \delta_{\{B_1 ... B_s\}} \\ &- \beta (1-\gamma) \sum_n \mu^{\alpha} \frac{\left(u^{\alpha}_{<\nu_1 ... \nu_n>} - u^{\alpha}_{<\nu_1 ... \nu_n>|E} \right)}{\omega_M^{\alpha}} \xi_s^m \delta_{\{B_1 ... B_s\}} = \sum_n \sum_{r=0}^{n} \frac{(2n+1)!!}{(n-r)!r!} \left(\gamma \beta \sigma_{r+s}^{n+m} - \xi_{r+s}^{n+m} \right) \\ &\qquad \frac{\left(u^{\alpha}_{<A_1 ... A_r \nu_1 ... \nu_{n-r}>} - u^{\alpha}_{<A_1 ... A_r \nu_1 ... \nu_{n-r}>|E} \right)}{\omega_M^{\alpha}} \delta_{\{A_1 ... A_r B_1 ... B_s\}} \end{aligned} \tag{2.34}$$

Here, $X = \frac{\hbar\omega}{k_B T}$ is the non-dimensional frequency. Moreover, the capital indices refer to the tangential, ν refers to the normal directions with respect to the surface, and $\delta_{\{B_1 ... B_s\}}$ is the generalized tangential unit tensor. Note that the above boundary conditions are an extension to the simplified form of boundary equations presented in Ref. [24]. Details for derivation of this relation can be found in Appendix E and F .

2.5 Closed system of moment equations and boundary conditions

2.5.1 Macroscopic equations

Substituting the description for the flux term Eq. (2.24), as well as the production terms Eqs. (2.27) and (2.28), provides a closed system of equations that can be solved to describe the thermal behavior of the crystal. We introduce the non-dimensional moments, time and space as

$$U^{\alpha}_{<i_1 i_2 ... i_n>} = \frac{u^{\alpha}_{<i_1,..i_n>}}{\omega_M^{\alpha}}, \quad \hat{t} = \frac{t c_0}{L}, \quad \hat{x} = \frac{x}{L}, \tag{2.35}$$

where L is the length scale of the system. Based on the desired accuracy, we can use a specific number of transport equations for the direction and frequency. In the current study we employ three directional moments $\left(u_0^\alpha,\, u_i^\alpha,\, u_{<ij>}^\alpha\right)$. As a required condition, we will show that further increase in the number of directional moments, i.e., $u_{<ijk>}^\alpha$, $u_{<ijkl>}^\alpha$..., will not cause any noticeable change in the solution. Considering three directional moments will lead to a set of $9 \times n_F$ macroscopic equations, where n_F is the number of considered powers of frequency. By considering a small deviation from the equilibrium state, we can linearize the convection term in the non-equilibrium moments, and write Eq. (2.21) as

$$\begin{aligned}
\frac{\partial U_0^1}{\partial \hat{t}} + \sum_{\eta=0}^{n_F} A_1^{1,\eta} \frac{\partial U_i^\eta}{\partial \hat{x}_i} &= 0 \,, \qquad (2.36)\\
\frac{\partial V_0^\alpha}{\partial \hat{t}} + \sum_{\eta=0}^{n_F} \left(A_1^{\alpha,\eta} - \frac{\partial U_{0|E}^\alpha}{\partial U_0^1} A_1^{1,\eta} \right) \frac{\partial U_i^\eta}{\partial \hat{x}_i} &= -\frac{1}{\mathrm{Kn}_R} \sum_{\substack{\eta=0\\ \neq 1}}^{n_F} J_0^{\alpha,\eta} V_0^\eta \qquad \alpha \geq 0, \neq 1 \,,\\
\frac{\partial U_i^\alpha}{\partial \hat{t}} + \sum_{\eta=0}^{n_F} A_2^{\alpha,\eta} \frac{\partial U_{<ij>}^\eta}{\partial \hat{x}_j} + \frac{1}{3} \sum_{\substack{\eta=0\\ \neq 1}}^{n_F} A_0^{\alpha,\eta} \frac{\partial V_0^\eta}{\partial \hat{x}_i} + \frac{1}{3} \frac{\partial \left(A_E^\alpha U_{0|E}^\alpha \right)}{\partial U_0^1} \frac{\partial U_0^1}{\partial \hat{x}_i} &= -\frac{1}{\mathrm{Kn}_R} \sum_{\eta=0}^{n_F} J_1^{\alpha,\eta} U_i^\eta \,,\\
\frac{\partial U_{<ij>}^\alpha}{\partial \hat{t}} + \frac{2}{5} \sum_{\eta=0}^{n_F} A_1^{\alpha,\eta} \frac{\partial U_{<i}^\eta}{\partial \hat{x}_{j>}} &= -\frac{1}{\mathrm{Kn}_R} \sum_{\eta=0}^{n_F} J_2^{\alpha,\eta} U_{<ij>}^\eta \,.
\end{aligned}$$

Here, α is the number of frequency powers in the non-equilibrium moment, which can be up to n_F. Moreover,

$$J_n^{\alpha,\eta} = J_{n,R}^{\alpha,\eta} + \frac{\mathrm{Kn}_R}{\mathrm{Kn}_N} J_{n,N}^{\alpha,\eta} \,,$$

and

$$\mathrm{Kn}_R = \frac{c_0 \overset{0}{\tau}_R}{L} \qquad \text{and} \qquad \mathrm{Kn}_N = \frac{c_0 \overset{0}{\tau}_N}{L} \,,$$

are the reference Knudsen numbers for the R and N-processes. The temperature and heat flux implicitly appear in the moments equations, and will be discussed in details in the sequel.

The boundary conditions for this system, are obtained from Eq. (2.34) as

$$\begin{aligned}
U_\nu^\alpha &= -\frac{(1-\beta)}{2(\beta+1)} \frac{\Delta T}{T_S} Y^\alpha (T)\, U_0^1 - \frac{(1-\beta)}{2(\beta+1)} V_0^\alpha - \frac{15}{16} \frac{(1-\beta)}{(\beta+1)} U_{<\nu\nu>}^\alpha \qquad \alpha \geq 0, \neq 1 \,, \qquad (2.37)\\
U_{<A_1\nu>}^\alpha &= -\frac{3}{8} \frac{(1-\gamma\beta)}{(\gamma\beta+1)} U_{A_1}^\alpha \qquad \alpha \geq 0, \neq 1 \,.
\end{aligned}$$

Here, we linearized the first term of Eq. (2.34) in the temperature difference $\Delta T = T_S - T$, to get

$$Y^{\alpha}(T) = \frac{\displaystyle\int\limits_{BZ} \frac{X^{\alpha+1}\exp(X)G(X)}{(\exp(X)-1)^2}dX}{X_M^{\alpha-1}\displaystyle\int\limits_{BZ} \frac{XG(X)}{\exp(X)-1}dX} \ .$$

The first equation in the system of moments (2.36) represents the transport equation for the energy moment, with no production on the right hand side, and will be discussed in the next section. The transport equations for the non-equilibrium scalar moments and vectorial moments are shown in the second and third equations (2.36).

The vectorial moments will be related to the phonon momentum using the constitutive relations. The transport equations for the vectorial moments include second-rank tensorial moments $U^{\eta}_{<ij>}$, that can be related to the phonon stress. Dreyer and Struchtrup [19] showed that using the system of moment including the phonon stress can successfully express the second sound in the crystal. Therefore, the system of moments (2.36) are expected to include the corresponding terms for the second sound.

2.5.2 Energy, temperature and heat flux

The energy moment U_0^1 appearing in the system of equations (2.36) varies with temperature as

$$U_0^1 = \frac{4\pi k_B^4 y}{\hbar^4 c_0^3 \omega_M}\left(\int_{BZ} \frac{X_M^2 X G(X)}{\exp(X)-1}dX\right)T^4.$$

Note that in the above equation X and X_M are also a function of temperature. In the case of linear dispersion relation with infinite Brillouin zone, i.e., Debye assumptions [42], this relation simplifies to

$$U^1_{0_{|D}} = \frac{4\pi^5 k_B^4 y}{15\hbar^4 c_0^3 \omega_M}T^4 \ .$$

However, this assumption is only valid at low temperatures. Variation of the energy moment relative to the Debye energy moment with respect to the temperature is shown in Fig. 2.2. It is observed that at room temperature the energy moment deviates from the Debye energy moment, which reiterates the limitation of the Debye assumptions.

Another look into Eq. (2.36) shows that energy flux appears as a summation over the

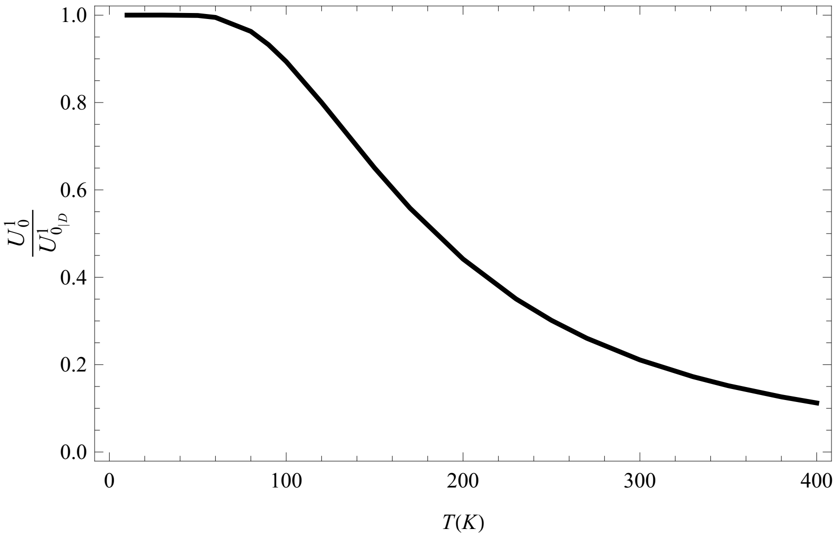

Figure 2.2: Variation of the energy moment relative to the Debye energy moment with respect to the temperature for Silicon

vectorial moments

$$Q_i = \sum_{\eta=0}^{n_F} A_1^{1,\eta} U_i^\eta \ . \tag{2.38}$$

Note that the non-dimensional heat flux Q_i, relates to the dimensional heat flux q_i as

$$Q_i = \frac{q_i}{c_o\left(\hbar\omega_M\right)} \ .$$

We use Eq. (2.38) to obtain the energy flux as a function of energy gradient, and derive the thermal diffusivity.

2.5.3 Thermal diffusivity and thermal conductivity

The thermal diffusivity, $\varkappa$ relates the heat flux to the gradient of energy as

$$q_i = -\varkappa \frac{\partial u_0^1}{\partial x_i} \ . \tag{2.39}$$

Equation (2.36)-3 shows the dependency of the vectorial moments on the gradient of energy moment, that will be used to obtain the thermal diffusivity. Considering that Fourier's law Eq. (2.39), is valid in the first order of Kn, we perform a Chapman-Enskog (CE) expansion [12] on the system of moments, to identify the first order terms contributing to the Fourier's heat flux.

We expand the non-equilibrium moments in the smallness parameter Kn_R as

$$\begin{aligned} V_0^\alpha &= V_{0,0}^\alpha + \mathrm{Kn}_R V_{0,1}^\alpha + O\left(\mathrm{Kn}_R^2\right) \ , \\ U_i^\alpha &= U_{i,0}^\alpha + \mathrm{Kn}_R U_{i,1}^\alpha + O\left(\mathrm{Kn}_R^2\right) \ , \\ U_{<ij>}^\alpha &= U_{<ij>,0}^\alpha + \mathrm{Kn}_R U_{<ij>,1}^\alpha + O\left(\mathrm{Kn}_R^2\right) \ . \end{aligned} \tag{2.40}$$

Then, we substitute this description in the system of moments. For example, Eq. (2.36)-2 reads

$$\frac{\partial\left(V_{0,0}^\alpha + \mathrm{Kn}_R V_{0,1}^\alpha + O\left(\mathrm{Kn}_R^2\right)\right)}{\partial\hat{t}} + \sum_{\eta=0}^{n_F}\left(A_1^{\alpha,\eta} - \frac{dU_{0|E}^\alpha}{dU_0^1} A_1^{1,\eta}\right) \frac{\partial\left(U_{i,0}^\eta + \mathrm{Kn}_R U_{i,1}^\eta + O\left(\mathrm{Kn}_R^2\right)\right)}{\partial\hat{x}_i} = -\sum_{\eta=0}^{n_F} \frac{1}{\mathrm{Kn}_R} J_0^{\alpha,\eta}\left(V_{0,0}^\eta + \mathrm{Kn}_R V_{0,1}^\eta + O\left(\mathrm{Kn}_R^2\right)\right) \ .$$

Collecting the powers of Kn_R^{-1} in the system of moments gives

$$V_{0,0}^{\alpha} = U_{i,0}^{\alpha} = U_{<ij>,0}^{\alpha} = 0 \ ,$$

that implies non of the above moments have zeroth order contributions. Applying the CE expansion to (2.36)-3 with the updated form of (2.40), and collecting the contribution of order Kn_R^0 gives

$$\frac{1}{3}\frac{\partial\left(A_E^{\alpha}U_{0|E}^{\alpha}\right)}{\partial U_0^1}\frac{\partial U_0^1}{\partial \hat{x}_i} = -\frac{1}{\mathrm{Kn}_R}\sum_{\eta=0}^{n_F} J_1^{\alpha,\eta}U_{i,1}^{\eta}. \tag{2.41}$$

Using the description of energy flux from (2.38), and the first order contribution of the vectorial moments (2.41), the thermal diffusivity can be written as

$$\varkappa = \varkappa^0 \sum_{\eta,\gamma=0}^{n_F} A_1^{1,\eta}\left(\left(J_1^{-1}\right)^{\eta\gamma}\frac{\partial\left(A_E^{\gamma}U_{0|E}^{\gamma}\right)}{\partial U_0^1}\right) \tag{2.42}$$

where

$$\varkappa^0 = \frac{1}{3}\tau_R^0 c_0^2 \ ,$$

is the reference thermal diffusivity, obtained by considering a constant relaxation time at the reference temperature.

Equation (2.42) shows that the thermal diffusivity predicted by the system of moments is a correction to the reference value, due to the frequency dependency in the relaxation time, i.e., the contribution of the production term $J_1^{\eta\gamma}$. It has been shown in Ref. [37] that the correction resulting from the Normal scattering process can be disregarded in the case of Silicon. Therefore, in order to adjust our relaxation time we assume that we only have R-process in our system, and neglect the N-process contribution.

Figure 2.3 shows the variation of the thermal conductivity with the temperature. Thermal conductivity, κ is related to the thermal diffusivity as

$$\kappa = \varkappa\rho C \ ,$$

where ρ is the mass density of the solid, and C is the specific heat obtained in Eq. (2.8). We considered 6 powers of frequency in our system, i.e., $n_F = 6$. In order to fit to the experimental data for thermal conductivity, we chose the cross-over between the two relaxation times in Eq. (2.15) to occur at 0.3 of the length of Brillouin zone, i.e., $\frac{\frac{\hbar\omega_C}{k_B T}}{BZ} = 0.3$. Note that since BZ in this expression also depends on the temperature, the

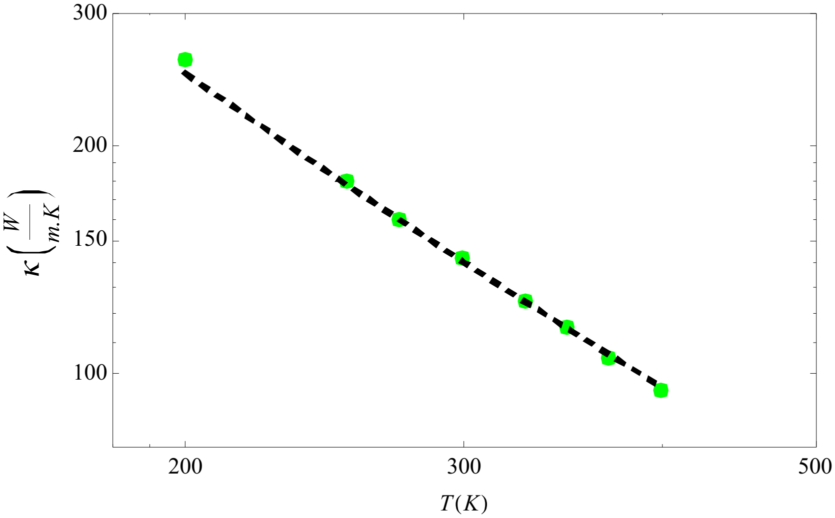

Figure 2.3: Variation of the thermal conductivity with the temperature for Silicon, line: system of moments, dots: experimental data in Ref. [42]

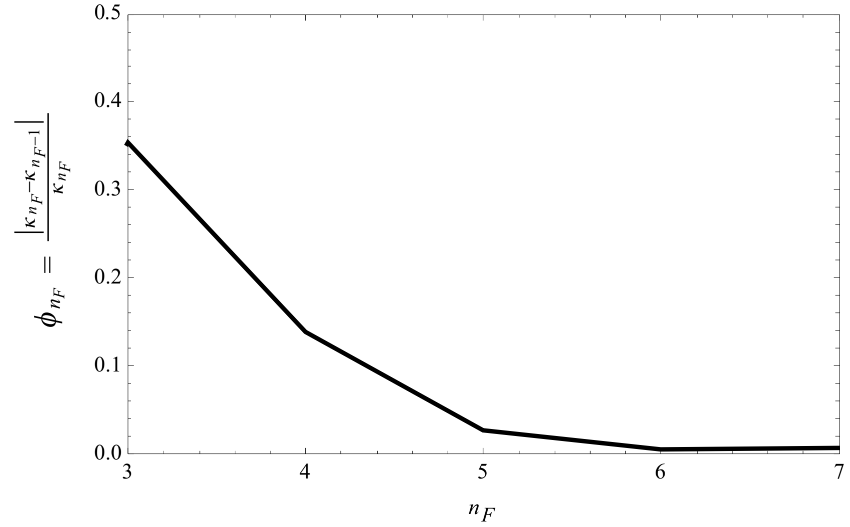

Figure 2.4: Variation of the relative change in the thermal conductivity with the number of considered frequency powers.

considered value for the cross-over frequency does not vary with the working temperature. The predicted results from the system of moments are in very good agreement with the experimental values for the Silicon. We could extend the comparison of the thermal conductivity to larger temperatures, however, we are interested in the room temperature comparison in the current study.

The effect of increasing the number of frequency powers on the thermal conductivity is depicted in Fig. 2.4. Here we show the relative changes in the thermal conductivity $\phi_{n_F} = \frac{|\kappa_{n_F}-\kappa_{n_F-1}|}{\kappa_{n_F}}$ with successive increase in the number of considered frequencies, n_F at $T = 300K$. We observed that the predicted results for thermal conductivity do not change noticeably by increasing the number of frequency powers to more than 6. Thus, we set $n_F = 6$ for the following results in this study.

2.6 Analytical solution in simple geometries

The system of moment equations (2.36) equipped with the boundary conditions (2.37) are a set of linear partial differential equations that can be analytically solved in simple geometries. First we study the behavior of one-dimensional wave obtained by system of moments, and then we investigate the one-dimensional Poiseuille flow for the phonon gas.

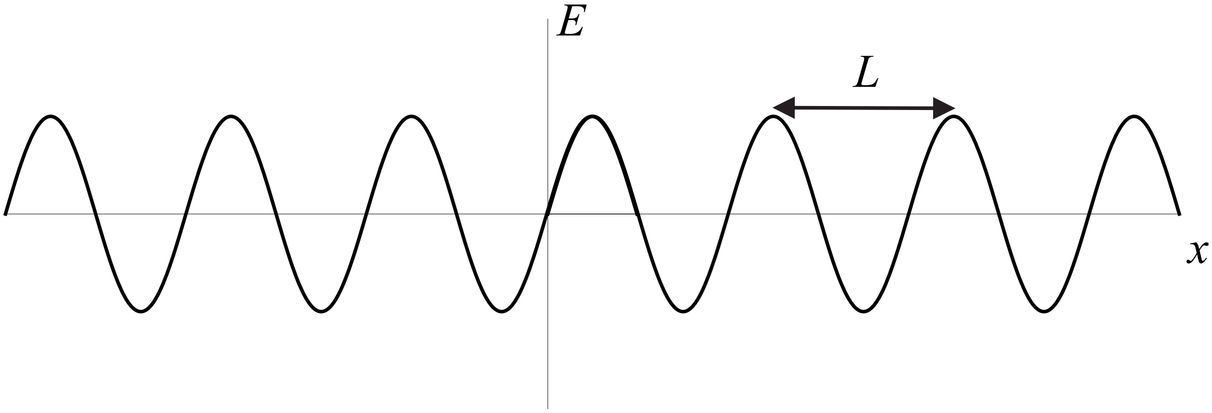

Figure 2.5: One-dimensional body with periodic initial condition

2.6.1 1-D Heat conduction with periodic initial condition

As the first application we look into the decay of energy amplitude with time in a one-dimensional body with periodic initial conditions such as Fig. 2.5 . Johnson et al. [38] experimentally studied this problem by interfering two laser beams, and exposing a wafer to the diffraction pattern. In this experiment, a sinusoidal energy pattern was initialized in a thin silicon wafer at room temperature, and the thermal decay was measured to determine a wavelength dependency of the damping coefficient. They observed that at room temperature, the thermal transport in Silicon significantly deviates from the diffusion model already at micron distances. More specifically, they showed that low frequency phonons, with rather large mean free paths that cannot be described by the diffusion model, significantly contribute to the heat transfer at micron distances.

Maznev et al. [52] investigated this problem by proposing a model in which the high-frequency phonons are described by the thermal diffusion equation, while the low-frequency phonons are described by the phonon-Boltzmann equation. They reported good agreement with the experimental data.

We use the moment method to predict the damping behavior as a function of the grating's wavelength, and compare it with the data reported in Ref. [52]. Due to the periodic nature of this problem, we do not need to use boundary conditions at both ends of the specimen, and will study the flow behavior in the bulk.

The depth of wafer used in Ref. [38] was much smaller than its length and width, such that the sinusoidal pattern remains homogenous throughout the entire specimen. Moreover, Johnson et al. used wafers with different thickness to study the effect of thickness (boundary conditions) on the heat flow. For simple analysis, we only consider a one-dimensional flow with infinite thickness to neglect effects of boundaries. Then, we validate our numerical results with the reported data in Ref. [38] for the infinite thickness.

System of moment solution

In one-dimension, we can write the linear system (2.36) as

$$\frac{\partial U_A}{\partial t} + A_{AB}\frac{\partial U_B}{\partial x} = -C_{AB}U_B \ , \tag{2.43}$$

where A_{AB} and C_{AB} correspond to the variable vector

$$U = \{U_0^1, V_0^\alpha, U_i^\alpha, U_{<ij>}^\alpha\} \ \alpha = 0, 1, ..., n_F \ .$$

Here, α is the number of frequency powers in the non-equilibrium moment, which can be up to n_F. Considering the periodic nature of the problem, we make the harmonic wave ansatz

$$U_A\left(x,t\right) = \widetilde{U}_A \exp\left(i\left(\Digamma x - \Omega t\right)\right) \ ,$$

where $\widetilde{U}_A$ is the complex amplitude, $\Digamma$ and Ω are, respectively, wavenumber and frequency of the harmonic wave. By inserting this relation in Eq. (2.43) we get the algebraic equation

$$\left(i\Omega\delta_{AB} - i\Digamma A_{AB} + C_{AB}\right)U_B = 0 \ ,$$

that only has non-trivial solutions when the determinant of the matrix inside the parenthesis becomes zero. This will lead to an eigenvalue problem, where Ω is the vector of eigenvalues for the matrix of $\Digamma A_{AB} + iC_{AB}$. For each eigenvalue there is a specific solution to the wave ansatz. By considering that only the energy moment was initially non-zero and equal to $\mathrm{E}\exp\left(i\Digamma x\right)$, the general solution can be obtained by adding all individual solutions together to form

$$U_A\left(x,t\right) = \mathrm{E}\sum_B Q_{AB}Q_{B1}^{-1}\exp\left(i\left(\Digamma x - \Omega_B t\right)\right) \ . \tag{2.44}$$

Here, Q_{AB} is the matrix of eigenvectors. We use our MATHEMATICA code to obtain the solution for the above expression. Note that the solution can be generated for an arbitrary number of moments, by simply expanding the dimensions of U_A, A_{AB} and C_{AB}.

Fourier's law solution

The linearized heat equation in one-dimension reads

$$\frac{\partial U_0^1}{\partial t} - \varkappa \frac{\partial^2 U_0^1}{\partial x^2} = 0 \ .$$

Using the wave ansatz leads to a quadratic relation between the frequency and the wavenumber

$$\Omega = -i\varkappa \digamma^2 \ ,$$

that is the case when diffusion is the dominant energy transfer mechanism. Using the Fourier law to solve the one-dimensional heat conduction problem gives

$$U_0^1 = \mathrm{E} \exp\left(-\varkappa \digamma^2 t\right) \cos\left(\digamma x\right) \ . \tag{2.45}$$

This equation shows that the Fourier law predicts a pure exponential decay for the energy moment by time. This exponential decay depends on the thermal diffusivity and the initial wavevector.

Results and discussion

Johnson et al. [38] conducted the thermal decay experiment on 15 transient gradient periods ranging from 2.4 to $25 \mu m$, and reported that within the whole range of grating periods the thermal decay remains exponential.

First, we use the system of moments to investigate if the energy moment follows an exponential decay. For this means, first we assume that the energy moment follows an exponential function such as Eq. (2.45), however, the coefficient in the exponential argument is not necessarily the thermal diffusivity $\varkappa$. Then, we consider t_1 and t_2 as two arbitrary times during the decay, and plot $-\log \frac{U_0^1}{\mathrm{E}}$ as a function of $\digamma^2 t$ in this period. This curve is compared with the predicted results from Eq. (2.44) for different values of grating period in Fig. 2.6.

For t_1 and t_2 we obtained the required time that the predicted energy by the system of moments drops to 80% and 20% of its initial value, respectively. We observed that as long as the grating period remains larger than $0.5 \mu m$, the decay follows a pure exponential curve, which is in accordance with the reported results in Ref. [38]. Moreover, it is observed that by increasing the grating length, the solution of system of moments approaches the Fourier's law solution, which is depicted by the red line.

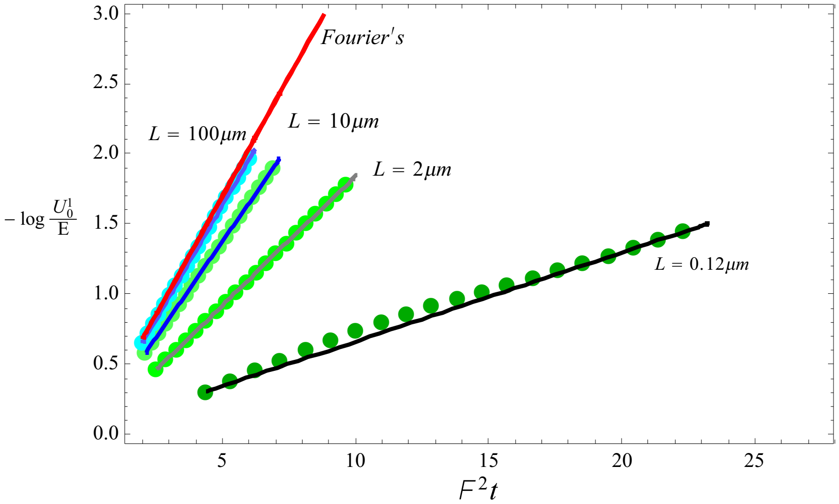

Figure 2.6: Variation of the energy decay with time for various grating periods, Markers: solution to Eq. (2.44), Lines: exponential function passing through t_1 and t_2, Red line: Fourier's solution in Eq. (2.45)

Considering that the decay curve remains exponential for $L > 0.5\mu m$, we define the decay parameter

$$\Gamma\left(\digamma^{2}\right) = \frac{\ln\left(\frac{U_0^1(0,t_1)}{U_0^1(0,t_2)}\right)}{t_2 - t_1} \; . \tag{2.46}$$

Note that as long as we have an exponential decay, the choice of t_1 and t_2 are arbitrary, and will not change the value of the decay parameter. For the Fourier law we have $\Gamma_F = \varkappa\digamma^{2}$, that shows a quadratic decay with the wavenumber.

Figure 2.7 shows the decay parameter Γ relative to the bulk Fourier decay as a function of the grating period for the moment solutions and the reported data in Ref. [38]. Johnson et al. [38] employed an effective thermal conductivity model, that takes into account the diffusion and ballistic transport of phonons, to report the energy decay when boundary scattering is not present.

For our numerical results we employed three forms of relaxation times: the cross-over relaxation time model Eq. (2.15) depicted by the black curve, Klemens model Eq. (2.14) depicted by the blue curve, and the constant relaxation time model as shown by the red curve. Although all employed relaxation time models predict the exact thermal conductivity (first order contribution) at this temperature, this figure demonstrates their short-coming in capturing higher order non-equilibrium phenomenon, and suggests the importance of employing appropriate relaxation times in the Callaway model.

We adjusted the free parameter in the relaxation time for the N-process Eq. (2.16), to get the best agreement with reported data. It is seen that at larger grating period the decay parameter approaches to unity, which shows the domination of diffusion in the heat transport mechanisms. It is observed that employing the appropriate relaxation time in the system of moments provides very good agreement with the reported results in Ref. [38].

In order to ensure the independency of the solution on the number of moments, we increase the number of directional moments n_D, and compared the relative deviation from the most accurate solution. Figure 2.8-a shows the variation of $\Phi_{n_D} = \frac{\left|\Gamma_{n_D} - \Gamma_S\right|}{\Gamma_{n_D}}$ with the number of considered directional moments, where Γ_S is the solution of our largest systems with $n_F = n_D = 7$. The comparison is conducted for 3 grating periods, $L = 1.5\mu m$ (square), $L = 2.5\mu m$ (circle) and $L = 10\mu m$ (triangle). It is observed that by considering 3 directional moments, the relative deviation from the solution of large system will be around 1%, and the solution is more or less converged. This system, that includes second rank tensorial moment, is rather simple for our analytical calculation, and will be used in

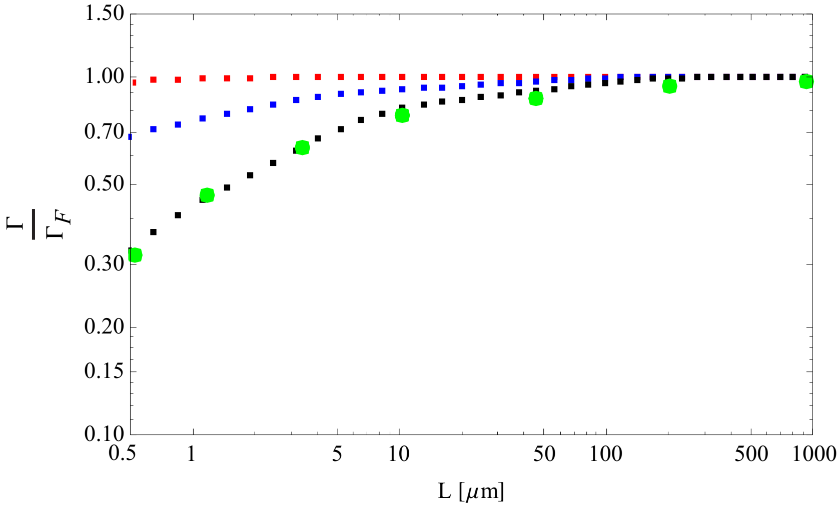

Figure 2.7: Variation of the decay parameter relative to the bulk Fourier decay with the grating period, green: reported data in Ref. [38], black: cross-over model, blue: Klemens model, red: constant relaxation time model

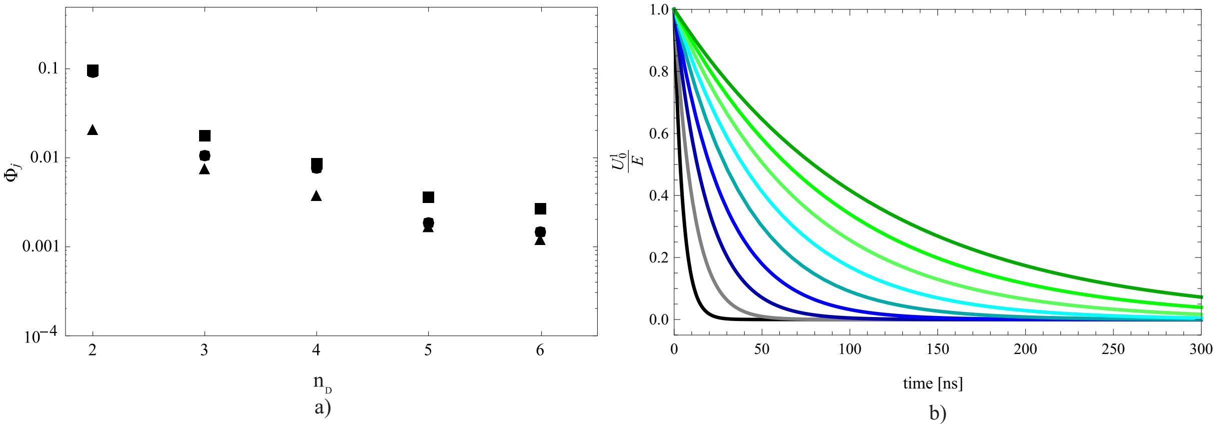

Figure 2.8: a) Relative changes in thermal decay parameter with the successive increase in the number of directional moments for $L = 1.5\mu m$ (squar), $L = 2.5\mu m$ (circle) and $L = 10\mu m$ (triangle). b) Energy decay for grating periods of $L = 2.3$ to $18\mu m$, corresponding to the reported results in Ref. [38].

the sequel.

Figure 2.8-b shows the energy decay traces for grating periods from 3.2 to $18\mu m$. This figure corresponds to the experimental results of Fig. 2 in Ref. [38]. It is seen that the thermal decay becomes slower at larger grating period. At larger grating period, it takes longer for heat to move from the peak to the null.

Note that in the experimental results of Ref. [38] the scattering of the phonons at the boundaries reduces the thermal conductivity (thickness effects). However, for our simple analytical calculation we assumed that the silicon specimen is wide enough that the boundary conditions do not play a role in the solution. The obtained results from the system of moments in Fig. 2.8-b are qualitatively similar to the experimental data of Fig. 2 in Ref. [38].

2.6.2 1-D Poiseuille flow of phonons

As another application we use the system of moments to solve one-dimensional Poiseuille flow of phonons in a heat conductor of thickness $2L$, as depicted in Fig. 2.9. We assume that there is a constant energy gradient of $\frac{\partial U_0^1}{\partial x}$ along the x-direction inside a semi-infinite silicon specimen, with adiabatic boundaries at $y = \pm L$. This problem is analogous to the one-dimensional pressure driven flow in fluid dynamics, where the pressure gradient in the fluid is replaced by energy gradients inside the solid.

As the first step to solve Poiseuille flow, we replace one of the vectorial moments

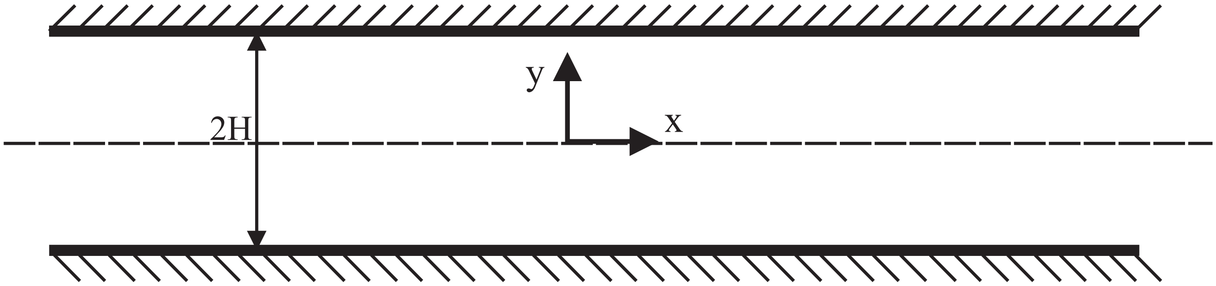

Figure 2.9: One-dimensional Poiseuille flow

with the energy flux Q_i, to have an explicit relation for energy flux in our equations. By this change of variable, providing the solution becomes more straightforward. Using the description for energy flux from Eq. (2.38) we replace U_i^1 as

$$U_i^1 = \frac{1}{A_1^{1,1}} Q_i - \sum_{\substack{\eta=0 \\ \eta\neq 1}}^{n_F} \frac{A_1^{1,\eta}}{A_1^{1,1}} U_i^\eta \ . \tag{2.47}$$

By considering the steady state condition, where all moments except for energy have zero gradient in x-direction, we can decouple Eq. (2.36) to get

$$\begin{aligned} \frac{\partial Q_y}{\partial \widehat{y}} &= 0 \ , \\ \sum_{\eta=0}^{n_F} A_2^{\alpha,\eta} \frac{\partial U^\eta_{<xy>}}{\partial \widehat{y}} + \frac{1}{3} \frac{\partial \left(A_E^\alpha U^\alpha_{0|E} \right)}{\partial U_0^1} \frac{\partial U_0^1}{\partial \widehat{x}} &= -\frac{1}{\mathrm{Kn}_R} \frac{J_1^{\alpha,1}}{A_1^{1,1}} Q_x - \frac{1}{\mathrm{Kn}_R} \sum_{\substack{\eta=0 \\ \eta\neq 1}}^{n_F} \left(J_1^{\alpha,\eta} - J_1^{\alpha,1} \frac{A_1^{1,\eta}}{A_1^{1,1}} \right) U_x^\eta \ , \\ \frac{1}{5} \frac{A_1^{\alpha,1}}{A_1^{1,1}} \frac{\partial Q_x}{\partial \widehat{y}} + \frac{1}{5} \sum_{\substack{\eta=0 \\ \eta\neq 1}}^{n_F} \left(A_1^{\alpha,\eta} - \frac{A_1^{\alpha,1}}{A_1^{1,1}} A_1^{1,\eta} \right) \frac{\partial U_x^\eta}{\partial \widehat{y}} &= -\frac{1}{\mathrm{Kn}_R} \sum_{\eta=0}^{n_F} J_2^{\alpha,\eta} U^\eta_{<xy>} \ , \end{aligned} \tag{2.48}$$

where $\mathrm{Kn}_R = \frac{c_0 \tau_R^0}{2L}$, and α is the frequency power in the non-equilibrium moment, which is considered to be up to n_F. The corresponding boundary conditions for this problem are obtained from Eq. (2.37)

$$U^\alpha_{<xy>} = -\frac{3}{8} \frac{(1-\gamma\beta)}{(\gamma\beta+1)} U_x^\alpha \ . \tag{2.49}$$

Note that by substituting Eq. (2.47) in the above relation, we can obtain the boundary condition for the energy flux moment.

We derive an expression for $U^\beta_{<xy>}$ from Eq. (2.48)-3 as

$$U^\beta_{<xy>} = -\frac{1}{5} \mathrm{Kn}_R \sum_{\gamma=0}^{n_F} \sum_{\eta=0}^{n_F} \left(J_2^{-1} \right)^{\beta,\gamma} F^{\gamma,\eta} \widetilde{U}_x^\eta$$

where

$$F^{\gamma,\eta} = \frac{A_1^{\gamma,1}}{A_1^{1,1}} \delta_\eta^1 + \left(A_1^{\gamma,\eta} - \frac{A_1^{\gamma,1}}{A_1^{1,1}} A_1^{1,\eta} \right) \ ,$$

and $\widetilde{U}_x^\eta$ is the vector of vectorial moments, with the energy flux Q_x on its second row, i.e., for $\eta = 1$. Moreover, we can obtain the contribution of Fourier-like energy flux from

Eq. (2.48)-2, and define

$$R_x^\alpha = -\frac{1}{3}\mathrm{Kn}_R \sum_{\eta=0}^{n_F} \left(B^{-1}\right)^{\alpha,\eta} \frac{\partial\left(A_E^\eta U_{0|E}^\eta\right)}{\partial U_0^1}\frac{\partial U_0^1}{\partial \widehat{x}} \ , \tag{2.50}$$

where

$$B^{\alpha,\eta} = \frac{J_1^{\alpha,1}}{A_1^{1,1}}\delta_\eta^1 + \left(J_1^{\alpha,\eta} - J_1^{\alpha,1}\frac{A_1^{1,\eta}}{A_1^{1,1}}\right) \ .$$

Note that we have the Fourier law for R_x^1, where we can see the relation between the energy flux and energy gradient.

In order to get a compact form of the governing equations, we subtract the Fourier-like contribution of the fluxes Eq. (2.50), from the vectorial moments, and define the variable vector

$$Z_x^\alpha = \{U_x^0 - R_x^0, Q_x - R_x^1, ..., U_x^{n_F} - R_x^{n_F}\}_\alpha \ .$$

Noting that the energy moment only has a gradient in the x-direction, the system of moments in (2.48) simplifies to an eigenvalue problem as

$$Z_x^\alpha = \frac{1}{5}\mathrm{Kn}_R^2 \sum_{\eta=0}^{n_F} M^{\alpha,\eta}\frac{\partial^2 Z_x^\eta}{\partial \widehat{y}^2} \ , \tag{2.51}$$

where

$$M^{\alpha,\eta} = \sum_{\varepsilon,\beta,\gamma} \left(H^{-1}\right)^{\alpha,\varepsilon} A_2^{\varepsilon,\beta} \left(J_2^{-1}\right)^{\beta,\gamma} F^{\gamma,\eta} \ .$$

Solving Eq. (2.51) gives the energy flux as

$$Q_x = Q_F\left(1 - \sum_\gamma \mathcal{V}^{1,\gamma}C^\gamma \cosh\left(\frac{\widehat{y}}{\mathrm{Kn}_R}\sqrt{\frac{5}{\lambda^\gamma}}\right)\right) \ , \tag{2.52}$$

where $\mathcal{V}^{\alpha,\gamma}$ is the matrix of eigenvectors, and λ^γ are the eigenvalues of $M^{\alpha,\eta}$, that depends on the considered relaxation time, dispersion relation and the number of frequency powers. Moreover, C^γ are the constants of integration that need be found from the boundary equation (2.49), and Q_F is the Fourier's heat flux

$$Q_F = -\frac{1}{3}\mathrm{Kn}_R \sum_{\eta,\gamma}^{n_F} A_1^{1,\eta}\left(\left(J_1^{-1}\right)^{\eta\gamma} \frac{\partial\left(A_E^\gamma U_{0|E}^\gamma\right)}{\partial U_0^1}\right)\frac{\partial U_0^1}{\partial \widehat{x}} \ .$$

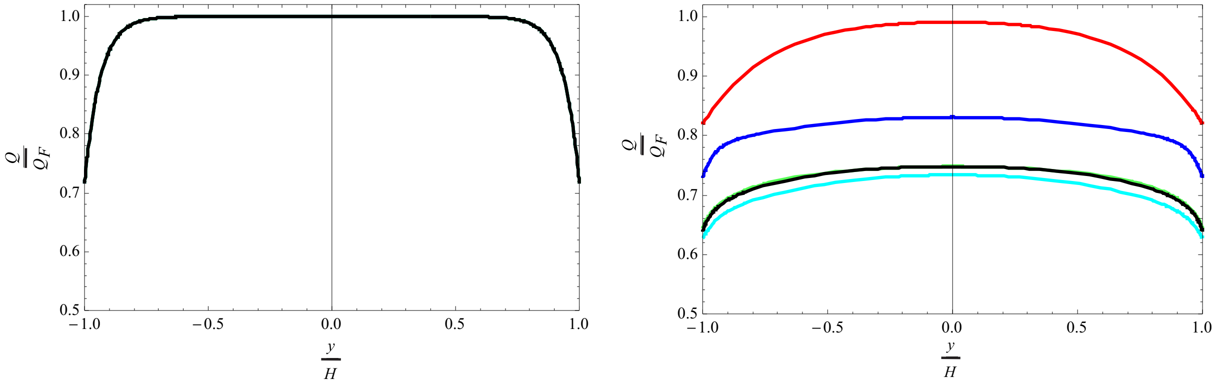

Figure 2.10: Heat flux predicted by the system of moments relative to the Fourier's heat flux for the Poiseuille flow of phonons at $\mathrm{Kn}_R = \mathrm{Kn}_N = 0.2$, $\beta = 1$ and $\gamma = 0.5$. a) Constant relaxation time model for $n_F = 2, 3, 5, 6, 7$. b) Cross-over relaxation time model for $n_F = 2, 3, 5, 6, 7$.

The system of moments gives a Knudsen layer correction to the Fourier solution. Figure 2.10 shows the changes in the heat flux due to the increasing number of considered frequency moments n_F for two models of relaxation time. In the case of constant relaxation time, the production matrix is diagonal, and increasing the number of frequency powers does not change the solution of the system. In this case, the deviation from the Fourier solution is mainly observed in the vicinity of the crystal boundaries.

By considering the frequency dependency in relaxation time we need sufficient number of frequency moments to get a converged solution. By employing 2 frequency powers, i.e., the red line, the rarefaction effects are mainly observed at the boundaries. As we increase n_F, the deviation from the Fourier's solution is also predicted in the bulk of the phonon gas, and the solution will be more or less the same for $n_F = 5, 6, 7$.

The effect of Knudsen number on the energy flux is depicted in Fig. 2.11-a. As the Knudsen number decreases the energy flux approaches to the plug flow solution, that is predicted by the Fourier law. Increasing rarefaction effects leads to a deviation from the Fourier's solution first at the boundaries, and then in the entire flow field.

Figure 2.11-b shows the effect of changing the relative portion of specularly reflected and isotropically scattered phonons on the energy flux. The plug flow solution is obtained when the reflection is purely specular $\gamma = 1$, which means that boundaries do not have any influence on the bulk. Increasing the portion of isotropically scattered phonons imposes a drag on the gas at the crystal boundary, which leads to Knudsen layer development, and emerging the rarefaction effects in the flow field.

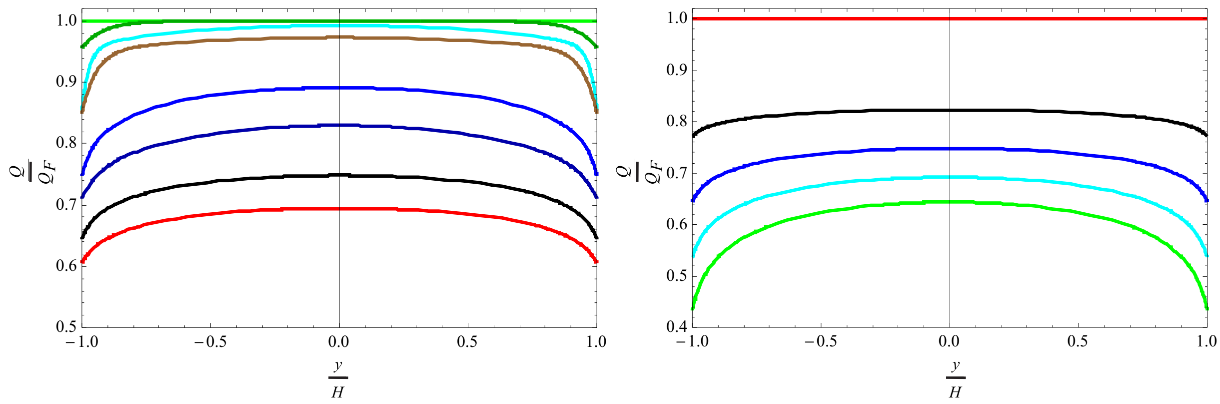

Figure 2.11: Heat flux predicted by the system of moments relative to the Fourier's heat flux for the Poiseuille flow of phonons. a) Effect of the Knudsen number $\text{Kn}_R = \text{Kn}_N = 0.0001 - 0.3$, $\beta = 1$ and $\gamma = 0.5$. b) Effect of γ on the solution $\gamma = 0, 0.25, 0.5, 0.75, 1$ and $\text{Kn}_R = \text{Kn}_N = 0.2$

2.7 Conclusion

We presented a set of macroscopic equations for phonon transport to describe the thermal properties of a crystal. We employed a quadratic dispersion relation in the finite Brillouin zone to express the dependency of frequency on the wave vector. The collision term in the right hand side of the phonon-Boltzmann equation is described by the Callaway model, where the relaxation time is depending on the frequency of phonons. Using this model, we proposed macroscopic moments that depend on the powers of frequency, and the polynomial of phonon's direction vector. Then, the transport equations for macroscopic moments are obtained from the phonon-Boltzmann equation. The closure to this system of equations is provided using the Grad distribution function.

We used the Grad method to provide boundary conditions for the system of moments. We considered three types of microscopic interactions between phonons and crystal boundaries: thermalization, specular reflection and isotropic scattering. The reflection kernel in the proposed boundary model is considered to be the superposition of kernels for these microscopic interaction types.

In order to validate the system of moments, we studied the thermal decay in a one-dimensional body with periodic initial condition. This problem was experimentally studied in Ref. [38]. We observed that the thermal decay deviates from the heat equation already at micron level. We employed different relaxation times in the Callaway model, and observed that by accounting for both low frequency and high frequency phonons in the relaxation time model, we get a good agreement with the reported data in Ref. [38]. As we employed different relaxation time models, we observed that although they all agree in predicting the thermal conductivity (first order rarefaction effect), not all of them can predict the thermal decay curve (higher order rarefaction effect).

As the second application, we solved the one-dimensional Poiseuille flow of phonons in a crystal with adiabatic surface. We observed that in this case, the system of moments predict a Knudsen layer correction to the Fourier's solution.

This study confirms the main role of *frequency dependent relaxation time* in predicting non-equilbrium heat transport in solids. By comparing our results with the reported data in Ref. [38], we get a validation that the current form of moment equations is capable of capturing the deviation from equilibrium state properly. We now aim to employ the boundary conditions to solve the two-dimensional flow of phonon gas to investigate the effect of thickness on the heat transport in the silicon specimen.

Acknowledgement

This research was supported by the Natural Sciences and Engineering Research Council (NSERC).

Chapter 3

Temperature Relaxation in Laser Induced Thermal Gratings Described by Phonon Hydrodynamics

Abstract: *We use phonon hydrodynamics to describe recent experiments on decay of thermal gratings in thin crystals [PRL 110, 025901 (2013)]. The system of moment equations for phonon transport are solved by considering that the crystal thickness H is much smaller than the grating length L. This allows to derive a one-dimensional set of equations for the signal decay, which has boundary drag (phonon- Poiseuille flow) incorporated. By considering a collision model that takes into account both low and high frequency phonons, we capture the experimental results. This quantitative agreement shows capabilities of moment method in capturing non-equilibrium in phonon transport.*

To be submitted to Physical Review Letters

Recently, Johnson et al. observed non-Fourier heat transfer in the relaxation of temperature in a sinusoidally heated thin silicon membrane [38]. Specifically, they exposed a $400nm$ thick membrane to two crossed laser beams, whose interference pattern lead to an initial sinusoidal temperature grating with wavelengths between $3.2\mu m$ and $25\mu m$. Due to heat transfer processes by phonons, the amplitude of the grating decays over time on the scale of tens or hundreds of nanoseconds. Assuming exponential decay, they determined a wavelength dependent decay parameter for the membrane, which for smaller wavelength deviates markedly from that given by the classical description of heat transfer by Fourier's law.

The text-book mean free path for silicon is $\lambda = 43nm$. Considering that in semiconductors heat is mostly transported by phonons, the ratio of phonon mean free path λ and the length scale of the flow L determines the regime of this energy transfer, i.e, diffusive or ballistic. At low temperatures most phonons have rather large mean free path, which leads to ballistic phonon transport. At room temperature, the mean free path for most phonons are in the range of nanometers, therefore, one does not expect deviation from the diffusion equation when the length scale is significantly larger than nanometers.

However, theoretical and experimental studies [40] have suggested that phonons with rather large mean free path play an important role at room temperature. Researchers proposed to revise the effective mean free path for silicon at room temperature to $260-300nm$ to account for phonons with large mean free path [14]. One study shows that phonons with mean free path exceeding than $1\mu m$ have an almost 40% contribution to the thermal conductivity in silicon at the room temperature [35].

For a mean free path of $200nm$ (say), the Knudsen numbers for the grated heating experiment–defined as mean free path over characteristic length–are below 0.1, and the Knudsen number for phonon flow through the membrane of thickness $400nm$ is about 0.5. From the given values of the Knudsen number one can explain the measured deviation from Fourier's law by the combined influence of membrane thickness and grating period. Johnson et al. explain the observation through phonon kinetic theory, specifically through the large differences between actual phonon mean free paths, as compared to the average; phonons with large mean free paths contribute significantly to heat transfer.

In this contribution, we ask whether the experimental findings can be described by phonon hydrodynamics, that is theories that extend the macroscopic description of heat transfer in solids to Knudsen numbers where Fourier's law is not valid anymore. This approach goes back to the seminal works by Guyer and Krumhansl [30, 31], who developed their equations to successfully describe heat pulse experiments, see [19] for a review of the experiments and various theories for their description.

We recently proposed a system of macroscopic moment equations with the corresponding boundary conditions to model phonon transport at moderate Knudsen number [61]. In this system the phonon velocity is not constant and varies with the phonon frequency. Also, relaxation times (for R and N-processes) are assumed to be functions of phonon frequency to properly model the relaxation process at low and high temperatures.

In the current study, we model the thermal grating experiment [38] as a transient Poiseuille flow of phonons. In this flow, the boundary drag of phonons leads to a reduction in the energy transfer and has to be considered in the equations. Our solutions of the moment system are in good agreement with the findings in the thermal grating experiment [38].

In our system of moment equations for phonon transport, non-dimensional macroscopic moments are defined as [61]

$$U^{\alpha}_{<i_1..i_n>} = \int_{BZ} \frac{\omega^{\alpha}}{\omega^{\alpha}_{M}} n_{<i_1 ... } n_{i_n>} f\left(\mathbf{x}, \mathbf{k}, t\right) d\mathbf{k} \ . \tag{3.1}$$

Here, indices in angular brackets denote the trace-free and symmetric part of the tensor, ω^{α} is the α-th power of phonon frequency, ω_M is the reference frequency, $n_{<i_1 ...} n_{i_n>} = \frac{k_{<i_1 ... i_n>}}{k^n}$ is the direction tensor of phonons, $f\left(\mathbf{x}, \mathbf{k}, t\right)$ is the phonon distribution function, $\mathbf{k}$ is the wavevector and BZ denotes the Brillouin zone, which depends on the working temperature of the system. Following Eq. (3.1), the energy density is obtained by

$$\frac{e\left(\mathbf{x}, t\right)}{\hbar \omega_M} = U^1_0\left(\mathbf{x}, t\right) \ .$$

The energy density flux and the momentum density of phonons are related to the vectorial moments U^{α}_{i}, by using the constitutive relations [61].

The balance equations for macroscopic moments are derived from the Callaway [9] model of phonon kinetic theory. We assumed frequency dependency in relaxation times and proposed "cross-over" model for U-processes [100, 61]

$$\tau_U\left(\omega\right) = \begin{cases} \frac{1}{B_U T \exp\left(-\frac{D}{T}\right)} \frac{1}{\omega^2}, & \omega \le \omega_C \\ \frac{1}{S_U T \exp\left(-\frac{D}{T}\right)} \frac{1}{\omega^4}, & \omega \ge \omega_C \end{cases} ,$$

to distinguish interactions of phonons at low and high frequencies, also we considered

[100, 61]

$$\tau_N(\omega) = \frac{1}{B_N T \omega^2} ,$$

for N-processes. Here T is the working temperature of the system, and B_U,S_U,D,B_N and ω_C are constants, please see Refs. [43, 55, 61] for the corresponding values of these constants.

The system of moment equations containing upto the second order tensorial moments reads

$$\begin{aligned}
\frac{\partial U_0^1}{\partial \hat{t}} + \frac{\partial Q_i}{\partial \hat{x}_i} &= 0 , \\
\frac{\partial V_0^\alpha}{\partial \hat{t}} + \sum_{\eta=0}^{n_F} \widetilde{A}_1^{\alpha\eta} \frac{\partial U_i^\eta}{\partial \hat{x}_i} &= -\frac{1}{\mathrm{Kn}_R} \sum_{\substack{\eta=0\\ \neq 1}}^{n_F} J_0^{\alpha\eta} V_0^\eta \quad \alpha \geq 0, \neq 1 , \\
\frac{\partial U_i^\alpha}{\partial \hat{t}} + \sum_{\eta=0}^{n_F} A_2^{\alpha\eta} \frac{\partial U_{<ij>}^\eta}{\partial \hat{x}_j} + \frac{1}{3} \sum_{\substack{\eta=0\\ \neq 1}}^{n_F} A_0^{\alpha\eta} \frac{\partial V_0^\eta}{\partial \hat{x}_i} + \frac{1}{3} \widetilde{A}_E^\alpha \frac{\partial U_0^1}{\partial \hat{x}_i} &= -\frac{1}{\mathrm{Kn}_R} \sum_{\eta=0}^{n_F} J_1^{\alpha\eta} U_i^\eta , \\
\frac{\partial U_{<ij>}^\alpha}{\partial \hat{t}} + \frac{2}{5} \sum_{\eta=0}^{n_F} A_1^{\alpha\eta} \frac{\partial U_{<i}^\eta}{\partial \hat{x}_{j>}} &= -\frac{1}{\mathrm{Kn}_R} \sum_{\eta=0}^{n_F} J_2^{\alpha\eta} U_{<ij>}^\eta .
\end{aligned} \tag{3.2}$$

Here, the first equations is the energy balance, with zero production in the right hand side. The second equation denotes the balance of non-equilibrium scalar moments, i.e., V_0^α. The balance of vectorial, i.e, U_i^α, and tensorial moments, i.e., $U_{<ij>}^\alpha$ are denoted in the third and fourth equations. The matrices of fluxes, i.e., $A_n^{\alpha\eta}$ and $\widetilde{A}_n^{\alpha\eta}$, and the matrix of productions, i.e., $J_n^{\alpha\eta}$ depend on the working temperature as well as the dispersion relation. The matrix of productions also depends on the relaxation times considered for the Callaway model. Please see Ref. [61] for a detailed description of these matrices. Note that the heat flux appearing in (3.2)-1 is a summation over vectorial moments

$$Q_i = \sum_{\eta=0}^{n_F} A_1^{1,\eta} U_i^\eta . \tag{3.3}$$

In the transport equations $\mathrm{Kn}_R = \frac{\overline{\tau}_R c_D}{H}$ appears in the right hand-side of equations, due to using non-dimensional time $\hat{t} = \frac{c_D t}{H}$ and non-dimensional space $\hat{x} = \frac{x}{H}$, where thickness H is the reference length scale. Also α is the frequency power in the non-equilibrium moments, which is considered to be up to n_F, i.e., maximum number of frequency moments.

In order to model the thermal grating experiment [38], we consider that the crystal of length L and thickness H is very thin $\left(\frac{H}{L} \ll 1\right)$, and has adiabatic boundaries at $\frac{y}{H} = \pm\frac{1}{2}$. Note that, although the measurements in the experiment were done in the ambient air, the effect of the thermal conductivity of air on the thermal grating decay in the membrane was negligible [38]. Energy transport in the crystal is along the x-coordinate, the y-coordinate is for thickness, and there is no variation along the z-coordinate.

Before studying the relaxation of the initial thermal grating, we look into the case of steady state phonon-Poiseuille flow. Considering that the crystal thickness is much smaller than the thermal grating length, the flow quickly approaches to the steady state condition at each cross section of the membrane. We consider that the crystal is subjected to a uniform energy gradient $\frac{\partial U_0^1}{\partial \widehat{x}}$, and other moments only have a gradient across the crystal, i. e., y-direction. Using these assumptions, the system of equations in (3.2) decouple, and gives

$$\begin{aligned} \frac{\partial Q_y}{\partial \widehat{y}} &= 0 \, , \\ \sum_{\eta=0}^{n_F} A_2^{\alpha\eta} \frac{\partial U_{<xy>}^{\eta}}{\partial \widehat{y}} + \frac{1}{3}\widetilde{A}_E^{\alpha}\frac{\partial U_0^1}{\partial \widehat{x}} &= -\frac{1}{\mathrm{Kn}_R}\sum_{\eta=0}^{n_F} J_1^{\alpha\eta} U_x^{\eta} \, , \\ \frac{1}{5}\sum_{\eta=0}^{n_F} A_1^{\alpha\eta}\frac{\partial U_x^{\eta}}{\partial \widehat{y}} &= -\frac{1}{\mathrm{Kn}_R}\sum_{\eta=0}^{n_F} J_2^{\alpha\eta} U_{<xy>}^{\eta} \, . \end{aligned} \tag{3.4}$$

The adiabatic boundary conditions read [61]

$$\begin{aligned} U_y^{\alpha}\left(\pm\frac{1}{2}\right) &= 0 \, , \\ U_{<xy>}^{\alpha}\left(\pm\frac{1}{2}\right) &= -\frac{3}{8}\chi U_x^{\alpha}\left(\mp\frac{1}{2}\right) \, , \end{aligned} \tag{3.5}$$

which are no-penetration normal to the flow direction, and slip condition for the tangential phonon momentum with χ as the slip coefficient. The solution to this system is obtained by eigenvalue-eigenvector analysis as

$$U_x^{\alpha} = \sum_{\eta=0}^{n_F} \mathcal{V}^{\alpha\eta} C^{\eta} \cosh\left(\sqrt{\frac{5}{\lambda^{\eta}}}\frac{\widehat{y}}{\mathrm{Kn}_R}\right) - \frac{1}{3}\mathrm{Kn}_R \sum_{\eta=0}^{n_F}\left(J_1^{-1}\right)^{\alpha\eta}\widetilde{A}_E^{\eta}\frac{\partial U_0^1}{\partial \widehat{x}} \, , \tag{3.6}$$

where α is the frequency power in the non-equilibrium moment which is considered to be up to n_F. Moreover, $\mathcal{V}^{\alpha\eta}$ and λ^{η} are, respectively, the matrix of eigenvectors and the vector of eigenvalues for

$$M^{\alpha\eta} = \sum_{\varepsilon,\beta,\gamma=0}^{n_F} \left(J_2^{-1}\right)^{\alpha\varepsilon} A_1^{\varepsilon\beta} \left(J_1^{-1}\right)^{\beta\gamma} A_2^{\gamma\eta} \ ,$$

and C^η are the constants of integration that must be obtained from the boundary equations (3.5). We used MATHEMATICA to evaluate all matrices, eigenvalues and eigenvectors. Equation (3.6) shows that the vectorial moments are not constant across the crystal.

Now we consider the relaxation of a sinusoidally heated thin crystal in time to model the thermal grating experiment [38]. In this experiment, only the cross sectional average of the temperature (or energy) is measured. We integrate the system of moments (3.2) across the crystal to find equations for the cross sectional averages of the variables, defined as

$$\overline{U}^{\alpha}_{<i_1 \dots i_n>} = \int_{-\frac{1}{2}}^{\frac{1}{2}} U^{\alpha}_{<i_1 \dots i_n>} d\widehat{y} \ .$$

After integration, and use of adiabaticity at boundaries, $U_y^\alpha\left(\pm\frac{1}{2}\right) = 0$, the boundary values for $U_x^a\left(\pm\frac{1}{2}\right)$ appear explicitly in the balance equation for vectorial moments, which require to be evaluated. When variation of energy moment–and energy gradient–are on the length scale L that is large compared to the thickness H of the crystal, the time variation of the energy gradient $\frac{\partial U_0^1}{\partial \widehat{x}}$ is slow compared with the time required for the phonon flow to approach the Poiseuille flow solution (3.6) locally at each cross section. By inserting the Poiseuille flow solution (3.6) for $U_x^\alpha\left(\pm\frac{1}{2}\right)$, that appeared due to using slip boundary conditions we get

$$\int_{-\frac{1}{2}}^{\frac{1}{2}} \left(\sum_{\gamma=0}^{n_F} A_2^{\alpha\gamma} \frac{\partial U_{xy}^{\gamma}}{\partial \widehat{y}} \left(\pm\frac{1}{2}\right) \right) d\widehat{y} = -\frac{1}{4}\chi \sum_{\eta}^{n_F} \mu^{\alpha\eta} \widetilde{A}_E^{\eta} \frac{\partial U_0^1}{\partial \widehat{x}} \ , \tag{3.7}$$

with

$$\mu^{\alpha\eta} = \mathrm{Kn}_R \sum_{\gamma=0}^{n_F} A_2^{\alpha\gamma} \left(J_1^{-1}\right)^{\gamma\eta} \left(1 + \frac{\sum\limits_{\varepsilon,\beta} A_2^{\alpha\varepsilon} \mathcal{V}^{\varepsilon\beta} C^{\beta} \cosh\left(\sqrt{\frac{5}{4\lambda^{\beta}}} \frac{1}{\mathrm{Kn}_R}\right)}{-\frac{1}{3}\mathrm{Kn}_R \sum\limits_{\eta,\gamma=0}^{n_F} A_2^{\alpha\gamma} \left(J_1^{-1}\right)^{\gamma\eta} \widetilde{A}_E^{\eta} \frac{\partial U_0^1}{\partial \widehat{x}}} \right) \ . \tag{3.8}$$

This leads to appearance of $\mu^{\alpha\eta}$, as the effect of boundary drag, explicitly in the balance of vectorial moments. The governing equations read

$$\begin{aligned}
\frac{\partial \overline{U}_0^1}{\partial \hat{t}} + \frac{\partial \overline{Q}_x}{\partial \hat{x}} &= 0 \ , \\
\frac{\partial \overline{V}_0^\alpha}{\partial \hat{t}} + \sum_{\eta=0}^{n_F} \widetilde{A}_1^{\alpha\eta} \frac{\partial \overline{U}_x^\eta}{\partial \hat{x}} &= -\frac{1}{\mathrm{Kn}_R} \sum_{\substack{\eta=0\\ \neq 1}}^{n_F} J_0^{\alpha\eta} \overline{V}_0^\eta \quad \alpha \geq 0, \neq 1 \ ,
\end{aligned} \tag{3.9}$$

$$\frac{\partial \overline{U}_x^\alpha}{\partial \hat{t}} + \sum_{\eta=0}^{n_F} A_2^{\alpha\eta} \left(\frac{2}{3} \frac{\partial \overline{U}_{xx}^\eta}{\partial \hat{x}} - \frac{1}{3} \frac{\partial \overline{U}_{yy}^\eta}{\partial \hat{x}} \right) + \frac{1}{3} \sum_{\substack{\eta=0\\ \neq 1}}^{n_F} A_0^{\alpha\eta} \frac{\partial \overline{V}_0^\eta}{\partial \hat{x}} + \frac{1}{3} \left(\widetilde{A}_E^\alpha - \frac{3}{4} \chi \sum_{\eta=0}^{n_F} \mu^{\alpha\eta} \widetilde{A}_E^\eta \right) \underline{\frac{\partial \overline{U}_0^1}{\partial \hat{x}}} = -\frac{1}{\mathrm{Kn}_R} \sum_{\eta=0}^{n_F} J_1^{\alpha\eta} \underline{\overline{U}_x^\eta} \ ,$$

$$\begin{aligned}
\frac{\partial \overline{U}_{<xx>}^\alpha}{\partial \hat{t}} + \frac{4}{15} \sum_{\eta=0}^{n_F} A_1^{\alpha\eta} \frac{\partial \overline{U}_x^\eta}{\partial \hat{x}} &= -\frac{1}{\mathrm{Kn}_R} \sum_{\eta=0}^{n_F} J_2^{\alpha\eta} \overline{U}_{<xx>}^\eta \ , \\
\frac{\partial \overline{U}_{<yy>}^\alpha}{\partial \hat{t}} - \frac{2}{15} \sum_{\eta=0}^{n_F} A_1^{\alpha\eta} \frac{\partial \overline{U}_x^\eta}{\partial \hat{x}} &= -\frac{1}{\mathrm{Kn}_R} \sum_{\eta=0}^{n_F} J_2^{\alpha\eta} \overline{U}_{<yy>}^\eta \ .
\end{aligned}$$

Before solving the system of equations above, we find the Fourier's, i.e., first-order, solution of the system of moments. Considering our constitutive equation (3.3) for heat flux, we need to obtain the first-order contribution of vectorial moments. We use the order of magnitude method and perform a Chapman-Enskog expansion with the smallness parameter Kn_R, on the system of moments (3.9) to identify the level of contribution of each moment. Please see Ref. [61] for a more detailed description of this method applied to the moment system. In the balance equation for the vectorial moments Eq. (3.9)-3, the underlined terms survive in the first order expansion, and the Fourier's heat flux follows

$$\overline{Q}_{\hat{x},F} = -\kappa_F \frac{\partial \overline{U}_0^1}{\partial \hat{x}} \ , \tag{3.10}$$

where κ_F is the non-dimensional thermal diffusivity which depends on the relaxation time, dispersion relation and the boundary effect

$$\kappa_F = \frac{1}{3} \mathrm{Kn}_R \sum_{\alpha,\beta=0}^{n_F} A_1^{1,\alpha} \left(J_1^{-1} \right)^{\alpha\beta} \widetilde{A}_E^\beta - \frac{1}{4} \mathrm{Kn}_R \chi \sum_{\alpha,\beta,\eta=0}^{n_F} A_1^{1,\alpha} \left(J_1^{-1} \right)^{\alpha\beta} \mu^{\beta\eta} \widetilde{A}_E^\eta \ . \tag{3.11}$$

Note that the first term in Eq. (3.11) is the bulk effect, and the second term shows the effect of boundary drag on the thermal diffusivity.

Now, in order to solve the system of transport equations (3.9), we assume that initially all moments except for energy are zero. The energy moment follows the sinusoidal form

$$\overline{U}_0^1 \left(0, \widehat{x}\right) = \exp\left(i \widehat{\Upsilon} \widehat{x}\right) \ ,$$

where $\widehat{\Upsilon}$ is the non-dimensional wave number of the initial disturbance. We consider the wave ansatz

$$\overline{U}_A \left(\widehat{x}, \widehat{t}\right) = \exp\left(i \left(\widehat{\digamma} \widehat{x} - \widehat{\Omega} \widehat{t}\right)\right) \ , \tag{3.12}$$

where $\widehat{\digamma}$ is the non-dimensional wave number which relates to the wave number reported in the experiment $\digamma$ by $\widehat{\digamma} = \digamma H$, and $\widehat{\Omega}$ is the non-dimensional frequency of the harmonic wave. Inserting this ansatz in Eq. (3.9) leads to an eigenvalue-eigenvector problem that can be solved as explained in Ref. [61].

For comparison we consider the solution of the same problem using Fourier's law (3.10), which yields the solution

$$\overline{U}_{0,F}^1 \left(\widehat{x}, \widehat{t}\right) = \exp\left(-\kappa_F \widehat{\digamma}^2 \widehat{t}\right) \cos\left(\widehat{\digamma} \widehat{x}\right) \ ,$$

This relation shows that Fourier's law predicts that the energy amplitude decays exponentially with the time constant $\kappa_F \widehat{\digamma}^2$.

For a given point at the peak of initial energy wave, the amplitude of energy moment will decay in time due to transfer of energy in the crystal. Johnson et al. [38] reported that this trend follows an exponential decay for the measured grating periods in the experiment. We also validated this claim in Ref. [61] for those reported grating periods, when the effect of boundaries is not considered. In order to make quantitative comparisons with the experiment, we define the decay parameter

$$\Gamma\left(\digamma^2\right) = \frac{\ln\left(\frac{\overline{U}_0^1(0,t_1)}{\overline{U}_0^1(0,t_2)}\right)}{t_2 - t_1}$$

that measures the decay of energy moment between two given times. Note that as long as we have an exponential decay, the choice of t_1 and t_2 are arbitrary, and will not change the value of the decay parameter.

First, we investigate the convergence of the decay parameter by increasing the number of frequency moments n_F. We consider n_F = 4,5,6,7,8 and compare the variation of Γ by wavenumber in Fig. 3.1. It is seen that the solution converges by considering 6

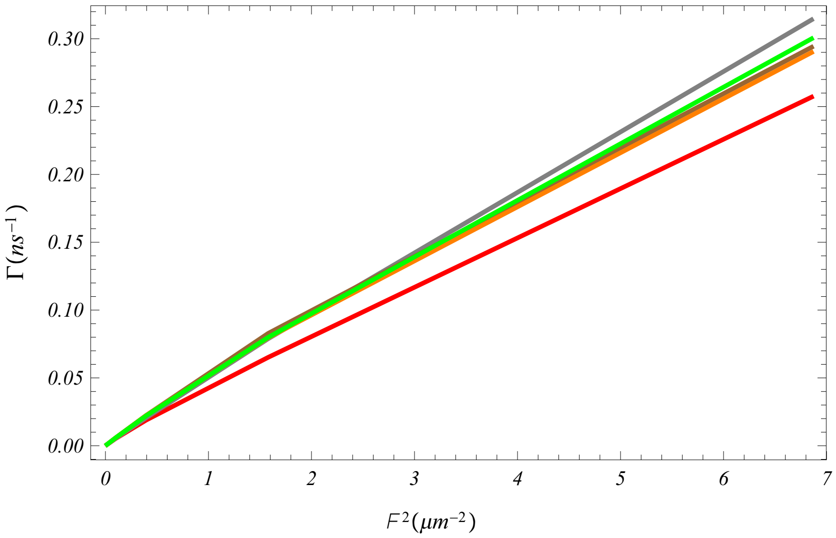

Figure 3.1: Decay parameter as a function of frequency moments, {Red,Gray Green, Orange, Black} correspond to $n_F = \{4,5,6,7,8\}$. Other parameters for this case: $H = 400nm$ and $\chi = \frac{5}{6}$

frequency moments. We observed that the required number of frequency moments to get a converged solution is very dependent on the complexity of the relaxation time model. In case of constant i.e., frequency-independent, relaxation times we get a converged solution by considering only 2 frequency moments.

Following [38], we consider 10 transient grating periods from $3.2\mu m$ to $18\mu m$, and plot the decay of energy in Fig. 3.2. The crystal thickness is set to $H = 400nm$ and the slip coefficient χ in Eqns. (3.9) serves as the free parameter to get a fit to the experimental data.

By considering a frequency dependent relaxation time, the phonon-Boltzmann equation has many characteristic times. Therefore, phonon populations of different frequencies will approach equilibrium at different rates, and the observed energy decay is an average of many different decay curves. From Fig. 3.2 we can see that the thermal decay becomes slower as the grating period increases: it takes longer for heat to move from grating peak to nulls. We used the same color codes as in the experiment to make the comparison simpler. It is worth noting that the moment solution of the phonon-Boltzmann equation shows an initial layer, which is due to the initial ballistic flight of the newly created phonons.

Johnson et al. reported that the thermal decay rate significantly deviates from the quadratic variation with wavenumber (i.e., Fourier solution) when grating period becomes

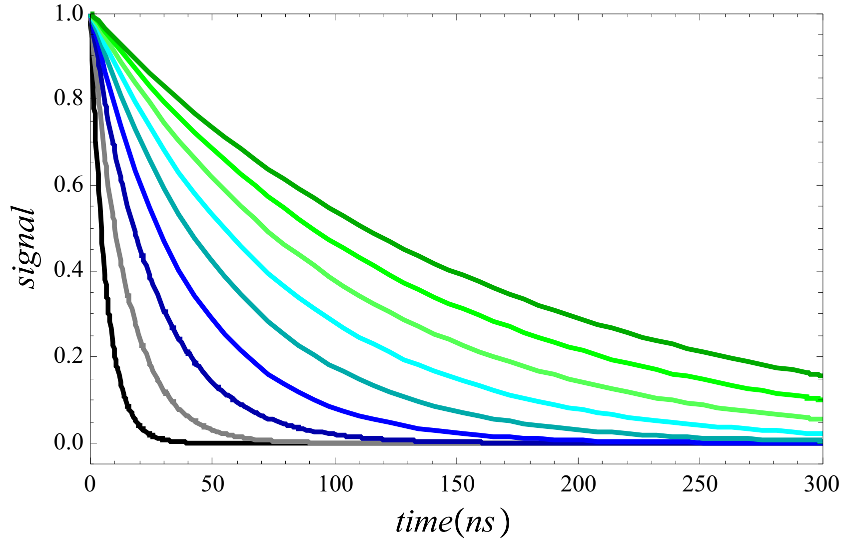

Figure 3.2: Decay of energy amplitude over time for transient grating period from $3.2\mu m$ to $18\mu m$. Shorter waves are damped more strongly. Other parameters are $H = 400nm$, $\chi = \frac{5}{6}$

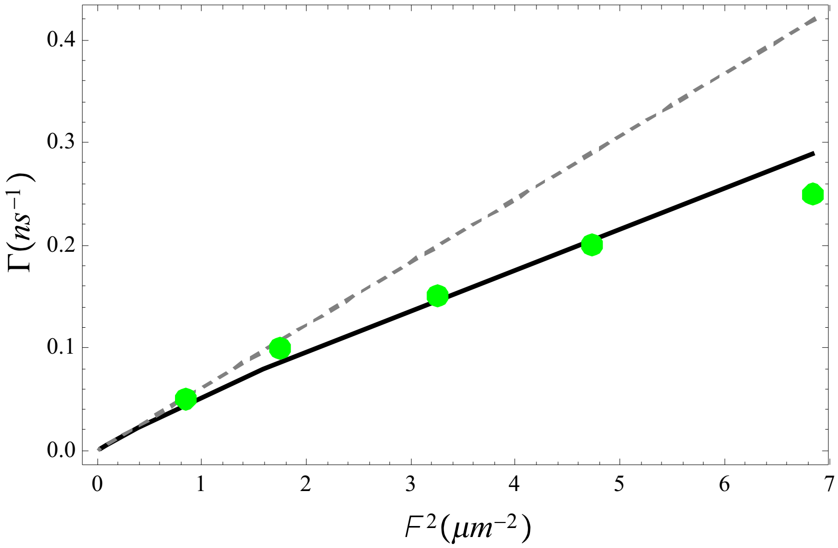

Figure 3.3: Variation of decay parameter with wavenumber in the thermal grating experiment. Green dots: experimental results [38], Dashed line: Fourier's solution, Solid line: Moment equations with the cross-over model, Other parameters are $H = 400nm$, $\chi = \frac{5}{6}$

smaller than $L = 10\mu m$ [38]. Now we aim to compare the decay rate for our model with the decay curve reported in the experiment. In our system of moment equations, the only free parameter at this point is the slip coefficient χ. We set $H = 400nm$ and fix the slip coefficient $\chi = \frac{5}{6}$ to fit to one of the reported experimental thermal grating coefficient, when $L = 3.5\mu m$. Now all parameters are fixed, and the moment equations are supposed to predict the thermal grating coefficient at other grating lengths, as depicted in Fig. 3.3. The behavior of the grating curve at other grating lengths agrees with the reported values in the experiment, and the deviation from the classical solution is well captured by the moment equations.[2]

Note that by using a few different relaxation models (see Ref. [61]), we observed that it is essential to use the appropriate model for low and high frequency phonons to capture the behavior reported in the experiment.

In Fig. 3.4 we look at the ratio of effective thermal diffusivity of wafer to the standard thermal diffusivity of bulk silicon, and compare it with the reported experimental data. Note that due to boundary drag, this ratio is always less than unity. Figure 3.4 demonstrates the variation of effective thermal diffusivity with the thermal grating length. In

---

[2] Although the deviation from the diffusion solution is also observed when the boundary effect is not considered (infinite thickness), we observed that by using the slip coefficient we can fit to the experimental measurements. In fact, increasing the slip coefficient shifts the tail of the decay curve downwards. We used $\chi = \frac{5}{6}$ to get the best fit to the reported values.

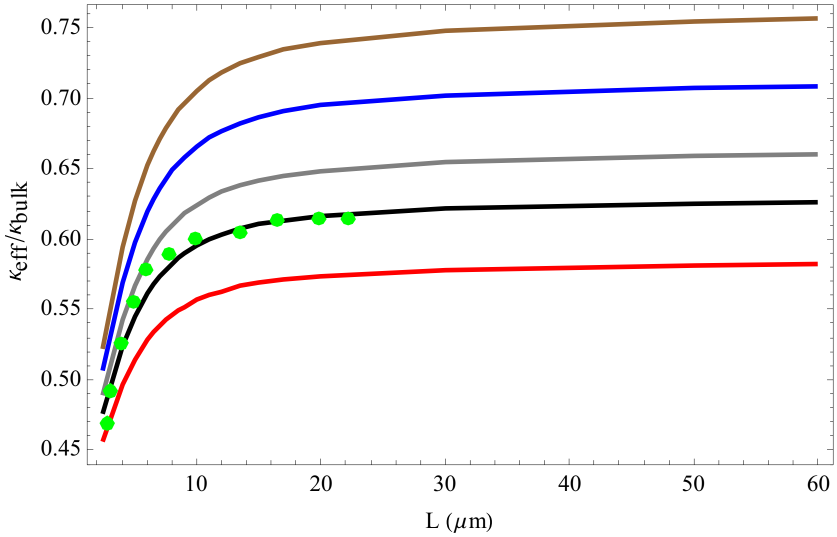

Figure 3.4: The ratio of the effective thermal diffusivity of the silicon wafer to the bulk diffusivity of silicon as a function of grating length. Green dots: Experimental results [38], Membrane thickness: $\{300, 400, 500, 700, 1000\}nm$ corresponds to {red,black,gray,blue,brown}

accordance with our results in Fig. 3.3, we observe a drastic change in the behavior when grating length becomes less than $10\mu m$. Figure 3.4 shows that increasing the thickness of the membrane leads to less influence of boundaries on the phonon transport. Our results when considering $H = 400nm$ are compared with the experimental data reported by Johnson et al. [38].

Originally, phonon hydrodynamics was derived for the description of heat transfer at rather low temperatures, e.g., as they are encountered in heat pulse experiments [19]. At low temperatures, most phonons have low energies, dispersion is weak, and the assumption that all phonons travel at the same (Debye-) speed is acceptable. These assumptions are not valid at higher temperatures.

Our study confirms the importance of choosing appropriate relaxation times in the Callaway model. Considering a constant relaxation time for systems of moments significantly simplifies the equations [23]; however, by performing this simplification some important features of transport equations are neglected. The relaxation time at room-temperature has to be frequency dependent, and proper models have to be considered at low and high frequencies. The textbook (average) value for the mean free path, obtained from the thermal diffusivity, is relevant only for small Knudsen numbers. For processes at not so small Knudsen numbers, variation of mean free path with frequency must be considered in any working model.

Over the past few years we have had good success in using the moment method to extend the validity of macroscopic equations up to early transition regime [84, 88]. This study shows that, similar to gas dynamics, the extension of macroscopic equations beyond the continuum regime for phonon transport using the moment method is promising [61, 23]. While efficient particle methods for simulation of phonon transport are available [65], macroscopic models like moment systems [19, 84, 61], offer an elegant alternative to provide fast and sufficiently accurate simulations when the Knudsen number is not too large.

The presented system of moment equations for phonon transport are valid at room temperature. However, considering their large size, solving this system is rather cumbersome. The next step will be using the order of magnitude method [85] to identify the order of contribution of each individual moment, to condense the current system into a smaller set of equations.

Acknowledgement

This research was supported by the Natural Sciences and Engineering Research Council (NSERC).

Chapter 4

DSMC and R13 Modeling of the Adiabatic Surface

Abstract: *Adiabatic wall boundary conditions for rarefied gas flows are described with the isotropic scattering model. An appropriate sampling technique for the direct simulation Monte Carlo (DSMC) method is presented, and the corresponding macroscopic boundary equations for the regularized 13-moment system (R13) are obtained. DSMC simulation of a lid driven cavity shows slip at the wall, which, as a viscous effect, creates heat that enters the gas while there is no heat flux in the wall. Analysis with the macroscopic equations and their boundary conditions reveals that this heat flux is due to viscous slip heating, and is the product of slip velocity and shear stress at the adiabatic surface. DSMC simulations of the driven cavity with adiabatic walls are compared to R13 simulations, which both show this non-linear effect in good agreement for* $\mathrm{Kn} < 0.3$.

Published in International Journal of Thermal Sciences **101** (2016), 9–23

4.1 Introduction

Significant reduction in size of electro mechanical systems extends the demands for modeling and interpreting the flow behavior of gasses to micro scales. As the mean free path λ, i. e., the average distance that a molecule travels between collisions becomes comparable with the flow length scale, L, the theoretical assumption in the conventional constitutive relations, i.e., the laws of Navier-Stokes and Fourier, lose their validity. The Knudsen number, which is the ratio of the mean free path to the characteristic length of the flow domain, $\mathrm{Kn} = \frac{\lambda}{L}$, is the main indicator of the degree of rarefaction in gases.

The Boltzmann equation describes the behavior of a gas flow at every degree of rarefaction [10]. However, due to the six dimensional phase space and the complexity associated with the molecular collision term, solving the Boltzmann equation is challenging, and numerically expensive. Some researchers propose to solve kinetic model equations using deterministic numerical schemes [74, 95]. These model equations have the same main characteristics as the Boltzmann equation, but avoid some of the complexity arising due to to the collision term.

Another method to approximate solutions of the Boltzmann equation, is to derive a set of macroscopic transport equations which can describe the flow behavior to various degrees of accuracy. The Grad moment method [26] extends the set of conventional hydrodynamic variables, such as, density, temperature, and velocity, by introducing stress, heat flux, and other higher moments. However, due to the hyperbolic nature, the Grad moment equations exhibit un-physical subshocks [101, 92].

The regularized 13 moments (R13) equations are derived by combining elements of the Grad and Chapman-Enskog methods, utilizing the concept of order of magnitude in the Knudsen number [82, 88]. As a result, the R13 equations are stable [85], accurate up to the third order in terms of Knudsen number, and benefit from a complete set of boundary conditions [86, 93].

Alternatively, the Boltzmann equation can be solved by stochastic schemes, commonly known as direct simulation Monte Carlo (DSMC) methods. The DSMC method, first proposed by Bird [5], converges to the Boltzmann equation in the limit of infinite number of simulating particles in each computational cell [97]. It is a statistical method where simulating particles travel and collide with each other and solid surfaces.

According to Maxwell's original paper [51], when the surfaces are microscopically rough *and* the incident molecules are performing multiple scattering, *or* are momentarily trapped *or* absorbed on the surface, we can expect the surface to behave as a diffusive reflector.

However, it is well known from experiments on molecular beams that diffusive reflection typically does *not* occur, beams are reflected in plumes that center on the reflection direction [10, 36]. To at least have some element of the plume, Maxwell amended his model by the possibility for specular reflection.

As listed in [5], the diffusive reflection law should be critically reviewed when one or more of the following factors are present:

> The ratio of the molecular weight of the gas to the surface molecules is small in comparison with unity.
>
> Or the translational energy of the molecules relative to the surface is larger than several electron volts.
>
> A smooth metal surface that has been outgassed through exposure to high vacuum and high temperature.

In the current study, we are modelling a rarefied gas of light atoms enclosed in a cavity with heavy surface molecules. In the collision, the (light) gas particle has little change of absolute kinetic energy, while its collision angle depends on the detailed microscopic geometry of collision with the (heavy) surface atom. The conventional assumptions for the diffuse surface cannot be employed here. At such a surface, particles thermalize with the wall, and leave in a Maxwell distribution– that is accompanied by marked exchanged between gas particle and the wall. The Maxwell model would allow the description of non-diffusive collisions only by accounting for more specular reflections. However, specular reflection are not expected, since the surface is never flat-on the microscopic level. Moreover, specularly reflecting walls exchange neither energy nor momentum, hence there is no shear force on the gas.

Modeling the reflecting particle from walls with defined temperature is straightforward [5]; however, in the case of an adiabatic surface, assigning a velocity to the reflecting particle from a wall with unknown temperature becomes non-trivial. Researchers have proposed methods to implement adiabatic boundary conditions for DSMC. Wang et al. [99, 98] introduced the inverse temperature sampling method to model the heat flux at the wall, and demonstrated that this method can correctly specify the heat flux at the surface. More recently, Akhlaghi et al. [1] proposed an iterative technique to impose the heat flux boundary condition in DSMC. In their method, an estimate to the wall temperature is initially made. Then as the solution evolves in time, the wall temperature is modified according to the predicted heat flux associated with the assumed temperature.

They showed that using the Maxwell model and adjusting the wall temperature iteratively, one can make the energy flux through a surface vanish, i.e., model an adiabatic Maxwell surface. Tzeng et al. [94], proposed a microscopic method to model the adiabatic surface. In this model the magnitude of the velocity vector for particles colliding with the adiabatic surface is kept constant before and after collision, while the normal component of the velocity is reversed. Then, the two other planar components are obtained by using a single random number, such that the magnitude of velocity vector remains unchanged in the collision. Although this microscopic treatment leads to zero energy transfer through the surface, the use of normal velocity reversal in this model seems not necessary true for the particles colliding with a rough wall.

In the current study the isotropic scattering kernel [44] is utilized to model the adiabatic surface in the DSMC and R13 equations. In this method the *no energy transfer* condition is directly imposed on each particle colliding with the adiabatic surface. This method is expected to be fast and more accurate in convergence of the DSMC solution compared to the iterative schemes. The appropriate sampling technique in the DSMC method is presented, and the corresponding boundary equations for the R13 equations are derived. Then we briefly discuss the steps required to model an adiabatic Maxwell surface using the macroscopic approach, and show the agreement between the macroscopic boundary conditions obtained from the adiabatic Maxwell model, and the isotropic scattering model for the R13 equations. Using the obtained boundary conditions, the DSMC and R13 equations are utilized to model a partly adiabatic cavity in the rarefaction regime. The DSMC results show that the heat flux profile has a component normal to the adiabatic surface. This heat generated is well captured by the R13 equations, which allows us to interpret it as the viscous slip heating in the boundary of the adiabatic surface. Indeed, the heat flow into the gas is the product of shear stress and slip velocity.

The remainder of the paper is organized as follows. The solution methods utilized in this study are introduced in Section 4.2. In Section 4.3 the boundary condition to model an adiabatic surface using the isotropic scattering kernel is described, then in Sec. 4.3.3 the microscopic approach for modeling the adiabatic surface in DSMC is introduced. The associated macroscopic boundary conditions for the R13 equations are derived in Section 4.3.4. The adiabatic Maxwell surface is presented in Sec. 4.3.5, and the appropriate wall temperature is introduced. Afterwards, in Section 4.4 the proposed boundary conditions are utilized to perform a microscopic and macroscopic modeling of the partly adiabatic lid driven cavity, and the obtained results are discussed. The paper ends with our conclusions in Section 4.5.

4.2 Governing equation and method of solution

4.2.1 Distribution function and Boltzmann equation

In kinetic theory a gas is described by the density distribution function $f\left(t, x_i, c_i\right)$ such that $fd\mathbf{x}d\mathbf{c}$ denotes the number of particles in the phase space element $d\mathbf{x}d\mathbf{c}$ at time t. The Boltzmann equation describes the evolution of the density distribution function in phase space $(\mathbf{x}, \mathbf{c})$ by accounting for the translational motion and collisions of the particles in the gas, as

$$\frac{\partial f}{\partial t} + c_k \frac{\partial f}{\partial x_k} + G_k \frac{\partial f}{\partial c_k} = \mathcal{S}\left(f, f\right), \tag{4.1}$$

where G_k is the external force acting on the gas. The term $\mathcal{S}\left(f, f\right)$ is the collision operator that describes the change of the distribution function due to interaction between particles.

Macroscopic quantities such as mass density ρ, velocity v_i, temperature T, shear stress σ_{ij} and heat flux q_i are moments of the distribution function, obtained by integration over velocity space $\mathbf{c}$,

$$\begin{aligned} \rho &= m\int f d\mathbf{c}\ , \quad v_i = \frac{m}{\rho}\int c_i f d\mathbf{c}\ , \quad 3\mathrm{R}T = \frac{m}{\rho}\int C^2 f d\mathbf{c}\ , \\ \sigma_{ij} &= m\int C_{<i}C_{j>} f d\mathbf{c}\ , \quad 2q_i = m\int C_i C^2 f d\mathbf{c}\ . \end{aligned} \tag{4.2}$$

Here, m is the mass of particle, R is the specific gas constant and $C_i = c_i - v_i$ is the peculiar velocity of the gas particles.

A rarefied gas is well described by the Boltzmann equation for all Knudsen numbers. However, the Boltzmann equation is difficult to solve deterministically due to six dimensional phase space description, as well as the non-linearity in the collision term.

4.2.2 DSMC method (Microscopic method)

The DSMC method is a statistical method, based on the kinetic theory of dilute gases, to model rarefied gas flows [5]. In this method, many independent simulating particles are used to model gaseous flows, where each particle represents a large number of real gas molecules. In the DSMC method the simulating particles are allowed to move and collide; however, the motion and collision of the particles are assumed to be decoupled. The time step is chosen as a fraction of the mean collision time to ensure pure motion in the elapsed movement time. In order to implement DSMC, the flow domain must be divided into computational cells. The cell size is chosen small enough to ensure small changes in the thermodynamic properties of the flow across each cell. To satisfy the cell size limitation in the current study, the mesh size in both directions of the square domain is chosen as 0.1λ. Within each cell, the macroscopic thermodynamic properties are sampled from molecular properties. Moreover, in each time step, only the particles within a computational cell are allowed to perform collisions. For the sake of accuracy, the cells are divided into sub-cells to facilitate the selection of collision pairs. The no-time-counter (NTC) method is used to chose the collision pairs in each computational cell, therefore the computational time is proportional to the number of the simulating particles [5]. Later on, in this paper, we will compare DSMC results with extended macroscopic R13 equations, which are more conventional for Maxwell molecules. Therefore, in the current study, the code of Roohi and co-workers [71, 16, 59, 58, 62] is modified to model Maxwell molecules in a cavity with adiabatic and diabatic walls. The fluid is argon as a Maxwell gas, with $m = 6.63 \times 10^{-26}$kg and a reference viscosity of $\mu_0 = 1.9549 \times 10^{-5}\mathrm{Pa} \cdot \mathrm{s}$. In order to relate the particle diameter, d, to the reference viscosity we used the relation [5]

$$d^2 = \frac{5\left(\alpha+1\right)\left(\alpha+2\right)\sqrt{mkT_0/\pi}}{4\alpha\left(5-2\omega\right)\left(7-2\omega\right)\mu_0} \ .$$

Here, k and m are, respectively, the Boltzmann constant and the molecular mass for the gas, and T_0 is the reference temperature. In order to model Maxwell molecules we set $\alpha = 2.13986$ and $\omega = 1$ [5]. Following [5], the Knudsen number is obtained as

$$\mathrm{Kn}_b = \frac{1}{L}\frac{1}{\sqrt{2}\pi d^2 n_0} \ ,$$

where n_0 is the reference number density. Another definition of the Knudsen number is based on the viscosity [81]

$$\mathrm{Kn} = \frac{\mu_0}{\rho_0\sqrt{\mathrm{R}T_0}L} \cong 1.27\mathrm{Kn}_\mathrm{b} \ . \tag{4.3}$$

Here, ρ_0 is the reference density. This definition of the Knudsen number, Kn, is related to Bird's definition of Knudsen number, Kn_b, for the Maxwell molecules as above. To avoid confusion, all results presented in this article are given in terms of the Knudsen number Kn in Eq. (4.3). The DSMC simulation starts with 32 particles located in each cell. As the flow reaches the steady state, the molecular properties are sampled over a large period of time to reduce the statistical scattering. In addition, a filtering post processor is used to minimize the scattering in the predicted results of thermodynamic properties. In this filtering, the sampled macroscopic properties, F, in cell N are averaged over a pattern of its neighboring cells, see [59],

$$\widetilde{F}_{(N)} = \frac{F_N + \sum_{I=1}^{I=N_n} F_I}{N_n + 1} \ .$$

4.2.3 R13/NSF equations (Macroscopic models)

The detailed derivation of the R13 equations from the Boltzmann equation can be found in [85, 69]; here we only present the final equations. Both macroscopic models consist of the conservation laws for mass, momentum, and energy,

$$\frac{D\rho}{Dt} + \rho\frac{\partial v_k}{\partial x_k} = 0 \ , \tag{4.4a}$$

$$\rho\frac{Dv_i}{Dt} + \frac{\partial p}{\partial x_i} + \frac{\partial \sigma_{ik}}{\partial x_k} = \rho G_i \ , \tag{4.4b}$$

$$\frac{3}{2}\rho\frac{D\theta}{Dt} + \left(p\,\delta_{ij} + \sigma_{ij}\right)\frac{\partial v_i}{\partial x_j} + \frac{\partial q_k}{\partial x_k} = 0 \ . \tag{4.4c}$$

Here, the pressure p obeys the ideal gases law, $p = \rho RT = \rho\theta$. Closure of the conservation laws (4.4a–4.4c) requires specification of the stress tensor, σ_{ik}, and the heat flux vector, q_k, as constitutive equations. In classical hydrodynamics, the NSF equations provide these constitutive relations from the laws of Fourier heat transfer and the Navier-Stokes relation for the stress, as

$$q_i = -\frac{15}{4}\mu\frac{\partial\theta}{\partial x_i}, \quad \sigma_{ij} = -2\mu\frac{\partial v_{\langle i}}{\partial x_{j\rangle}} \ . \tag{4.5}$$

The indices inside angular brackets denote the symmetric trace-free part of tensors [81].

In extended hydrodynamics theory, however, stress and heat–flux follow full balance equations as [27, 47, 81]

$$\frac{D\sigma_{ij}}{Dt} + \frac{4}{5}\frac{\partial q_{\langle i}}{\partial x_{j\rangle}} + \sigma_{ij}\frac{\partial v_k}{\partial x_k} + 2\sigma_{k\langle i}\frac{\partial v_{j\rangle}}{\partial x_k} + \frac{\partial m_{ijk}}{\partial x_k} = -2\rho\theta\frac{\partial v_{\langle i}}{\partial x_{j\rangle}} - \frac{\rho\theta}{\mu}\sigma_{ij} \ , \tag{4.6}$$

$$\begin{aligned}\frac{Dq_i}{Dt} + \frac{5}{2}\sigma_{ik}\frac{\partial\theta}{\partial x_k} - \frac{\theta\sigma_{ik}}{\rho}\frac{\partial\rho}{\partial x_k} - \frac{\sigma_{ik}}{\rho}\frac{\partial\sigma_{kl}}{\partial x_l} + \theta\frac{\partial\sigma_{ik}}{\partial x_k} + \frac{7}{5}\left(q_k\frac{\partial v_i}{\partial x_k} + q_i\frac{\partial v_k}{\partial x_k}\right) \\ + \frac{2}{5}q_k\frac{\partial v_k}{\partial x_i} + \frac{1}{6}\frac{\partial\mathit{\Delta}}{\partial x_i} + \frac{1}{2}\frac{\partial R_{ik}}{\partial x_k} + m_{ijk}\frac{\partial v_j}{\partial x_k} = -\frac{5}{2}\rho\theta\frac{\partial\theta}{\partial x_i} - \mathrm{Pr}\frac{\rho\theta}{\mu}q_i\ , \quad (4.7)\end{aligned}$$

where Pr is the Prandtl number, which is $\frac{2}{3}$ for Maxwell molecules, and close to $\frac{2}{3}$ for other molecule types. The coefficients ($\frac{4}{5}$, 1, 2, ...,Pr) are valid for Maxwell molecules. Some of the coefficients change with the molecule types more significantly (up to 20%). The R13 equations for other molecule types were derived in [88], where the method is outlined and coefficients are given for hard sphere molecules. Also for other molecule types, the R13 equations are of third order of accuracy in terms of Knudsen number. Here we are more interested in the modelling of the adiabatic surface, and used the R13 equations in their most convenient form, which is for Maxwell molecules. The modelling of the adiabatic surface can be extended to all molecule types. In Eqs. (4.6,4.7) the higher moments m_{ijk}, $\mathit{\Delta}, R_{ij}$, appear as unknown fluxes. Grad's original closure in [26] gives $\mathit{\Delta} = R_{ij} = m_{ijk} = 0$, while in the R13 equations these quantities are obtained as [69, 93]

$$\begin{aligned}\mathit{\Delta} &= 5\frac{\sigma_{kl}\sigma_{kl}}{\rho} + \frac{56}{5}\frac{q_k q_k}{p} - 12\mu\left(\theta\frac{\partial\left(q_k/p\right)}{\partial x_k}\right)\ , \\ R_{ij} &= \frac{20}{7}\frac{\sigma_{k\langle i}\sigma_{j\rangle k}}{\rho} + \frac{192}{75}\frac{q_{\langle i}q_{j\rangle}}{p} - \frac{24}{5}\mu\left(\theta\frac{\partial\left(q_{\langle i}/p\right)}{\partial x_{j\rangle}}\right)\ , \qquad (4.8) \\ m_{ijk} &= \frac{20}{15}\frac{q_{\langle i}\sigma_{jk\rangle}}{p} - 2\mu\left(\theta\frac{\partial\left(\sigma_{\langle ij}/p\right)}{\partial x_{k\rangle}}\right)\ .\end{aligned}$$

A Chapman-Enskog expansion of equations (4.6) and (4.7) shows that the R13 equations are of third order accuracy in the Knudsen number [85, 81].

4.3 Boundary conditions

The boundary conditions describe the interaction between the gas molecules and the surface. In kinetic theory this is done by prescribing the velocity probability density of the molecules after hitting the wall. Since the actual microscopic interaction between gas particles and a solid boundary is quite complicated, it is common to use simplified models. Many gas-surface interaction models have been proposed [10]. The Maxwell accommodation model is the one most widely used as the boundary condition for the Boltzmann equation [77, 10, 81] and in DSMC simulations [5], which assumes particles

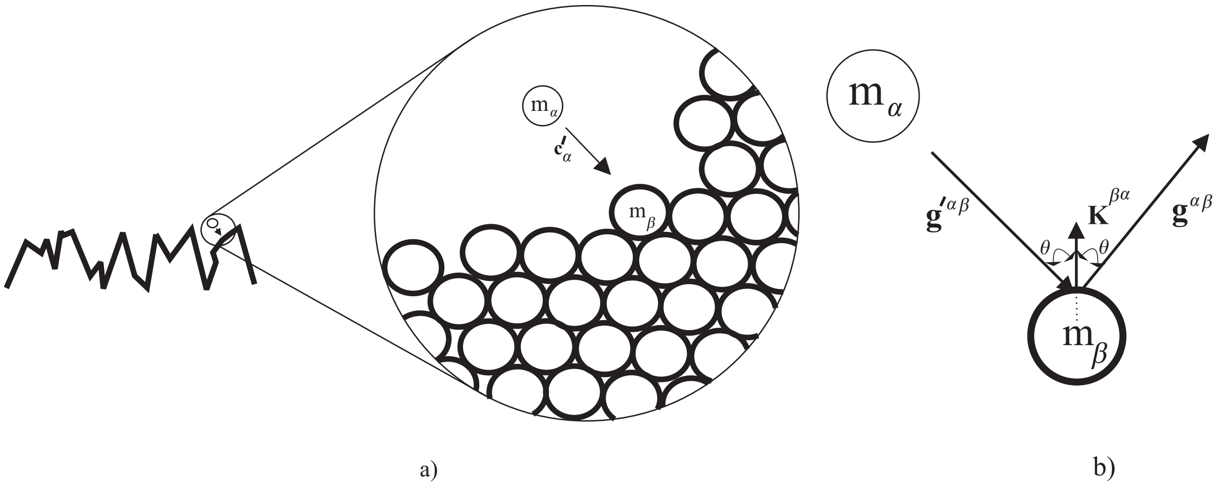

Figure 4.1: Gas and rough surface interaction at the molecular level, a) Collision of a light gas particle with a heavy surface particle, b) Dynamics of collision on the relative velocities plane when $\frac{m_\alpha}{m_\beta} \ll 1$.

are either thermalized with the surface or specularly reflected.

4.3.1 Dynamics of gas-surface interaction

When the surface is microscopically rough and the mass ratio of gas particle and surface particle is close to unity, the gas particles might be trapped and perform multiple collisions with the surface to thermalize with the wall [5]. In this case the surface is behaving as a diffusive reflector. However, when the mass ratio of gas and surface particle is not close to unity, the assumption of the diffusive reflection must be critically reviewed [5].

Figure 4.1-a shows a light gas particle of mass m_α and velocity $\mathbf{c}'_\alpha$ colliding with a heavy surface particle of mass m_β and velocity $\mathbf{c}'_\beta$. Using the dynamics of collision [47] to obtain the post collision velocities, $\mathbf{c}_\alpha$ and $\mathbf{c}_\beta$, we have

$$\begin{aligned}
\mathbf{c}_\alpha &= \mathbf{c}'_\alpha + 2\frac{m_\beta}{m_\alpha + m_\beta}\mathbf{K}^{\beta\alpha}\left(\mathbf{K}^{\beta\alpha}.\mathbf{g}'^{\beta\alpha}\right) , \\
\mathbf{c}_\beta &= \mathbf{c}'_\beta - 2\frac{m_\alpha}{m_\alpha + m_\beta}\mathbf{K}^{\beta\alpha}\left(\mathbf{K}^{\beta\alpha}.\mathbf{g}'^{\beta\alpha}\right) .
\end{aligned}$$

Here, $\mathbf{K}^{\beta a}$ is the apsidal vector, defined as [47]

$$\mathbf{K}^{\beta\alpha} = \frac{\mathbf{g}'^{\beta\alpha} - \mathbf{g}^{\beta\alpha}}{\left|\mathbf{g}'^{\beta\alpha} - \mathbf{g}^{\beta\alpha}\right|} .$$

The relative velocities before and after collision are

$$\mathbf{g}'^{\beta\alpha} = \mathbf{c}'_\beta - \mathbf{c}'_\alpha \text{ and } \mathbf{g}^{\beta\alpha} = \mathbf{c}_\beta - \mathbf{c}_\alpha \ .$$

Since there is a large difference between the masses, $m_\alpha \ll m_\beta$, we have

$$\frac{m_\alpha}{m_\alpha + m_\beta} = \varepsilon \quad , \quad \frac{m_\beta}{m_\alpha + m_\beta} = 1 - \varepsilon \ ,$$

where $\varepsilon \ll 1$. Assuming that the surface is stationary, the average velocity of the surface particle is zero $\overline{\mathbf{c}'_\beta} = 0$. Therefore, in average, the relative velocity before collision is $\mathbf{g}'^{\beta\alpha} = -\mathbf{c}'_\alpha$. The post collision velocity of the light particle simplifies to

$$\mathbf{c}_\alpha = \left(\mathbf{I} - 2\left(1 - \varepsilon\right)\mathbf{K}^{\beta\alpha}\mathbf{K}^{\beta\alpha}\right) \cdot \mathbf{c}'_\alpha \ , \tag{4.9}$$

where $\mathbf{I}$ is the unit tensor. In order to obtain the magnitude of post collision velocity of the light particle, we multiply both sides of Eq. (4.9) with $\mathbf{c}_\alpha$ to get

$$|\mathbf{c}_\alpha|^2 = \left[\delta_{jk} + 4\left(\varepsilon^2 - \varepsilon\right) K_j^{\beta\alpha} K_k^{\beta\alpha}\right] c'_{j\,\alpha} c'_{k\,\alpha} \ . \tag{4.10}$$

Note that in Eq. (4.10), we used $K_i^{\beta\alpha} K_i^{\beta\alpha} = 1$. By assuming a very small value for ε we have

$$|\mathbf{c}_\alpha| \simeq \left|\mathbf{c}'_\alpha\right| .$$

Therefore, as a result of the collision between a very light gas particle and a heavy wall particle, the light gas particle will be reflected with almost the same kinetic energy, which subsequently leads to very small thermal accommodation. Thomas [91] reported that the thermal accommodation coefficient becomes significantly less than unity, when the mass ratio of gas particle and surface particle in the experiment is small. The momentum exchange between the gas and surface leads to a different reflection direction for the gas particle, which is dependent on the detailed microscopic geometry of collision with the surface. Figure 4.1-b demonstrates the collision between two particles in the plane of the relative velocities with the apsidal vector $\mathbf{K}$. For a rough surface as in Fig. 4.1-a, it is expected that the reflected particle has no preferred direction. All possible reflection directions will have the same likelihood, that is the direction will be isotropically distributed.

4.3.2 Adiabatic surface model (isotropic scattering)

The adiabatic boundary condition implies no-energy-transfer through the surface, where energy is conserved for each individual particle. The total transport of energy through a wall with the normal in n-direction, as seen in the rest frame of the wall, can be written as

$$U_n = m \int c_n^W \frac{\left(c^W\right)^2}{2} f d\mathbf{c} = q_n + \sigma_{tn}\mathcal{V}_t + \mathcal{V}_n \left(\frac{1}{2}\rho\mathcal{V}^2 + \frac{5}{2}\rho RT\right) ,$$

where $c_i^W = c_i - v_i^W$ is the particle velocity in the rest frame of the wall, and $\mathcal{V}_t = v_t - v_t^W$ is the tangential slip velocity. At a non-accumulating, adiabatic surface at rest we have $v_i^W = v_n = e_n = 0$, therefore,

$$q_n = -\mathcal{V}_t\sigma_{tn} \; . \tag{4.11}$$

From Eq. (4.11) we can see that, while the overall energy flux vanishes, there is a non-convective heat flux q_n, which transfers the heat of slip friction, $-\mathcal{V}_t\sigma_{tn}$, into the gas. We denote this effect as *viscous slip heating*; A detailed discussion will follow in the sequel.

We are interested in adiabatic surfaces with friction. These cannot be described by the pure specular Maxwell model, where an adiabatic wall is necessarily frictionless. An adiabatic surface can be modeled utilizing the fully diffusive Maxwell surface, if the wall temperature is adjusted in each surface element so that the macroscopic heat flux follows from Eq. (4.11). This model, however, requires an iterative scheme to modify the microscopic boundary conditions in the DSMC method. In the macroscopic method, on the other hand, this process is rather straightforward and we will be further discussed in Sec. 4.3.5.

We now turn our attention to processes where the particles leaving the surface are isotropically reflected while the magnitude of their velocities is that of the incoming particle. Thus, the collision with the surface does not change the kinetic energy of the individual particle, so that the surface is adiabatic in the rest frame of the wall. Some particles exchange momentum with the wall so that there is friction on the surface [44, 83].

Accordingly, the phase density of the particles in an infinitesimal neighborhood of the wall is

$$\bar{f} = \begin{cases} f^*(c_i^W, x_i, t), & c_k^W n_k \geq 0 \\ f(c_i^W, x_i, t) & c_k^W n_k \leq 0. \end{cases} \tag{4.12}$$

Here, f^* in (4.12) denotes the phase density of particles leaving the wall ($c_k^W n_k \geq 0$). The function f^* must be chosen such that the wall does not accumulate particles, it must be isotropic in velocity, i.e.,

$$f^*(c_i^W, x_i, t) = f^*(|c^W|, x_i, t). \tag{4.13}$$

It is convenient to introduce spherical coordinates $\left\{|c^W|,\ \vartheta,\ \phi\right\}$ for the velocity space, i.e., with the direction vector ξ_i,

$$c_i^W = |c^W|\xi_i = |c^W|\left\{\sin\vartheta\cos\phi,\quad \sin\vartheta\sin\phi,\quad \cos\vartheta\right\}_i ,$$

where $|c^W| \in [0,\ \infty]$, $\vartheta \in [0,\ \pi]$, $\phi \in [0,\ 2\pi]$, and $d\Omega = \sin\vartheta d\vartheta d\phi$. Writing the conservation of the normal number flux of the gas to the wall with the assumption of isotropic distribution function, Eq.(4.13), gives

$$f^*(|c^W|) = \frac{\int_{\pi/2}^{\pi}\int_0^{2\pi} c_k n_k f \sin\vartheta d\phi d\vartheta}{\int_{\pi/2}^{\pi}\int_0^{2\pi} c_k n_k \sin\vartheta d\phi d\vartheta}. \tag{4.14}$$

4.3.3 Microscopic boundary conditions for adiabatic surface in DSMC

In order to implement a boundary condition in the DSMC method, the velocity vector for a reflected particle is obtained by sampling from a specific distribution function. In other words, at first the distribution function for the reflecting particle is specified, and then the velocity vector is obtained by sampling from the corresponding distribution function

In the DSMC method changes in the total energy of a particle due to the collision with a solid surface determines the amount of energy that flows through the wall. Monatomic particles only have translational energy. Therefore, implementing the adiabatic boundary condition on a surface is equivalent to requiring an equal amount of translational energy before and after collision with a solid surface. For a particle colliding with a surface, the translational energy before collision is

$$U' = \frac{1}{2}m(c_x'^2 + c_y'^2 + c_z'^2) = \frac{1}{2}mc'^2 ,$$

where m is the particle mass, and the apostrophe denotes the molecular state before the collision. As a particle reflects from the adiabatic surface, the velocity vector must have the same magnitude, but different direction. Assuming that the particles have the isotropic probability for scattering in all directions, the scattering kernel $P\left(\mathbf{c}' \to \mathbf{c}\right)$ for a particle reflecting from a surface with the normal in the $y-$direction is [44]

$$P\left(\mathbf{c}^{'} \rightarrow \mathbf{c}\right) = \frac{1}{\pi c^3} c_y \delta\left(c^{'} - c\right).$$

Here, $\mathbf{c}$ is the particle velocity vector after collision with the surface. Sampling requires the cumulative probabilities, which are best defined based on spherical coordinates $\{c, \theta, \phi\}$ so that

$$P\left(\mathbf{c}^{'} \rightarrow \mathbf{c}\right) d\mathbf{c} = \frac{1}{\pi c^3} c \cos\phi \delta\left(c^{'} - c\right) c^2 dc \sin\phi d\phi d\theta = \left[\delta\left(c^{'} - c\right) dc\right]\left[\frac{1}{2\pi} d\theta\right]\left[2\cos\phi \sin\phi d\phi\right]. \tag{4.15}$$

The delta function indicates that the absolute velocity of the leaving particle is deterministic, $c = c'$. However, the direction of the leaving particle is subject to the process of random isotropic scattering. By considering the the cumulative probabilities

$$F_\theta = \int_0^\Theta \frac{1}{2\pi} d\theta \quad , \quad F_\phi = \int_0^\Phi 2\cos\phi \sin\phi d\phi \ .$$

Here, Θ, Φ are the angles for the particles leaving. The integrals for the cumulative probabilities F_θ, F_ϕ can be solved analytically to give

$$\Theta = 2\pi F_\theta \ , \tag{4.16}$$

$$\Phi = \arcsin(\sqrt{F_\phi}) \tag{4.17}$$

By converting back to Cartesian coordinates, and noting that $\cos(\arcsin(x)) = \sqrt{1 - x^2}$, the velocity of the randomly scattered particle is

$$\begin{aligned} c_x &= c^{'} \sqrt{F_\phi} \cos(2\pi F_\theta) \ , \\ c_y &= c^{'} \sqrt{1 - F_\phi} \ , \\ c_z &= c^{'} \sqrt{F_\phi} \sin(2\pi F_\theta) \ . \end{aligned} \tag{4.18}$$

Using this method, particles hitting the surface are reflected into arbitrary directions while carrying the same translational energy as before the collision.

It is also worth noting that by following the same methodology we can model an adiabatic moving surface in DSMC. The observer on the wall frame, which moves with the velocity of $\mathbf{V}_W$, measures the incoming particle's velocity as

$$\mathbf{c}'^W = \mathbf{c}' - \mathbf{V}_W \ .$$

The components of the reflecting velocity vector, still in the rest frame of the wall, are obtained as

$$\begin{aligned} c_x^W &= c'^W \sqrt{F_\phi} \cos(2\pi F_\theta) \ , \\ c_y^W &= c'^W \sqrt{1 - F_\phi} \ , \\ c_z^W &= c'^W \sqrt{F_\phi} \sin(2\pi F_\theta) \ . \end{aligned}$$

Finally, the velocity of the reflecting particle in the rest frame is $\mathbf{c} = \mathbf{c}^W + \mathbf{V}_W$.

4.3.4 Macroscopic boundary conditions for adiabatic surface in R13/NSF equations

To find the macroscopic boundary conditions, we follow the method outlined in [26, 93]. We consider the continuity of normal fluxes over an infinitesimal surface area element which gives

$$m \int \Psi_A c_k^W n_k \, f \, d\mathbf{c}^W = m \int \Psi_A c_k^W n_k \, \bar{f} \, d\mathbf{c}^W \ , \tag{4.19}$$

where Ψ_A are polynomials of the particle velocity, c_i^W. Integrating (4.19) yields relations between the moments in the gas and the wall properties (θ_W, v_i^W) that serve as boundary conditions for the moments.

To perform the integrations in Eq. (4.19), the velocity distribution function f and the appropriate velocity functions Ψ_A are required. For the R13 system, the phase density in the gas is approximated by a Grad-type distribution that reads [81]

$$f_{R13} = f_M(1 + \Phi) \ , \tag{4.20}$$

where f_M denotes the local Maxwellian and

$$\Phi = \left(\frac{1}{8} - \frac{C^2}{12\theta} + \frac{C^4}{120\theta^2}\right)\frac{\Delta}{\rho\theta^2} + \frac{C_i C_j}{2\rho\theta^2}\sigma_{ij} - \frac{1}{\rho\theta^2}\left(1 - \frac{C^2}{5\theta}\right)C_j q_j + \frac{C_i C_j C_k}{6\rho\theta^3}m_{ijk} - \frac{1}{4\rho\theta^3}\left(1 - \frac{C^2}{7\theta}\right)C_i C_j R_{ij}.$$

Here, $C_k = c_k^W - \left(v_k - v_k^W\right)$ is the peculiar velocity (i.e., the velocity in the rest frame of the gas), with $C_k n_k = c_k^W n_k$.

Grad observed that, in order to get meaningful boundary conditions, the velocity functions $\mathit{\Psi}_A$ must be even in the normal component of the particle velocity $c_k^W n_k$ [26]. For example, if we consider a surface with the normal in $y-$direction ($y = x_2$), we take

$$\mathit{\Psi}_A = \left\{1, C_x, C^2, C_y C_y, C_x C_x, C^2 C_x\right\} \ , \tag{4.21}$$

which correspond to the fluxes

$$m \int \mathit{\Psi}_A c_k^W n_k \, f d\mathbf{c} = \left\{\rho v_y, \sigma_{xy}, q_y, m_{yyy}, m_{xxy}, R_{xy}\right\} \ . \tag{4.22}$$

Using the isotropic distribution function for the reflecting particles, Eq. (4.12), and performing the integrations for Eq. (4.19), we obtain the boundary conditions

$$\begin{aligned}
v_y &= 0 \ , \\
\sigma_{xy} &= \sqrt{\frac{2}{\pi\theta}}\left(-\frac{1}{2}m_{xyy} - \frac{1}{5}q_x - P\mathcal{V}_x\right)n_y \ , \\
q_y &= -\sigma_{xy}\mathcal{V}_x \ , \\
R_{xy} &= 11\theta\sigma_{xy} + \sqrt{\frac{2}{\pi\theta}}\left(36\theta\mathcal{V}_x\left(P - \frac{2}{3}\rho\theta - \frac{3}{8}\sigma_{yy} + \frac{1}{112}\frac{R_{yy}}{\theta}\right) + 5\theta m_{xyy}\right)n_y \ , \\
m_{xxy} &= -\frac{1}{10}\sigma_{xy}\mathcal{V}_x + \sqrt{\frac{2}{\pi\theta}}\left(\frac{3}{2}\mathcal{V}_x^2\left(P - \frac{1}{2}\ \rho\theta\right) - \theta\left(\sigma_{xx} - \frac{1}{4}\sigma_{yy}\right) - \frac{1}{14}R_{xx} + \frac{1}{56}R_{yy}\right)n_y \ , \\
m_{yyy} &= \frac{1}{5}\sigma_{xy}\mathcal{V}_x + \sqrt{\frac{2}{\pi\theta}}\left(-\mathcal{V}_x^2\left(P - \frac{1}{2}\rho\theta\right) - \frac{3}{28}R_{yy} - \frac{3}{2}\theta\sigma_{yy}\right)n_y \ .
\end{aligned} \tag{4.23}$$

Here, $\mathcal{V}_x = v_x - v_x^W$ is the slip velocity and $P = \rho\theta + \frac{1}{2}\sigma_{yy} - \frac{1}{120}\frac{\Delta}{\theta} - \frac{1}{28}\frac{R_{yy}}{\theta}$. The integrals of f_{R13} over the solid angle, as required in Eq. (4.14), cannot be solved algebraically, hence we expanded f_{R13} in the non-equilibrium quantities $\left\{\mathcal{V}_i, \sigma_{ij}, q_i, \ldots\right\}$ to second order. Note that this is *not* a linearization in the orders of Knudsen number, but in the deviation from equilibrium state. For small lid velocity, as considered here, this deviation is small, hence, it should be sufficient to only consider up to the second order.

From the boundary conditions we can see that, while the isotropically scattering wall is adiabatic, the normal heat flux q_y does not vanish. Indeed, as we expected from Eq. (4.11), slip friction creates heat that must go into the gas.

The corresponding slip boundary conditions for the NSF equations can be obtained from the boundary conditions for the R13 equations (4.23) by considering the first order terms in Knudsen number, as [87]

$$\begin{aligned} v_y &= 0 \,, \\ \sigma_{xy}^{NSF} &= -\sqrt{\frac{2}{\pi\theta}}\left(\rho\theta\mathcal{V}_x + \frac{1}{5}q_x^{NSF}\right)n_y \,, \\ q_y^{NSF} &= 0 \,. \end{aligned} \tag{4.24}$$

Note that, since the viscous slip heating is of second order in terms of the Knudsen number, it does not show in the NSF limit, hence $q_y = 0$ at the wall.[2]

4.3.5 Adiabatic Maxwell surface

Another method for modeling the adiabatic surface is based on the Maxwell boundary conditions. Adiabatic boundaries are achieved by *adjusting* the local wall temperature such that the energy flux vanishes. The particles reflecting from the wall follow the Maxwell distribution,

$$f_W = \frac{\rho^W}{m\sqrt{2\pi\theta^W}^3}\exp\left(-\frac{|c_k - v_k^W|^2}{2\theta^W}\right) \,, \tag{4.25}$$

where θ^W and v_k^W being the known temperature and velocity of the surface [10]. Moreover, ρ^W must be obtained such that particles do not accumulate at the wall.

Considering the frame of reference in which the wall is at rest, the microscopic velocity of the gas particle is $c_k^W = c_k - v_k^W$ and the velocity distribution function $\bar{f}$ of the gas in an infinitesimal neighborhood of the wall is given by

$$\bar{f} = \begin{cases} f_W, & c_k^W n_k \geq 0 \\ f(c_i^W, x_i, t), & c_k^W n_k \leq 0, \end{cases} \tag{4.26}$$

where $f(c_k^W, x_k, t)$ is the velocity distribution function in the gas.

Inserting the distribution function (4.20) and performing the integration in equation

---

[2] The viscous slip heating effect, as predicted by the energy balance and reported by other researchers [32], will also appear in the boundary equations for the NSF if we include terms up to the second order of accuracy in Knudsen number. Since the bulk equations in the NSF are first order accurate in Knudsen number, for consistency, we only considered terms up to the first order at the boundary, which does not include viscous slip heating.

(4.19) for the Maxwell model Eq. (4.26) leads to the wall-boundary conditions [93]

$$\begin{aligned}
v_y &= 0 \;, \\
\sigma_{xy} &= \sqrt{\frac{2}{\pi\theta}}\left(-P\mathcal{V}_x - \frac{1}{5}q_x - \frac{1}{2}m_{xyy}\right)n_y \;, \\
q_y &= \sqrt{\frac{2}{\pi\theta}}\left(-2P\mathcal{T} + \frac{1}{2}P\mathcal{V}_x^2 - \frac{1}{2}\theta\sigma_{yy} - \frac{1}{15}\Delta - \frac{5}{28}R_{yy}\right)n_y \;, \\
R_{xy} &= \sqrt{\frac{2}{\pi\theta}}\left(P\theta\mathcal{V}_x - \frac{11}{5}\theta q_x - \frac{1}{2}\theta m_{xyy} - P\mathcal{V}_x^3 + 6P\mathcal{V}_x\mathcal{T}\right)n_y \;, \\
m_{xxy} &= \sqrt{\frac{2}{\pi\theta}}\left(-\frac{1}{14}R_{xx} - \theta\sigma_{xx} + \frac{1}{5}\theta\sigma_{yy} - \frac{1}{5}P\mathcal{T} + \frac{4}{5}P\mathcal{V}_x^2 - \frac{1}{150}\Delta\right)n_y \;, \\
m_{yyy} &= \sqrt{\frac{2}{\pi\theta}}\left(\frac{2}{5}P\mathcal{T} - \frac{3}{5}P\mathcal{V}_x^2 - \frac{7}{5}\theta\sigma_{yy} + \frac{1}{75}\Delta - \frac{1}{14}R_{yy}\right)n_y \;.
\end{aligned} \tag{4.27}$$

Here, $\mathcal{T} = T - T_W$ denotes the temperature jump. In order to obtain the adiabatic boundary condition from the Maxwell boundary equations, we have to adjust the heat flux to mimic the no energy transfer condition, Eq.(4.11), and set $q_y = -\mathcal{V}_x\sigma_{xy}$, to account for the viscous slip heating. The temperature jump corresponding to the adiabatic fully diffusive Maxwell surface is obtained from $(4.27)_3$ as

$$\mathcal{T} = T - T_W = -\frac{1}{4}\frac{\theta\sigma_{yy}}{P} - \frac{1}{30}\frac{\Delta}{P} - \frac{5}{56}\frac{R_{yy}}{P} + \frac{1}{4}\mathcal{V}_x^2 - \frac{1}{4}\frac{m_{xyy}V_x}{P} - \frac{1}{10}\frac{q_x\mathcal{V}_x}{P} \;. \tag{4.28}$$

By substituting the corresponding wall temperature, T_W, into the Maxwell boundary conditions for the diffusive wall (4.27), we obtain *the same* boundary conditions for the isotropically scattering adiabatic surface, Eq. (4.23).

The above calculation shows that whether we adjust the temperature of the surface to get adibaticity at the wall, or use the isotropic scattering kernel to obtain the corresponding macroscopic boundary condition, the results, at least on the level of R13 equations, are the same. Both models lead to the adiabatic surface. However, adjusting the temperature in the microscopic DSMC model leads to an iterative scheme. The wall temperature should be modified for each iteration so that the final temperature distribution on the wall can mimic the no-energy-transfer from the surface. On the other hand, if we use the isotropic scattering kernel, there is no need to prescribe the temperature, and the wall temperature will be obtained accordingly.

We also note that the proposed method of modeling the adiabaticity using the isotropic scattering kernel is more consistent with the underlying physics of light gas particles interacting with heavy surface particles outlined in Sec. 4.3 A. The adiabatic Maxwell surface is a well-working model, however, the complexity in nature of this wall, i.e., adjusting the temperature of each individual surface element, seems rather unphysical.

4.4 Results and discussion

4.4.1 Micro lid driven cavity

We consider the partly adiabatic two-dimensional lid driven micro cavity, depicted in Fig. 4.2-a and compare the DSMC, R13 and NSF results in rarefaction regime. All walls except for the driven lid are assumed to be adiabatic; the top wall is fully diffusive and isothermal at $T = 273K$. The corresponding boundary conditions for a fully diffusive surface in DSMC and R13 equations are well studied and can be found in [68]. This geometry serves as a test for the implementation of the adiabatic boundary conditions (4.18) for DSMC and (4.23) for R13 equations. The top lid velocity is $U_{Wall} = 50$ ms^{-1}and computation are for Knudsen numbers Kn = 0.05, 0.1, 0.3. The side length of the cavity walls is fixed at $L = 1\mu$m and rarefaction occurs due to the reduction of the pressure in the cavity.

Figure 4.2-b shows the heat flux variation for the DSMC results along the four walls of cavity when $U_{Wall} = 50ms^{-1}$and Kn = 0.05. The heat flux of the monatomic rarefied flow through the walls is obtained by

$$q'' = \frac{B \times m}{2 \times N \times t} \sum_{i=1}^{N} \frac{\left[\left(c_x'^2 + c_y'^2 + c_z'^2\right)_i - \left(c_x^2 + c_y^2 + c_z^2\right)_i\right]}{A_i} .$$

Here, B is the number of real gas molecules represented by each DSMC particle, N is the number of particle-surface collisions taking place in the process of sampling, t is the elapsed time in the sampling, and A is the area of the cell through which the particle transfer energy to the surface.

Figure 4.2-b demonstrates that the adiabatic boundary condition Eq. (4.18), for DSMC indeed guarantees the full adiabaticity on the fixed walls. This is not so in Refs. [99, 1], where adiabaticity is implemented by an iterative scheme that sets the local boundary temperature such that the local heat flux into the wall vanishes; as a result, one observes oscillation of heat flux on the walls. We emphasize that by following the methodology in the current study, as one sets a surface to be adiabatic by isotropic scattering, there is no

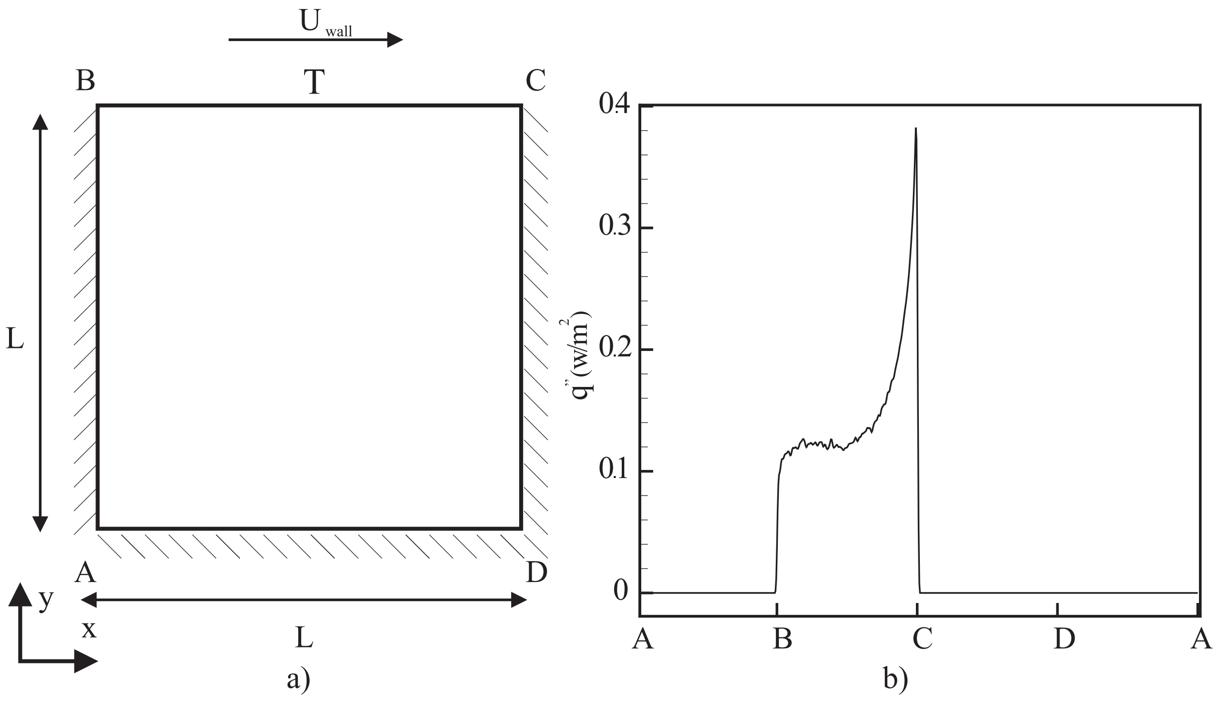

Figure 4.2: a) Adiabatic cavity geometry, b) Heat flux through the walls of cavity at $U_{Wall} = 50ms^{-1}$, Kn = 0.05

need to prescribe any temperature for the wall. We also note that the iterative schemes are less exact, and more time consuming. To us, the modelling of an adiabatic surface by isotropic scattering appear more natural.

4.4.2 Grid dependency

In order to perform the grid dependency test for DSMC, we use three grids composed of 100×100, 200×200 and 300×300 cells, and compare the heat flux profile along the driven lid when $U_{Wall} = 100$ ms^{-1}and Kn = 0.1. Figure 4.3-a demonstrates that the results for 200×200 and 300×300 are numerically equivalent, while the 100×100 grid gives insufficient results; therefore we used 200×200 grid cells for the following results.

To determine an appropriate mesh size for the R13 solution, a grid dependency test was conducted as well. Since solving the macroscopic transport equations takes considerable less amount of time than the DSMC approach, various meshes of size $N = 40, 50, 100, 200, 400$ were tested. For these cases the relative percentage changes in the net heat flux along the driven lid was monitored as the grid was refined successively. The results are plotted in Fig. 4.3-b. It is evident from Fig. 4.3-b that the relative percentage change in the net heat flux between two successive grid sizes is less then 0.2% as the grid is refined beyond 100×100. Therefore, for the following R13 results the grid with 100×100 cells is used.

It is also worth noting that a typical simulation with the R13 equations (as well as NSF) with a grid size of 100×100 takes about 20 minutes on a single quad core desktop PC. Whereas, depending on the flow parameters and the value of the Knudsen number, the corresponding DSMC simulation takes up to 70 hours of the computational time.

4.4.3 Velocity profile

Figure 4.4 shows the velocity components on the two centerlines of the cavity for $U_{wall} = 50$ ms^{-1} in the rarefied regime. For the small Knudsen number (Kn = 0.05) the three approaches– DSMC, R13 and NSF equations predict the same results for the velocity. As the Knudsen number increases we observe a deviation in the results of the continuum approaches from the molecular method; however, the predicted results of the R13 method are in better agreement with DSMC data, as compared to NSF.

A closer look into Fig. 4.4-c shows that the largest deviation in the predicted velocity by R13 from the DSMC solution takes place in the Knudsen layer at the side walls. Note that in this rarefaction regime the Knudsen layer almost covers the entire flow

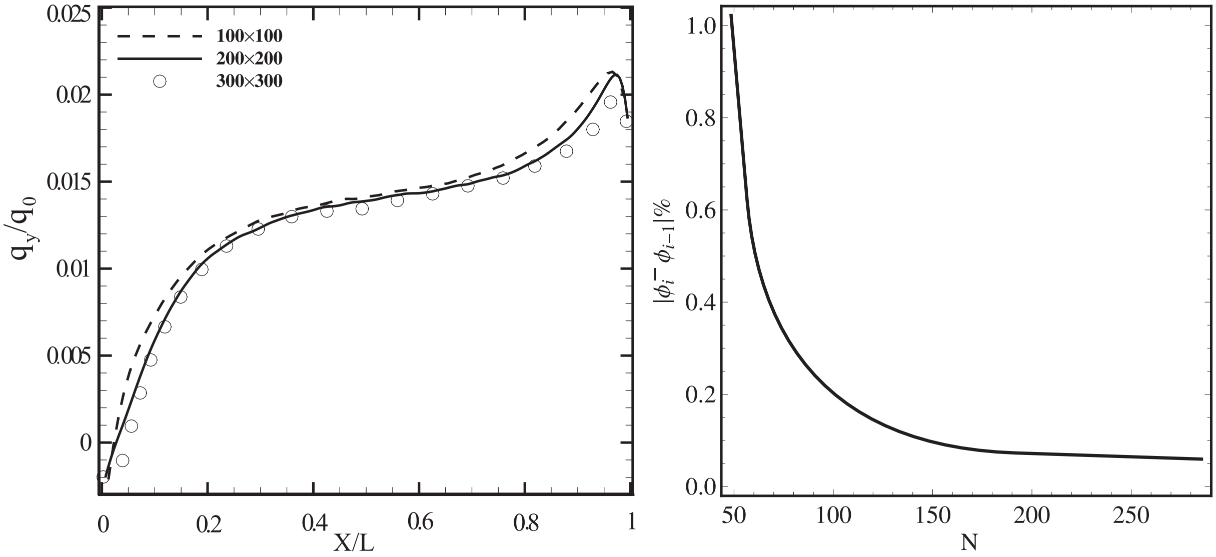

a) DSMC

b) R13

Figure 4.3: Grid dependency study test: a) vertical heat flux along the driven lid for DSMC method at Kn = 0.1, b) variation of relative percentage changes in the net heat flux by number of grid points along the driven lid for R13 solution at Kn = 0.1

field. The R13 equations, by benefiting from the Knudsen layer terms, can provide an approximation to the Knudsen layer, however, in the presence of large non-equilibrium effects this approximation becomes less accurate. The NSF equations, on the other hand, do not include the Knudsen layer terms at all and their results deviates from the DSMC solution, almost in the entire domain in Fig. 4.4-c.

4.4.4 Temperature profile

Variation of the flow temperature on the centerlines of the cavity with U_{wall} = 50 ms^{-1} are depicted in Fig. 4.5. This figure illustrates that up to Kn = 0.1, the R13 equation can accurately predict the temperature variation along the two centerlines. As Knudsen number increases, the R13 equations slightly underpredict the flow temperature (less than 1%) in close vicinity of the left adiabatic wall. As shown in Fig. 4.5, the flow temperature increases and decreases near the right and left walls, respectively. As the rarefied flow approaches the right wall it undergoes a compression which subsequently increases the flow temperature. The R13 equations can capture the increase and decrease of the flow temperature close to the side walls with a slight difference in the temperature magnitude in the non-equilibrium regime.

4.4.5 Heat flux; Viscous slip heating

Heat lines

Figure 4.6 shows the heat flux streamlines inside the cavity for the three approaches when Kn = 0.05. Similar to the case of a cavity with isothermal wall [59], the unconventional “cold-to-hot” heat transfer is observed. By using the macroscopic equations, Rana et al. [69] showed that this so called anti-Fourier heat flux is due to domination of the non-dimensional shear stress gradient over the temperature gradient. For a more detailed description of this rarefaction effect see [69].

A closer look into the DSMC and R13 shows that the associated curved structures of the heat flux lines are properly captured by the continuum method. Most interestingly, the DSMC and R13 results show heat apparently leaving the adiabatic surface while this effect is not observed in NSF. This heat is not coming from the walls, but created in the slip layer by friction.

In fact, the particles in the cell adjacent to the adiabatic surfaces collide with each other (and not the surface), which subsequently leads to viscous heat generation in the

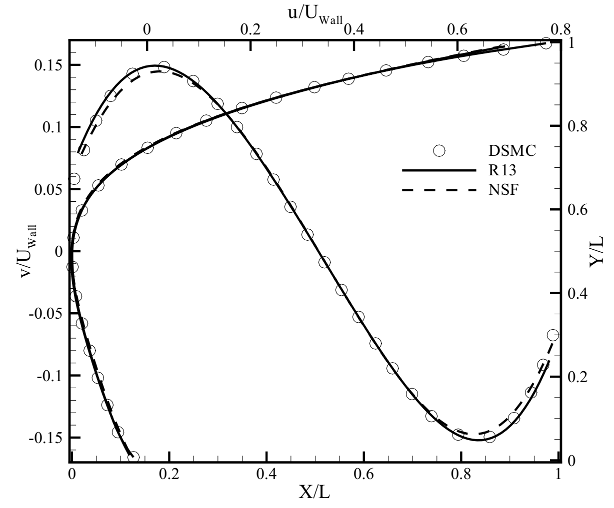

a) Kn=0.05

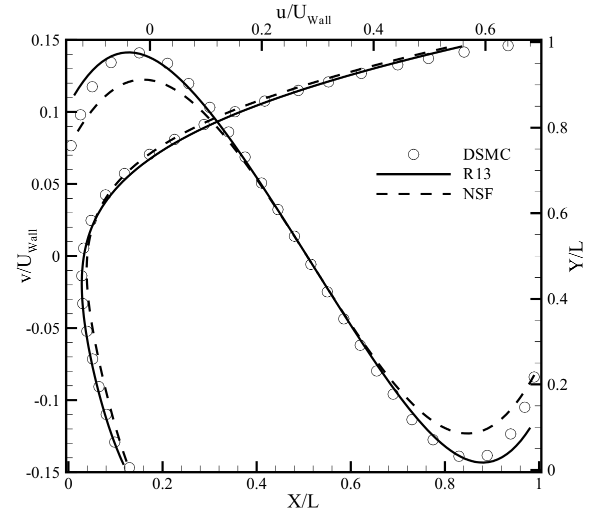

b) Kn=0.1

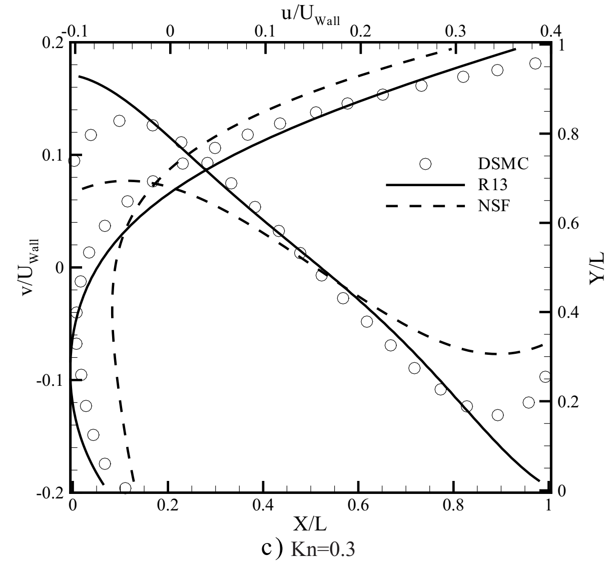

c) Kn=0.3

Figure 4.4: Comparison of horizontal and vertical velocity components on the vertical and horizontal centerlines of the cavity for U_{wall} = 50 ms^{-1}, a) Kn = 0.05, b) Kn = 0.1, c) Kn = 0.3

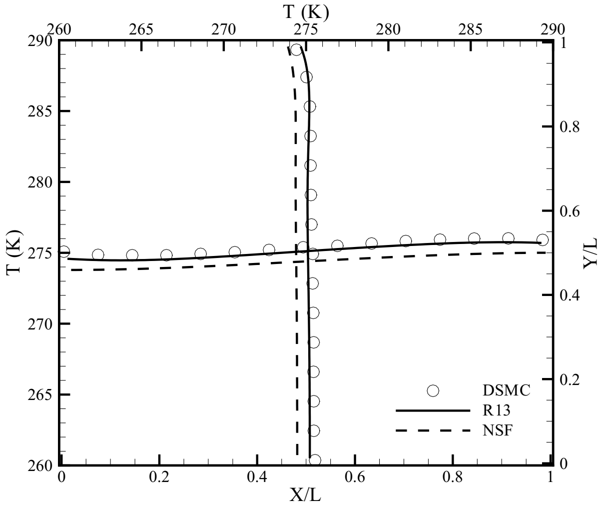

a) Kn=0.05

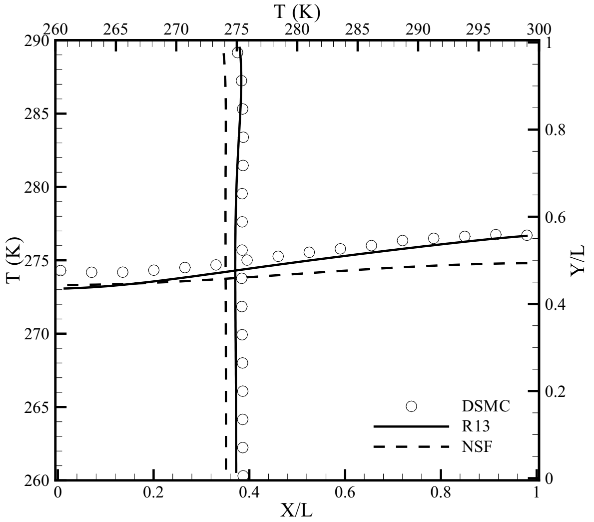

b) Kn=0.1

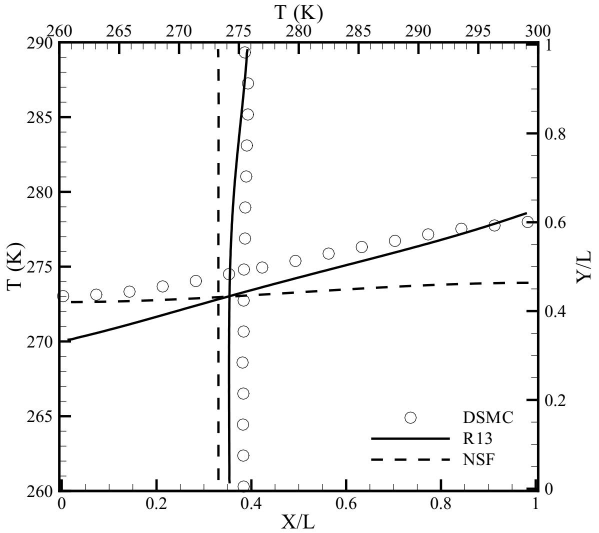

c) Kn=0.3

Figure 4.5: Comparison of temperature profiles on the horizontal and vertical centerlines of cavity for U_{wall} = 50 ms^{-1}, a) Kn = 0.05, b) Kn = 0.1, c) Kn = 0.3

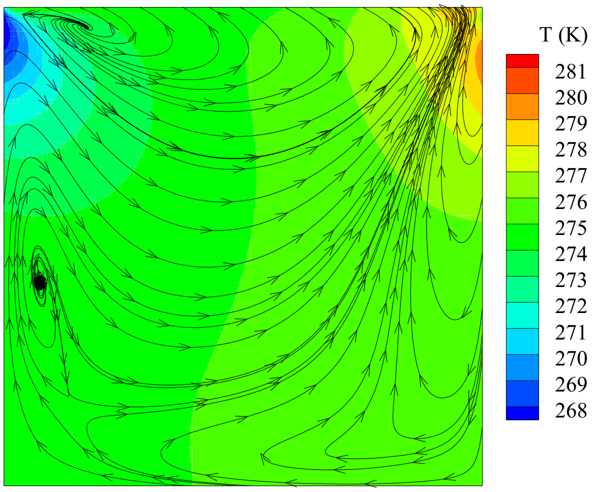

a) R13

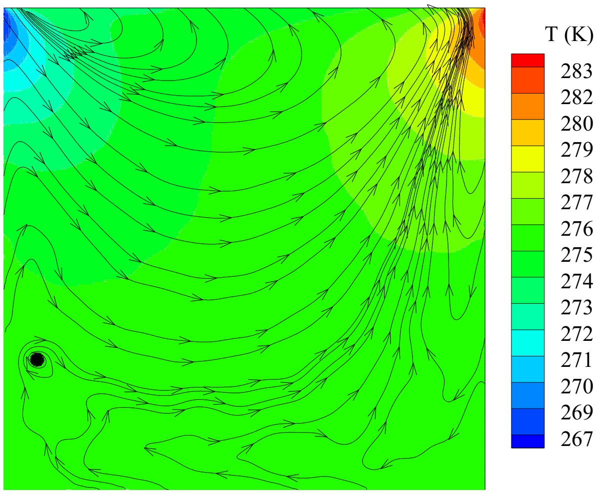

b) DSMC

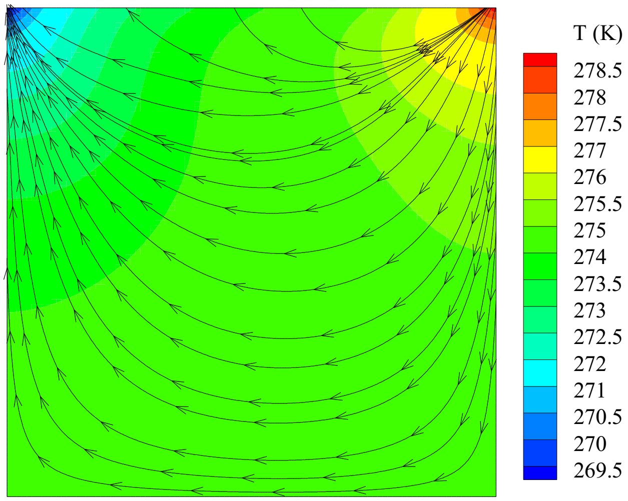

c) NSF

Figure 4.6: Heat flux streamlines and temperature contour inside the cavity at Kn = 0.05, a) R13, b) DSMC, c)NSF

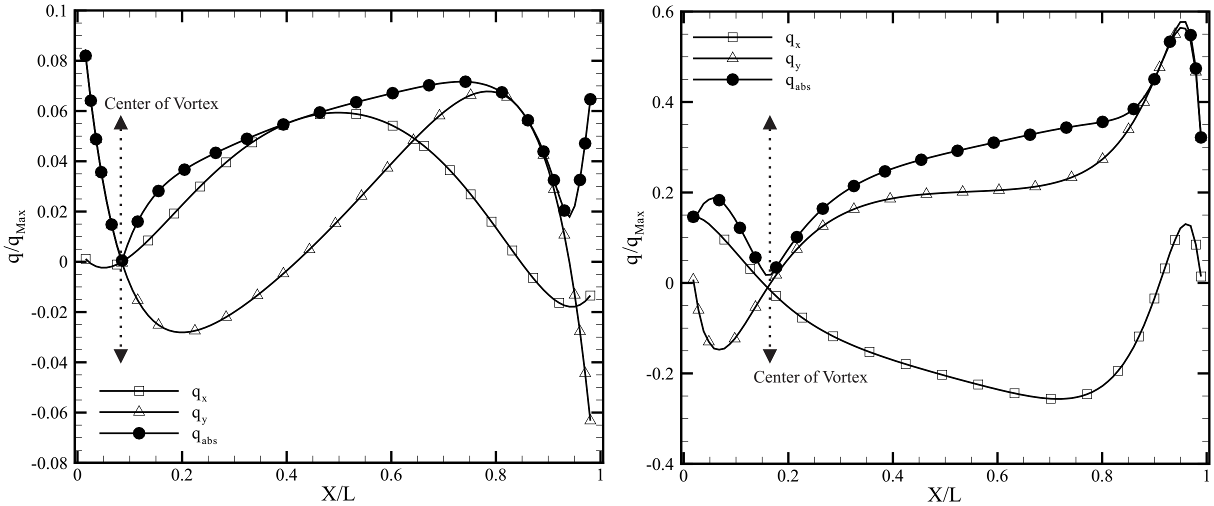

a) $\frac{y}{L} = 0.42$ b) $\frac{y}{L} = 0.95$

Figure 4.7: Component of the relative heat flux vector across the two vortices for R13 results, a) $Y/L = 0.42$, b)$Y/L = 0.95$

boundary cells. This heat cannot escape into the adiabatic wall; consequently, it will be directed towards the gas. Figure 4.6-a demonstrates that the R13 equations also predicts the viscous heat generation in the boundary due to rarefaction. In fact, Eq. (4.23) shows that the normal component of the heat flux in the proximity of the adiabatic surface boundary condition is a product of the slip velocity and the shear stress on the boundary, $q_y = -\sigma_{xy}\mathcal{V}_x$.

Comparison of the heat lines for the R13 and DSMC results also shows the appearance of a heat flux vortex in the bottom left and a heat source in the top left side of the cavity. Figure 4.7 shows the heat flux profile along the two horizontal lines passing through the centre of bottom vortex, $Y/L = 0.42$ and the top source at $Y/L = 0.95$ for R13 results. The maximum value of heat flux in the entire domain ($q_{\max} = 0.0187$) is used to non-dimensionalize the heat flux components. Figure 4.7-a demonstrates that the absolute value of the heat flux vector becomes zero at the center of the bottom vortex, which consequently leads to circulation of the heat lines around it. Note that the DSMC solution for heat flux lines in this region suffers markedly from large noises. Figure 4.7-b illustrates that the heat source on the top left corner appears due to the very small value of absolute heat flux in this region.

Heat flux along the centerlines

Comparison of the heat flux profiles along the two centerlines of the cavity is depicted in Fig. 4.8. This figure illustrates that the R13 equations can accurately predict the values of heat flux along the two centerlines in the adiabatic cavity. In addition, Fig. 4.8 shows that increasing the rarefaction effects, i.e., larger Knudsen number, enlarges the heat flux magnitude predicted by the NSF equations notably; however, the heat flux magnitude predicted by the R13 method is not significantly increased over the Knudsen regime. The small increment of the vertical heat flux over the horizontal centerlines for R13 results can be due to small increment role of the Knudsen layer as well as the third order terms in the heat flux governing equation, Eq. (4.7).

4.4.6 Shear stress

Shear stress distribution

Figure 4.9 shows the shear stress distribution overlaid on the velocity streamlines when Kn = 0.05 for the three methods of solution. The shear stress is nondimensionlized with respect to $\sigma_o = \rho_0 R T_0$. The R13 equations can accurately predict the shear stress distribution inside the cavity; however, NSF predict that the shear stress contours are generated at the top two corners.

Shear stress on the driven lid

In order to investigate the accuracy of the employed methods in more detail, we illustrate the shear stress profile along the driven lid in Fig. 4.10. The R13 equations provide very accurate results for the magnitude of the shear stress in the vicinity of driven lid. As the lid velocity increases, the shear stress in the flow field enlarges. A closer look into Fig. 4.10 shows that the value of the shear stress predicted by R13 is in maximum deviation from the DSMC results around the two top corners of the cavity where the flow undergoes sudden changes. Therefore, in this region the local Knudsen number is significantly larger than the global Knudsen number, which indeed limits the accuracy of the shear stress equation close to the top corners.

Drag coefficient

Although the R13 equations do not fully predict the accurate local values, they describe the overall behavior of the flow rather well. Therefore, we were encouraged to determine

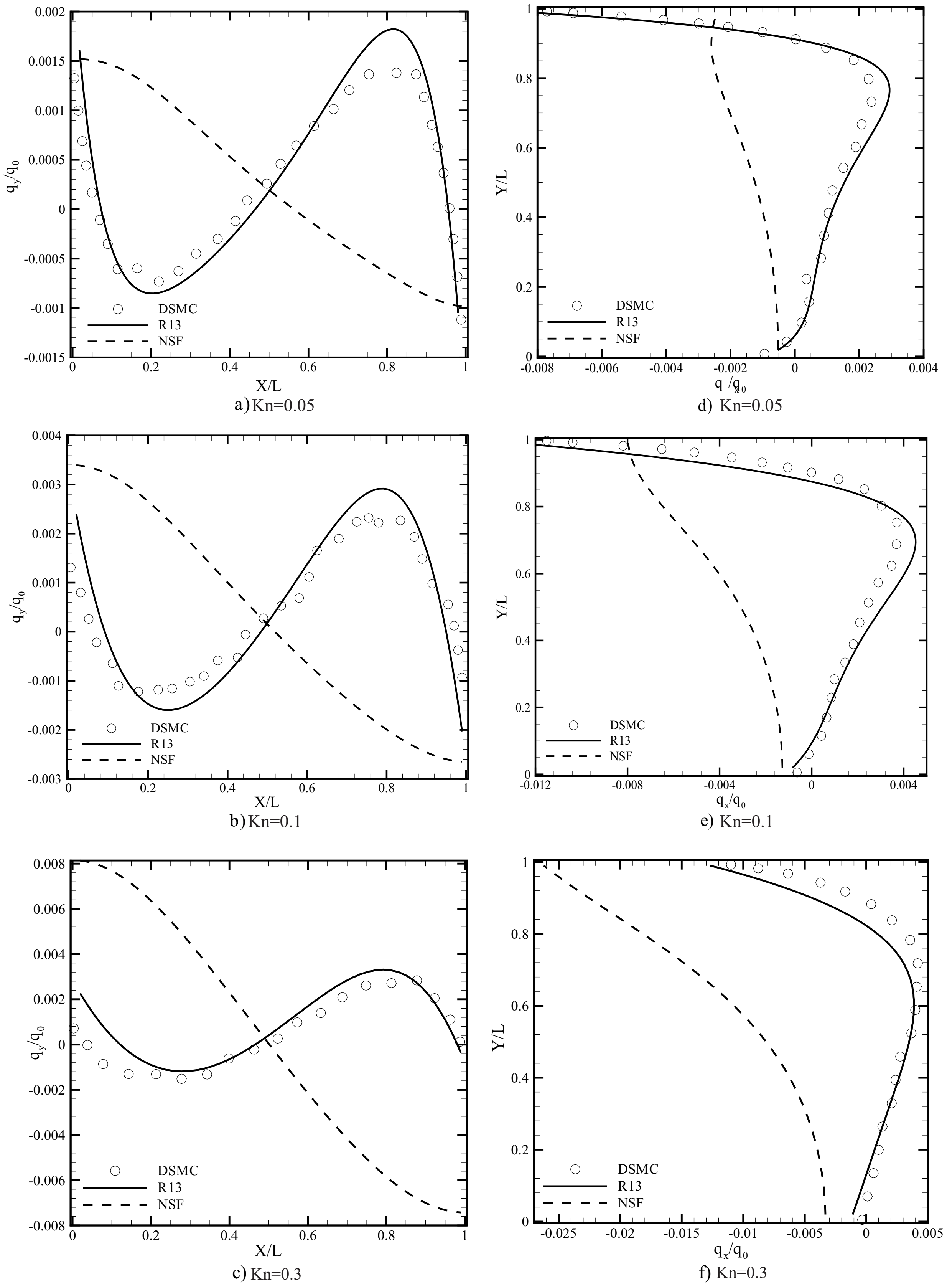

a) Kn=0.05
d) Kn=0.05
b) Kn=0.1
e) Kn=0.1
c) Kn=0.3
f) Kn=0.3

Figure 4.8: Heat flux over the centerlines of the cavity, a&d) Kn=0.05, b&e) Kn=0.1, c&f) Kn=0.3

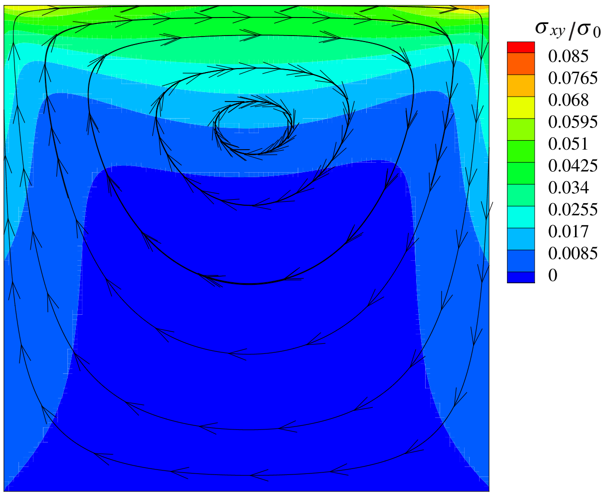

a) R13

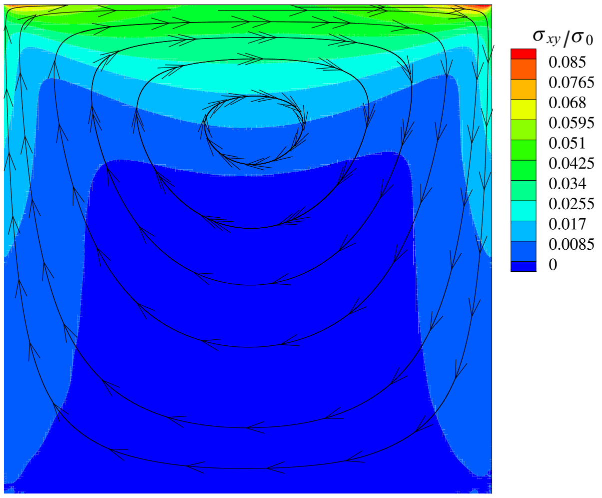

b) DSMC

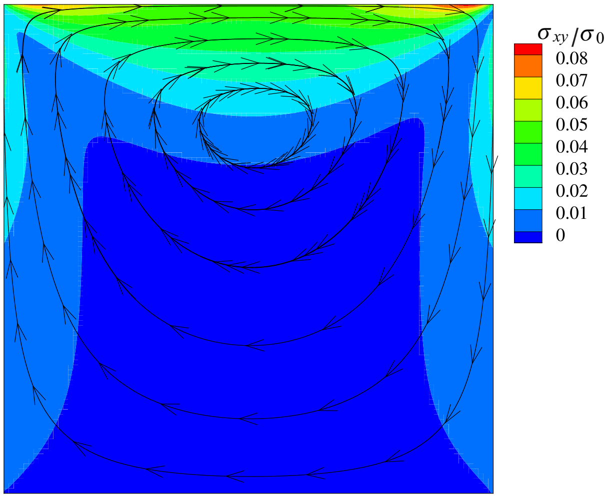

c) NSF

Figure 4.9: Velocity streamlines and shear stress contour for U_{Wall} = 50 ms^{-1} and Kn = 0.05, a)R13, b)DSMC, c)NSF

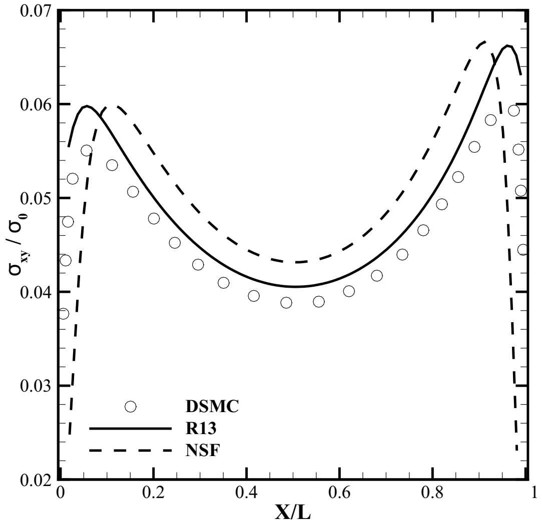

a) Kn=0.05

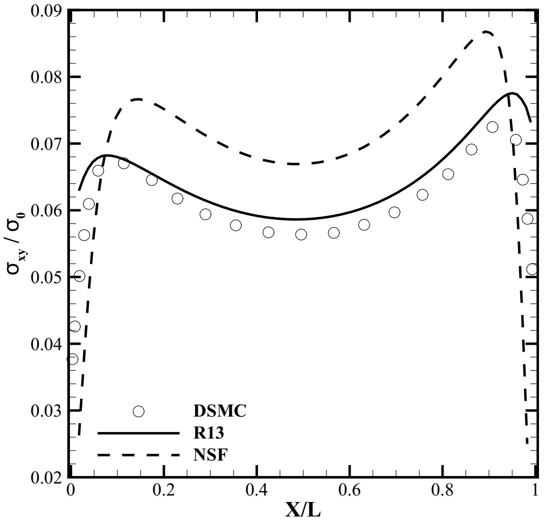

b) Kn=0.1

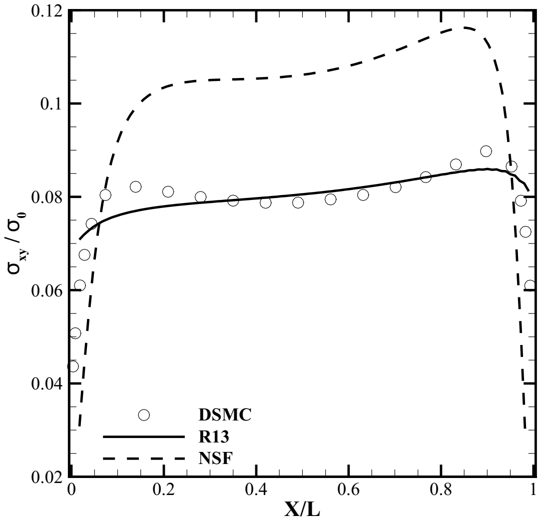

c) Kn=0.3

Figure 4.10: Comparison of shear stress along the driven lid of the cavity: a)Kn = 0.05, b)Kn = 0.1, c)Kn = 0.3

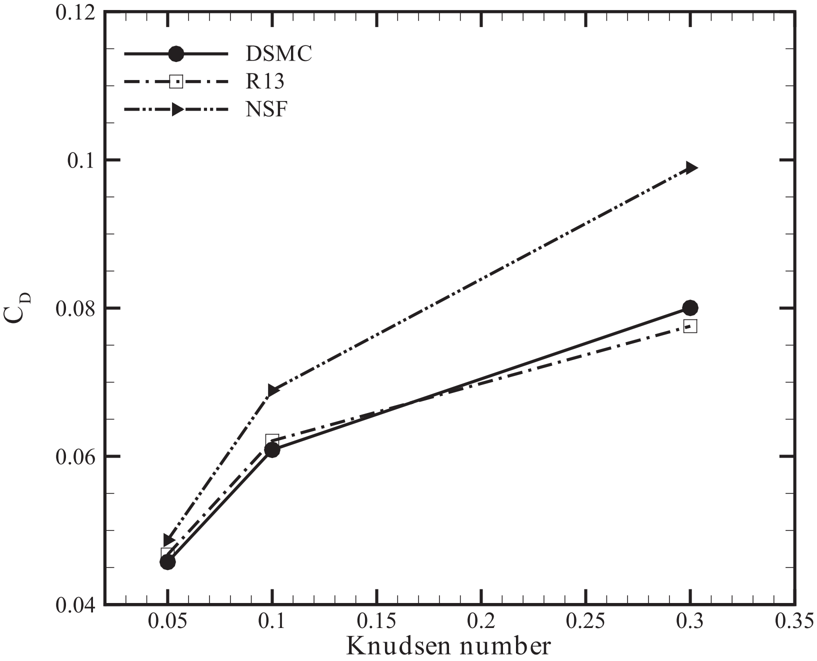

Figure 4.11: Comparison of the drag coefficient obtained from the three methods

the R13 drag coefficient and compare it with the DSMC results. The drag coefficient on the driven lid is obtained by

$$C_D = \frac{\int_0^L \sigma_{xy} dx}{\sigma_0 L}$$

Figure 4.11 shows the variation of the drag coefficient with the Knudsen number. Comparison of the R13 results with the DSMC data demonstrates that the R13 equations can accurately predict the drag coefficient up to Kn = 0.3. This figure is a good indicator of the capabilities in the R13 equations when predicting the global flow behaviors.

4.4.7 Cavity with specular reflecting walls

Another method to model the adiabaticity of the surface is to use the specular reflection kernel. In this method, the process of particle surface collision guaranties no-energy-transfer through the wall, however, the gas undergoes a perfect slip condition at the surface. Figure 4.12 shows the DSMC results for the lid driven cavity with 3 specular walls. The top driven lid is assumed to be a diffusive reflector at $T = 273\,K$.

Figure 4.12-a shows the heat lines overlaid on the temperature distribution. Compared to Fig. 4.6-b, a similar range of temperature is predicted inside the domain. However, the heat lines are completely different. More interestingly, the shear stress distribution, Fig.

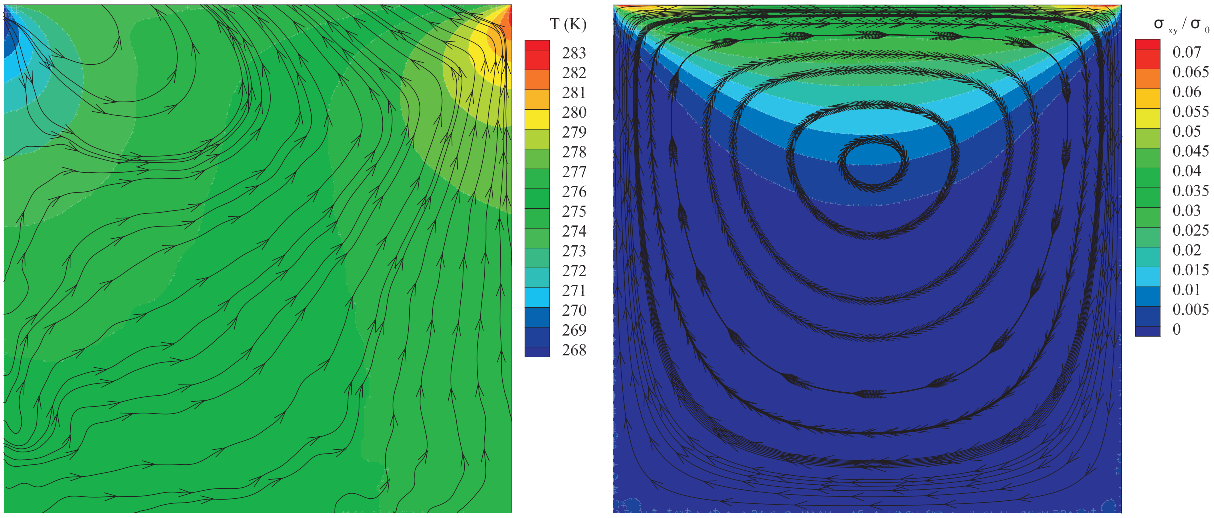

a)

b)

Figure 4.12: Flow formation predicted by DSMC inside a lid driven cavity with three specular walls and diffusive driven lid, $U_W = 50\,\frac{m}{s}$, Kn = 0.05. a) Heat flux streamlines overlaid on the temperature distribution, b) Velocity streamlines overlaid on the shear stress distribution.

4.12-b, shows a rather large shear stress close to the top lid, while the rarefied flow in the rest of the domain exhibits small shear stress. The perfect slip condition on the wall leads to a very small shear stress distribution inside the flow field. Since the assumption of the perfectly smooth surface at the microscopic level, specular reflection, is not realistic, such modelling of adiabaticity is not of our interest.

4.5 Conclusion

In the current study microscopic and macroscopic models are employed to model adiabatic surfaces. When a gas with light particles interacts with a rough surface of heavy particles, the gas-surface interaction can be considered adiabatic, and the reflecting particles have no preference in the reflection direction (isotropic scattering). In the DSMC method the isotropic scattering kernel is utilized to ensure the no-energy-transfer condition on each particle colliding with the adiabatic surface. The corresponding macroscopic boundary equations for the isotropic scattering distribution functions are obtained for the R13 equations. By taking into account the second order nonlinearity in the normal heat flux to an adiabatic surface, the viscous slip heating effect appears. The generation of heat due to intermolecular collision in the adjacent cell to the adiabatic surface (microscopic approach) can be well captured, and interpreted, by the product of the slip velocity and the shear stress on the adiabatic wall (macroscopic approach). The viscous slip heating that occurs at all slip boundaries can be more clearly identified in the case of adiabatic surface. Comparison of the solution for temperature, shear stress and heat flux profiles obtained from R13 and DSMC methods demonstrates the capability of the R13 equations in predicting the flow behaviors upto Kn = 0.3.

To be more general, the reflection of a particle from a surface can be modeled as a superposition of the diffusive reflection, specular reflection and isotropic scattering [83]. Therefore, using a general reflection kernel for the particle based method, which can model the three possible scenarios, seems to be essential.

Acknowledgement

This research was supported by the Natural Sciences and Engineering Research Council NSERC.

Chapter 5

Velocity Dependent Maxwell Boundary Conditions in DSMC

Abstract: *Recently Struchtrup [Phys. Fluids 25, 112001 (2013)] proposed an extension to the original Maxwell boundary conditions for the Boltzmann equation which introduces velocity dependent accommodation coefficients. These boundary conditions are implemented into the direct simulation Monte Carlo (DSMC) method. The effect of the velocity dependent Maxwell (VDM) boundary conditions on thermal transpiration phenomena is studied for two-dimensional micro-cavities. Variation of the three microscopic parameters provided by the VDM boundary condition yields changes in slip velocity, temperature jump and the thermal transpiration effect. The results indicate that the strength of thermal transpiration can change and, depending on the values of the coefficients, the rarefied flow can be driven from warmer toward colder regions.*

Published in International Journal of Heat and Mass Transfer **87** (2015), 151160

5.1 Introduction

The interactions between gas particles and a solid surface are complex. It is unlikely that a general mathematical model be developed that can adequately describe the gas–surface interactions for different combinations of gases and surfaces at all conditions. However, by using microscopic simulation methods, such as direct simulation Monte Carlo (DSMC) [5] and molecular dynamics (MD) [54], better understanding of the interaction can be obtained. This knowledge helps in developing phenomenological models which can provide better fit to the experimental data.

Experiments with molecular beams show that the beam is scattered into a plume-like structure around the line of specular reflection [10, 36]. The structure of the reflected beam becomes particularly important when scattered particles are free to move for a long distance inside the bulk gas. The Knudsen number, Kn, is defined as the ratio between the mean free path of the gas particles and the flow characteristic length scale, $Kn = \frac{\lambda}{L}$. Special attention should be given to the reflection kernel when the Knudsen number becomes large.

This plume-like structure is described and captured by the Cercignani-Lampis (CL) model [11, 48], where the shape of the reflection plume strongly depends on the values of the normal and tangential accommodation coefficients, α_n and α_t. In this model, the collision outcome depends on the velocity of impacting particle with the surface. Although the CL model can be fitted to slip velocity and temperature jump, it does not provide sufficient flexibility to be fitted to the data for thermal transpiration coefficient [72].

For moderate Knudsen numbers, i.e., in the transition flow regime, the particles reflected from the surface travel a rather short distance before their first inter-molecular collision. In this regime the exact shape of the reflection plume is not required to express boundary conditions, but an appropriate approximation can deliver the chemistry of gas-surface interaction. This provides room for a simpler model than CL, which can be fitted to the thermal transpiration coefficient. The original Maxwell accommodation model [51], due to its simplicity, cannot predict different accommodation coefficients for the slip velocity and temperature jump.

Epstein [21] considered the effect of impact velocity on the reflection kernel, and proposed an extension to the Maxwell model. In this model the degree of thermal accommodation is determined based on the impact energy of the colliding particle.

Recently, Struchtrup [83] added the isotropic scattering kernel to the Maxwell's boundary condition to also account for nearly adiabatic surface with friction [57]. Also this model, by considering the impact velocity of the particles, allows to incorporate velocity dependent accommodation coefficients into the microscopic description. In the velocity dependent Maxwell (VDM) boundary condition, a particle colliding with the surface is either thermalized, specularly reflected, or scattered in an arbitrary direction, where the probabilities for the different processes depend on the impact velocity. The model provides wide flexibility for the choice of the velocity dependent accommodation coefficients. A particular model was suggested in Ref. [83], based on the assumption that the gas-wall interaction can be described as a thermally activated process, where particles with higher velocities are more likely to be specularly reflected or isotropically scattered from the surface, while particles with smaller velocity are more likely to be thermalized. The corresponding macroscopic boundary conditions for slip velocity and temperature jump were obtained from the first order Chapman-Enskog expansion.

Thermally-driven flows inside a two-dimensional enclosure have been studied in the literature [68, 96]. Vargas et al. [96] examined the effect of Knudsen number, surface temperature gradient and the geometry aspect ratio on the flow formation inside a micro cavity. They observed that the interplay between thermal transpiration and the viscous stresses in the boundary determines the direction of tangential velocity close to the wall. They also reported that close to the continuum regime thermal transpiration dominates, and the gas flows from colder to warmer regions.

The importance of boundary conditions in the thermal-driven flows has also attracted the attention of other researchers [8, 78]. Cai [8] used the Maxwell boundary condition to study the flow formation inside a cavity subjected to a temperature profile on the wall. He considered two cases of continuum and free molecular regimes to see the effect of Knudsen number on the rarefied flow. Kosuge et al. [46] used the Maxwell and the CL model to study the steady flow between parallel plates with sinusoidal temperature distribution at large Knudsen numbers. They demonstrated that considering the CL model leads to a steady flow between the plates, whereas for the Maxwell-type model the gas remains at rest.

In the current study, the velocity vector for particles reflecting from the surface is derived, and the required steps to implement the VDM boundary conditions into a DSMC solver are presented. To study the effects of thermal transpiration, rarefied flows inside a two-dimensional thermal cavity with temperature gradient along the surface are considered. The effects of the three independent coefficients incorporated in the VDM boundary conditions on the vortex formation, and strengthening or weakening of the rarefaction effects are studied. The results indicate that, in contrast to the CL model, the VDM boundary condition provides opportunity for fitting to experimental data for transpiration flow.

The remainder of the paper is organized as follows. A short description of the DSMC method employed in this study is presented in Sec. 5.2. The general reflection kernel for the VDM boundary conditions is rephrased in section 5.3.1; then the reflecting velocity for use in the DSMC method is obtained and presented. The geometry considered in this study is presented in Sec. 5.4.1, and the boundary conditions are tested in a micro cavity to ensure the persistency of the Maxwell distribution function. Afterward, the flow formation inside a micro cavity with temperature gradient is studied in Sec. 5.4.2. A brief description of the thermal transpiration flow is presented, and the possibility of inverse transpiration flow is discussed in section 5.4.3. We shortly mention the hydrodynamic boundary equations for the VDM model, and use the Grad equations to explain the flow formation. The DSMC solution for the thermal cavity in larger rarefaction regime is presented in Sec. 5.4.4. The paper ends with our conclusions in section 5.5.

5.2 DSMC Method

The DSMC method is a numerical tool to solve the Boltzmann equation by using the statistical simulation of molecular processes based on the kinetic theory of dilute gases [5]. In this method, many independent simulating particles are used to model gaseous flows, where each particle represents a large number of real gas molecules. For the current study, we modified our DSMC solver [59, 58, 62, 68, 57] by implementing the VDM boundary condition. In this code, the selection of collision pairs is based on the no-time-counter (NTC) method, therefore the computational time is proportional to the number of the simulating particles [5]. The fluid is argon as a Maxwell molecule with $m = 6.63 \times 10^{-26}$kg and the reference viscosity of $\mu_0 = 1.9549 \times 10^{-5}$Pa.s. The Knudsen number is defined as [81]

$$Kn = \frac{\mu_0}{\rho_0 \sqrt{\mathrm{R} T_0} L} \ . \tag{5.1}$$

Here, ρ_0 is the reference density, and L indicates the characteristic length of the flow. The DSMC simulation starts with 32 particles located in each cell. As the flow reaches the steady state, the molecular properties are sampled over a large period of time to reduce the statistical scattering. In addition, a filtering post processor is used to minimize the scattering in the thermodynamic properties. In this filtering, the sampled macroscopic properties, F, in cell N are averaged over a pattern of its neighboring cells [59]

$$\widetilde{F}_{(N)} = \frac{F_N + \sum_{I=1}^{I=N_n} F_I}{N_n + 1} .$$

5.3 VDM boundary conditions

5.3.1 Reflection kernel

The reflection kernel for the generalized Maxwell model can be written as a superposition of diffuse reflection, specular reflection, and isotropic scattering [83],

$$P\left(\mathbf{c}' \to \mathbf{c}\right) = \Theta\left(c'\right) \frac{|c_n| f_0 \Theta(c)}{\int\limits_{c_n>0} |c_n| f_0 \Theta(c) d\mathbf{c}} + \left(1 - \Theta\left(c'\right)\right) \times$$
$$\left[\gamma \delta\left(c_k' - c_k + 2n_j c_j n_k\right) + (1-\gamma) \frac{1}{\pi} \frac{|c_n|}{c'^3} \delta\left(c' - c\right)\right] . \quad (5.2)$$

Here, c_k' and c_k denote velocities of incoming and outgoing particles, respectively, c' and c are the respective absolute values, and $c_n = c_k n_k$ is the contribution normal to the wall. The velocity dependent accommodation coefficient $\Theta\left(c'\right)$ is the probability that an incoming particle will be diffusively reflected, and the coefficient γ is introduced so that $\gamma\left(1 - \Theta\left(c'\right)\right)$ is the probability that a particle will be specularly reflected.

Many meaningful models for the coefficients $\Theta(c)$ and γ can be developed [21]. In the following we use the model suggested in Ref. [83], where $\gamma = const$, and thermalization is assumed as a thermally activated process,

$$\Theta\left(c'\right) = \Theta_0 \exp\left(\frac{\varepsilon - \alpha \frac{m}{2} c'^2}{kT_W}\right) . \quad (5.3)$$

Here, the dimensionless coefficient α is a measure for the strength of the activation, where $\alpha = 0$ as a case without activation, corresponds to the original Maxwell model with fully diffusive walls. Moreover, ϵ considers the effect of energy bounce on the reflected particle, and Θ_0 is a constant depending on the wall structure. Note that these coefficients can be varied so that the results fit to the experimental data. In the following we assume that $\Theta_0 = 1$ and $\epsilon = 0$ unless otherwise mentioned. In Eq. (5.2), $f_0 = 2\beta\sqrt{\pi} f_M / \rho$ is the reduced

Maxwell distribution in the rest frame, which with the above notation can be written as, with $\beta = \sqrt{\frac{m}{2kT}}$,

$$f_0 = \frac{2}{\pi}\beta^4 \exp\left(-\beta^2 c^2\right) \; .$$

The probability function, Eq. (5.3), varies between 0 and 1, and depends on the velocity c' of the particle colliding with the surface. To determine whether the particle is diffusively reflected or scattered, a random number, $R_1 \in [0,1]$ is drawn, such that the particle undergoes a diffuse reflection if $R_1 < \Theta\left(c'\right)$. If, however, $R_1 > \Theta\left(c'\right)$, a second random number $R_2 \in [0,1]$ is drawn, and the scattering is specular for $R_2 < \gamma$, and isotropic for $R_2 > \gamma$. For each of these cases, the reflection kernel is selected according to the following rules:

5.3.2 Diffusive reflection, $R_1 < \Theta\left(c'\right)$

The first term of Eq. (5.2) determines the velocity of a diffusively reflecting particle, i.e., the reflection kernel is

$$P_D\left(\mathbf{c}' \to \mathbf{c}\right) = \frac{|c_n|\, f_0 \Theta\left(c\right)}{\int\limits_{c_n > 0} |c_n|\, f_0 \Theta\left(c\right) d\mathbf{c}} \; .$$

To proceed, we consider the particle velocity in cylindrical coordinates, so that $\mathbf{c} \to \{c_n, c_r, \theta\}$ and $d\mathbf{c} = c_r dc_n dc_r d\theta$. For the implementation into DSMC we need the cumulative probability that a particle leaves with a velocity below $\{V_n, V_r, \Omega\}$, defined as

$$F_n F_r F_\Omega = \int_0^{V_n} \int_0^{V_r} \int_0^{\Omega} P_D\left(\mathbf{c}' \to \mathbf{c}\right) c_r dc_n dc_r d\theta \; . \tag{5.4}$$

Here, F_n, F_r and F_Ω are the cumulative probabilities for the velocity vector in cylindrical coordinates. Making f_0 and $\Theta\left(c\right)$ explicit, and performing all integrations, we find at first

$$F_n F_r F_\Omega = \frac{2\int_0^{V_n} \beta^2 c_n \exp\left(-\left(1+\alpha\right)\beta^2 c_n^2\right) dc_n}{2\int_0^{\infty} \beta^2 c_n \exp\left(-\left(1+\alpha\right)\beta^2 c_n^2\right) dc_n} \frac{2\int_0^{V_r} \beta^2 c_r \exp\left(-\left(1+\alpha\right)\beta^2 c_r^2\right) dc_r}{2\int_0^{\infty} \beta^2 c_r \exp\left(-\left(1+\alpha\right)\beta^2 c_r^2\right) dc_r} \frac{\int_0^{\Omega} \frac{d\theta}{2\pi}}{\int_0^{2\pi} \frac{d\theta}{2\pi}} \; . \tag{5.5}$$

The above integrals can be calculated analytically, and Eq. (5.4) simplifies to

$$\begin{aligned} F_n &= 1 - \exp\left(-\left(1+\alpha\right)\beta^2 V_n^2\right) \; , \\ F_r &= 1 - \exp\left(-\left(1+\alpha\right)\beta^2 V_r^2\right) \; , \\ F_\Omega &= \frac{\Omega}{2\pi} \; . \end{aligned}$$

Solving the above equations for the three upper limits of integral gives

$$\begin{aligned} V_n &= \frac{1}{\sqrt{1+\alpha}}\frac{1}{\beta}\sqrt{-\ln\left(1-F_n\right)}\ , \\ V_r &= \frac{1}{\sqrt{1+\alpha}}\frac{1}{\beta}\sqrt{-\ln\left(1-F_r\right)}\ , \\ \Omega &= 2\pi F_\Omega. \end{aligned}$$

By converting back to the Cartesian coordinates for a surface with normal in $y-$direction, the reflecting velocities are obtained as

$$\begin{aligned} c_x &= \frac{1}{\sqrt{1+\alpha}}\frac{1}{\beta}\sqrt{-\ln\left(1-F_r\right)}\cos\left(2\pi F_\Omega\right)\ , \qquad (5.6) \\ c_y &= \frac{1}{\sqrt{1+\alpha}}\frac{1}{\beta}\sqrt{-\ln\left(1-F_n\right)}\ , \\ c_z &= \frac{1}{\sqrt{1+\alpha}}\frac{1}{\beta}\sqrt{-\ln\left(1-F_r\right)}\sin\left(2\pi F_\Omega\right)\ . \end{aligned}$$

The cumulative probabilities are uniformly distributed in $[0,1]$. The velocity of the thermalized particle is determined by drawing three random numbers for $\{F_n, F_r, F_\Omega\}$, and computing the velocity from the above.

Compared to the corresponding expressions for the standard Maxwell boundary conditions, the VDM boundary condition contains the factor $\frac{1}{\sqrt{1+\alpha}}$ that is due to the velocity dependence of the accommodation coefficient $\Theta\left(c'\right)$. Assuming $\alpha = 0$ gives the conventional Maxwell boundary conditions for the diffusive wall [5].

5.3.3 Specular reflection, $R_1 > \Theta\left(c^{'}\right)$ and $R_2 < \gamma$

A particle is specularly reflected if $R_1 > \Theta\left(c^{'}\right)$ and $R_2 < \gamma$. The reflection kernel

$$P_{Sp}\left(\mathbf{c}^{'} \rightarrow \mathbf{c}\right) = \delta\left(c_k^{'} - c_k + 2n_j c_j n_k\right)\ ,$$

describes the deterministic specular reflection of the particle, with the after-collision velocity

$$c_x = c_x^{'}\ ,\ \ c_y = -c_y^{'}\ ,\ \ c_z = c_z^{'}\ .$$

5.3.4 Isotropic scattering, $R_1 > \Theta\left(c^{'}\right)$ and $R_2 > \gamma$

Isotropic scattering occurs when $R_1 < \Theta\left(c^{'}\right)$and $R_2 > \gamma$, and the corresponding reflection kernel is

$$P_{Sc}\left(\mathbf{c}^{'} \to \mathbf{c}\right) = \frac{1}{\pi}\frac{|c_n|}{c^{'3}}\delta\left(c^{'} - c\right) \ .$$

By using spherical coordinates, $\{c, \theta, \phi\}$ we can write

$$P\left(\mathbf{c}^{'} \to \mathbf{c}\right) d\mathbf{c} = \frac{1}{\pi c^{'3}} c\cos\phi\delta\left(c^{'} - c\right) c^{2} dc \sin\phi d\phi d\theta = \left[\delta\left(c^{'} - c\right) dc\right]\left[\frac{1}{2\pi} d\theta\right]\left[2\cos\phi\sin\phi d\phi\right] \ .$$

The delta function indicates that the absolute velocity of the leaving particle is deterministic, $c = c'$. However, the direction of the leaving particle is subjected to the process of random scattering, and as before we consider the cumulative probabilities

$$F_\theta = \int_0^\Theta \frac{1}{2\pi} d\theta \ \ , \ F_\phi = \int_0^\Phi 2\cos(\phi)\sin(\phi)\, d\phi \ ,$$

The integrals for the cumulative probabilities F_θ, F_ϕ can be solved analytically to give

$$\Theta = 2\pi F_\theta \ , \quad \Phi = \arcsin(\sqrt{F_\phi}) \tag{5.7}$$

By converting back the velocity components to the Cartesian coordinates, and noting that $\cos(\arcsin(x)) = \sqrt{1 - x^2}$, the velocity of the scattered particle is

$$\begin{aligned} c_x &= c^{'}\sqrt{F_\phi}\cos(2\pi F_\theta) \ , \qquad (5.8) \\ c_y &= c^{'}\sqrt{1 - F_\phi} \ , \\ c_z &= c^{'}\sqrt{F_\phi}\sin(2\pi F_\theta) \ . \end{aligned}$$

The cumulative probabilities are uniformly distributed in $[0, 1]$. The velocity of the isotropically scattered particle is determined by drawing two random numbers for $\{F_\phi, F_\theta\}$, and computing the velocity from the above.

5.4 Results and discussion

5.4.1 Persistency of Maxwell distribution in micro-cavity

We consider a square micro-cavity as depicted in Fig. 5.1-a. The temperature of the wall in the micro-cavity, T, varies along the x and y-directions as indicated. We are interested in transpiration flow, where the driving force for the flow in the cavity is the temperature gradient along the surfaces.

In the DSMC method particles are initially distributed according to the Maxwellian distribution function [5]. In this section we ensure that in a system without perturbation the Maxwell distribution persists, when particles collide with the VDM boundary condition and reflect back to the flow. For this test, the rarefied flow in the micro-cavity is left to itself, and the microscopic velocity distribution function as well as the macroscopic velocity profile are obtained. The wall temperatures in the micro-cavity are prescribed as

$$T_B = T_L = T_T = T_R = 300\ K\ .$$

The coefficients for the VDM boundary conditions assumed in this test are

$$\varepsilon = 0, \quad \alpha = 0.5, \quad \gamma = 0.7 \quad \Theta_0 = 1\ .$$

Figure 5.1-b demonstrates the normalized horizontal velocity distribution function for a computational cell in the top left corner of the cavity. It is observed that the distribution obtained from the DSMC simulation agrees with the local Maxwellian distribution, obtained from the local values for density, velocity and temperature. The horizontal macroscopic velocity distribution inside the cavity in Fig. 5.1-c shows that the persistency of the Maxwellian distribution is well guaranteed by the implementation of this new set of boundary conditions.

5.4.2 Micro-cavity

The flow formation inside the micro-cavity is considered for the case where the temperature of the side walls varies linearly, specifically we set

$$T_B = 600\ \mathrm{K} \quad T_T = 300\ \mathrm{K} \quad T_L(y) = T_R(y) = T_B\left(1 + \frac{y}{L}\right)\ .$$

Figure 5.2 shows the effect of the coefficients Θ_0, α and γ on the velocity streamlines

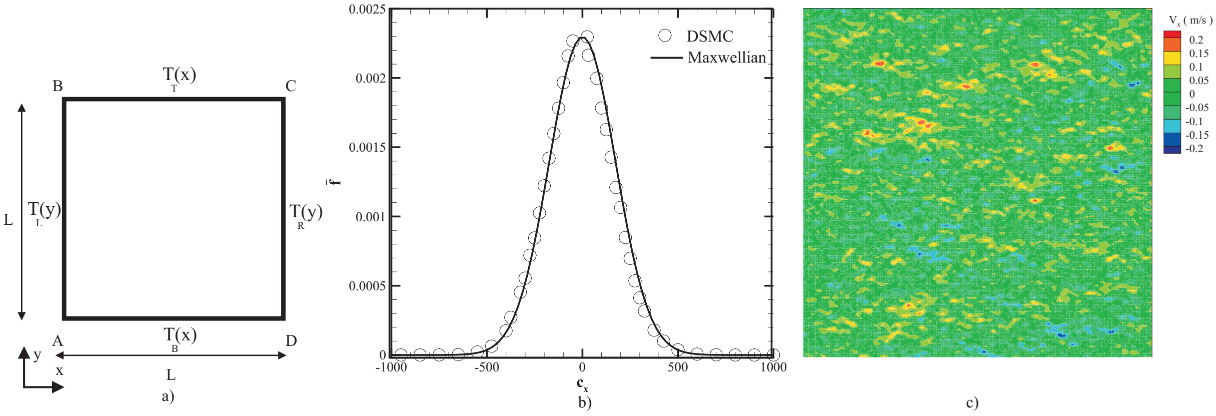

a) b) c)

Figure 5.1: Persistency of the Maxwell distribution in micro-cavity, a) cavity geometry, b) normalized microscopic horizontal velocity distribution function, c) macroscopic horizontal velocity distribution in the micro-cavity.

and the temperature distribution inside the cavity.

The left column in Fig. 5.2 shows the DSMC results when the reflection kernel *does not* depend on the velocity of impacting particle, $\alpha = 0$. The right column, on the other hand, shows the flow formation when dependency of the reflection on the impact velocity is considered, $\alpha \neq 0$.

Starting from the fully diffusive surface, Fig. 5.2-a we observe that the tangential component of the velocity vector close to the vertical wall is downward: thermal transpiration pushes the rarefied flow towards the bottom (i.e., the warmer) side of the cavity.

Considering the impact velocity on the reflection kernel using the VDM boundary condition, decreases the magnitude of the vertical velocity close to the vertical walls. As we increase α and γ, an additional vortex which drives the rarefied flow toward the upper (i.e., colder) side of the cavity appears (Figs. 5.2-e,f). In other words, sufficiently large values of α and γ in the VDM boundary condition lead to a decreased strength of the thermal transpiration phenomenon, and the appearance of warm-to-cold vortices.

In order to confirm the effect of impact velocity on the formation of the secondary vortex, we performed the simulation when the reflection kernel does not depend on the impact velocity $\alpha = 0$, but contains diffusive, specular and isotropic scattering. In order to have a comparable setting we adjust Θ_0 such that it is the average probability for a diffusive reflection, defined as $\bar{\Theta} = \int_{c_n<0} \Theta\left(c\right) c_n f_M d\mathbf{c} / \int_{c_n<0} c_n f_M d\mathbf{c}$ which gives $\bar{\Theta} = \left(1+\alpha\right)^{-2}$. For comparison with the case for $\alpha = 0.2$, we hence chose $\Theta_0 = 0.7$, and perform the simulation for two values of γ. As depicted in Fig. 5.2-b,c, the secondary vortex does not appear when the reflection kernel is independent of the impact velocity. This figure indicates that, in the case of VDM boundary condition, the dependency of the reflection kernel on the impact velocity is required to weaken/increase the strength of the thermal transpiration effect.

Smaller transpiration effects in the VDM boundary condition allows other non-equilibrium phenomena, such as thermal stresses, to play a more important role in determining the flow direction close to the surface. The reversed direction of velocity close to the surface also suggests the possibility of reversed transpiration flow, where the rarefied flow is driven from warm to cold; this will be discussed in greater detail in Sec. 5.4.3.

Comparing the temperature distributions inside the cavity shows that the VDM boundary condition leads to smaller temperature gradients inside the cavity. Since not all particles are forced to thermalize with the surface after collision, the wall information will not be completely transferred to the flow field, so that the temperature jump is larger, which leads to smaller maximum, and larger minimum temperature inside the cavity.

Figure 5.3 shows the rarefied flow properties along the vertical line $\frac{X}{L} = 0.95$, which lies inside the Knudsen layer of the right wall. The VDM boundary condition allows some particles to reflect back to the flow without exchanging momentum, or energy, with the surface, which subsequently decreases the shear stress along the wall. It is also seen that the effect of changing γ on the tangential velocity is quite different for standard Maxwell and the VDM boundary condition. In the case of standard Maxwell boundary condition, the tangential velocity is not much dependent on γ. As α and γ increases, the shear stress and the vertical velocity become smaller in magnitude, see Figs. 5.3-a,b, and the velocity changes sign when the small vortex close to the right wall appears. Figure 5.3-c shows smaller gradient of temperature for the new reflection kernel, which appears to be unaffected by the coefficients in the VDM model.

5.4.3 Forward and inverted transpiration flow

Thermal transpiration takes place when two particles coming from the cold (smaller thermal velocity) and warm (higher thermal velocity) regions exchange momentum with the surface at the same location. Figure 5.4 shows an schematic of the particle-surface interaction for the two types of boundary conditions.

The left figure shows the collisions for the classical Maxwell boundary model, where the accommodation is independent of impact velocity. Since the collision kernel is isotropic, the average reflection velocities for the particle colliding with the wall is perpendicular to the wall, as indicated by the dashed vectors. Therefore, in average, the complete tangential

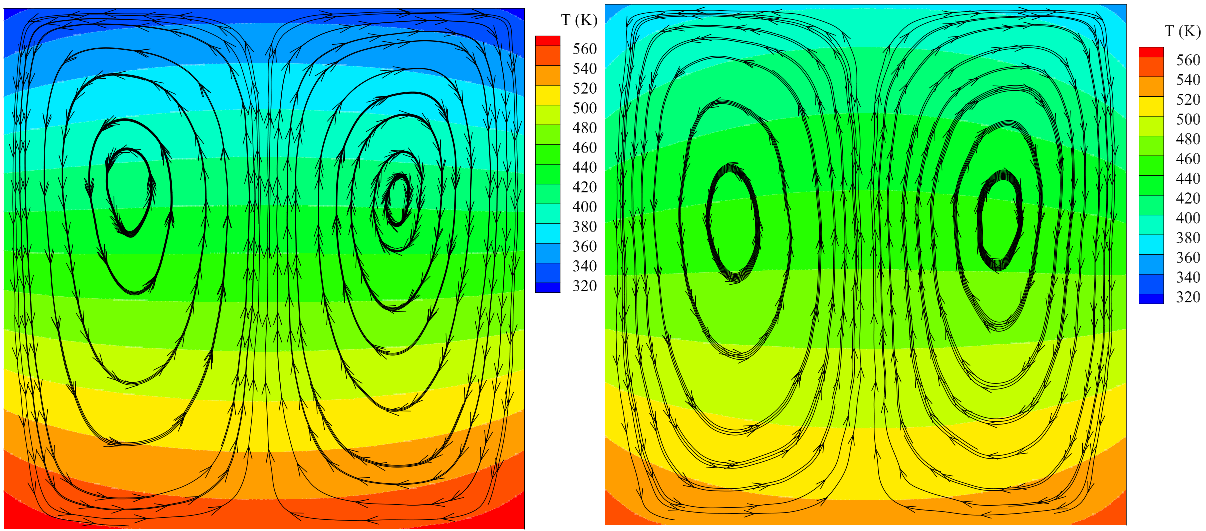

a) Fully diffusive: $\Theta_0 = 1 \quad \alpha = 0$

d) $\Theta_0 = 1 \quad \alpha = 0.2 \quad \gamma = 0.2$

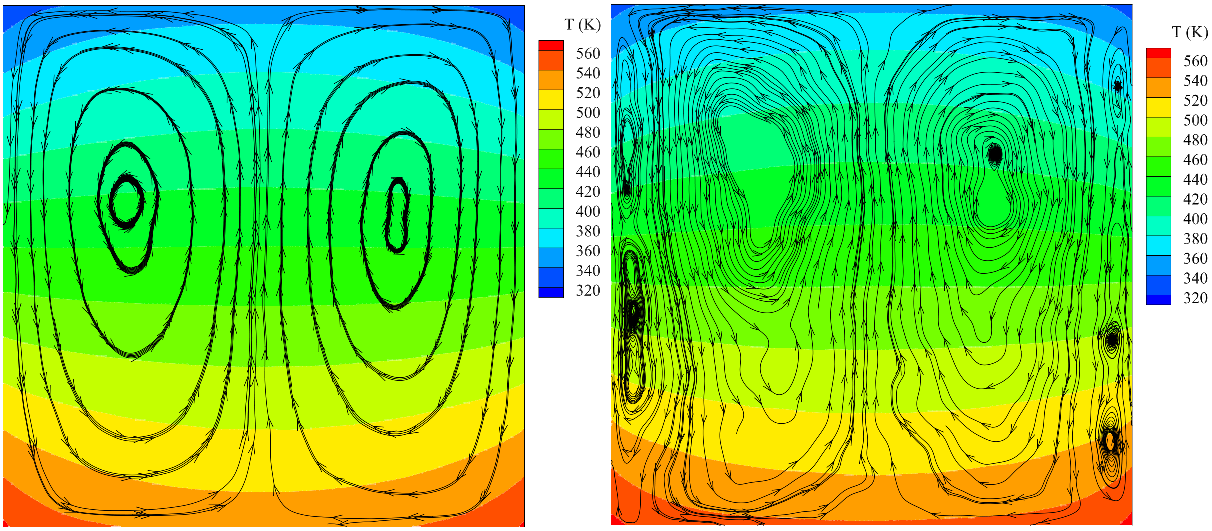

b) $\Theta_0 = 0.7 \quad \alpha = 0 \quad \gamma = 0.2$

e) $\Theta_0 = 1 \quad \alpha = 0.1 \quad \gamma = 0.9$

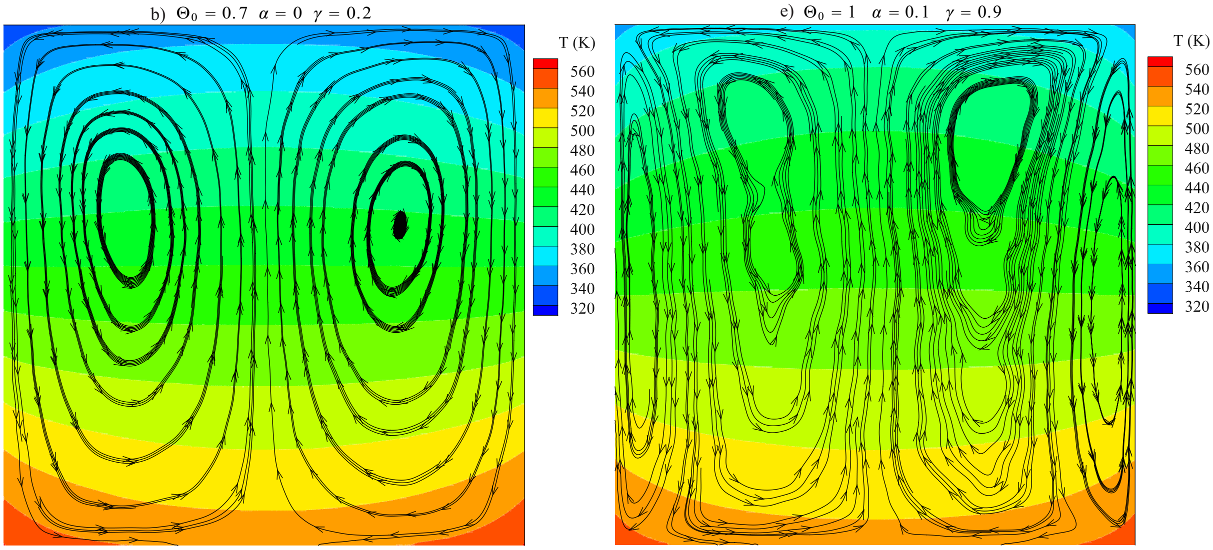

c) $\Theta_0 = 0.7 \quad \alpha = 0 \quad \gamma = 0.9$

f) $\Theta_0 = 1 \quad \alpha = 0.2 \quad \gamma = 0.9$

Figure 5.2: Velocity streamlines overlaid on the temperature distribution, $Kn = 0.1$, $\varepsilon = 0$.

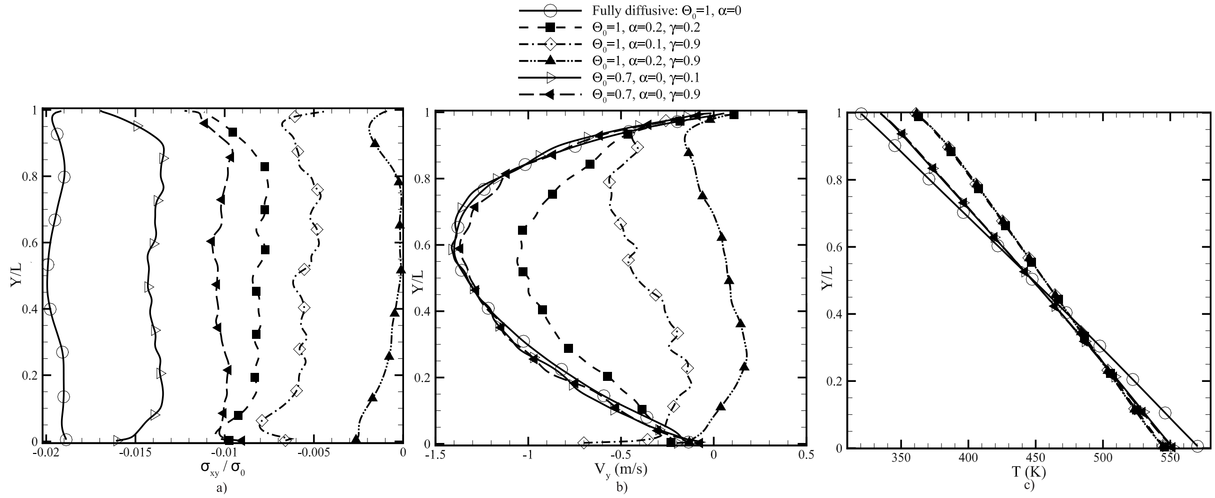

Figure 5.3: The effect of Θ_0, α and γ coefficient on the flow properties along $\frac{X}{L} = 0.95$ for $Kn = 0.1$, $\varepsilon = 0$.

momentum of an incoming particle is transferred to the wall. Since the particle coming from the warmer region has a higher impact velocity, it can induce a greater force on the wall, so that the net force on the wall points toward the colder region, see F_W in Fig. 5.4-a. As a reaction, the wall drives the rarefied flow toward the warmer region by imposing a shear force on the flow, F_G. Consequently, the gas moves in the direction of the wall temperature gradient.

In the VDM boundary condition, as shown in the right figure, a particle with higher velocity c' relative to the surface has a higher chance, $\gamma(1 - \Theta(c'))$, to be specularly reflected, which implies no exchange of tangential momentum. Accordingly, a larger number of slower particles–coming from the colder region–transmit their tangential momentum to the wall, compared to a smaller number of fast particles–coming from the warmer region. As α increases, larger number of particles with high impact velocity skip the thermalization process with the surface, and reflect back to the bulk without any momentum exchange. For relatively large values of α and γ, the colder particles will transfer more tangential momentum than the warmer particles, which results in a net force on the wall toward the warmer region. That is, the force F_W changes its sign as compared to the standard transpiration flow, see Fig. 5.4-b. This leads to the movement of the gas relative to the wall, from warm to cold. It is also worth noting that the magnitude of shear force on flow, F_G, becomes smaller since less momentum is transferred due to more specular reflections.

While the above argument shows the theoretical possibility of inverted transpiration

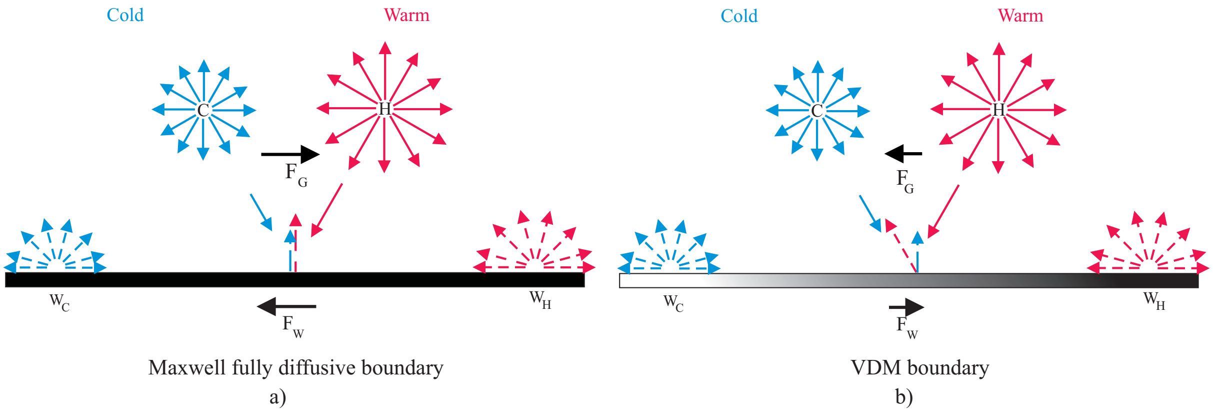

Maxwell fully diffusive boundary
a)

VDM boundary
b)

Figure 5.4: Thermal transpiration effect over the conventional Maxwell and VDM boundary conditions.

flow, it is not clear that the occurrence of the secondary vortices in the VDM model can actually be attributed to this effect. In order to examine the transpiration phenomena on the microscopic level, we used DSMC results to compare the tangential momentum that particles exchange with the right wall of the micro-cavity. We keep the thermal configuration of the cavity as in Sec. 5.4.2, and define the tangential momentum exchange between a particle and the surface as

$$M_j = m\overline{\left(c_t^{'} - c_t\right)_j} \ .$$

Here, $c_t^{'}$ and c_t are the tangential velocities before and after collision with the surface element j, and the overbar indicates the time average of the microscopic quantity. Particles with positive tangential impact velocity, $c_t^{'} > 0$, come from a warmer region (they move upward), i.e., they have larger thermal velocity, and exchange the momentum M_j^H with the surface. Particles with negative tangential impact velocity, $c_t^{'} < 0$ come from the colder region (they move downward) and exchange the momentum M_j^C with the surface. Figure 5.5 shows the variation of exchanged momentum for the VDM boundary condition along the surface. The tangential momenta are non-dimensionalized with respect to $M^0 = m\sqrt{2\frac{k}{m}T_B}$.

As the coefficients α and γ increase, we observe a decrease in the exchanged momentum from both, colder and warmer particles. This result is in accordance with the reduction of shear stress inside the Knudsen layer in Fig. 5.3-a . However, the decrease in the warmer momentum exchange, M_j^H is larger than the decrease in colder exchange M_j^C. For larger α and γ, the warmer particles have a higher chance to be specularly reflected, which implies that no tangential momentum is exchanged with the surface. The total momentum exchange, obtained from adding the two sources of tangential momentum, determines the direction of thermal transpiration force. It is observed that increasing the coefficients in the VDM boundary conditions can reduce the strength of the thermal transpiration effect, and in an extreme case, Fig. 5.5-c, lead to a small reversed transpiration force.

Figure 5.5-b shows that for the case of Fig. 5.2-f where an inverted velocity at the wall is observed, the momentum transfer–and thus the transpiration force–still has the same direction as for the fully diffusive surface, but it is much weaker. Blow-ups of the total momentum exchange are inserted in Fig. 5.5 for a detailed comparison. Hence, we must conclude that in this case the inverted tangential velocity at the wall *cannot* be attributed to the inversion of the transpiration force, but most likely results from a much weaker transpiration force at the boundary, which subsequently leads to domination of thermal

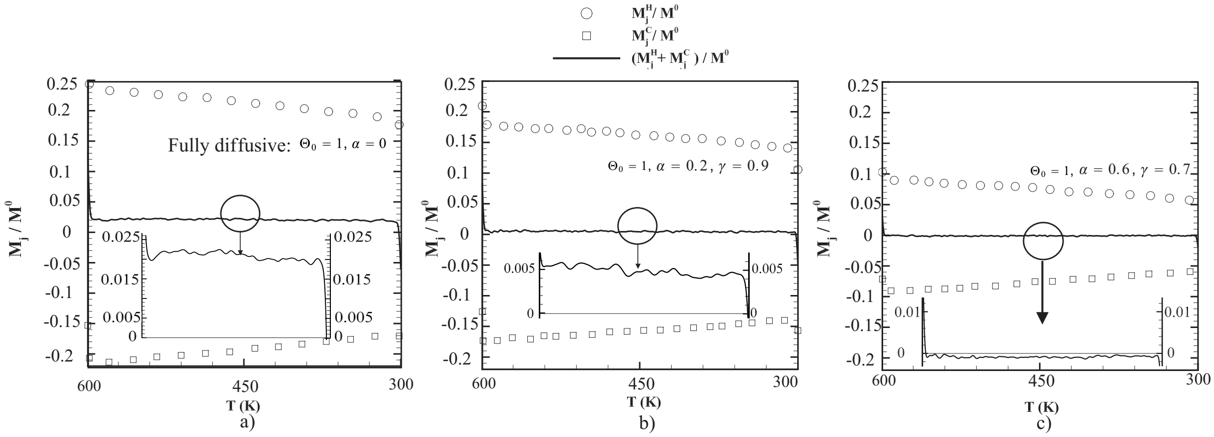

a) b) c)

Figure 5.5: Variation of the tangential momentum exchange on particle-surface level along the right wall for $Kn = 0.1$, $\varepsilon = 0$ and $\Theta_0 = 1$.

stresses in the bulk.

In the original paper [83], the tangential velocity on the boundary is obtained utilizing the first order Chapman-Enskog expansion. Using Bird's notation for the shear stress [5], the tangential velocity was written as

$$\frac{\mathcal{V}_t}{\sqrt{\frac{k}{m}T_W}} = \frac{2-\chi}{\chi}\sqrt{\frac{\pi}{2}}\frac{\sigma_{nt}}{p} - \frac{\omega}{5}\frac{q_t}{p\sqrt{\frac{k}{m}T_W}} \; . \tag{5.9}$$

Here, $\mathcal{V}_t$ is the tangential velocity at the boundary, χ is the momentum accommodation coefficient, p is the pressure and ω is the coefficient for the strength of the thermal transpiration effect. We can see that the interplay between the shear stress σ_{nt} and the tangential heat flux, q_t determines the direction of the tangential velocity close to the surface. Choosing an appropriate set of α and γ in the VDM boundary condition enables us to reduce the influence of thermal transpiration, so that the shear stress dominates in determining the direction of the flow.

The shear stress, in the presence of small velocity and rather large thermal gradient in the flow field, is mainly influenced by the thermal stresses. Using the Grad equations [81] the shear stress in the bulk can be approximated as

$$\sigma_{tn} = \sigma_{tn}^{(1)} + \sigma_{tn}^{(2)} \; , \tag{5.10}$$

where the superscript shows the order in Knudsen number. Following Grad equations for the Maxwell molecule, and linearizing the shear stress in moments (small Knudsen number), we can write

$$\begin{aligned} \sigma_{tn}^{(1)} &= 2\mu \frac{\partial V_{<t}}{\partial x_{n>}} , \\ \sigma_{tn}^{(2)} &= \frac{4}{5}\frac{\mu}{p}\frac{\partial q_{<t}}{\partial x_{n>}} . \end{aligned} \tag{5.11}$$

Grad description for the shear stress shows that the thermal stresses are one order in Knudsen number higher than the viscous stresses. This means that thermal stresses will become important when the rarefaction is large (high Knudsen number regime); or when we are dealing with a flow at low velocity gradient and rather large heat flux gradient.

In order to confirm the role of thermal stresses in our thermal cavity flow, we used the DSMC result to obtain the shear stress in the first and second order, Eq. 5.11, along the horizontal centerline of the cavity. Figure 5.6 shows the total stress, σ_{xy} as well as the viscous $\sigma_{xy}^{(1)}$ and thermal stresses $\sigma_{xy}^{(2)}$ for two choices of boundary condition coefficients. The solid line indicates the variation of the total stress in the horizontal centerline of the cavity. Note that the description of the shear stress in Eq. (5.10) is only valid in the bulk of the flow. When dealing with the Knudsen layer (in the vicinity of the walls) higher order moments can play a role and dominate in determining the shear stress.

For the fully diffusive surface, Fig. 5.6-a, the shear stress starts from a positive value close to the left wall and becomes negative as we pass the center of the cavity. The flow in this case is mainly driven by the boundaries, i.e., thermal transpiration. The tangential transpiration force accelerates the flow in the vicinity of the surface, which subsequently leads to appearance of the largest value of the shear stress at the wall. For the fully diffusive surface the total shear stress, σ_{xy} follows the trend of first order viscous stress $\sigma_{xy}^{(1)}$ in the bulk of the flow, i.e., outside of the Knudsen layer ($\frac{X}{L} \in [0.2, 0.8]$). A quick look at Fig. 5.3-b shows that the rarefied flow gets to its maximum velocity for the case of fully diffusive surface, and slows down for the VDM boundary conditions. This means that the viscous stress can take over the thermal stress, and dominate in determining the total stress for the fully diffusive surface. Figure 5.6-a also shows that the value of thermal stress in this case is very small, and rather close to zero in the main bulk of the flow. In this case it is safe to say that the thermal stresses do not play a big role in determining the shear stress. The imposed disturbance from the boundaries, coming from the thermal transpiration, is damped via the viscous stresses.

In the second case, Fig. 5.6-b, the total shear stress profile is different than what we observed for the fully diffusive surface, and changes sign multiple times along the

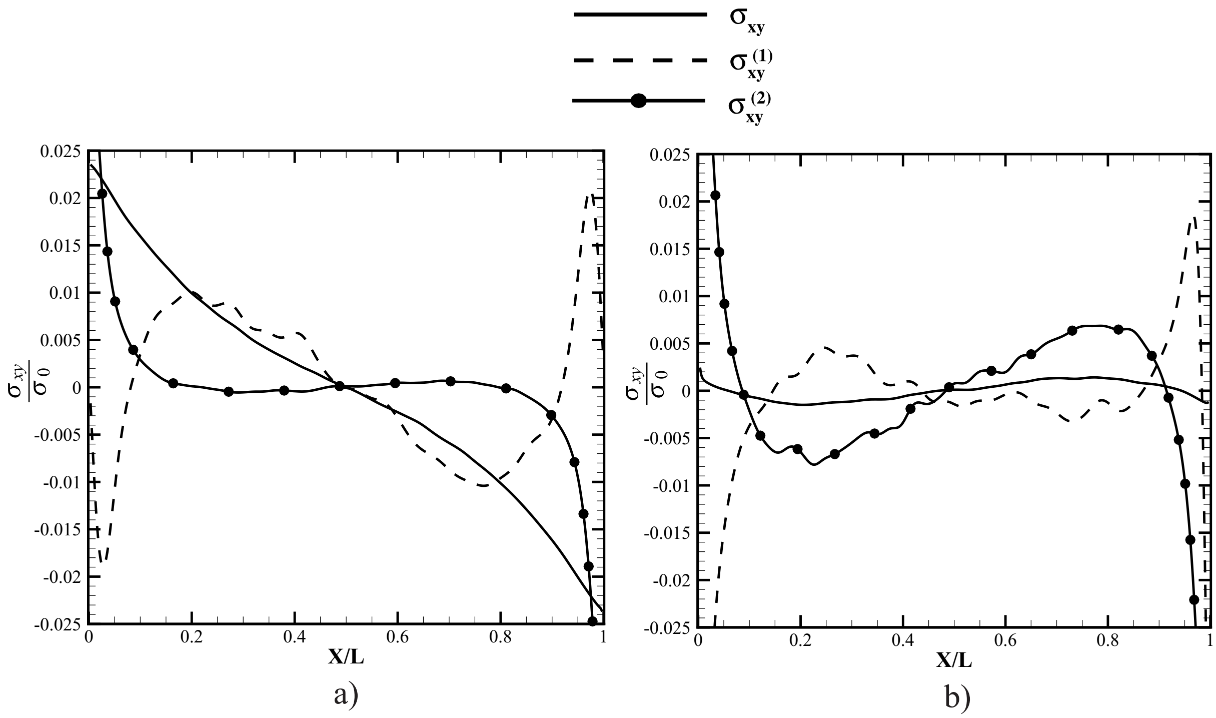

Figure 5.6: Variation of shear stress component along the horizontal centerline of the cavity, a) Fully diffusive surface: $\alpha = 0, \Theta_0 = 1$ b) $\Theta_0 = 1$ $\alpha = 0.2$ $\gamma = 0.9$

horizontal centerline. Interestingly, the shear stress is one order of magnitude smaller in this case. Keeping in mind that the main source of disturbance in the flow field is the temperature gradient on the wall, the VDM boundary condition permits rather large number of particles to reflect back to the bulk without being influenced by the surface, i.e., specular reflection. In addition, the shear stress *does not* follow the trend of the velocity gradient, but rather has the same trend as the thermal stresses. Small values of the velocity, compared to the rather large values of the temperature gradient, in the flow field leads to domination of the thermal stresses in determining the total shear stress. This figure confirms the role of the thermal stresses in the secondary vortices appears in Fig. 5.2-e.

It is also interesting to note that the very small values of the shear stress (close to zero) in this case implies that there is a balance between the thermal stresses and the viscous stress, $\sigma_{tn}^{(1)} = -\sigma_{tn}^{(2)}$. In a way, existence of rather large thermal gradient in the flow field drives the flow, and as a reaction, the viscous stresses damp the rarefied flow movement.

Above, we used the equations that are only valid for evaluating the bulk of the flow. As said above, we believe that in the cases of Fig. 5.2-e,f the main driving force for the flow pattern are thermal stresses in the bulk–the secondary vortices most likely appear to bridge between the temperature driven bulk flow, and the boundaries.

5.4.4 Effect of Knudsen number

Following the discussion about the interplay between the first and second order of shear stress, and the capability of the VDM boundary conditions to manipulate their strength, we studied the effect of Knudsen number on the flow formation in the thermal cavity. To have a comparable set, we chose $Kn = 1$ and consider the same values of α and γ as in Sec. 5.4.2. Figure 5.7 shows the temperature distribution overlaid on the velocity streamlines inside the cavity. As was expected, rarefied flow experiences rather smaller temperature gradients in higher Knudsen regime, which is attributed to the larger temperature jump at this Knudsen number.

More interestingly, the vortex formation is different from what we observed at $Kn = 0.1$. Even for the fully diffusive surface, the secondary vortex in the vicinity of the side walls appears, and drives the flow from warm-to-cold. At this Knudsen number the Knudsen layer covers the entire cavity, and large rarefaction effects inside the domain leads to a large secondary vortex in the flow field. As we increase α the primary vortex,

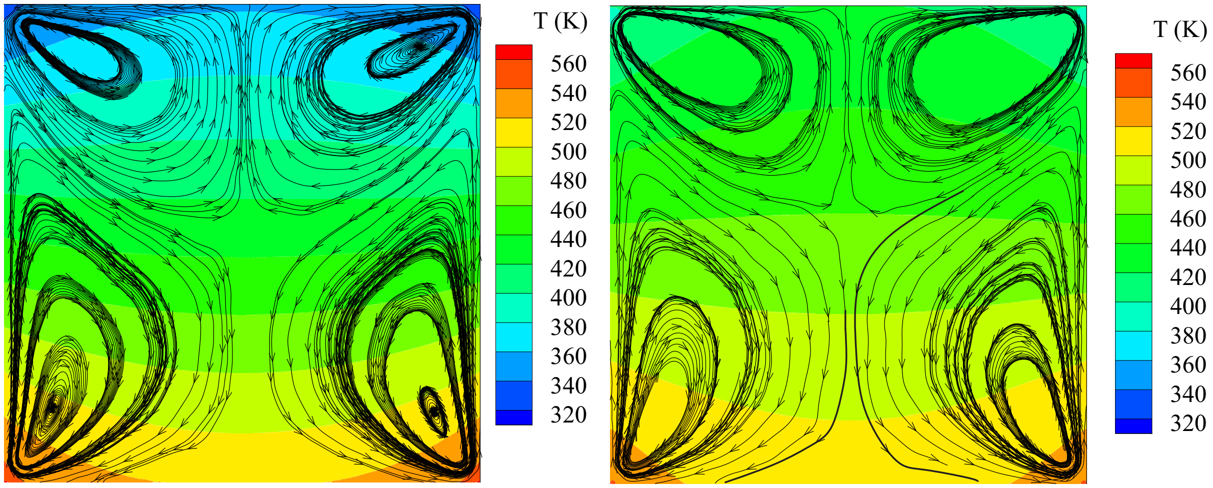

a) Fully diffusive: $\Theta_0 = 1 \quad \alpha = 0$

b) $\Theta_0 = 1 \quad \alpha = 0.2 \quad \gamma = 0.2$

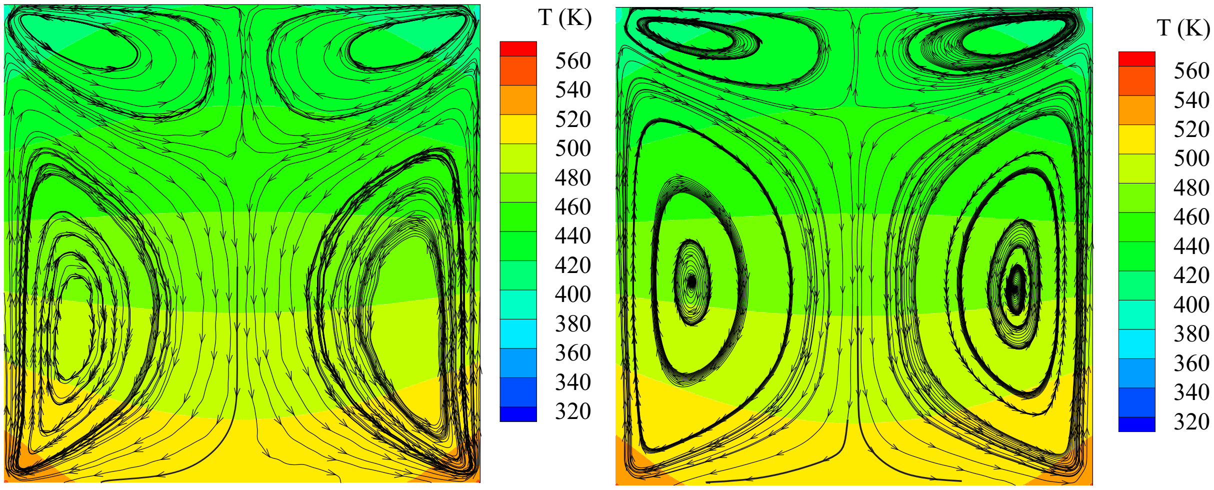

c) $\Theta_0 = 1 \quad \alpha = 0.1 \quad \gamma = 0.9$

d) $\Theta_0 = 1 \quad \alpha = 0.2 \quad \gamma = 0.9$

Figure 5.7: Temperature distribution overlaid on the velocity streamlines at $Kn = 1$ and $\varepsilon = 0$

corresponding to the thermal transpiration, decreases in size and get pushed to the top corners of the cavity.

Figure 5.8 shows the flow properties in the vicinity of the right wall along $\frac{X}{L} = 0.95$. It is seen that the vertical velocity close to the wall is changing sign for all choices of α and γ, which is in accordance with the appearance of primary and secondary vortices in Fig. 5.7 . More interestingly, the larger positive value of the vertical velocity, i.e., warm-to-cold flow at $Kn = 1$ implies the rarefaction nature of the secondary vortex. The temperature profile close to the surface remains unchanged with respect to the corresponding coefficients in the VDM boundary conditions.

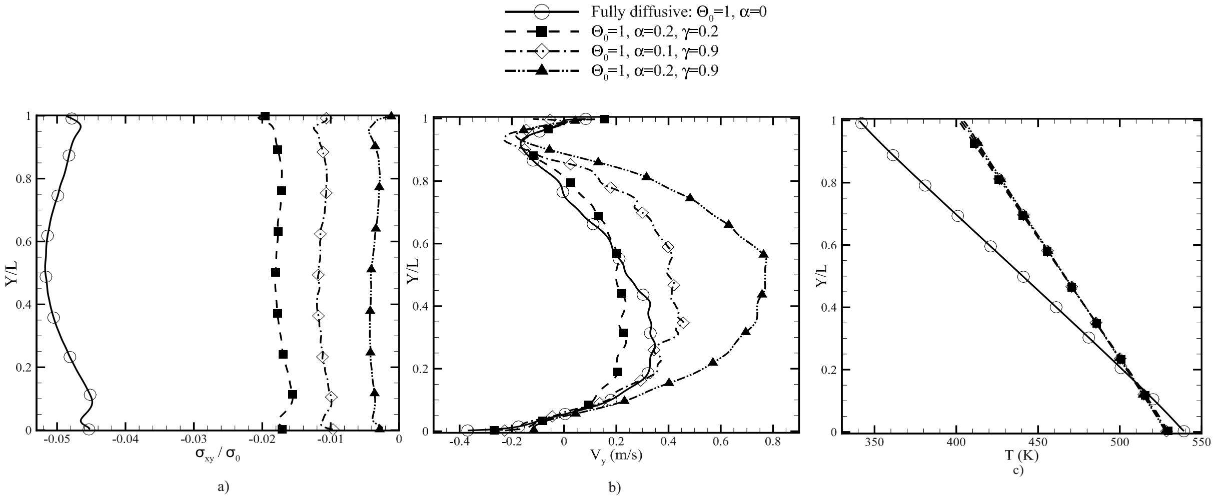

Figure 5.8: The effect of α and γ on the flow properties along $\frac{X}{L}$ = 0.95 for Kn = 1, ε = 0.

5.5 Conclusions

Velocity dependent Maxwell (VDM) boundary conditions are used in DSMC method to study the thermal transpiration effect. The flow formation inside a micro-cavity with the temperature gradient on the surface is studied. Thermal transpiration phenomena drives the rarefied flow from colder region toward the warmer region for the fully diffusive surface. However, as the reflection kernel becomes dependent on the velocity of colliding particle to the surface, thermal transpiration becomes smaller in value. Particles with larger velocity (coming from the warm region) reflect back to the flow without being thermalized with the surface, while the slower particle (coming from the colder region) thermalize with the surface. As a result, using the VDM boundary condition, we can decrease/increase the strength of the thermal transpiration effect. This argument theoretically suggest the possibility of appearance of reversed thermal transpiration effect which drives the rarefied flow from warmer toward colder region. We observed the appearance of warm-to-cold vortices for certain choices of corresponding coefficients in the VDM boundary condition, and used DSMC to investigate their nature. Our study attributes the emerging warm-to-cold vortices to the thermal stresses in the bulk of the flow. In fact, the VDM boundary condition weakens the thermal transpiration effect, and subsequently permits the thermal stresses to dominate in determining the direction of the rarefied flow.

In classical hydrodynamics, transpiration flow is described by incorporating the wall temperature gradient as a driving force into the slip boundary condition. The DSMC simulations in the current study, show the inverted flow direction only at the boundary, while large vortices appear in the bulk. This flow behavior, most likely, is due to thermal stresses in the bulk, which cannot be described in classical hydrodynamics. Therefore, kinetic theory methods, like DSMC, direct numerical simulation[63], or advanced moment methods [90] must be used for the description, and understanding, of these flows. The VDM model is flexible, and can be incorporated in any of these advanced methods.

We note the lack of reliable experimental data that would be needed to fit the coefficients of the model.

Acknowledgement

The authors would like to sincerely thank Professor Stefan Stefanov and Ehsan Roohi for their fruitful comments on this work. This research was supported by the Natural Sciences and Engineering Council (NSERC).

Chapter 6

Thermal Stress vs. Thermal Transpiration: A Competition in Thermally Driven Cavity Flows

Abstract: *The velocity dependent Maxwell (VDM) model for the boundary condition of a rarefied gas, recently presented by Struchtrup [Phys. Fluids* ***25****, 112001 (2013)], provides the opportunity to control the strength of the thermal transpiration force at a wall with temperature gradient. Molecular simulations of a heated cavity with varying parameters show intricate flow patterns for weak, or inverted transpiration force. Microscopic and macroscopic transport equations for rarefied gases are solved to study the flow patterns, and identify the main driving forces for the flow. It turns out that the patterns arise from a competition between thermal transpiration force at the boundary, and thermal stresses in the bulk.*

Published in Physics of Fluids **27** (2015), 112001

6.1 Introduction

The behavior of rarefied gases differs from the predictions of classical hydrodynamics in many ways [10, 12, 77, 5, 81]. When the Knudsen number $\mathrm{Kn} = \lambda/L$, defined as the ratio of mean free path λ and macroscopic relevant length scale L, is sufficiently small, classical hydrodynamics prevails, with well known effects such as stresses caused by velocity gradients, as expressed in the Navier-Stokes law, and heat flux caused by temperature gradients, as expressed in Fourier's law. When, however, the Knudsen number becomes larger, so-called rarefaction effects influence the flow, such as heat flux not driven by a temperature gradient, but by gradients of stresses, and *thermal stresses* caused not by velocity gradients, but by gradients of heat flux [45, 7, 102, 69].

Moreover, also the interaction between gas and solid boundaries depends on the degree of rarefaction. In classical hydrodynamics, one commonly assumes no-slip-no-jump boundary conditions, where the gas at the wall assumes velocity and temperature of the wall. Rarefaction leads to deviation of this behavior, so that the gas experiences velocity slip and temperature jump at the wall [10, 77, 81]. A particularly interesting boundary effect is *transpiration flow* (also known as thermal creep flow), [77, 73, 46, 68] where velocity slip is induced by a temperature gradient in the wall, i.e., the gas is forced into motion at the boundary. Based on this effect, small amounts of gas can be moved in Knudsen pumps[2]. The interplay between the thermal stress and the thermal transpiration, and their contribution to the slip velocity has been studied using the asymptotic theory [76, 79, 3].

A rarefied gas may be subjected to *two* different thermal forces: (a) a transpiration force due to a temperature gradient in the wall, (b) thermal stresses, due to temperature gradients in the bulk of the gas. These two forces might be acting in the same direction, hence amplifying each other, or they might be acting against each other. In the following, we will examine both cases, based on a recently presented microscopic model for wall boundary conditions that allows to control the strength and direction of transpiration flow[83]. Specifically, we shall consider a gas confined in a closed cavity with temperature gradients in the walls that induce transpiration flow, and simultaneously cause a temperature profile in the bulk that induces thermal stresses. Simulations are performed with the direct simulation Monte Carlo method, which provides a microscopic solution, and with various macroscopic models, such as Navier-Stokes-Fourier equations, and the regularized 13 moment (R13) equations.

The direct simulation Monte Carlo method (DSMC) is a particle based microscopic method for solving the Boltzmann equation [5, 97, 33]. While it provides accurate solutions, it is numerically costly, but it does not give further insight into the observations. The DSMC method allows to determine macroscopic quantities such as temperature, velocity, stress and heat flux, but it is, e.g., unable to distinguish between frictional and thermal contributions to stress.

Macroscopic methods derive equations directly for the macroscopic quantities, and relations between, e.g., stress and gradients of velocity and heat flux are directly present in the equations. As will be demonstrated below, this allows a deeper understanding and analysis of the observed flow patterns, i.e., between cause and effect.

Three different macroscopic models will be used for simulation and discussion: (a) the Navier-Stokes-Fourier (NSF) equations of classical hydrodynamics[10, 12, 77, 5, 81]; (b) equations for slow non-isothermal flow (SNIF) which add thermal stresses to NSF[45, 7, 82]; (c) the regularized 13 moment equations (R13) which give a further extension to hydrodynamics incl. coupling between temperature, velocity, stress and heat flux in the bulk, as well as a reasonable approximation to the Knudsen layers at walls[81, 85, 87, 88, 93].

The three sets of equations can be found as approximations of the Boltzmann equation, based on suitable expansions in the Knudsen and Mach numbers. The NSF equations arise as the *first* order approximation in Kn, the SNIF equations are a reduced *second* order approximation in Kn for small Mach numbers, and the R13 equations are a full *third* order approximation in Kn for arbitrary Mach numbers.

The jump and slip boundary conditions for the macroscopic sets are derived from the boundary condition for the Boltzmann equation with the reflection kernel for velocity dependent accommodation model (VDM) presented in Ref. [83], which allows to influence the strength and direction of the transpiration force. This reflection kernel is a generalization of Maxwell's accommodation model[51] with velocity dependent accommodation coefficients. Although the Cercignani-Lampis-Lord model [11, 48] improved the simplicity in the original Maxwell model, by providing two different coefficients to fit to the slip velocity and temperature jump, it does not allow to vary the strength of the transpiration force [72]. The VDM model, on the other hand, provides sufficient flexibility to be fitted to the data for thermal transpiration coefficient.

In Ref. [60] the VDM boundary condition has been incorporated in the DSMC method, and was used to simulate the flow formation in a cavity with temperature gradient on the surface in the early transition regime. While using the Maxwell fully diffusive surface resulted in only two large transpiration vortices in the flow field, we observed that certain sets of coefficients in the VDM boundary conditions can lead to appearance of secondary vortices in front of the walls. However, with only a DSMC solution at hand, we could only speculate on the origin of the observed flow patterns as being an interplay between thermal stresses and transpiration forces.

In the current study we employ the VDM model to obtain the macroscopic boundary equations for the NSF, SNIF and R13 equations, which simplify to the conventional boundary conditions for the Maxwell model in the case of vanishing velocity dependency on the reflection kernel. Then, we use the DSMC, R13, SNIF and NSF equations to study the flow formation inside a cavity with temperature gradient on the surface. Analysis of the results obtained from the macroscopic equations allows us to understand the flow patterns from the interplay between transpiration forces and thermal stresses. In particular it becomes clear that for inverted transpiration force the narrow vortex in the Knudsen layer at the wall is driven by the transpiration force while the larger vortex in the bulk is driven by thermal stresses. NSF cannot describe this behavior, since it cannot account for thermal stresses, and SNIF cannot describe vortex at the wall, since it cannot describe Knudsen layer effects. The R13 equations give a good approximation to the DSMC results and allow to analyze the flow pattern as the result of the competition between thermal stresses and transpiration flow. The VDM boundary conditions permits manipulating the strength of the thermal transpiration process, which subsequently provides a room for the thermal stresses to play a bigger role in determining the flow formation. Although the flow is in the mid-slip regime, our simulation reveals that the Knudsen layer terms are required to accurately model the DSMC results with a set of macroscopic equations.

6.2 Microscopic description

6.2.1 Distribution function and Boltzmann equation

In kinetic theory the state of a monatomic gas is described by the distribution function, $f\left(t,x_i,c_i\right)$, defined such that the number of particles in a phase space element $d\mathbf{x}d\mathbf{c}$ at time t is given by $fd\mathbf{x}d\mathbf{c}$, where c_k is the particle velocity, and x_i is the location in space. The Boltzmann equation relates the time evolution of the distribution function to the translation and collision of the particles in the gas as [12, 10]

$$\frac{\partial f}{\partial t}+c_k\frac{\partial f}{\partial x_k}=\mathcal{S}\left(f,f\right)\ , \tag{6.1}$$

where we ignored external body forces, and $\mathcal{S}(f,f)$ is the collision term.

Macroscopic properties of the gas are moments of the distribution function. In particular, mass density ρ, velocity v_i, temperature T, shear stress σ_{ij} and heat flux q_i are given by

$$\begin{aligned} \rho &= m\int f d\mathbf{c} \ , \ \ v_i = \frac{m}{\rho}\int c_i f d\mathbf{c} \ , \ \ 3RT = \frac{m}{\rho}\int C^2 f d\mathbf{c} \ , \\ \sigma_{ij} &= m\int C_{\langle i}C_{j\rangle} f d\mathbf{c} \ , \ \ 2q_i = m\int C_i C^2 f d\mathbf{c} \ , \end{aligned} \tag{6.2}$$

where the integration is performed over the velocity space $\mathbf{c}$ and m denotes the mass of a particle, R is the specific gas constant and $C_i = c_i - v_i$ is the peculiar velocity of the gas particles.

6.2.2 Boundary conditions

In order to describe the gas-surface behavior we need the distribution function at an infinitesimal neighborhood of the wall, which in the rest frame of the wall reads

$$\bar{f} = \begin{cases} f^*(c_i, x_i, t), & c_k^W n_k \geq 0 \\ f(c_i, x_i, t), & c_k^W n_k \leq 0. \end{cases} \tag{6.3}$$

Here, the phase density of particles leaving the wall ($c_k^W n_k \geq 0$) is expressed through the reflection kernel $\mathcal{P}$ as

$$f^* = \frac{1}{|c_n|}\int_{c_n^W<0} f\left(c_k^{'}\right)\mathcal{P}\left(c_k^{\prime} \to c_k\right)\left|c_n^{\prime}\right| d\mathbf{c}^{\prime} \ . \tag{6.4}$$

In the velocity dependent Maxwell boundary condition, the reflection kernel is a superposition of diffusive reflection, specular reflection and isotropic scattering, [83]

$$\begin{aligned} \mathcal{P}\left(\mathbf{c}^{'} \to \mathbf{c}\right) = \Theta\left(c^{'}\right)\frac{|c_n|\exp\left(-\frac{mc^2}{2kT}\right)\Theta(c)}{\int\limits_{c_n>0}|c_n|\exp\left(-\frac{mc^2}{2kT}\right)\Theta(c)\,d\mathbf{c}} + \left(1-\Theta\left(c^{'}\right)\right) \\ \left[\gamma\delta\left(c_k^{'} - c_k + 2n_j c_j n_k\right) + (1-\gamma)\frac{1}{\pi}\frac{|c_n|}{c^{'3}}\delta\left(c^{'} - c\right)\right] \ . \end{aligned} \tag{6.5}$$

Here, the particles colliding with and being reflected from the surface have the velocities $c_k^{\prime}$ and c_k, respectively. The normal component of the velocity to the surface is denoted by $c_n = c_k n_k$, and c is the absolute value of the particle velocity. The velocity dependent accommodation coefficient $\Theta\left(c^{'}\right)$ is the probability that a colliding particle will have a thermalizing collision. Moreover, $\left(1 - \Theta\left(c^{'}\right)\right)\gamma$ is the probability that the incoming particle will be specularly reflected.

Many meaningful models for the coefficients $\Theta(c')$ and γ can be developed[21]. We follow the model suggested in Ref. [83], where $\gamma = const$ and the thermalization is assumed as a thermally activated process

$$\Theta\left(c^{'}\right) = \Theta_0 \exp\left(\frac{\varepsilon - \alpha\frac{m}{2}c^{'2}}{kT_W}\right) = \Theta_0\left(T_W\right)\exp\left(\frac{-\alpha\frac{m}{2}c^{'2}}{kT_W}\right) . \tag{6.6}$$

In this relation the strength of the activation process is denoted by the non-dimensional coefficient α. Moreover, ϵ considers the effect of energy bounce on the reflected particle, and Θ_0 is a constant depending on the wall structure. This model reduces to the original Maxwell model, when there is no activation process and no energy bounce, i.e., for $\alpha = \epsilon = 0$. The three independent coefficients in the VDM model, i.e., α, γ and $\Theta = \Theta_0 \exp\left(\frac{\varepsilon}{kT_W}\right)$, can be used to fit to the experimental results[83]. In the current study, we set $\Theta = 1$, and explore the influence of the coefficients α and γ.

6.2.3 DSMC Method

The DSMC method is a statistical particle method for the solution of the Boltzmann equation; each simulating particle represents a large number of real gas molecules [5]. Due to its statistical nature, the DSMC method requires large computational overhead, especially when the average flow velocity is small, but the results are highly accurate. We have presented an implementation of the VDM boundary conditions for DSMC in Ref. [60], where we also studied the influence of the boundary coefficients α and γ on the flow pattern in a heated cavity. The flow patterns observed and discussed there are the same as those discussed below, albeit for different Knudsen numbers. In Ref. [60] we tried to explain the observation by means of macroscopic quantities, in particular thermal stresses, but the arguments were not conclusive. Therefore, we now proceed by solving the the problem with various sets of macroscopic transport equations, which will allow us to understand the flow details better.

6.3 Macroscopic transport equations

The macroscopic description of rarefied flows requires models that go beyond the Navier-Stokes-Fourier (NSF) equations of classical hydrodynamics. In recent years we have had good success with describing rarefied flows at moderate Knudsen numbers by the R13 equations, which we will use here as well. We also will consider the NSF equations with jump and slip boundary conditions, and an extension of the latter which includes thermal stresses and is appropriate for slow non-isothermal flows (SNIF).

All models are based on the conservation laws for mass, momentum, and energy, but use different equations for stress σ_{ij} and heat flux q_i. The conservation laws read

$$\begin{aligned} \frac{D\rho}{Dt} + \rho\frac{\partial v_k}{\partial x_k} &= 0\ , \\ \rho\frac{Dv_i}{Dt} + \frac{\partial p}{\partial x_i} + \frac{\partial \sigma_{ik}}{\partial x_k} &= 0\ , \\ \frac{3}{2}\rho\frac{D\theta}{Dt} + \left(p\,\delta_{ij} + \sigma_{ij}\right)\frac{\partial v_i}{\partial x_j} + \frac{\partial q_k}{\partial x_k} &= 0\ , \end{aligned} \tag{6.7}$$

where $\frac{D}{Dt} = \frac{\partial}{\partial t} + v_k \frac{\partial}{\partial x_k}$ is the convective derivative, $p = \rho RT = \rho\theta$ is the pressure obeying the ideal gases law, and $\theta = RT$ is the temperature in units of specific energy.

6.3.1 R13 equations

In the R13 equations, stress σ_{ij} and heat flux q_k are considered as flow variables with their own balance equations, which read for Maxwell molecules [85, 84, 81, 69],

$$\frac{D\sigma_{ij}}{Dt} + \underline{\underline{\frac{4}{5}\frac{\partial q_{\langle i}}{\partial x_{j\rangle}}}} + \sigma_{ij}\frac{\partial v_k}{\partial x_k} + 2\sigma_{k\langle i}\frac{\partial v_{j\rangle}}{\partial x_k} + \frac{\partial m_{ijk}}{\partial x_k} = -\frac{\rho\theta}{\mu}\left(\underline{2\mu\frac{\partial v_{\langle i}}{\partial x_{j\rangle}} + \sigma_{ij}}\right)\ , \tag{6.8}$$

$$\begin{aligned} \frac{Dq_i}{Dt} + \frac{5}{2}\sigma_{ik}\frac{\partial\theta}{\partial x_k} - \frac{\theta\sigma_{ik}}{\rho}\frac{\partial\rho}{\partial x_k} - \frac{\sigma_{ik}}{\rho}\frac{\partial\sigma_{kl}}{\partial x_l} + \theta\frac{\partial\sigma_{ik}}{\partial x_k} + \frac{7}{5}\left(q_k\frac{\partial v_i}{\partial x_k} + q_i\frac{\partial v_k}{\partial x_k}\right) \\ + \frac{2}{5}q_k\frac{\partial v_k}{\partial x_i} + \frac{1}{6}\frac{\partial\Delta}{\partial x_i} + \frac{1}{2}\frac{\partial R_{ik}}{\partial x_k} + m_{ijk}\frac{\partial v_j}{\partial x_k} = -\frac{2}{3}\frac{\rho\theta}{\mu}\left(\underline{\frac{15}{4}\mu\frac{\partial\theta}{\partial x_i} + q_i}\right)\ . \end{aligned} \tag{6.9}$$

Indices inside angular brackets denote the symmetric trace-free part of tensors,[81]. The coefficients ($\frac{4}{5}$, 1, 2, ...) are valid for the Maxwell molecules. The R13 equations for other molecule types were derived in Ref. [88], where the method is outlined and coefficients are given for hard sphere molecules. Here, we are interested in comparing the thermal stress and thermal transpiration, and used the R13 equations in their most convenient form, which is for Maxwell molecules. In the equations above, $\mu = \mu_0 \frac{\theta}{\theta_0}$ is the shear viscosity with μ_0 is viscosity at a reference temperature θ_0. The underlined terms in the equations will be discussed in subsequent sections. The balance equations (6.8, 6.9) contain the higher moments m_{ijk}, Δ, R_{ij} which are given by the constitutive equations[69]

$$\begin{aligned}
\Delta &= 5\frac{\sigma_{kl}\sigma_{kl}}{\rho} + \frac{56}{5}\frac{q_k q_k}{p} - 12\mu\left(\theta\frac{\partial\left(q_k/p\right)}{\partial x_k}\right) , \\
R_{ij} &= \frac{20}{7}\frac{\sigma_{k\langle i}\sigma_{j\rangle k}}{\rho} + \frac{192}{75}\frac{q_{\langle i}q_{j\rangle}}{p} - \frac{24}{5}\mu\left(\theta\frac{\partial\left(q_{\langle i}/p\right)}{\partial x_{j\rangle}}\right) , \qquad (6.10) \\
m_{ijk} &= \frac{20}{15}\frac{q_{\langle i}\sigma_{jk\rangle}}{p} - 2\mu\left(\theta\frac{\partial\left(\sigma_{\langle ij}/p\right)}{\partial x_{k\rangle}}\right) .
\end{aligned}$$

The R13 equations are an extension of the well-known 13 moment equations of Grad[26], where these higher order moments vanish, $R_{ij} = m_{ijk} = \Delta = 0$. These higher order terms are obtained by the regularization technique in the R13 set, and the analysis of the R13 equations show that these contributions are directly linked to the occurrence of Knudsen layers. By means of the Chapman-Enskog expansion it can be shown that the R13 equations are of third order accuracy in terms of the Knudsen number[85, 81]. We point out that over the years our work produced subtle changes in the above constitutive equations; the form presented above was derived in Ref. [69] based on the requirement that the full non-linear and linearized forms of the R13 equations require the same set of boundary equations.

6.3.2 SNIF equations

The equations for slow non-isothermal flow can be obtained from a reduction of the R13 equations which considers Knudsen number and Mach number as scaling parameters. This scaling is appropriate for small velocity with rather large temperature gradients[7], where the Knudsen number has the same order as the Mach number [82]. After the scaling, only the single and double underlined terms in the R13 equations (6.8, 6.9) remain, so that stress and heat flux are given by [82]

$$\sigma_{ij} = -2\mu\frac{\partial v_{\langle i}}{\partial x_{j\rangle}} - \frac{4}{5}\frac{\mu}{p}\frac{\partial q_{\langle i}}{\partial x_{j\rangle}} = -2\mu\frac{\partial v_{\langle i}}{\partial x_{j\rangle}} + \frac{3\mu^2}{p}\left[\frac{\partial^2\theta}{\partial x_{\langle i}\partial x_{j\rangle}} + \frac{1}{\theta}\frac{\partial\theta}{\partial x_{\langle i}}\frac{\partial\theta}{\partial x_{j\rangle}}\right] , \tag{6.11}$$

$$q_i = -\frac{15}{4}\mu\frac{\partial\theta}{\partial x_i} . \tag{6.12}$$

Here, the heat flux (6.12) is given by Fourier's law, while the stress differs from NSF. The first term in the right hand side of Eq. (6.11) is the viscous stress, i.e., the Navier-Stokes relation, and the second term describes the thermal stress.

6.3.3 NSF equations

For the laws of classical hydrodynamics, only first order terms in the Knudsen number are considered, while the Mach number is not restricted[12, 81]. In this scaling, the thermal stresses are not considered, and stress and heat flux are given by the single-underlined terms in (6.8, 6.9), i.e., the Navier-Stokes relation and Fourier's law,

$$\sigma_{ij} = -2\mu\frac{\partial v_{\langle i}}{\partial x_{j\rangle}} \quad , \quad q_i = -\frac{15}{4}\mu\frac{\partial\theta}{\partial x_i} \quad . \tag{6.13}$$

6.3.4 Macroscopic boundary conditions

For the solution of boundary value problems with the macroscopic models (R13, SNIF, NSF) we require macroscopic boundary conditions that must be derived from the microscopic boundary condition, Eq. (6.3). For this we follow the method outlined in Refs. [26, 93]. Considering the continuity of the normal flux of a microscopic property Ψ_A over an infinitesimal surface element δA, gives (as seen from the rest frame of the wall)

$$m\int \Psi_A c_k n_k \, f \, d\mathbf{c}\delta A = m\int \Psi_A c_k n_k \, \bar{f} \, d\mathbf{c}\delta A , \tag{6.14}$$

where Ψ_A are suitable polynomials of the particle velocity, c_i. Performing the integration in the above equation provides a relation between the wall properties (θ_W, v_i^W) and the moments in the gas, that serve as the boundary conditions for moments.

The integration in Eq. (6.14) requires an expression of the distribution function f in terms of the variables, which for the R13 system is a Grad-type distribution of the form[81]

$$f_{R13} = f_M(1 + \Phi) . \tag{6.15}$$

Here, $f_M = \frac{\rho/m}{\sqrt{2\pi\theta}^3}\exp\left[-\frac{C^2}{2\theta}\right]$ denotes the local Maxwellian, and

$$\Phi = \left(\frac{1}{8} - \frac{C^2}{12\theta} + \frac{C^4}{120\theta^2}\right)\frac{\Delta}{\rho\theta^2} + \frac{C_{\langle i}C_{j\rangle}}{2\rho\theta^2}\sigma_{ij} - \frac{1}{\rho\theta^2}\left(1 - \frac{C^2}{5\theta}\right)C_j q_j$$
$$+\frac{C_{\langle i}C_j C_{k\rangle}}{6\rho\theta^3}m_{ijk} - \frac{1}{4\rho\theta^3}\left(1 - \frac{C^2}{7\theta}\right)C_{\langle i}C_{j\rangle}R_{ij} \ .$$

Note that in the rest frame of the wall the peculiar velocities are given by $C_k = c_k - \mathcal{V}_i$, where $\mathcal{V}_i = v_k - v_k^W$ is the slip velocity.

The appropriate velocity functions Ψ_A in Eq. (6.14) are chosen based on Grad's observation[26], that meaningful boundary conditions are obtained when the velocity function Ψ_A is even in the normal component of the particle velocity $c_k n_k$. The appropriate functions for the R13 equations are, for a wall with the normal in the y-direction[93],

$$\Psi_A = \left\{1, C_x, C^2, C_y C_y, C_x C_x, C^2 C_x\right\} \ . \tag{6.16}$$

R13 boundary equations

Using Eq. (6.15) for the distribution function, and performing the integration in Eq. (6.14) for the corresponding VDM distribution function leads to a complete set of jump and slip boundary conditions for the R13 equations. The dependence of the wall kernel (6.5) on velocity leads to a coupling of boundary conditions. For instance, the two boundary conditions for $\Psi_A c_n = C_x c_y$ and $\Psi_A c_n = C^2 C_x c_y$ both contain the shear stress σ_{xy} and the higher moment R_{xy}. In order to have unique boundary conditions for σ_{xy} also for the reduced models, we de-coupled the two conditions such that we have separate boundary conditions for σ_{xy} and R_{xy}. In the same manner, we had to de-couple the boundary conditions for q_y and m_{yyy}. After decoupling, the boundary conditions can be written as (with $\mathcal{T} = \theta - \theta_w$)

$$\begin{aligned}
\mathcal{V}_y &= 0\ , \\
\sigma_{xy} &= \sqrt{\frac{2}{\pi\theta}}\left(-\lambda_{(1,1)}p\mathcal{V}_x - \frac{1}{5}\lambda_{(1,2)}q_x - \frac{1}{2}\lambda_{(1,3)}m_{xyy}\right)n_y\ , \\
q_y &= \sqrt{\frac{2}{\pi\theta}}\left(-\lambda_{(2,1)}\left(2p\mathcal{T}+\frac{1}{2}\theta\sigma_{yy}\right) - \frac{1}{15}\lambda_{(2,2)}\Delta - \frac{5}{28}\lambda_{(2,3)}R_{yy}\right)n_y\ , \\
R_{xy} &= \sqrt{\frac{2}{\pi\theta}}\left(\lambda_{(3,1)}p\theta\mathcal{V}_x - \frac{11}{5}\lambda_{(3,2)}\theta q_x - \frac{1}{2}\lambda_{(3,3)}\theta m_{xyy}\right)n_y\ , \\
m_{xxy} &= \sqrt{\frac{2}{\pi\theta}}\left(-\frac{1}{14}\hat{\lambda}_{(4,1)}R_{xx} - \frac{1}{14}\lambda_{(4,2)}R_{yy} - \lambda_{(4,3)}\theta\sigma_{xx} + \frac{1}{5}\lambda_{(4,4)}\theta\sigma_{yy} - \frac{1}{5}\lambda_{(4,5)}p\mathcal{T} - \frac{1}{150}\lambda_{(4,6)}\Delta\right)n_y\ , \\
m_{yyy} &= \sqrt{\frac{2}{\pi\theta}}\left(\frac{2}{5}\lambda_{(5,1)}p\mathcal{T} - \frac{7}{5}\lambda_{(5,2)}\theta\sigma_{yy} + \frac{1}{75}\lambda_{(5,3)}\Delta - \frac{1}{14}\lambda_{(5,4)}R_{yy}\right)n_y\ .
\end{aligned} \tag{6.17}$$

The above boundary conditions are linearized in the non-equilibrium quantities $\{\mathcal{V}_x, \mathcal{T}, \sigma_{ij}, q_i, \Delta, R_{ij}, m_{ijk}\}$. This assumption can lead to a small deviation from the DSMC results, when modeling strong non-equilibrium in the Knudsen layer. The nonlinear form of the boundary condition, due to the dependency of the reflection kernel on the particle velocity, becomes very complicated, and is not discussed in here. The coefficients $\lambda_{(i,j)}$ depend on the details of the wall collision kernel. For the standard Maxwell model, where $\alpha = \epsilon = 0$ and $\Theta = const$ is the accommodation coefficient, we have $\lambda_{(i,j)} = \frac{\Theta}{2-\Theta}$ and $\hat{\lambda}_{(4,1)} = 0$; this agrees with the boundary conditions for the R13 equations given in Refs. [93, 84].

In Ref. [83] boundary conditions for NSF where determined from the VDM model and a reduced distribution function, for which $\Delta = R_{ij} = m_{ijk} = 0$. While the boundary conditions for σ_{xy} and q_y in Ref. [83] have the same form as above, the corresponding coefficients differ slightly from those computed here, since the coupling to other boundary conditions (for R_{xy} or m_{yyy}) was not included.

The expressions for the $\lambda_{(i,j)}$ as functions of the parameters α and γ are tedious, and their details are not presented. Instead, we show the variations of the corresponding coefficients for the boundary conditions of shear stress and heat flux, which describe velocity slip and temperature jump.

The first row of Fig. 6.1 shows the coefficients $\lambda_{(1,1)}$, $\lambda_{(1,2)}$ and $\lambda_{(1,3)}$ that determine slip effects. The strength and direction of thermal transpiration flow is determined by the ratio $\lambda_{(1,2)}/\lambda_{(1,1)}$, which for the classical Maxwell model is always positive. For the VDM model, however, for certain values of α and γ this ratio can become rather small, or even

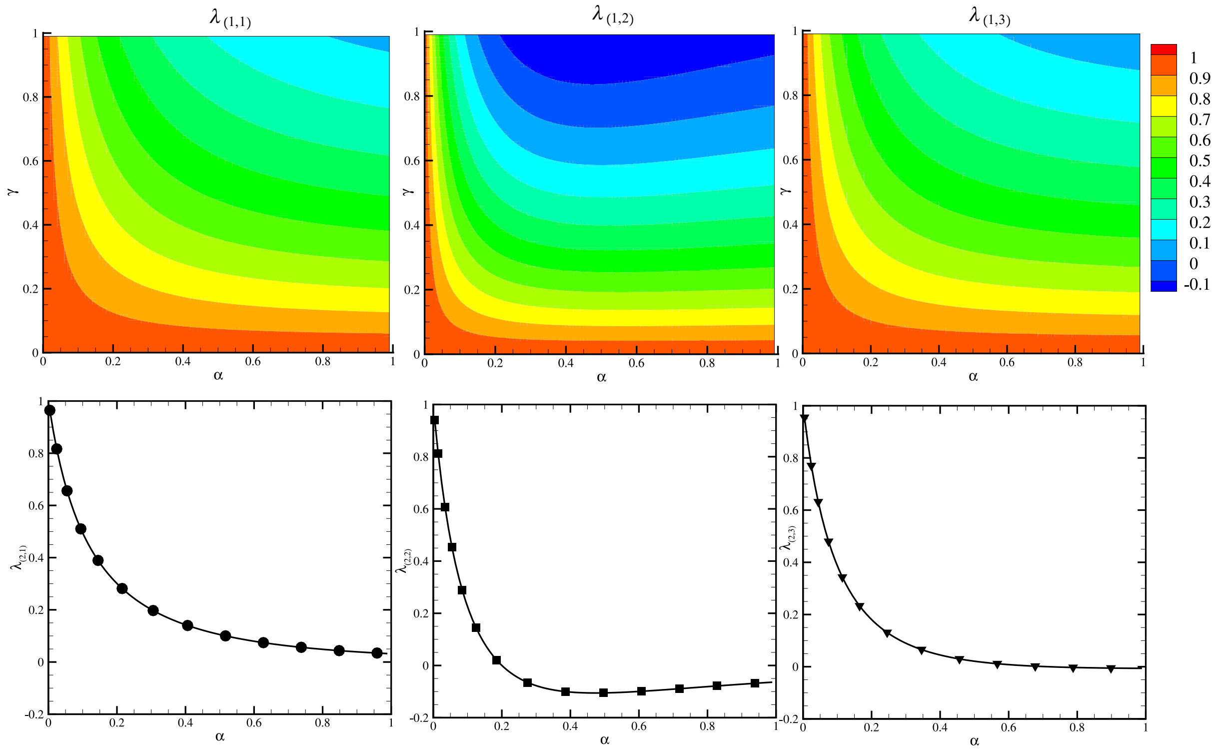

Figure 6.1: Variation of the VDM coefficients $\lambda_{(i,j)}$ in the boundary conditions (6.17). First row: coefficients for shear stress as functions of α and γ; Second row: coefficients for heat flux as functions of α.

negative, such indicating that the transpiration force can be small, or even inverted. This possibility was already pointed out in Ref. [83].

The second row of Fig. 6.1 shows the coefficients for the normal heat flux boundary condition, $\lambda_{(2,1)}, \lambda_{(2,2)}$ and $\lambda_{(2,3)}$, which depend only on α, but not on γ, since for both, specular reflection and isotropic scattering, the energy transfer remains zero.

SNIF/NSF boundary conditions

For the SNIF and NSF equations, only the boundary conditions for normal velocity, shear stress and normal heat flux are required, which are obtained from Eq. (6.17) by removing all contributions of higher moments, so that

$$\begin{aligned}
\mathcal{V}_y &= 0 , \\
\sigma_{xy} &= \sqrt{\frac{2}{\pi\theta}}\left(-\lambda_{(1,1)} p \mathcal{V}_x - \frac{1}{5}\lambda_{(1,2)} q_x\right) n_y , \\
q_y &= \sqrt{\frac{2}{\pi\theta}}\left(-2\lambda_{(2,1)} p \mathcal{T} - \frac{1}{2}\lambda_{(2,1)} \theta \sigma_{yy}\right) n_y .
\end{aligned} \tag{6.18}$$

Note that the coefficients $\lambda_{(i,j)}$ are the same as above, which implies the possibility of inverted transpiration flow also for the SNIF and NSF equations.

6.4 Results and discussion

6.4.1 Geometry and methods of solution

In the current study, we consider a square micro-cavity as depicted in Fig. 6.2. We are interested to study the interplay between thermal transpiration and thermal stress. We consider a problem that is governed by temperature effects, with no mechanical driving forces. For this means we consider a cavity with fixed temperatures at bottom and top, and linear variation of the temperature along the side walls,

$$T_B = 600 \text{ K} \quad T_T = 300 \text{ K} \quad T_L(y) = T_R(y) = T_B\left(1 + \frac{y}{L}\right) .$$

All boundaries of the cavity are at rest, so that the temperature gradients along the wall and inside the flow field are the sole driving forces for the rarefied flow field.

For all simulations, we consider argon ($R = 208\frac{\text{J}}{\text{kgK}}$) as Maxwell molecules with an initial equilibrium state at $T_0 = 273$ K, $\mu_0 = 1.955 \times 10^{-5}$Pa s in a quadratic cavity of side length $L = 1\mu$m. The initial density ρ_0 is set such that the initial Knudsen number is $\text{Kn}_0 = \frac{\mu_0}{\rho_0\sqrt{\theta_0}L} = 0.04$; for an average temperature $\bar{T} = \frac{1}{2}(T_B + T_T) = 450$K this corresponds to the Knudsen number $\text{Kn} = \text{Kn}_0\sqrt{\frac{\bar{T}}{T_0}} = 0.051$. These values are sufficiently small so that one will expect good results from all three macroscopic models.

We solve the R13, SNIF and NSF equations with the method presented in Ref. [69] and use the DSMC code discussed in Ref. [60].

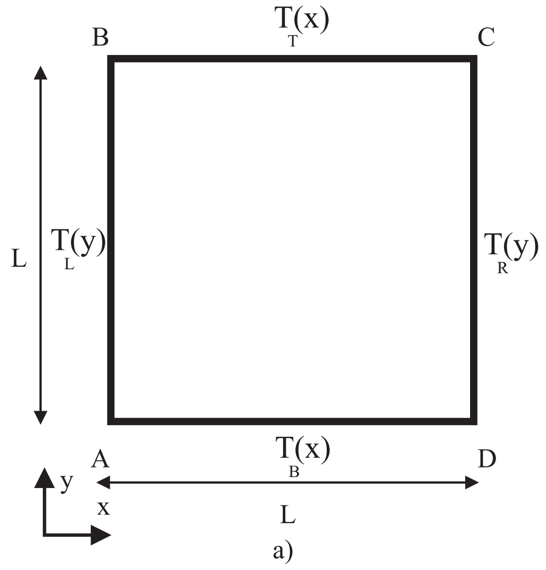

Figure 6.2: Geometry and prescribed wall temperatures for the cavity.

6.4.2 Standard thermalizing surface (Thermal transpiration flow)

First we consider the standard Maxwell surface for which $\alpha = 0$, $\Theta_0 = 1$. With these parameters, we have the coefficients $\lambda_{(1,1)} = \lambda_{(1,2)} = 1$, hence their ratio $\lambda_{(1,2)}/\lambda_{(1,1)} = 1$ is positive, and we expect standard transpiration force at the wall.

Thermal transpiration is a boundary effect that occurs when gas particles coming from warmer and colder regions of the flow hit the wall at the same surface element. Particles coming from the warmer region are faster, and thus induce larger tangential forces on the surface compared to particles from the colder region, which are slower. As a reaction, the wall is pushed towards the colder region, or, when the wall is at rest, the rarefied gas is driven from cold to warm, which is observed here.

We compare the exact solution from DSMC with solutions for the macroscopic models in Fig. 6.3, which shows the velocity streamlines overlaid on the temperature distribution inside the cavity with fully diffusive surface. Microscopic and macroscopic methods exhibit two primary vortices in the flow field which push the flow from cold to warm at the side walls.

Microscopic method and the three macroscopic methods give rather similar temperature profiles in the cavity. We note that the temperature profiles only have small curvature, which implies that the thermal stresses, as expressed by the term $\frac{4}{5}\frac{\partial q_{\langle i}}{\partial x_{j\rangle}}$ in R13, Eq. (6.8) and in SNIF, Eq. (6.11), will be relatively small. Hence, in this case, the thermal stresses play only a minor role, and thus NSF, which cannot describe thermal stresses, gives rather similar results for the flow fields.

A detailed look into the temperature lines in Fig. 6.3 shows an almost symmetrical distribution with respect to the horizontal centerline. Considering that we have a flow in the vertical direction, one would expect that the isothermal lines be influenced by the direction of the flow, and stray away from the symmetrical distribution. However, the small values of velocity (small convection effect), in comparison to the large value of temperature ratio (large conduction effect), causes the temperature lines not be significantly influenced. As a result we can observe that isothermal lines are rather symmetrical in the domain.

Figure 6.4 compares the flow properties along the horizontal centerline of the cavity, i.e., at $\frac{y}{L} = 0.5$. Figure 6.4 shows that the three macroscopic methods predict the flow velocity in the bulk of the gas, in the interval $\frac{x}{L} \in [0.1, 0.9]$, in good agreement to the DSMC simulation. However, in the proximity of the wall, i.e., in the Knudsen layer, only the R13 equations capture the wall vortex velocity. It is the presence of the Knudsen

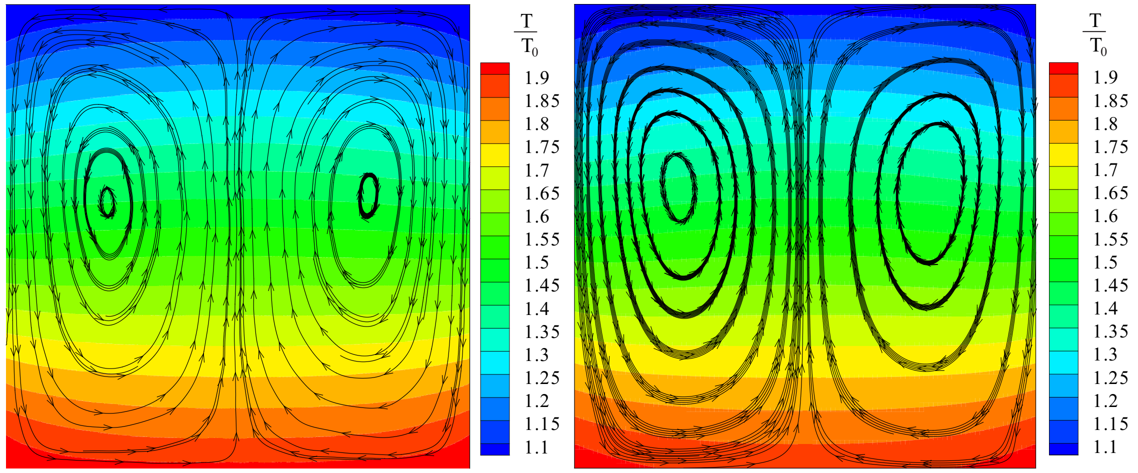

a) DSMC b) R13

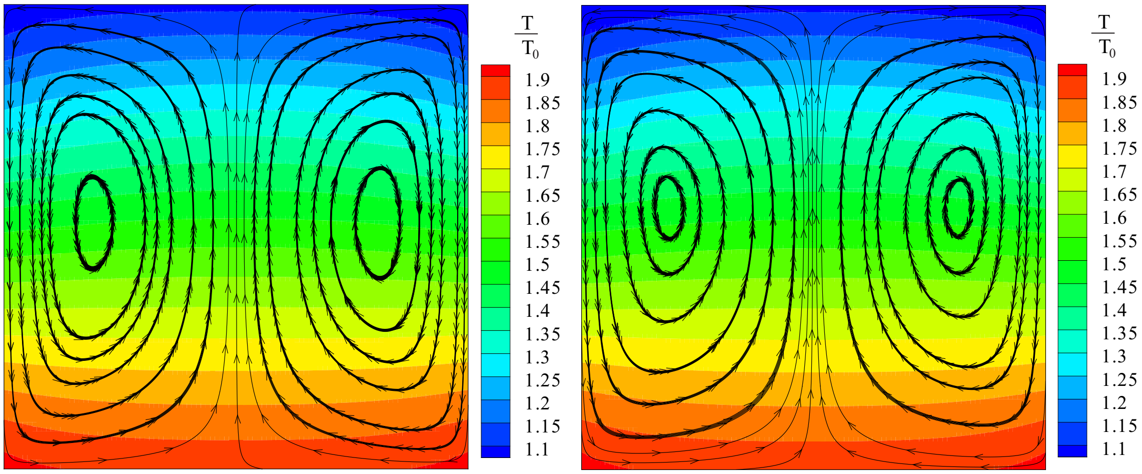

c) SNIF d) NSF

Figure 6.3: Velocity streamlines overlaid on the temperature distribution for fully diffusive surface: $\alpha = 0, \Theta_0 = 1$ at $\mathrm{Kn}_0 = 0.04$

layer terms, R_{ij}, m_{ijk} and Δ , in the R13 equations that leads to a better agreement with the DSMC solution in the proximity of the surface.

Figure 6.4-b shows that the NSF and SNIF equations slightly overpredict the temperature of the gas. Moreover, the small increase in the temperature inside the Knudsen layer is only captured by the R13 equations. The variation of shear stress along the centerline is depicted in Fig. 6.4-c. The difference in the predicted shear stress by the SNIF equations, and the agreement between the NSF results and the DSMC data, implies the main role of the viscous stresses in the case of cavity with the Maxwell surface, while thermal stresses are slightly overemphasized in SNIF. The agreement between between the R13 and DSMC in predicting normal heat flux, particularly in the Knudsen layer, is shown in Fig. 6.4-d.

6.4.3 Surface with inverted transpiration force

Thermal transpiration-Thermal stress flow

Next we employ the VDM boundary conditions, and consider $\alpha = 0.2$, $\gamma = 0.9$ and $\Theta_0 = 1$. With these parameters, we have the coefficients $\lambda_{(1,1)} = 0.4613$ and $\lambda_{(1,2)} = -0.0294$, hence their ratio $\lambda_{(1,2)}/\lambda_{(1,1)} = -0.0637$ is negative, and we expect inverted transpiration force at the wall. Note that this ratio also reflects the strength of the transpiration force, which therefore has far smaller magnitude here than in the previous case, where it is 16 times larger.

Inverted transpiration flow occurs when most of the faster gas particles coming from the warmer region are specularly reflected, so that they do not exchange tangential momentum with the surface, while most of the the slower particles coming form the colder region are thermalized or isotropically scattered, and hence transmit momentum to the surface. As a reaction, the wall is pushed towards the warmer region, or, when the wall is at rest, the rarefied gas is driven from warm to cold[60]. While it is unlikely that this behavior can be found in existing materials, it can be properly modeled and analyzed in the realm of kinetic theory. For us, it provides an interesting configuration that highlights the strength and weaknesses of the models under consideration.

Figure 6.5 shows the velocity streamlines overlaid on the temperature distribution for this case. The DSMC method (Fig. 6.5-a) predicts two sets of counter rotating vortices: Two primary vortices that drive the flow from cold to warm in the bulk of the flow, and two small vortices in the Knudsen layers that rotate from warm to cold. The temperature contours show more curvature than before, so that thermal stress contributions can be

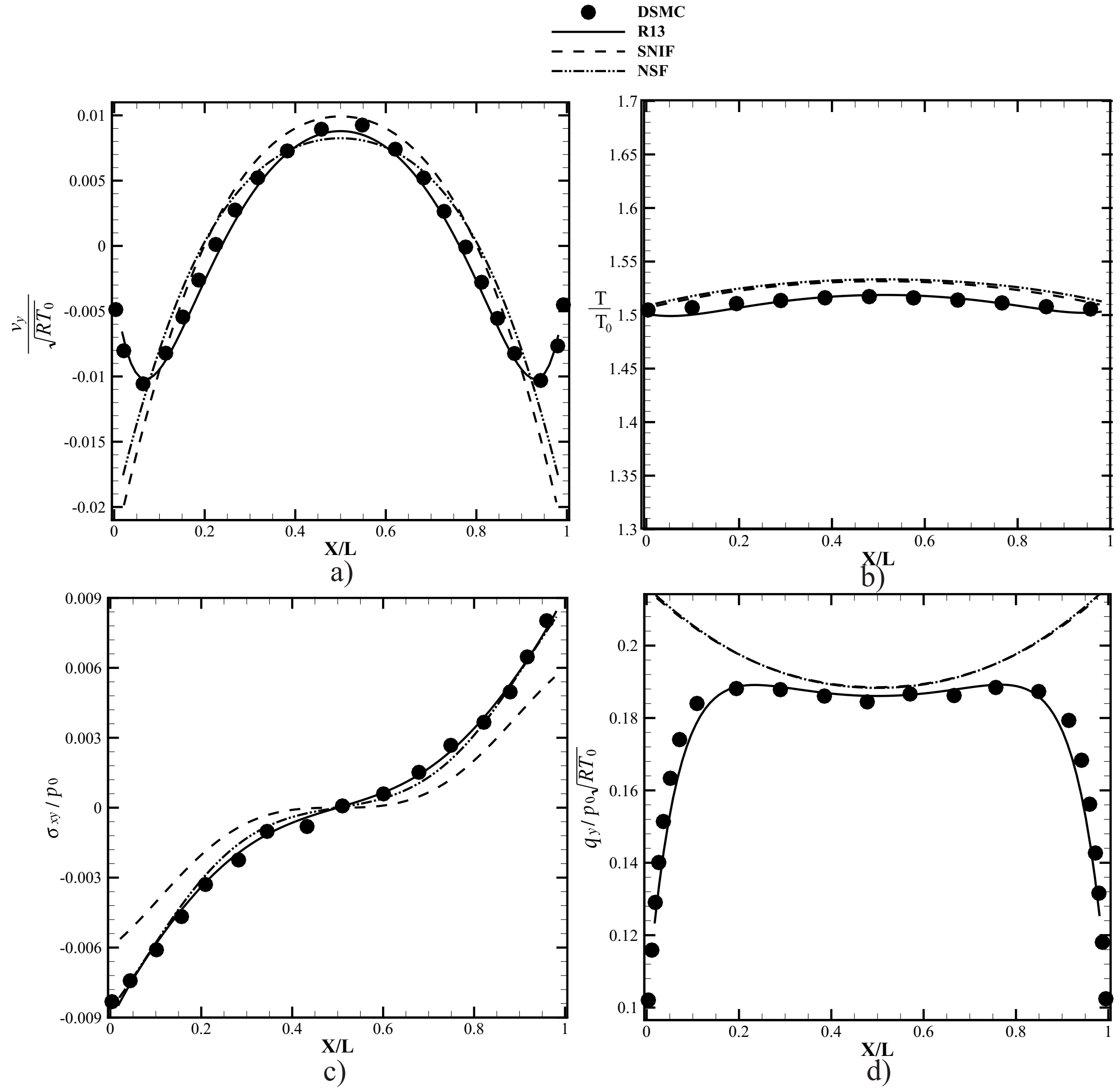

a) b) c) d)

Figure 6.4: Rarefied flow properties along horizontal centerline of the cavity for fully diffusive surface, $\alpha = 0, \Theta_0 = 1$ at $\mathrm{Kn}_0 = 0.04$. a) Vertical velocity, b) Temperature, c) Shear stress, d) Vertical heat flux.

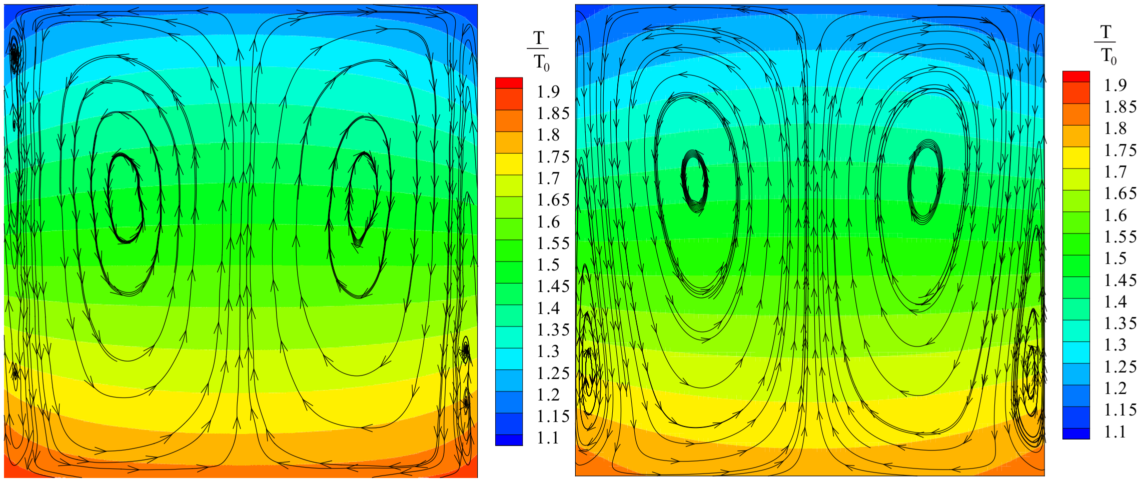

a) DSMC b) R13

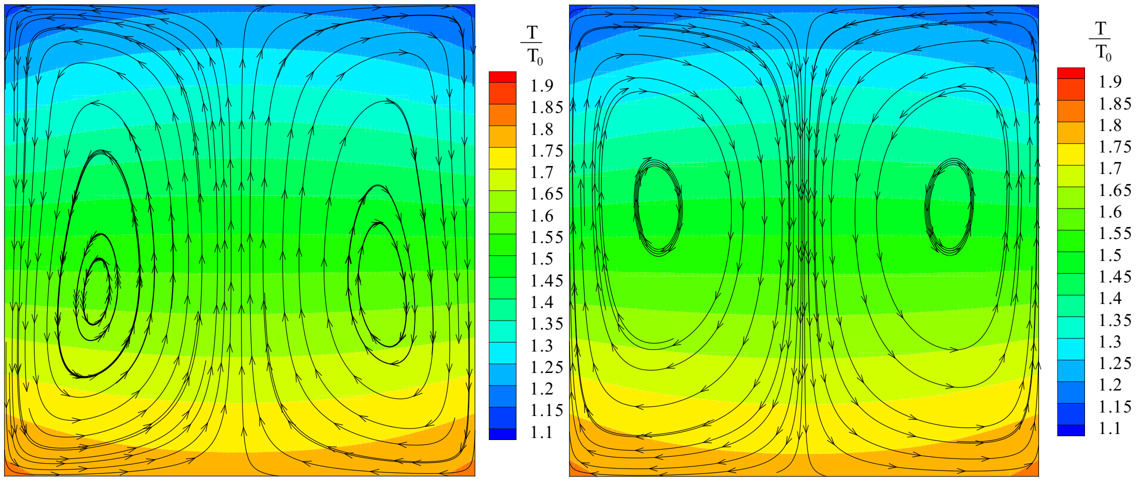

c) SNIF d) NSF

Figure 6.5: Velocity streamlines overlaid on the temperature distribution for the VDM boundary conditions, $\alpha = 0.2$, $\gamma = 0.9$ and $\Theta_0 = 1$ at $\mathrm{Kn}_0 = 0.04$.

expected to play a more prominent role.

We now use the macroscopic models to interpret the DSMC result. The R13 equations (Fig. 6.5-b) predict the same set of vortices as DSMC, and show good agreement with the DSMC results. The SNIF (Fig. 6.5-c) and NSF (Fig. 6.5-d) equations, however, both fail to predict these vortices in the flow field, with the SNIF result showing only two cold-to-warm (primary) vortices, and NSF predicting only two warm-to-cold (secondary) vortices.

The NSF equations do not account for thermal stresses, so that the only driving force for the flow is the—inverted (and small)!—transpiration force at the wall. Accordingly, the NSF equations predict the inversion of the thermal transpiration to drive the flow from warm to cold.

The SNIF equations, on the other hand, account for thermal stress in the bulk, as well as for the—small (and inverted)!—transpiration force at the wall. While the transpiration force tries to push the gas at the wall from warm to cold, the thermal stresses push in the opposite direction. Since the ratio $\lambda_{(1,2)}/\lambda_{(1,1)}$ is rather small, the transpiration force is weak, and the thermal stresses prevail, so that the gas at the wall moves from cold to warm.

The R13 equations describe a larger number of rarefactions effects, in particular they reasonably reproduce Knudsen layers at the wall. With this, they can reproduce the behavior of the gas as predicted by the DSMC simulation.

Comparing all models, the following picture emerges: the observed flow pattern is the result of competition between the thermal transpiration at the boundary and the thermal stresses in the bulk, which are both due to the thermal profile induced by the wall temperatures. In the presence of the standard Maxwell boundary condition the thermal transpiration at the wall amplifies the thermal stress in the bulk, and drive the flow from cold-to-warm. That leads to appearance of two large vortices as in Fig. 6.3. These vortices are mainly induced by the thermal transpiration force (first order effect in Knudsen number) and can be captured by all the macroscopic methods.

However, if we change the magnitude and direction of the thermal transpiration force at the boundary, so that it acts against the thermal stress, we can, more clearly, observe the interplay between these two force. Figure 6.5 shows the weak inverted transpiration force at the boundary that can only move a small amount of the gas close to the wall. This force does not suffice to overcome the thermal stresses in the bulk; as a result we observe two types of vortices in this problem. A narrow transpiration driven vortex at the wall, and the wider thermal stress driven vortex in the bulk.

Note that thermal stress can also play a role at the boundary, and lead to so-called ”thermal stress slip flow”, in Ref. [76] . However, in the current study, by accessing to different macroscopic methods, we can identify the source for each emerging vortices. Predicting the warm-to-cold vortex in the vicinity of the wall, by both NSF and R13 equations suggests that this vortex must be due to the (inverted) thermal transpiration effect.

For more insight into the capability of the different models, Fig. 6.6 shows the flow properties along the horizontal centerline of the cavity. DSMC, R13 and SNIF have a good agreement to DSMC for the vertical velocity v_y in the bulk of the gas. Considering that thermal stress is included in the the SNIF but not the NSF equations, the deviation

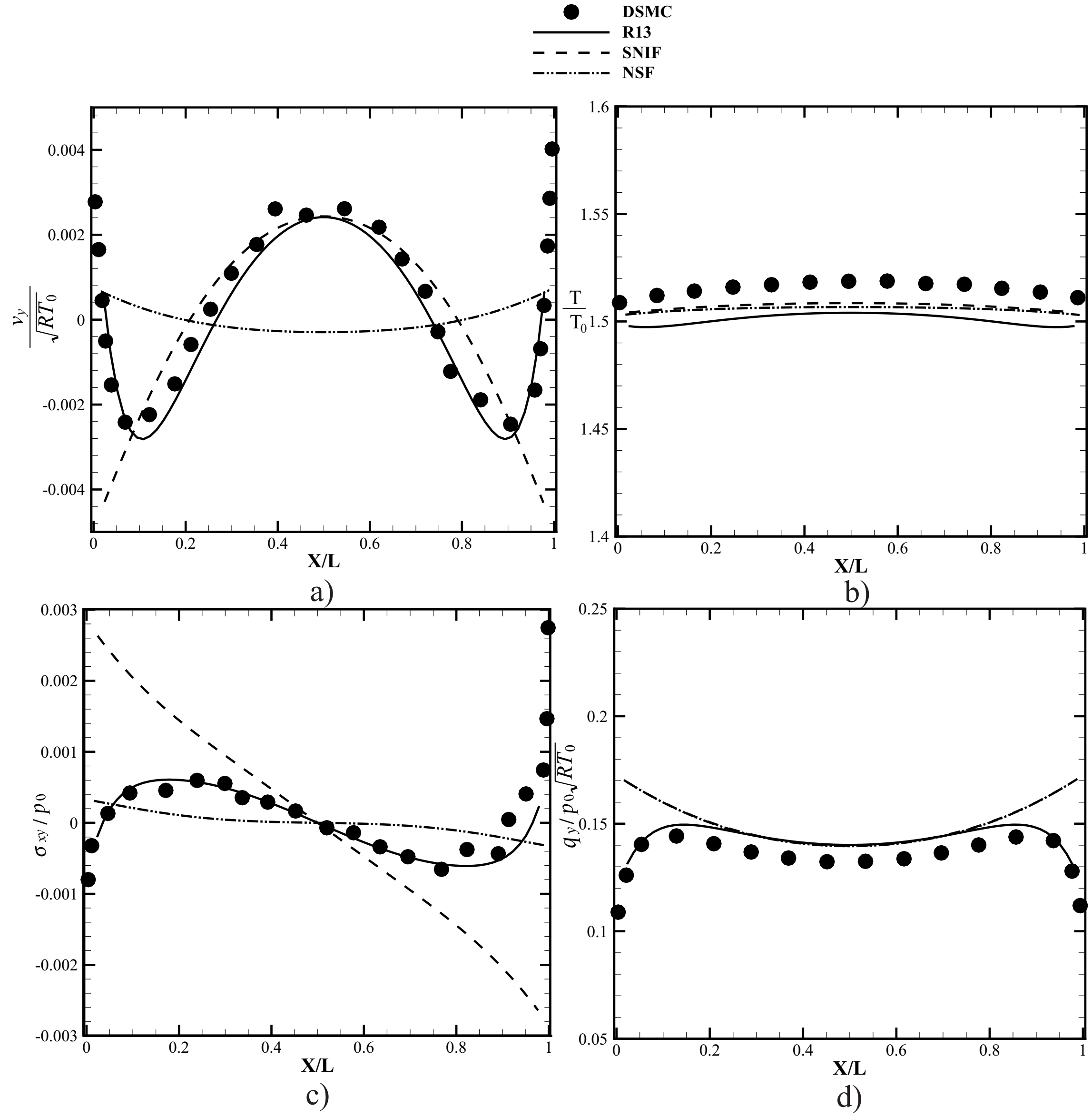

a)

b)

c)

d)

Figure 6.6: Rarefied flow properties along horizontal centerline of the cavity with $\alpha = 0.2$, $\gamma = 0.9$ and $\Theta_0 = 1$ at $\mathrm{Kn}_0 = 0.04$. a) Vertical velocity, b) Temperature, c) Shear stress, d) Vertical heat flux.

of the NSF results from the DSMC data shows the main role of the thermal stresses in this case. The deviation between SNIF and R13 results for the vertical velocity is large in the Knudsen layer, where the boundary effects dominate the flow behavior.

The temperature variation along the centerline is shown in Fig. 6.6-b. It is seen that the *relative* deviation of the three macroscopic models from the DSMC result is small, $\frac{T_{DSMC}-T_{R13}}{T_B-T_T} < 0.01$. This deviation can be attributed to the linearization of the boundary conditions, and rather large temperature ratio between the bottom and top walls.

The variation of the shear stress along the horizontal centerline is depicted in Fig. 6.6-c, where good agreement between DSMC and R13 results is evident. NSF and SNIF equations, however, show marked deviations, which are a further reflection of their inability to describe the flow field. The variation of vertical heat flux along the horizontal centerline is shown in Fig. 6.6-d. The effect of Knudsen layer that leads to reduction of the heat flux in the proximity of the surface is only captured by the R13 equations.

It is worth noting that the scale of velocity in Fig. 6.6 suggests that modeling this flow with DSMC is extremely difficult, and time consuming. For the sake of comparison with macroscopic methods (specially NSF), we were restricted on the magnitude of Knudsen number. Moreover, increasing the temperature ratio $\frac{T_B}{T_T}$ to more than 2 is not recommended for the macroscopic methods, due to the employed linearization in deriving R13 equations and boundary conditions. The resulting *small* velocity from considered temperature ratio leads to appearance of statistical noises in our DSMC results. By performing a statistical error study, we found that the noise to signal ratio for the *raw* DSMC results of Fig. 6.5-a is approximately 10%. Also, we used a macroscopic filtering post-processor, as explained in Ref. [60], to extract the macroscopic moments from the raw DSMC results. This, will reduces the remaining noises in the DSMC solution to some degrees, and gives rather acceptable results. This problem, is a good example for the importance of employing accurate macroscopic equations for modeling low speed microflows.

Thermal stress flow

Next, we consider the case where thermal stress (almost) takes over the entire flow field, and drives the rarefied flow. For this means, we decrease the Knudsen number to $Kn = 0.02$, and the temperature ratio to $\frac{T_B}{T_T} = 1.5$, while keeping the same coefficients in the VDM boundary condition as before. The velocity streamlines overlaid on temperature distributions are depicted in Fig. 6.7. In here, the width of Knudsen layer, where the (inverted) transpiration force tries to move the flow from warm-to-cold becomes smaller.

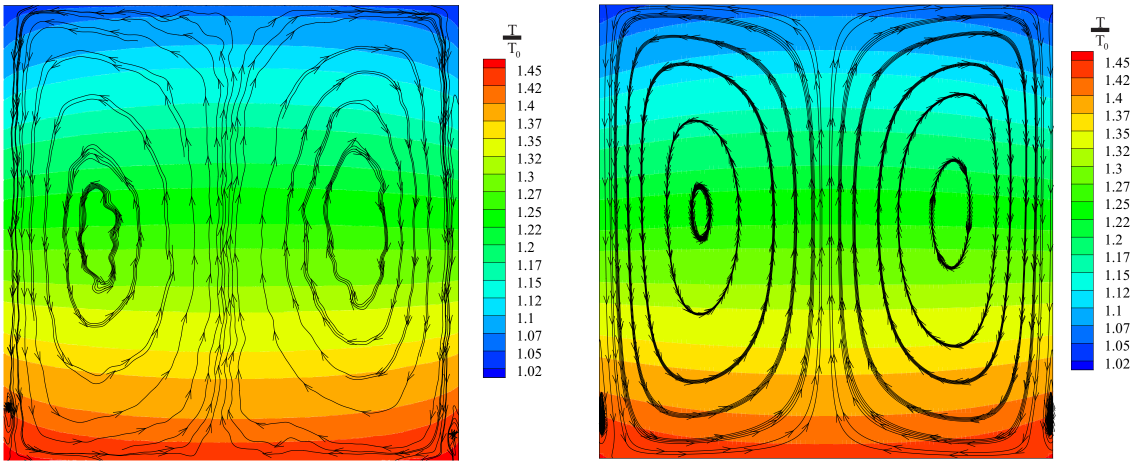

a) DSMC

b) R13

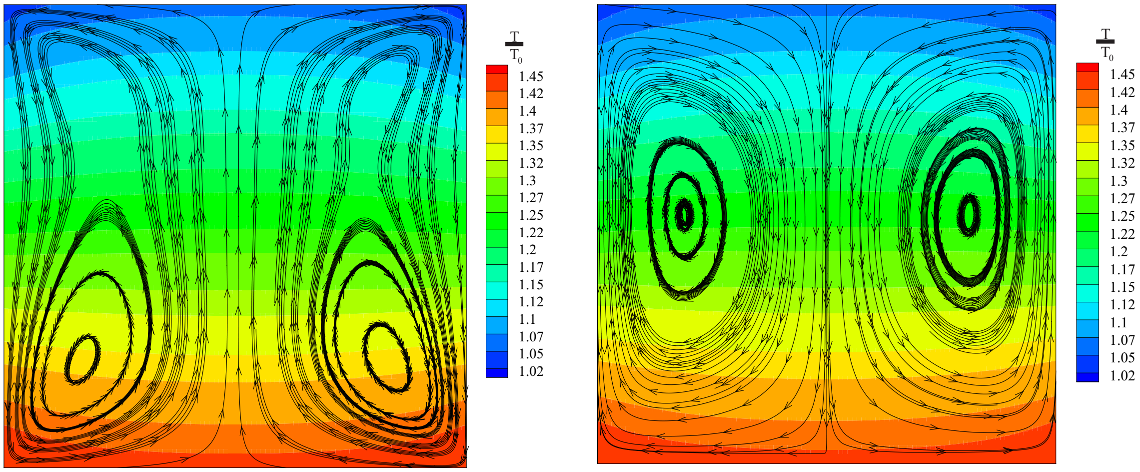

c) SNIF

d) NSF

Figure 6.7: Velocity streamlines overlaid on the temperature distribution for the VDM boundary conditions when $\frac{T_B}{T_T} = 1.5$, $\alpha = 0.2$, $\gamma = 0.9$ and $\Theta_0 = 1$ at $\mathrm{Kn}_0 = 0.02$.

Similar to the previous case, neither the NSF nor the SNIF equations can resolve the interplay between the two thermal forces, and they both fail to predict the flow pattern.

The R13 and DSMC methods, however, predict two dominant thermal stress vortices in the bulk, as well as two small transpiration vortices in the vicinity of bottom corners. The smaller thermal gradient on the wall as well as smaller width of Knudsen layer pushes the transpiration vortices to the vicinity of bottom corners.

The flow properties along the horizontal centerline of the cavity is shown in Fig. 6.8. Due to the smaller temperature ratio in this case, the linearization technique employed in R13 equations remains more accurate, and the results have better agreement with the DSMC solution. Note that by decreasing the Knudsen number and temperature ratio, we weaken the driving forces in the thermal cavity. This is observed in the smaller magnitude of the velocity in Fig. 6.8-a. As a result, we can see that the temperature, shear stress and heat flux profiles become more flat, and approach to the case of thermal cavity with pure conduction.

6.5 Conclusion

Thermally driven flows are driven by the thermal transpiration force at the boundary, and the thermal stresses in the bulk. The Maxwell boundary model with velocity dependent accommodation coefficient allows to change the size and direction of the thermal transpiration force, which leads to marked changes in the balance of transpiration force and thermal stresses. The simulation of the thermally driven cavity shows that macroscopic methods are extremely useful tools for the interpretation of rarefied flows.

The transpiration force can be introduced into the jump and slip boundary conditions for classical hydrodynamics (NSF equations). However, since the NSF equations do not describe thermal stresses at all, they fail in the description of flows which are dominated by thermal stresses, and their interplay with a transpiration force. The equations for slow non-isothermal flow (SNIF) add the description of thermal stresses to classical hydrodynamics, and hence fare somewhat better. However, they fail for the flow considered here, since they can only describe the behavior in the bulk, but cannot resolve the flow field in the Knudsen layer in front of the wall. The regularized 13 moment equations (R13) account for a larger number of rarefaction effects, and give a good approximation to the flow even in the Knudsen layer, hence they can provide a reasonably accurate description of all aspects of the flow.

While the DSMC method, and other microscopic methods to solve the Boltzmann equation, are highly accurate, they consume large numerical resources and time, and they cannot provide clear interpretations of the results. Macroscopic methods generally can only provide approximations to the exact microscopic solutions, but they are much cheaper, and faster, to solve. Moreover, since the equations relate macroscopic quantities with clear meaning, macroscopic models are rather helpful for the interpretation of flows. The presented simulations indicate that it is best to use macroscopic models that can (reasonably) capture all rarefaction effects, e.g., the R13 equations, rather than models that describe only selected effects.

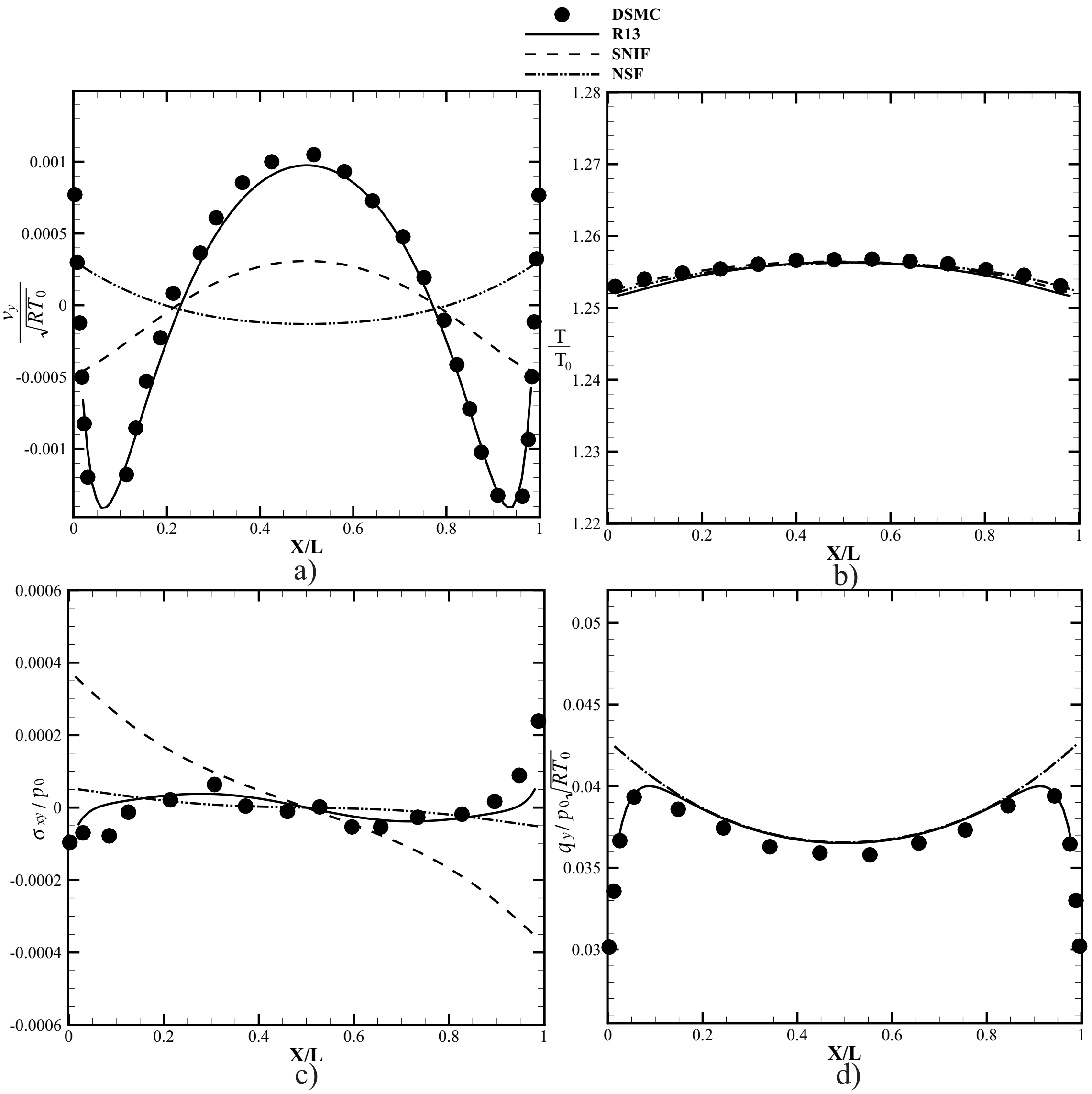

Figure 6.8: Rarefied flow properties along horizontal centerline of the cavity when $\frac{T_B}{T_T} = 1.5$, $\alpha = 0.2$, $\gamma = 0.9$ and $\Theta_0 = 1$ at $\mathrm{Kn}_0 = 0.02$. a) Vertical velocity, b) Temperature, c) Shear stress, d) Vertical heat flux.

Acknowledgement

This research was supported by the Natural Sciences and Engineering Research Council (NSERC).

Chapter 7

Conclusions

In this dissertation we looked into the phonon transport in solids, as well as the gas-surface interactions in conventional gas dynamics. We focused on the rarefaction regime, where the classical theory break down, and used the *moment method* as a tool to derive extend macroscopic equations for this regime.

7.1 Phonon transport

7.1.1 Achievements

In the first part of this study we used the moment method to derive macroscopic sets of equations that describe phonon transport in the crystal lattice at room temperature. The quadratic dispersion relation is employed to express dependency of frequency on wavevector of phonons at room temperature. The Brillouin zone is considered to be a sphere with a temperature dependent radius, and the relaxation time in Callaway model is considered to be frequency dependent to extend the validity of our model to room temperature. The resulting system of equations are then closed using Grad closure method.

We used Grad method to provide boundary conditions for the system of moments. We considered three types of microscopic interactions between phonons and crystal boundaries: thermalization, specular reflection and isotropic scattering. The reflection kernel in the proposed boundary model is considered to be the superposition of kernels for these microscopic interaction types.

This system of equations were then analytically solved in a few simple geometries, and the deviation in their solutions from the classical theory were discussed. Employing the moment equations to describe the heat transport, we obtained good agreement with the reported data in the thermal grating experiment. We showed the importance of relaxation time model in predicting phonon characteristics, and capturing rarefaction effects at room temperature. By employing different relaxation time models, we observed that although they all give the same thermal conductivity (first order rarefaction effect), not all of them can predict the thermal decay curve (higher order rarefaction effect) reported in the thermal grating experiment.

The relaxation time at room temperature not only has to be frequency dependent, but also must distinguish between low and high frequency phonons. We observed that the text-book value for phonon mean free path in silicon is out-dated and this value should be reconsidered when modeling heat transfer at room-temperature.

Our results confirm that, similar to gas dynamics, the extension of macroscopic equations beyond the continuum regime for phonon transport, using the moment method, is promising. While efficient particle methods for simulation of phonon transport are also available, macroscopic models provide fast and sufficiently accurate simulations when Knudsen number is not too large.

7.1.2 Recommendations and future work

Free parameters in the model

Considering that in this work we proposed a mathematical model with the aim of predicting the results in the thermal grating experiment, it is helpful to mention the degrees of freedom in our model to clarify how we can use the system of moments in similar experiments.

The first two free parameters are related to the dispersion relation. They are used to fit to the experimental values for specific heat at the desired temperature range. Note that this is before defining macroscopic moments, or deriving moments equations. Considering that the specific heat is an equilibrium quantity, these parameters are chosen by using the equilibrium distribution function for phonons. After parameters are fixed, such that the phonon model can properly predict the specific heat on that temperature range, they will not be altered in the sub-sequel work.

The second free parameter is related to the relaxation time for the R-processes. After deriving the set of macroscopic balance equations, we relate the first order contribution of the heat flux to the energy gradient, using the thermal diffusivity. The value of the cross over frequency ω_C in the relaxation time model is fixed such that we get the correct thermal diffusivity at the desired temperature range. Note that, since N-processes do not play a role in changing the thermal conductivity, their contributions are neglected at this point. Now the value for ω_C is fixed, and will not change throughout the modeling.

At this point we have a system of macroscopic moment equations that is fitted to the specific heat (zero's order effect) and the thermal conductivity (first order effect). Now we use this system in modeling the experiment to capture the higher order effects.

Modeling the thermal grating experiment with the system of moments, *without* considering the boundary effects (infinite thickness) also shows deviation from the diffusion solution. Meaning that, the system of equations predict higher order effects that, indeed, lead to deviation from Fourier's solution when the grating length is at micron scale.

In the thermal grating experiment the boundary plays an important role in reducing the heat transfer due to the scattering of phonons at the walls. This effect is addressed by using the slip parameter incorporated in the boundary model. This coefficient is the next free parameter that can be altered to fit to the reported experimental results. It is important to note that using the slip coefficient in this stage comes very simple and natural. We did not have to change any fundamental value or coefficient in the model to get a good prediction of the experiment, which shows the capability of the model in expressing heat transport process.

Considering that in the thermal grating experiment, the decay parameters for a range of grating lengths were reported, we only chose one grating length and used the slip coefficient to fit our thermal decay to the experimental corresponding value. At this point all parameters were fixed and the model was expected to predict the thermal decay in other grating lengths. We observed that the model provided good agreement with the experimental values for other grating lengths.

We observed that in the thermal grating experiment changing the corresponding value for the relaxation time in N-processes does not play a notable role in the thermal decay curve. Therefore, we used the corresponding value reported in the literature to fix it.

Recommendations

> The presented system of moment equations for phonon transport are valid at room temperature. However, considering their large size, solving this system in a two-dimensional geometry is rather complicated. The next step would be using the order of magnitude method to identify the order of contribution of each individual moment, to condense the current system into a smaller set of equations. One should aim for an extended form of Guyer-Krumhansl equations [29], with the extended

validity at the room temperature. It is expected that the coefficient in this condensed form of equations depend on the working temperature of the system.

It is worth noting that the author of this dissertation has studied the derivation of a regularized form of moment equations for phonon transport using the order of magnitude method. Indeed, we obtained the extended form of Guyer-Krumhansl equations, with the temperature dependent coefficients. However, we observed that by increasing the number of frequency moments, the values of these coefficients do not converge. More specifically, the convergence is very dependent on the form of relaxation times considered in the model, and by considering the "cross-over" model we lose this convergence. The reasons for this behavior are unclear at present, and demand further research.

The current form of moment equations are linear. It is worth looking into the effect of non-linearity in the solution, and compare the non-linear results with the decay curve in the thermal grating experiment.

A two-dimensional numerical scheme can be developed to solve the current form of equations. In this dissertation we only used analytical schemes to solve the one-dimensional form of moment equations for phonons. Considering that we observed interesting rarefaction effects in two-dimensional geometries in conventional gas dynamics, it is encouraged to look into the two-dimensional heat transport problems.

Considering the DSMC results for phonon transport in the literature, a comparison with the DSMC results in a simple two-dimensional geometry should be performed. Similar to conventional gas-dynamics the DSMC and moment equations can inform each other to validate the macroscopic solution and interpret the microscopic results.

7.2 Gas-Surface interactions in conventional gas dynamics

7.2.1 Achievements

In the second part of this study we considered velocity dependency in the reflection kernel for gas-surface interactions in conventional gas dynamics, and used the Direct Simulation Monte Carlo (DSMC) method and the regularized 13-moment (R13) equations to study thermally driven flows, i.e., flows that are driven by the thermal transpiration force at the boundary, and the thermal stress in the bulk. These two rarefaction effects are not predicted by the classical (Navier-Stokes-Fourier) equations.

Thermal transpiration is a first order boundary effect that happens in the Knudsen layer, where the larger impacting velocities of particles coming from the hotter region compared to particles coming from the colder region of the rarefied flow, impose a net drag on the surface towards the colder region. This leads to the motion of rarefied flow toward the hotter region. Although the classical hydrodynamics does not predict this rarefaction effect, it can be introduced into the jump and slip boundary conditions to extend the application of these equations to the slip regime.

Thermal stress is a second order effect in the bulk of the rarefied flow, and the R13 equations describe it as the gradient of the heat flux vector that contributes to the shear stress. Thermal stress can be added to the classical hydrodynamics to form the slow non-isothermal flow (SNIF) equations, which are expected to provide a better approximation for thermally driven flows.

We use the DSMC method as well as the NSF, SNIF and R13 equations to model a thermal cavity, and observed good agreement between the DSMC and R13 solutions. The SNIF equations, however, failed to predict the flow patterns in this study. Although SNIF equations can provide a better description in the bulk, they cannot resolve the flow field in the Knudsen layer in front of the wall. Our simulations showed that the DSMC method and R13 equations can inform each other. We can validate the results of the macroscopic equations by comparison to the DSMC simulations, and then, in turn, interpret the DSMC results in terms of macroscopic quantities.

By using isotropic scattering kernel to model a cavity with three adiabatic surfaces, we observed viscous slip heating effect. This second order rarefaction effect is the generation of heat due to intermolecular collisions in the adjacent cell to the adiabatic surface (observed by the DSMC approach), which is well captured, and interpreted, by the product of the slip velocity and the shear stress on the adiabatic wall (interpreted by the R13 equations).

7.2.2 Recommendations and future work

Using experimental values for the gas-surface interactions, the free parameters in the velocity dependent Maxwell boundary conditions can be fixed, depending on the type of the gas and surface.

Appendix A

Distribution Function

Maximizing the entropy density function for phonons under the constraint of our moment definition Eq. (2.17), leads to

$$f_G = \frac{y}{\exp\left(\frac{\hbar}{k_B}\sum_{\beta=0}^{n_F}\sum_{m=0}^{n_D}\Lambda^{\beta}_{<i_1\dots i_m>}\omega^{\beta}n_{<i_1}\dots n_{i_m>}\right)-1} \ , \tag{A.1}$$

where $\Lambda^{\beta}_{<i_1\dots i_m>}$ are the Lagrange multipliers. Comparing this form with the equilibrium distribution function, Eq. (2.5), suggests that in equilibrium, i.e., $m = 0$ and $\beta = 1$, all Λ are zero, except for

$$\Lambda^1 = \frac{1}{T} \ ,$$

Now we separate the equilibrium part from the non-equilibrium contribution, and define

$$\lambda^{\beta}_{<i_1\dots i_m>} = \Lambda^{\beta}_{<i_1\dots i_m>} - \frac{1}{T}\delta^0_m\delta^1_\beta \ ,$$

that leads to $\lambda^1 = 0$ in the equilibrium. By considering a small deviation from the equilibrium state, we can linearize the distribution function in the non-equilibrium Lagrange multipliers to obtain

$$f_G = f_E - \frac{y\exp(\frac{\hbar\omega}{k_BT})}{(\exp(\frac{\hbar\omega}{k_BT})-1)^2}\sum_{\beta=0}^{n_F}\sum_{m=0}^{n_D}(\lambda^{\beta}_{<i_1\dots i_m>}(\frac{\hbar\omega}{k_BT})^{\beta}n_{<i_1}\dots n_{i_m>}) \ .$$

The unknown $\lambda^{\beta}_{<i_1\dots i_m>}$ are determined as functions of the moments, by substituting this

---

This Appendix is related to Chapter 2 Sec. 2.3.2.

distribution function into Eq. (2.17), and performing the integration over the Brillouin zone. For this means, first we switch to the spherical coordinates with $d\mathbf{k} = dk d\Omega$, where Ω as the solid angel, and define the density of states $g(\omega)$ as

$$g(\omega) = k^2 \frac{dk}{d\omega} , \tag{A.2}$$

to only deal with the frequency in our system of equations. Moreover, we introduce non-dimensional functions

$$X = \frac{\hbar\omega}{k_B T} \quad \text{and} \quad G(X) = \frac{c_0^3}{\omega_M^2} g(\omega), \tag{A.3}$$

where c_0 is the Debye velocity, and ω_M is the reference frequency

$$\omega_M = \frac{2c_0}{a} .$$

By introducing the matrix $I_{\alpha\beta}$ as

$$I_{\alpha\beta} = \int_{BZ} \frac{X^{\alpha+\beta} \exp(X) G(X)}{(\exp(X) - 1)^2} dX ,$$

and the frequency function

$$\Phi^\eta = \frac{\exp(X)}{(\exp(X) - 1)^2} \sum_\beta X^\beta I^{-1}_{\beta\eta} ,$$

we obtain the Grad distribution function as in Eq. (2.22).

Appendix B

Flux term

By substituting the distribution function in Eq. (2.23), we get

$$F^{\alpha}_{<i_1 i_2 .. i_n>} = c_0 \left(\frac{\displaystyle\int_{BZ} \frac{\mathcal{B}(X) X^{\alpha} G(X)}{\exp(X)-1} dX}{\displaystyle\int_{BZ} \frac{X^{\alpha} G(X)}{\exp(X)-1} dX} u^{\alpha}_{0|E} \delta^{0}_{n} + \sum_{\substack{\eta=0 \\ \neq E}}^{n_F} \left(\int_{BZ} \mathcal{B}(X)\, X^{\alpha} \Phi^{\eta} X_M^{\eta-\alpha} G(X) dX \right) \left(u^{\eta}_{<i_1,..i_n>} - u^{\eta}_{<i_1,..i_n>|E} \right) \right),$$

where the first term only has contribution to the scalar flux term, $n = 0$. By separating the above relation for the two cases of scalar, and non-scalar flux terms we get Eq. (2.24) with

$$A^{\alpha}_{E} = \frac{\displaystyle\int_{BZ} \frac{\mathcal{B}(X) X^{\alpha} G(X)}{\exp(X)-1} dX}{\displaystyle\int_{BZ} \frac{X^{\alpha} G(X)}{\exp(X)-1} dX} \quad \text{and} \quad A^{\alpha,\eta}_{n_p} = X_M^{\eta-\alpha} \int_{BZ} \mathcal{B}(X)\, X^{\alpha} \Phi^{\eta} G(X) dX \ .$$

Note that $\mathcal{B}(X)$ is the non-dimensional group velocity

$$\mathcal{B}(X) = \frac{1}{c_0} \frac{\partial \omega}{\partial k} \ .$$

This Appendix is related to Chapter 2 Sec. 2.3.2.

Appendix C

R-process production term

By considering a small deviation from the equilibrium state we express the distribution function for R-process as

$$f_R = f_E - y\frac{X\exp\left(X\right)}{\left(\exp\left(X\right)-1\right)^2}\left(\gamma_R T - 1\right)\ . \tag{C.1}$$

Using the distribution function Eq. (2.22), and solving Eq. (2.10) for γ_R, to express this deviation as a function of moments gives

$$\gamma_R = \frac{1}{T}\left(1 - \frac{a^3}{32\pi y}\frac{\sum\limits_{\substack{\eta=0,\\ \neq E}}^{n_F} X_M^{\eta+1}\int_{BZ}\frac{X\Phi^{\eta}G(X)}{\Psi_R(X)}dX}{\int_{BZ}\frac{X^2\exp(X)G(X)}{\Psi_R(X)(\exp(X)-1)^2}dX}\frac{v_0^{\eta}}{\omega_M^{\eta}}\right)\ . \tag{C.2}$$

Here, Ψ_R is the non-dimensional relaxation time for R-process

$$\Psi_R\left(X\right) = \frac{\tau_R\left(\frac{k_B T}{\hbar}X\right)}{\tau_R^0}\ .$$

This Appendix is related to Chapter 2 Sec. 2.3.2.

Using Eq. (C.1) to obtain the R-production moment in Eq. (2.25) we get Eq. (2.27) with

$$\begin{aligned}
J_{0,R}^{\alpha,\eta} &= X_M^{\eta-\alpha}\left(\int_{BZ}\frac{X^{\alpha}\Phi^{\eta}}{\Psi_R(X)}G(X)\,dX - \frac{\int_{BZ}\frac{X\Phi^{\eta}G(X)}{\Psi_R(X)}dX}{\int_{BZ}\frac{X^2\exp(X)G(X)}{\Psi_R(X)(\exp(X)-1)^2}dX}\int_{BZ}\frac{X^{\alpha+1}\exp(X)\,G(X)}{\Psi_R(X)(\exp(X)-1)^2}dX\right), \\
J_{n,R}^{\alpha,\eta} &= X_M^{\eta-\alpha}\int_{BZ}\frac{X^{\alpha}\Phi^{\eta}}{\Psi_R(X)}G(X)\,dX\ .
\end{aligned}$$

Appendix D

N-Process production term

Similar to the R-process, first we assume a small deviation from the equilibrium state to express f_N as

$$f_N = f_E - y\left(\frac{X\exp\left(X\right)}{\left(\exp\left(X\right)-1\right)^2}\left(\gamma_N T - 1\right) + \frac{\exp\left(X\right)\sqrt{\mathcal{B}\left(X\right)G\left(X\right)}}{\left(\exp\left(X\right)-1\right)^2}\frac{\hbar\omega_M}{k_B c_0}\xi_j n_j\right) .$$

Then we solve Eq. (2.11) for γ_N and ξ_i to get

$$\gamma_N = \frac{1}{T}\left(1 - \frac{a^3}{32\pi y}\frac{\sum\limits_{\substack{\eta=0,\\ \neq E}}^{n_F} X_M^{\eta+1}\int_{BZ}\frac{X\Phi^\eta G(X)}{\Psi_N(X)}dX}{\int_{BZ}\frac{X^2\exp(X)G(X)}{\Psi_N(X)(\exp(X)-1)^2}dX}\frac{v_0^\eta}{\omega_M^\eta}\right) , \tag{D.1}$$

and

$$\xi_i = -\frac{3a^4}{64\pi}\frac{k_B}{\hbar y}\sum_\eta\frac{\int\frac{\sqrt{\mathcal{B}(X)}\Phi^\eta X_M^{\eta+1}G(X)^{\frac{3}{2}}}{\Psi_N(X)}dX}{\int\frac{\mathcal{B}(X)\exp(X)G(X)^2dX}{\Psi_N(X)(\exp(X)-1)^2}}\frac{u_i^\eta}{\omega_M^\eta} .$$

Here, Ψ_N is the non-dimensional relaxation time for N-process

$$\Psi_N\left(X\right) = \frac{\tau_N\left(\frac{k_B T}{\hbar}X\right)}{\tau_N^0} .$$

This Appendix is related to Chapter 2 Sec. 2.3.2.

By accessing to the distribution function for the N-process, we can obtain the production moments in Eq. (2.28) with

$$\begin{aligned}
J_{0,N}^{\alpha,\eta} &= X_M^{\eta-\alpha}\left(\int_{BZ}\frac{X^{\alpha}\Phi^{\eta}}{\Psi_N\left(X\right)}G\left(X\right)dX - \frac{\int_{BZ}\frac{X\Phi^{\eta}G(X)}{\Psi_N(X)}dX}{\int_{BZ}\frac{X^2\exp(X)G(X)}{\Psi_N(X)(\exp(X)-1)^2}dX}\int_{BZ}\frac{X^{\alpha+1}\exp\left(X\right)G\left(X\right)}{\left(\exp\left(X\right)-1\right)^2\Psi_N(X)}dX\right) \quad , \\
J_{1,N}^{\alpha,\eta} &= X_M^{\eta-\alpha}\left(\int_{BZ}\frac{X^{\alpha}\Phi^{\eta}}{\Psi_N\left(X\right)}G\left(X\right)dX - \frac{\int_{BZ}\frac{\sqrt{\mathcal{B}(X)}\Phi^{\eta}G(X)^{\frac{3}{2}}}{\Psi_N(X)}dX}{\int_{BZ}\frac{\exp(X)\mathcal{B}(X)G(X)^2}{\Psi_N(X)(\exp(X)-1)^2}dX}\int_{BZ}\frac{X^{\alpha}\sqrt{\mathcal{B}\left(X\right)}\exp\left(X\right)G\left(X\right)^{\frac{3}{2}}}{\left(\exp\left(X\right)-1\right)^2\Psi_N(X)}dX\right) \\
J_{n,N}^{\alpha,\eta} &= X_M^{\eta-\alpha}\int_{BZ}\frac{X^{\alpha}\Phi^{\eta}}{\Psi_N\left(X\right)}G\left(X\right)dX \ .
\end{aligned}$$

Appendix E

Distribution function for the isotropic scattering

As mentioned in 2.4.1, for this type of interaction the impacting phonon with the surface is reflected in a random direction

$$f_{Sc} = \frac{1}{\pi c} \int_{n_k \nu_k < 0} c \left(-n_k \nu_k \right) f_G d\Omega$$

Using Grad distribution function in the above relation, and further simplification gives

$$f_{Sc} = f_E - \frac{a^3}{32\pi} \sum_{\eta,m} \frac{(2m+1)!!}{m!} \Phi^\eta X_M^{\eta+1} \left(\frac{u^\eta_{<j_1,..j_m>} - u^\eta_{<j_1,..j_m>|E}}{\omega^\eta_M} \right) \int_{k_i \nu_i < 0} n_{j_1 \ldots} n_{j_m} n_k \nu_k d\Omega \quad \text{(E.1)}$$

Note that here we use the direction vector with trace to simplify the integration over the half space. Without losing the generality, we consider a surface with the normal in the z-direction, so that the normal unit vector to the surface reads $\nu_i = \{0, 0, 1\}_i$. Moreover, we use the normal-tangential framework with respect to the surface, where the direction vector can be written as $n_i = \{\nu, \tau_A\}_i$ with $\nu = n_i \nu_i = \cos\theta$ and $\tau_A = \{\sin\theta\cos\phi, \sin\theta\sin\phi\}$. Using this notation we can express the tensorial moments with normal and tangential components. For example the second order tensor $u_{<ij>}$ can be written as

$$u^\alpha_{<ij>} = \begin{bmatrix} u^\alpha_{<AB>} & u^\alpha_{<A\nu>} \\ u^\alpha_{<B\nu>} & u^\alpha_{<\nu\nu>} \end{bmatrix}_{ij}$$

This Appendix is related to Chapter 2 Sec. 2.4.2.

where the capital indices, A and B denote the tangential directions. Note that the trace-free condition reads $u^{\alpha}_{<AA>} + u^{\alpha}_{<\nu\nu>} = 0$. Following the same method, the higher order tensors can be expressed as

$$\left(\frac{u^{\eta}_{<j_1,..j_m>} - u^{\eta}_{<j_1,..j_m>|E}}{\omega^{\eta}_{M}}\right) n_{j_1}...n_{j_m} = \sum_{r=0}^{m} \frac{m!}{r!\,(m-r)!} \left(\frac{u^{\eta}_{<A_1...A_r\nu...\nu>} - u^{\eta}_{<A_1...A_r\nu...\nu>|E}}{\omega^{\eta}_{M}}\right) \tau_{A_1}...\tau_{A_r}\nu^{m-r}$$

Using this relation in Eq. (E.1) we can get

$$f_{Sc} = f_E - \frac{a^3}{32\pi^2}\sum_{\eta,m}\frac{(2m+1)!!}{m!}\Phi^{\eta}X^{\eta+1}_{M}\sum_{r=0}^{m}\frac{m!}{r!\,(m-r)!} \left(\frac{u^{\eta}_{<A_1...A_r\nu...\nu>} - u^{\eta}_{<A_1...A_r\nu...\nu>|E}}{\omega^{\eta}_{M}}\right)\int_{\nu<0}\tau_{A_1}...\tau_{A_r}\nu^{m-r+1}d\Omega\ .$$

The integral only has non-zero value for even numbers of r, which can be written as

$$-\frac{1}{\pi}\int_{\nu<0}\tau_{A_1}...\tau_{A_r}\nu^{m-r+1}d\Omega = \begin{cases} \sigma^{m}_{r}\,\delta_{\{A_1..A_r\}} & r \text{ even} \\ 0 & r \text{ odd} \end{cases} \tag{E.2}$$

here $\delta_{\{A_1..A_r\}}$ is the generalized tangential unit tensor, that has $(r-1)!!$ terms. For example

$$\delta_{\{AB\}} = \delta_{AB} \quad \text{and} \quad \delta_{\{ABCD\}} = \delta_{AB}\delta_{CD} + \delta_{AC}\delta_{BD} + \delta_{AD}\delta_{BC}\ .$$

By taking the traces from Eq. (E.2), we obtain

$$\sigma^{m}_{r} = (-1)^{m-r}\,\frac{\Gamma\left(1+\frac{m-r}{2}\right)\Gamma\left(1+\frac{r}{2}\right)}{r!!\,\Gamma\left(2+\frac{m}{2}\right)}\ ,$$

where Γ is the Gamma function. Using the tensorial calculation, we simplify the product of the tonsorial moments with the unit tangential tensors as

$$\left(\frac{u^{\eta}_{<A_1...A_r\nu...\nu>} - u^{\eta}_{<A_1...A_r\nu...\nu>|E}}{\omega^{\eta}_{M}}\right)\delta_{\{A_1..A_r\}} = (r-1)!!\,(-1)^{\frac{r}{2}}\left(\frac{u^{\eta}_{<v...\nu>} - u^{\eta}_{<v...\nu>|E}}{\omega^{\eta}_{M}}\right)_{|m}\ . \tag{E.3}$$

Here, the subscript m denotes the moment with m indices. The distribution function for the isotropic scattering can now be written as

$$f_{Sc} = f_E + \frac{a^3}{32\pi} \sum_{\eta,m} \Phi^\eta X_M^{\eta+1} \mu^m \left(\frac{u^\eta_{<v\ldots\nu>} - u^\eta_{<v\ldots\nu>|E}}{\omega^\eta_M} \right)_{|m} , \tag{E.4}$$

where

$$\mu^m = \sum_{\substack{r=0 \\ r \text{ even}}}^{m} (-1)^{m-\frac{r}{2}} \frac{(r-1)!!}{r!!} \frac{(2m+1)!! \left(\frac{r}{2}\right)!}{r! \, (m-r)!} \frac{\Gamma\left(1+\frac{m-r}{2}\right)}{\Gamma\left(2+\frac{m}{2}\right)} .$$

Equation (E.4) relates the distribution function for the particles that isotropically scattered from the surface to the normal components of the non-equilibrium moments.

Appendix F

Obtaining Eq. (2.34)

Starting from Eq. (E.2), first we need to substitute the Grad distribution function. In here, the directional integration has a different sign compared to Eq. (E.2),

$$-\frac{1}{\pi}\int_{\nu>0}\tau_{A_1}\ldots\tau_{A_r}\nu^{m-r+1}d\Omega=\begin{cases}\xi_r^m\delta_{\{A_1..A_r\}} & r \text{ even}\\ 0 & r \text{ odd}\end{cases}$$

where $\xi_r^m=|\sigma_r^m|$. The right hand side Eq. (2.33) can be written as

$$\begin{aligned}\int_{\nu>0}\omega^\alpha\tau_{B_1}\ldots\tau_{B_s}\nu^{m-s+1}f_G d\mathbf{k}&=\frac{8\pi\omega_M^\alpha}{a^3X_M^{\alpha+1}}\left(\int_{BZ}X^\alpha f_E G\left(X\right)dX\right)\xi_s^m\delta_{\{B_1\ldots B_s\}}\\&+\frac{1}{4}\sum_n\sum_{r=0}^n\frac{(2n+1)!!}{r!\,(n-r)!}\xi_{r+s}^{n+m}\left(u^\alpha_{<A_1\ldots A_r\nu_1\ldots\nu_{n-r}>}-u^\alpha_{<A_1\ldots A_r\nu_1\ldots\nu_{n-r}>|E}\right)\delta_{\{A_1\ldots A_rB_1\ldots B_s\}}\ .\end{aligned}$$

The contribution for the diffusive particles on the left hand side of Eq. (2.33) can be written as

$$(1-\beta)\int_{\nu>0}\omega^\alpha\tau_{B_1}\ldots\tau_{B_s}\nu^{m-s+1}f_E\left(T_s\right)d\mathbf{k}=\frac{8\pi\omega_M^\alpha}{a^3X_M^{\alpha+1}}(1-\beta)\left(\int_{BZ}X^\alpha f_E\left(T_s\right)G\left(X\right)dX\right)\xi_s^m\delta_{\{B_1\ldots B_s\}}\ .$$

This Appendix is related to Chapter 2.

For the specularly reflected particles we have

$$\begin{aligned}\beta\gamma\int_{\nu>0}\omega^{\alpha}\tau_{B_1}\ldots\tau_{B_s}\nu^{m-s+1}f_S d\mathbf{k} =&\beta\gamma\left(\frac{8\pi\omega_M^{\alpha}}{a^3X_M^{\alpha+1}}\left(\int_{BZ}X^{\alpha}f_E G\left(X\right)dX\right)\sigma_s^m\delta_{\{B_1\ldots B_s\}}\right.\\ &\left.+\frac{1}{4}\sum_n\sum_{r=0}^{n}\frac{(2n+1)!!}{r!\,(n-r)!}\sigma_{r+s}^{n+m}\left(u^{\alpha}_{<A_1\ldots A_r\nu_1\ldots\nu_{n-r}>}-u^{\alpha}_{<A_1\ldots A_r\nu_1\ldots\nu_{n-r}>|E}\right)\delta_{\{A_1\ldots A_rB_1\ldots B_s\}}\right)\ ,\end{aligned}$$

and for the isotropic scattering, by using Eq. (E.4) we get

$$\begin{aligned}\beta\left(1-\gamma\right)\int_{\nu>0}\omega^{\alpha}\tau_{B_1}\ldots\tau_{B_s}\nu^{m-s+1}f_{Sc}d\mathbf{k} = &\ \beta\left(1-\gamma\right)\left(\frac{8\pi\omega_M^{\alpha}}{a^3X_M^{\alpha+1}}\right.\\ &\left.\left(\int_{BZ}X^{\alpha}f_E G\left(X\right)dX\right)+\frac{1}{4}\sum_n\mu^{\alpha}\left(u^{\alpha}_{<\nu_1\ldots\nu_n>}-u^{\alpha}_{<\nu_1\ldots\nu_n>|E}\right)\right)\xi_s^m\delta_{\{B_1\ldots B_s\}}\ .\end{aligned}$$

Substituting these relations in Eq. (2.33), we obtain Eq. (2.34).

Bibliography

[1] H. Akhlaghi, E. Roohi, and S. Stefanov. A new iterative wall heat flux specifying technique in DSMC for heating/cooling simulations of mems/nems. *Int. J. Therm. Sci.*, 59:111–125, 2012.

[2] K. Aoki, P. Degond, L. Mieussens, S. Takata, and H. Yoshida. A diffusion model for rarefied flows in curved channels. *SIAM MMS*, 6(4):1281–1316, 2008.

[3] K. Aoki, Y. Sone, and Y Waniguchi. A rarefied gas flow induced by a temperature field: numerical analysis of the flow between two coaxial elliptic cylinders with different uniform temperatures. *Comput. Math. Appl.*, 35:15–28, 1998.

[4] P.L. Bhatnagar, E.P. Gross, and M. Krook. A model for collision processes in gases. i. small amplitude processes in charged and neutral one-component systems. *Phys. Rev.*, 94:511–525, 1954.

[5] G. A. Bird. *Molecular gas dynamics and the direct simulation of gas flows.* Oxford University Press, 1994.

[6] G. A. Bird. *The DSMC method.* CreateSpace Independent Publishing Platform, 2013.

[7] A. V. Bobylev. Quasistationary hydrodynamics for the Boltzmann equation. *J. Stat. Phys.*, 80:1063–1083, 1995.

[8] C. Cai. Heat transfer in vacuum packaged micro–electro–mechanical system devices. *Phys. Fluid*, 20:017103, 2008.

[9] J. Callaway. Model for lattice thermal conductivity at low temperatures. *Phys. Rev.*, 113:1046–1051, 1959.

[10] C. Cercignani. *Theory and application of the Boltzmann equation.* Scottish Academic Press, 1975.

[11] C. Cercignani and M. Lampis. Kinetic models for gas-surface interactions. *Transp. Theory Stat. Phys*, 1:101–114, 1971.

[12] S. Chapman and T. G. Cowling. *The mathematical theory of non–uniform gases.* Cambridge University Press, 1970.

[13] L. Chaput. Direct solution to the linearized phonon Boltzmann equation. *Phys. Rev. Lett.*, 110:265506, 2013.

[14] G. Chen. Thermal conductivity and ballistic-phonon transport in the cross-plane direction of superlattices. *Phys. Rev. B*, 57:14958–14973, Jun 1998.

[15] G. Chen. Particularities of heat conduction in nanostructures. *J. Nanopart. Res.*, 2:199–204, 2000.

[16] M. Darbandi and E. Roohi. DSMC simulation of subsonic flow through nanochannels and micro/nano steps. *Int. Commun. Heat Mass*, 38:1444–1449, 2011.

[17] R. Debye. Zur theorie der spezifischen wärmen. *Ann. Phys.*, 39, 1912.

[18] W. Dreyer. Maximisation of the entropy in non-equilibrium. *J. Phys. A: Math. Gen.*, 20:6505, 1987.

[19] W. Dreyer and H. Struchtrup. Heat pulse experiments revisited. *Contin. Mech. Thermodyn.*, 5:3–50, 1993.

[20] A. Einstein. Die Plancksche theorie der strahlung und die theorie der spezifischen wärme. *Ann. d. Phys.*, 22, 1907.

[21] M. Epstein. Predicting continuum breakdown of rarefied micro/nano flows using entropy and entropy generation analysis. *AIAA journal*, 5:1797, 1967.

[22] M. I. Flik, B. I. Choi, and K. E. Goodson. Heat transfer regimes in microstructures. *ASME J. Heat Transfer*, 114:666–674, 1992.

[23] M. Fryer. *The macroscopic transport equations of phonons in solids, MSc thesis.* University of Victoria, 2012.

[24] M. Fryer and H. Struchtrup. Moment model and boundary conditions for energy transport in the phonon gas. *Continuum Mech. Thermodyn.*, 26:593–618, 2013.

[25] J. R. Goldman and J. A. Prybyla. Ultrafast dynamics of laser-excited electron distributions in silicon. *Phys. Rev. Lett.*, 72:1364–1367, Feb 1994.

[26] H. Grad. On the kinetic theory of rarefied gases. *Commun. Pure Appl. Math.*, 2:331–407, 1949.

[27] H. Grad. *Principles of the kinetic theory of gases.* Handbuch der Physik. Springer, 1958.

[28] R. J. Gutfeld and A. H. Nethercot. Heat pulses in quartz and sapphire at low temperatures. *Phys. Rev. Lett.*, 12:641, 1964.

[29] R. A. Guyer and J. A. Krumhansl. Dispersion relation for second sound in solids. *Phys. Rev.*, 133:14117, 1964.

[30] R. A. Guyer and J. A. Krumhansl. Solution of the linearized phonon Boltzmann equation. *Phys. Rev.*, 148:7668, 1966.

[31] R. A. Guyer and J. A. Krumhansl. Thermal conductivity, second sound and phonon hydrodynamic phenomena in non-metallic crystals. *Phys. Rev.*, 148:778, 1966.

[32] N. Hadjiconstantinou. Dissipation in small scale gaseous flows. *ASME. J. Heat Transfer*, 125:944–947, 2003.

[33] N. Hadjiconstantinou, A. Garcia, M. Bazant, and G. He. Statistical error in particle simulations of hydrodynamic phenomena. *J. Comput. Phys.*, 187:274–297, 2003.

[34] N. G. Hadjiconstantinou and A. L. Garcia. Statistical error in particle simulations of low mach number flows. *Proceedings of the First MIT conference on computational Fluid and solid mechanics*, 2001.

[35] A. Henry and G. Chen. Microscale heat conduction in dielectric thin films. *J. Comput. Theor. Nanosci*, 5:12, 2008.

[36] J. J. Hinchen and W.M. Foley. Scattering of molecular beams by metallic surfaces. *Proceedings of the fourth international symposium on rarefied gas dynamics*, 1966.

[37] M. G. Holland. Analysis of lattice thermal conductivity. *Phys. Rev.*, 132:2461, 1963.

[38] J.A. Johnson, A.A. Maznev, J. Cuffe, J.K. Eilason, A.J. Minnich, T. Kehoe, C.M. S. Torres, G. Chen, and K.A. Nelson. Direct measurement of room-temperature nondiffusive thermal transport over micron distances in a silicon membrane. *Phys. Rev. Lett.*, 110:025901, 2013.

[39] D. Joseph and L. Preziosi. Heat waves. *Rev. Mod. Phys.*, 61, 1989.

[40] Y. S. Ju and K. E. Goodson. Phonon scattering in silicon films with thickness of order 100 nm. *Applied Physics Letters*, 74(20):3005–3007, 1999.

[41] G.E. Karniadakis, A. Beskok, and N. Aluru. *Microflows and Nanoflows: Fundamentals and simulation.* Springer, New York, 2005.

[42] C. Kittel. *Introduction to solid state physics.* John Wiley & sons, Hoboken, 1996.

[43] P. G. Klemens. *Solid state physics.* Academic press, New York, 1958.

[44] T. Klinc and I.Kuščer. Slip coefficients for general gas surface interaction. *Phys. Fluids*, 15:10118, 1972.

[45] M. N. Kogan, V. S. Galkin, and O. G. Fridlender. Stresses produced in gases by temperature and concentration inhomogeneities, New types of free convection. *Sov. Phys. Usp.*, 19:420–428, 1976.

[46] S. Kosuge, K. Aoki, S. Takata, R. Hattori, and D. Sakai. Steady flows of a highly rarefied gas induced by nonuniform wall temperature. *Phys. Fluid*, 23:030603, 2011.

[47] G. M. Kremer. *An introduction to the Boltzmann equation and transport processes in gases.* Springer, 2010.

[48] R. G. Lord. Some extensions to the Cercignani–Lampis gas–surface scattering kernel. *Phys. Fluids A*, 3:706–710, 1991.

[49] A. Majumdar. *Microscale energy transport in solids.* Taylor and Francis, Washington DC, 1998.

[50] AA. Majumdar. Microscale heat conduction in dielectric thin films. *ASME. J. Heat Transfer*, 115:7–16, 1993.

[51] J. C. Maxwell. On stresses in rarefied gases arising from inequalities of temperature. *Philos. Trans. R. Soc. London*, 170:231–256, 1879.

[52] A. A. Maznev, J. A. Johnson, and K. A. Nelson. Onset of nondiffusive phonon transport in transient thermal grating decay. *Phys. Rev. B*, 84:195206, 2011.

[53] A. A. Maznev, K. A. Nelson, and J. A. Rogers. Optical heterodyne detection of laser-induced gratings. *Opt. Lett.*, 23:1319–1321, 1998.

[54] E. Meiburg. Comparison of the molecular dynamics method and the direct simulation technique for flows around simple geometries. *Phys. Fluids*, 29:3107–3113, 1986.

[55] N. Mingo, L. Yang, D. Li, and A. Majumdar. Predicting the thermal conductivity of si and ge nanowires. *Nano Letters*, 3:1713 –1716, 2003.

[56] A. Mohammadzadeh, A. Rana, and H. Struchtrup. Thermal stress vs. thermal transpiration: A competition in thermally driven cavity flows. *Phys. Fluids*, 27:112001, 2015.

[57] A. Mohammadzadeh, A.S. Rana, and H. Struchtrup. DSMC and R13 modeling of the adiabatic surface. *Int. J. Thermal Sciences*, 101:9–23, 2016.

[58] A. Mohammadzadeh, E. Roohi, and H. Niazmand. A parallel DSMC investigation of monatomic/diatomic gas flow in micro/nano cavity. *Numer. Heat Tr. A*, 63, 2013.

[59] A. Mohammadzadeh, E. Roohi, H. Niazmand, S. Stefanov, and R.S. Myong. Thermal and second-law analysis of a micro- or nano-cavity using direct-simulation Monte Carlo. *Phys. Rev. E*, 85:056310, 2012.

[60] A. Mohammadzadeh and H. Struchtrup. Velocity dependent Maxwell boundary conditions in DSMC. *Int. J. Heat Mass Transfer*, 87:151–160, 2015.

[61] A. Mohammadzadeh and H. Struchtrup. A moment model for phonon transport at room temperature. *Continuum Mech. Therm., First Online Doi:10.1007/s00161-016-0525-y*, page 28, 2016.

[62] H. Niazmand, A. Mohammadzadeh, and E. Roohi. Predicting continuum breakdown of rarefied micro/nano flows using entropy and entropy generation analysis. *Int. J. Mod. Phys. C*, 24:1350029–1350029, 2013.

[63] T. Ohwada, Y. Sone, and K. Aoki. Numerical analysis of the Poiseuille and thermal transpiration flows between two parallel plates on the basis of the Boltzmann equation for hardsphere molecules. *Phys. Fluids A*, 1:2042, 1989.

[64] R. Peierls. Zur kinetischen theorie der wärmeleitung in kristallen. *Annalen der physik*, pages 1055–1101, 1929.

[65] J.-P. M. Péraud and N. G. Hadjiconstantinou. Efficient simulation of multidimensional phonon transport using energy-based variance-reduced monte carlo formulations. *Phys. Rev. B*, 84:205331, 2011.

[66] J-P. M. Peraud and N.G. Hadjiconstantinou. An alternative approach to efficient simulation of micro/nanoscale phonon transport. *Appl. Phys. Lett.*, 101:153114, 2012.

[67] E. Pop, R. W. Dutton, and K. E. Goodson. Analytic band Monte Carlo model for electron transport in Si including acoustic and optical phonon dispersion. *J. Appl. Phys.*, 96:4998, 2004.

[68] A. S. Rana, A. Mohammadzadeh, and H. Struchtrup. A numerical study of the heat transfer through a rarefied gas confined in a micro cavity. *Cont. Mech. Thermodyn*, 27:433–446, 2014.

[69] A.S. Rana, M. Torrilhon, and H Struchtrup. A robust numerical method for the R13 equations of rarefied gas dynamics: application to lid driven cavity. *J. Comput. Phys.*, 236:169, 2013.

[70] V. Romano and A. Rusakov. 2D numerical simulations of an electron-phonon hydrodynamical model based on the maximum entropy principle. *Comput. Methods Appl. Mech. Eng.*, 199:2741–2751, 2010.

[71] E. Roohi, M. Darbandi, and V. Mirjalili. Direct Simulation Monte Carlo solution of subsonic flow through micro/nanoscale channels. *J. Heat Transf.*, 131:92402, 2009.

[72] F. Sharipov. Application of the Cercignani–Lampis scattering kernel to calculations of rarefied gas flows. ii. slip and jump coefficients. *Eur. J. Mech. B/Fluids*, 22:133–143, 2003.

[73] F. Sharipov and V. Seleznev. Data on internal rarefied gas flows. *J. Phys. Chem. Ref. Data*, 27:657–706, 1998.

[74] F. M. Sharipov and E. A. Subbotin. On optimization of the discrete velocity method used in rarefied gas dynamics. *ZAMP*, 44:572–577, 1993.

[75] D.W. Snoke. *Solid state physics; essential concepts.* Addison-Wesley, San Francisco, 2009.

[76] Y. Sone. Flows induced by temperature fields in a rarefied gas and their ghost effect on the behavior of a gas in the continuum limit. *Annu. Rev. Fluid Mech.*, 32:779–811, 2000.

[77] Y. Sone. *Kinetic theory and fluid dynamics.* Birkhauser, Boston, 2002.

[78] Y. Sone. Comment on heat transfer in vacuum packaged micro–electro–mechanical system devices phys. fluids 20, 017103, (2008). *Phys. Fluid*, 21:119101, 2009.

[79] Y. Sone and T Doi. Ghost effect of infinitesimal curvature in the plane couette flow of a gas in the continuum limit. *Phys. Fluids*, 16:952–971, 2004.

[80] H. Struchtrup. Stable transport equations for rarefied gases at high orders in the Knudsen number. *Phys. Fluids*, 16:3921, 2004.

[81] H. Struchtrup. *Macroscopic transport equations for rarefied gas flows.* Springer, Berlin, 2005.

[82] H. Struchtrup. Scaling and expansion of moment equations in kinetic theory. *J. Stat. Phys.*, 125:565–587, 2006.

[83] H. Struchtrup. Maxwell boundary condition and velocity dependent accommodation coefficient. *Phys. Fluids*, 25:112001, 2013.

[84] H. Struchtrup and P. Taheri. Macroscopic transport models for rarefied gas flows: a brief review. *IMA J. Appl. Math.*, 76:672, 2011.

[85] H. Struchtrup and M. Torrilhon. Regularization of Grad's 13 moment equations: Derivation and linear analysis. *Phys. Fluids*, 15:2668, 2003.

[86] H. Struchtrup and M. Torrilhon. H-theorem, regularization, and boundary conditions for linearized 13–moment equations. *Phys. Rev. Lett.*, 99:014502, 2007.

[87] H. Struchtrup and M. Torrilhon. Higher-order effects in rarefied channel flows. *Phys. Rev. E*, 78:046301, 2008.

[88] H. Struchtrup and M. Torrilhon. Regularized 13 moment equations for hard sphere molecules: Linear bulk equations. *Phys. Fluids*, 25:052001, 2013.

[89] See supplemental material at http://link.aps.org/ supplemental/10.1103/PhysRevLett.110.025901 for further information on methods and analysis.

[90] P. Taheri and H. Struchtrup. Rarefaction effects in thermally-driven microflows. *Physica A*, 389:3069–3089, 2010.

[91] L.B. Thomas. *In fundamental of gas-surface interactions.* Academic Press, New York, 1967.

[92] M. Torrilhon and H. Struchtrup. Regularized 13-moment equations: Shock structure calculations and comparison to Burnett models. *J. Fluid. Mech.*, 513:171–198, 2004.

[93] M. Torrilhon and H. Struchtrup. Boundary conditions for regularized 13–moment–equations for micro–channel flows. *J. Comp. Phys.*, 227:1982, 2008.

[94] P.Y. Tzeng, C.Y. Soong, M.H. Liu, and T.H. Yen. Atomistic simulation of rarefied gas natural convection in a finite enclosure using a novel wall-fluid molecular collision rule for adiabatic solid walls. *International Journal of Heat and Mass Transfer*, 51(34):445 – 456, 2008.

[95] D. Valougeorgis and S. Naris. Acceleration schemes of the discrete velocity method: Gaseous flows in rectangular microchannels. *SIAM J. Sci. Comput*, 25:534–552, 2003.

[96] M. Vargas, G. Tatsios, and D. Valougeorgis. Rarefied gas flow in a rectangular enclosure induced by non-isothermal walls. *Phys. Fluid*, 26:057101, 2014.

[97] W. Wagner. A convergence proof for Bird's Direct Simulation Monte Carlo method for the Boltzmann equation. *J. Stat. Phys*, 66:1011, 1992.

[98] Q. Wang, X. Yan, and Q. He. Heat-flux-specified boundary treatment for gas flow and heat transfer in microchannel using direct simulation monte carlo method. *Int. J. Numer. Meth. Engng.*, 74:1109–1127, 2008.

[99] Q. W. Wang, C. L. Zhao, M. Zeng, and Y. N. Wu. Numerical investigation of rarefied diatomic gas flow and heat transfer in a microchannel using DSMC with uniform heat flux boundary condition-part I: Numerical method and validation. *Numer. Heat Tr-B*, 53:160–173, 2008.

[100] A. Ward and D. A. Broido. Intrinsic phonon relaxation times from first-principles studies of the thermal conductivities of si and ge. *Phys. Rev. B*, 81:085205, 2010.

[101] W. Weiss. Continuous shock structure in extended thermodynamics. *Phys. Rev. E*, 52:5760, 1995.

[102] E. Yariv. Thermophoresis due to strong temperature gradients. *Siam J. Appl. Math.*, 69:453–472, 2008.

[103] Peter YU and Manuel Cardona. *Fundamentals of semiconductors*. Springer-Verlag Berlin Heidelberg, 2010.